

Numerical simulation of flow and compression of green sand

Hovad, Emil; Hattel, Jesper Henri; Larsen, Per Leif; Thorborg, Jesper

Publication date:
2017

Document Version
Publisher's PDF, also known as Version of record

[Link back to DTU Orbit](#)

Citation (APA):

Hovad, E., Hattel, J. H., Larsen, P. L., & Thorborg, J. (2017). Numerical simulation of flow and compression of green sand. Kgs. Lyngby: Technical University of Denmark (DTU).

DTU Library

Technical Information Center of Denmark

General rights

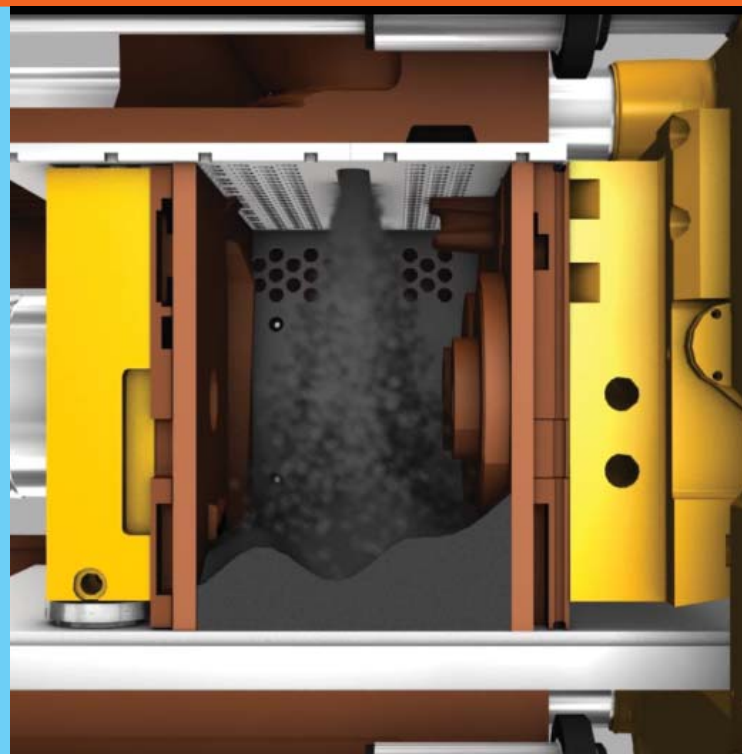
Copyright and moral rights for the publications made accessible in the public portal are retained by the authors and/or other copyright owners and it is a condition of accessing publications that users recognise and abide by the legal requirements associated with these rights.

- Users may download and print one copy of any publication from the public portal for the purpose of private study or research.
- You may not further distribute the material or use it for any profit-making activity or commercial gain
- You may freely distribute the URL identifying the publication in the public portal

If you believe that this document breaches copyright please contact us providing details, and we will remove access to the work immediately and investigate your claim.

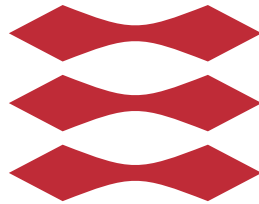
Numerical simulation of flow and compression of green sand

PhD Thesis



Emil Hovad
February 2017

DTU



Numerical simulation of flow and compression of green sand

Emil Hovad

Department of Mechanical Engineering
Technical University of Denmark

A thesis submitted for the degree of
Doctor of Philosophy
February 2017

Title of the thesis:

Numerical simulation of flow and compression of green sand

Ph.D. Student: Emil Hovad

E-mail: emilh@mek.dtu.dk

Main Supervisor:

Jesper Henri Hattel

Technical University of Denmark

E-mail: jhat@mek.dtu.dk

Co-supervisors:

Jesper Thorborg

Magma GmbH

Technical University of Denmark

E-mail: jest@mek.dtu.dk

Jens Honore Walther

Technical University of Denmark

E-mail: jhw@mek.dtu.dk

Per Larsen

DISA Industries A/S, Højager 8, Høje Taastr., 2630 Taastrup, Denmark

E-mail: per.larsen@noricangroup.com

Address:

Department of Mechanical Engineering, Section of Manufacturing Engineering Technical
University of Denmark Produktionstorvet, Building 425, 2800 Kgs. Lyngby, Denmark

Copyright © 2017 Emil Hovad

Preface

This work has been carried out at the Department of Mechanical Engineering (MEK), Technical University of Denmark (DTU) and DISA Industries a/s, during the period 15.08.2013-14.02.2017. The work was supervised by Professor Jesper H. Hattel (MEK), co-supervised by PhD Jesper Thorborg (MEK and MAGMA), PhD Per Larsen (Innovation Manager at DISA Industries a/s) and Professor Jens H. Walther (MEK). The work was funded by Innovation Fund Denmark project [Grant number. 1355-00087B] in collaboration with the Danish company DISA Industries A/S in the period 15-08-2013 to 14-08-2016.

A big thanks to Jesper H. Hattel for giving great help with respect to acquiring knowledge, academic rigor, writing articles, the PhD thesis and being a good supervisor overall. A great thanks goes out to Jesper Thorborg for his great contribution to the PhD project. His great emphasis's on structure, details and presenting knowledge in a structured manner has helped me tremendously with regards to my PhD project and my work in general. Thanks to Per Larsen from DISA for helping the PhD project with experimental knowledge and setting up experiments. A very big thanks to DISA Industries A/S and Per Larsen for giving me time to focus on relevant tasks with respect to my research regarding simulating the sand shot in the DISAMTIC process. A big thanks to Jens H. Walther for a great help, patience and special knowledge with respect to simulating granular flow in the commercial software package of STAR-CCM+ and additionally helping me with writing articles. A big thanks to associate professor Jon Spangenberg for motivation, insight and understanding that sometimes it can be stress-full being a PhD student and for good suggestions regarding writing the PhD thesis and articles in general. Thanks to associate professor Niels Tiedje (MEK) for the use of the foundry equipment and other suggestions with respect to the project. Thanks to Lars Georg Kiørboe for the use of the Ring shear tester at DTU CHEMICAL ENGINEERING, Department of Chemical and Biochemical Engineering.

signature



Abstract

The focus of the industrial PhD project was concentrated on the production of the sand mold (green sand) which gives the cast component its final geometrical shape. In order to ensure a high quality of the cast component, it is important to control the manufacturing process of the mold itself so that it is homogeneous and stable. Therefore gaining a basic understanding of how the flow and deposition of green sand should be characterized and modelled was important, so that it could be used for simulation of the manufacturing process of the sand mold.

The flowability of the green sand is important when the sand flows down through the hopper filling the chamber with sand during the sand shot. The flowability of green sand is mostly governed by the amount of water and bentonite which both decrease it. The flowability and the internal forces thus control how well you can fill a complex mold geometry in which shadowing from ribs and other geometric obstacles may be present. If the flow stops prematurely it might hinder the mould from being completely filled or result in too high variation in the material density which could influence the final surface of the cast part. The wet bridges created by the bentonite makes the sand grains stick together where the bentonite and water make the green sand very cohesive and by squeezing the mixture it obtains mechanical properties that stabilizes the mold to acquire a strong mold for the casting process. Therefore the green sand flowability is important during the sand shot for a proper filling of the chamber, and subsequently the solid mechanical properties during the squeezing process are important for the final strength of the mold. This is problematic since these mechanical behaviours have an inverse relationship, e.g if the green sand is too dry then the green sand flowability will be very high and the strength of the mold will be low and vice versa at least for the wet green sand up to a certain water content level. Therefore, obtaining the correct green sand condition and improving the filling of the mold during the sand shot are of great importance.

The Discrete Element Method (DEM) was chosen as the numerical model since the discrete nature of the method simulates the granular structure of the green sand with good agreement. The DEM model uses a rolling resistance model to emulate the non-spherical quartz sand particles' resistance to rolling as well as a cohesive model to emulate the binding of the quartz sand particles from the bentonite.

The green sand was characterized with a ring shear tester where the yield locus was

found and a new way to define the flowability was suggested. The ring shear tester was used to obtain the static friction coefficients for the DEM model. A sand pile experiment was used to investigate the simple mechanical behaviour of green sand from the measured height. From this height the DEM model was also calibrated with respect to obtaining the values of the rolling resistance and obtaining the parameter in cohesive model.

The project dealt with the flow of the sand particles and the deposition of sand during the production of sand molds using the sand shot in the DISAMATIC process. The deposition of the green sand in the chamber was investigated with a special cavity design where air vents were placed inside the cavities. The air vents are used to transport the green sand with an airflow during the sand shot. By changing the air vents settings in the chamber and in the cavities it was possible to improve the filling in the narrow passages in the cavity design, thereby improving the final sand mold as well. The sand shot with the cavity design was simulated by the discrete element method (DEM) modelling the flow of the green sand combined with classical computational fluid dynamics (CFD) for modelling the airflow in the chamber and the airflow through the air vents. These experiments and simulations gave beneficial insights to the DISAMATIC process and how to improve it. Additionally fluidization properties of green sand were investigated with a fluidized bed and the newly developed Anton Paar Powder Cell was used to obtain the fluidized viscosity.

Commercial aspects

Knowledge was acquired about the filling of the mold chamber with green sand in a special designed cavity geometry. The settings of the air vents together with the air pressure initially applied in the air tank gave valuable ideas for improving the filling in the cavities thereby improving the final mold. Furthermore, it was possible to apply the commercial software of STAR-CCM+ using the combined CFD-DEM model to simulate the process with a 3-D slice representation of the geometry successfully. This makes it more feasible to develop a stand-alone code in the future for simulating the DISAMATIC process. The sand shot in the DISAMATIC process might also be modelled with a continuum model where the ring shear tester could give indications of the solid mechanical behaviour of the green sand and the Anton Paar Powder Cell could be used for obtaining the fluidized viscosities of the green sand.

Resumé

ErhvervsPhD projektet omhandlede produktion af støbeforme i grønsand. Støbeformen giver den støbte metalkomponent sin endelige geometriske udformning. For at sikre en høj kvalitet af den støbte komponent, er det vigtigt at kontrollere fremstillingsprocessen af selve formen, således at den er homogen og stabil. Derfor er det vigtigt at få en grundlæggende forståelse og viden om hvordan sandet flyder og aflejres. Denne viden opnås via karakterisering af sandet med forskellige typer af forsøg. Når sandet er karakteriseret vha. forsøgene, kan disse forsøg anvendes til at kalibrere en computermodel. Den kalibrerede computermodel kan efterfølgende anvendes til simulering af DISAMATIC processens sandskud.

Flydeevnen af grønsandet er vigtigt, når det strømmer ned gennem sandsiloen og fylder kammeret under sandskuddet. Flydeevnen af sandet er hovedsageligt styret af mængden af vand og bentonit, som begge formindsker flydeevnen. Denne flydeevne og de interne spændinger i materialet er afgørende for hvor godt en kompleks kammergeometri kan fyldes, hvor geometriske forhindringer kan være til stede. Hvis sandet stopper med at flyde for tidligt, kan det forhindre formen i at blive helt fyldt eller resulterer i en forhøjet variation i densiteten, dette kan potentielt påvirke udformningen af den endelige metalkomponents overflade. Sandkornene klæber sig sammen pga. bentonitten og vandet, hvor bentonitten skaber små broer, som klæber de individuelle sandkorn sammen. Når blandingen trykkes sammen opnås der dermed mekaniske egenskaber, der stabiliserer formen. Grønsandets flydeevne er derfor vigtig i sandskuddet for at opnå en korrekt fyldning af kammeret og derefter er gode faststofmekaniske egenskaber opnået under presseprocessen vigtige for den endelige styrke af formen. Dette er problematisk, eftersom disse to mekaniske egenskaber har et omvendt forhold, fx hvis sandet er for tørt vil flydeevnen være høj, og styrken af formen vil være lav og det omvendte er tilfældet for vådt sand, i det mindste op til et vist vandindhold. Derfor er tilstanden af grønsandet vigtig, så man kan opnå en optimal fyldning af formen under sandskuddet.

Discrete Element Method (DEM) blev valgt som den numeriske metode, idet den diskrete karakter af metoden simulerer den granulære struktur af sandet med god overensstemmelse. DEM modellen bruger en rullemodstandsmodel for at efterligne de ikke-sfæriske kvartssandkorns modstand mod rulning og en kohæsionsmodel til at efterligne bindingen af kvartssandskornene fra bentonitten.

Sandet blev karakteriseret med en ring shear tester, hvor den kunne detektere yield locus og en ny måde at definere flydeevnen er blevet foreslået. Ring shear tester'en blev anvendt til at bestemme friktionskoefficienterne anvendt i DEM modellen. Et sandbunkeforsøg blev anvendt til at undersøge den simple mekaniske opførsel af sandet, hvor karakteriseringen blev opnået ud fra højden af bunken. Fra denne højde kunne DEM modellen også blive kalibreret med henblik på fremskaffelsen af værdien for rullemodstanden og man fandt også kohæsions parameteren.

Projektet behandlede strømmningen af sandpartiklerne og aflejringen af dem ved fremstillingen af sandformen under sandskuddet i DISAMATIC processen. Aflejringen af grønsandet i kammeret blev undersøgt med et særligt hulrumsdesign, hvor luftventiler blev placeret inde i hulrummene. Luftventilerne bruges til at transportere sandet via luftstrømme under sandskuddet. Ved at ændre ventilindstillingerne i kammeret og i hulrummene var det muligt at forbedre fyldningen i de smalle passager i hulrumsdesignet, og derved forbedre den endelige sandform. Sandskuddet i hulrumsdesignet blev simuleret med DEM metoden kombineret med klassisk Computational Fluid Dynamics (CFD) til modellering af luftstrømmen i kammeret og luftstrømmen gennem luftventilerne. Disse eksperimenter og simuleringer gav indsigt i DISAMATIC processen og hvordan man kan forbedre den. Derudover blev fluidiseringsegenskaberne af grønsandet undersøgt med en fluidized bed test og den nyudviklede Anton Paar Powder Cell blev anvendt til at finde den fluidiserede viskositet.

Kommercielle aspekter

Viden blev erhvervet om fyldningen af kammeret med grønsand med den specielt designede hulrumsgeometri. Indstillingerne for luftventilerne sammen med lufttrykket i lufttanken gav værdifulde ideer til forbedring af fyldningen i hulrummene og derved forbedre den endelige støbeform. Desuden var det muligt at anvende den kommercielle software pakke STAR-CCM+ med en kombineret CFD-DEM-model til at simulere processen med en 3-D skive som repræsenterede geometrien med succes. Dette gør det muligt at udvikle en selvstændig kode i fremtiden, som kan simulere DISAMATIC processen. Sandskuddet i DISAMATIC processen kunne også blive modelleret med en kontinuumsmodel, hvor ring shear tests kunne give indikationer af den faste mekaniske opførsel af sandet og Anton Paar Powder Cell testen kunne anvendes til at bestemme den fluidiserede viskositet af sandet.

List of publications

Appended articles

1. E. Hovad, P. Larsen, J. H. Walther, J. Thorborg and J. H. Hattel. Flow dynamics of green sand in the DISAMATIC moulding process using discrete element method (DEM), IOP Publishing, IOP Conference Series: Materials Science and Engineering, 84, 1, 012023, 2015, 17578981, 1757899x. PAPER [1].
2. E. Hovad, J. Spangenberg, P. Larsen, J.H. Walther, J. Thorborg and J.H. Hattel, Simulating the DISAMATIC process using the discrete element method - a dynamical study of granular flow, Powder Technology, 303, 228 - 240, 2016, 0032-5910. PAPER [2].
3. E. Hovad, J. Spangenberg, P. Larsen, J.H. Walther, J. Thorborg and J.H. Hattel, Cavity prediction in sand mould production applying the DISAMATIC process, Submitted to Powder Technology in 2017. PAPER [3].
4. E. Hovad, J. Spangenberg, P. Larsen, J. Thorborg and J.H. Hattel, An analytical solution describing the shape of a yield stress material subjected to an overpressure, AIP Conference Proceedings, 2016, 1738, 1, eid = 030049, PAPER [4].
5. J. Spangenberg, R. Cepuritis, E. Hovad, G. W. Scherer and S. Jacobsen, Shape effect of crushed sand filler on rheology: a preliminary experimental and numerical study, Rilem publications, Rilem State of the Art Reports, 193-202, 2016, 22110852, 22110844. PAPER [5].
6. J. Masoud, J. Spangenberg, E. Hovad, R. Comminal, J. H. Hattel, K. I. Hartmann and D. Schuutz, RHEOLOGICAL CHARACTERIZATION OF GREEN SAND FLOW, Proceedings of the ASME 2016 International Mechanical Engineering Congress and Exposition, 2016. PAPER [6].
7. E. Hovad, J. Spangenberg, P. Larsen, J. Thorborg and J.H. Hattel, An non-dimensionlized analytical solution describing the shape of a yield stress material subjected to an overpressure. PAPER [7].

Contents

List of content	xiii
List of figures	xxii
List of tables	xxiv
1 Introduction	1
1.1 The DISAMATIC process	1
1.2 Research in the field of green sand test, sand casting and simulations	3
1.3 The main objectives of the thesis	4
1.4 Thesis overview	5
2 Material characterization of the green sand	7
2.1 Introduction	7
2.2 The green sand	8
2.2.1 Green sand composition	8
2.2.2 Tests to determine the green sand composition	8
2.2.3 Qualitative mechanical behaviour of the green sand	10
2.2.4 The green sand batch preparation and the simple foundry tests	10
2.2.5 Results of the simple foundry tests	13
2.2.6 Conclusion of the simple foundry tests	18
2.3 Five mechanical behaviours in the DISAMATIC process	19
2.3.1 High load flow (1)	20
2.3.2 The low load flow (2)	36
2.3.3 Fluidized flow (3)	44
2.3.4 The confined compression (4)	46
2.3.5 The un-confined strength (5)	47
2.4 Overall conclusion of all the experiments	51
3 The Discrete Element Method and its calibration	53
3.1 Introduction	53
3.2 Introduction to DEM in general	53
3.2.1 The numerical model applied	54
3.3 Calibrating the DEM model for applications	58

3.3.1	Simulating the high load flow regime (1)	58
3.3.2	Simulating the low load flow regime (2)	61
3.3.3	Simulating the fluidized flow regime (3)	71
3.3.4	Simulating the solid mechanics regime (4)-(5)	71
3.4	Conclusion	72
4	Simulating the rib chamber geometry	73
4.1	Introduction	73
4.2	The rib chamber geometry and the DISAMATIC process	73
4.3	Monitoring the DISAMATIC experiments	74
4.4	Simulation settings for the DISAMATIC process	75
4.4.1	Calculating the inlet velocity and the particle flow rate	76
4.4.2	The particle velocity distribution	77
4.4.3	The 2-D sensitivity study	78
4.4.4	Definition of the filling times for the DEM simulation	80
4.5	Results of the simulations and the experiments	81
4.5.1	The filling times $t_1 - t_6$	81
4.5.2	The qualitative flow behaviour	86
4.6	Conclusion	92
5	Simulating the cavity chamber geometry	93
5.1	Introduction	93
5.1.1	Settings of the air vents	95
5.2	Governing equations	96
5.2.1	Governing equation and the Discrete Element Method	96
5.2.2	Governing equation for the air phase	96
5.3	Simulation settings for the DISAMATIC process	97
5.3.1	The CFD model and the boundary conditions for the airflow	97
5.3.2	Boundary condition for the granular flow	98
5.4	Results of the DISAMATIC process and simulations	99
5.4.1	The experimental measured air pressures and the filling times	99
5.4.2	The simulated filling times	101
5.4.3	Sand deposited in the two cavities	102
5.5	Conclusion	107
5.5.1	The experiments	107
5.5.2	The simulations	107
6	Conclusion and future Work	109
6.1	The material characterization of green sand	109
6.2	Calibration of the DEM model	110
6.3	The sand shot and the simulations	111
6.4	Future work	112

A	The green sand composition	123
A.1	Introduction	123
A.2	The green sand mixture and general sand properties	123
A.3	Determination of active bentonite contents	124
A.4	Total contents of fines	126
A.5	Particle size distribution with a sieve analysis	127
A.5.1	Summarized results of the tests performed until now	129
A.6	Loss on ignition test	129
A.7	Results and conclusion	130
B	Anton Paar Powder Cell tests of the green sand	131
B.1	Introduction	131
B.2	The experiment	132
B.3	Results	134
B.4	Conclusion	136
C	Fluidized bed tests of the green sand	137
C.1	Introduction to fluidization	137
C.1.1	The fluidization equipment	138
C.2	Fluidization theory	138
C.2.1	Algorithm for detecting minimum fluidization velocity (v_{mf}) and the constant pressure drop (ΔP_{mf}).	140
C.3	Results of the experiment	141
C.3.1	Experiment 1-6	142
C.3.2	Experiment number 7	146
C.4	Conclusion	147

List of Figures

1.1	The DISAMATIC process: 1. The sand shot. 2. Squeezing the mold. 3. Moving the mold to the chamber front and stripping off the swing plate (SP). 4. Mold close-up where the pressure plate (PP) pushes the mold out of the molding chamber. 5. Stripping off the PP where the PP is stripped from the mold and returns to its starting position in the molding chamber. 6. Closing the molding chamber and repeating a new cycle. The edited figure and text are from [8].	2
2.1	The green sand mixture. The figure is from [8].	8
2.2	The size distribution of the green sand applied in the project. The figure is from [9].	9
2.3	The wet bridges created in the bentonite from the water make the bentonite cohesive and thereby the sand grains will stick together. The pictures are from the slides in [10](http://www.sut.ac.th/engineering/Metal/ru/GREEN20%SAND.pdf).	10
2.4	The mixer together with the bucket containing the homogeneously mixed green sand.	11
2.5	The heater applied for the water content test (left) and the scale (right).	11
2.6	Green sand (left), is sieved into the cylinder and the density is found ρ (middle) and finally the ramming station is used to determine the compactability of the sand mixture by 3 rammings and the compacted density ρ_3 (right). The edited figure is originally from PAPER [2].	12
2.7	The water contents as a function of compactability of all the batches. The average value of the batches are shown with a cross and an individual color (green line used twice for batch 1 and batch 7). The standard deviations are shown for both the compactability and the water contents as a horizontal line and a vertical line respectively.	13
2.8	The water contents tests plotted in consecutive order for the high compactability (batch 6), the medium compactability (batch 3) and the low compactability (batch 8).	14
2.9	(IV) The density as a function of compactability where the compactability is in percentage % and the non-compacted density is denoted ρ and the compacted density is denoted ρ_3 with the units of $[\frac{kg}{m^3}]$	15

2.10	The compactability plotted for the consecutive tests for the three batches with high compactability batch 6 (red line), medium compactability batch 3 (black line) and low compactability batch 8 (blue line).	16
2.11	The density as a function of compactability with respect to the number of rammings 1-10. The first ramming starts from the left indicated by the number. The cross placed in the middle shows the average value of the batches with an individual color. The dotted lines are the standard deviations of compactability % as a horizontal line and the standard deviations of density [$\frac{kg}{m^3}$] as a vertical line.	17
2.12	(Top) The sequence in the DISAMATIC process (1)-(5). (Middle) The performed experiments placed on the Mohr circle (I)-(V). (Bottom) The five names of the mechanical behaviours.	19
2.13	The high load flow in the DISAMATIC process and the ring shear test placed on the Mohr circle.	21
2.14	Mohr circle. The figure is taken from [11]	22
2.15	(Left) A vertical stress is applied and (right) additionally a shear stress is applied. The figure is from [11].	23
2.16	(a) The ring shear procedure illustrated. (b) Illustration of finding the yield locus. (c) Experimental procedure for finding the points.(d) The experimental determination of the yield locus. The figures in the top (a) and (b) are from [11].	24
2.17	Yield locus and the three internal friction angles: φ_e (black dotted line) is the linearized yield locus angle, φ_{lin} (red line) is the effective angle of friction and φ_{sf} (blue line) the angle of internal friction at steady-state flow from the pre-shear point (σ_{pre}, τ_{pre}). The normal stress is in the direction of the x-axis (σ) and the shear stress is in the direction of the y-axis (τ). The major principal stress is σ_1 and the minor principal stress σ_2 for the confined sample (large circle) and the major principal stress is σ_c for the unconfined sample (small circle). The cohesion value found from the ring shear tester of the material is denoted τ_c . Note the edited figure and text is from PAPER [2] and originally from [11] where the theory is from [12].	25
2.18	Flowability function. The figure is taken from [11].	26
2.19	The selected normal loads ($\sigma_{w1}, \sigma_{w2}, \sigma_{w3}, \dots$) and the shear stresses history, τ_w (left figure). The wall yield locus found from the steady-state points (right figure). Note the edited figures and text are from PAPER [2] and originally from [11] where the theory is from [12].	27
2.20	(Ia) The Mohr Coulomb circle for the wet green sand (batch 2) and the dry green sand (batch 7).	28
2.21	(Ia) The Mohr Coulomb circles for the three selected batches.	30
2.22	(Ia) The angles: the repose angle α (black dots), the effective angle of friction φ_e (green dots), the linearized yield locus angle φ_{lin} (blue dots), the angle of internal friction at steady-state flow φ_{sf} (red dots) as a function of the compactability.	31

2.23 (Ia) The yield stress on the left y-axis (red) and the flowability (FFc) on the right y-axis (blue) as a function of the compactability on the x-axis.	31
2.24 (Ib) The wall sliding friction for the wet green sand (batch 2) and dry green sand (batch 7).	32
2.25 (Ib) The coulomb sliding friction for the three selected batches.	33
2.26 (Ic) The density as a function of stress found with the ring shear tester. The average value and the dotted line is the standard deviation of the density in $[\frac{kg}{m^3}]$	34
2.27 (Left side) The low load flow in the DISAMATIC process. (Right side) The performed experiments placed on the Mohr circle.	36
2.28 (Left) The hopper experiment can be seen with the sieve on the top, the hopper, orifice lid and finally the box in the bottom. (Middle) In the 3-D illustration the hopper measurement can be seen with the length $l=300$ mm, width of $a=180$ mm, orifice $c=40$ mm and the box measurements with the internal width $w_1=120$ mm, external width $w_2=134$, the height of the box $d=82$ mm, the measured height of the sand pile is denoted h_p and the drop height of $h_1=169$ mm and hopper height of $h_2=150$ mm. (Right) Sand pile experiment where the height h_p was found by a laser projected onto the ruler on the back. Note the box side and bottom thickness is 7 mm. The edited figure and text is originally from PAPER [2].	37
2.29 (a) The slump cylinder experiment setup. (b) The final slump where the two diameters of the sand pile is measured (denoted l_x, l_y) in orthogonal directions to each other.	39
2.30 (a) The slump box experiment setup. (b) The final slump where the slump length l_p are measured	39
2.31 (IIa) The sand pile experiments average heights (h_p) for all the batches. The standard deviation for compactability is shown as a line in the horizontal direction and the standard deviation for the pile height is shown as a line in the vertical direction.	40
2.32 (IIb) The slump cylinder lengths (l_p) for all the batches. The standard deviation for compactability is shown as a line in the horizontal direction and the standard deviation for the slump length is shown as a line in the vertical direction.	41
2.33 (IIc) The box test average slump lengths ($l_{p, 2-D}$) for all the batches. The standard deviation for compactability is shown as a line in the horizontal direction and the standard deviation for the slump length is shown as a line in the vertical direction.	42
2.34 (Left) The low load flow in the DISAMATIC process. (Right) The performed experiments placed on the Mohr circle. (Bottom) The simulation showing the fluidized flow of the DEM particles on the left side.	44

2.35	(Top) (4) Squeezing of the mold (confined compression) and (5) casting of the part and (un-confined strength) which is the solid mechanical behaviour of DISAMATIC process. (Bottom) The experiments performed in the project placed on the Mohr circle where (IV) the rammer creates a sample of green sand (confined compression). This sample is inserted into the STM machine performing (V) the uni-axial compression test (un-confined strength). The figure † in the left corner shows the deformation of a parts due to residual stresses and the figure is from [13].	46
2.36	The strength testing machine with the parts identified. A similar figure was first originally presented in [14].	48
2.37	Stress-strain curves made on the STM machine for one batch. The x-axis is the displacement with the units of [mm] and the y-axis is the stress with units of [$\frac{N}{cm^2}$]	48
2.38	(V) The compression tests for the three selected batches.	50
3.1	Particle i -th impact with particle j -th where the velocity is decomposed into a normal \vec{F}_n and tangential direction \vec{F}_t . The edited figure is from [15] . . .	54
3.2	Particle i - th impact with particle j - th, the force exerted on the i - th particle in the normal direction is $\vec{F}_{n_{ij}}$ and in the tangential direction is \vec{T}_i^{tot} . The edited figure is from PAPER [1].	55
3.3	Calibrating the DEM model at high load flow (1).	59
3.4	The low load flow calibration (2).	61
3.5	(left) The sand pile and the density inside the box for the 3-D simulation ρ_{DEM} . (Middle) The density inside the standard tube. (Right) The recalculated density in the slump simulation. The edited figure to the left are originally from PAPER [2].	62
3.6	(Top) The slump cylinder experiment. (Bottom) The simulation of the slump cylinder test and an illustration of the slump length algorithm. . . .	64
3.7	The height of the simulated sand pile (h_p) as function of the particle-particle rolling resistance ($\mu_{r,p-p}$). The black line is the mean height of the green sand pile experiment of $h_p = 0.054 \pm 0.002m$ with standard deviation of $\sigma = 0.002m$ (the two grey lines). The figure and the text are originally from article PAPER [2].	67
3.8	The height of the simulated sand pile (h_p) as function of the particle-particle rolling resistance ($\mu_{r,p-p}$). The black diamond is the mean height of the green sand pile experiment of $0.054 \pm 0.002m$ with the standard deviation of $\sigma = 0.002 m$ (black horizontal lines). The figure and the text are originally from PAPER [3].	67
3.9	Plot of the density: The black diamond is the mean density of the green sand pile experiment of $902 \pm 30 \frac{kg}{m^3}$ with plus/minus the standard deviation of $\sigma = 30 \frac{kg}{m^3}$ (thin black line). The simulated density as a function of the particle-particle rolling resistance ($\mu_{r,p-p}$) with the DEM simulations settings having the cohesion value of $W_{p-p} = 0.3 \frac{J}{m^2}$ (blue dotted line). . . .	68

3.10 (a) The black diamond is the mean length (diameter) of the green sand slump experiment of 0.186 ± 0.0548 m with the standard deviation of $\sigma = 5.48$ mm (thin black line). The simulated slump length as a function of the particle-particle rolling resistance ($\mu_{r,p-p}$) with the DEM simulations settings having the cohesion value of $W_{p-p} = 0.3 \frac{\text{J}}{\text{m}^2}$ (blue dotted line). (b) The selected simulation with the particle-wall rolling resistance of $\mu_{r,p-w} = 0.5$ 69

4.1 (left) The sand shot starts when the compressed air (P_{start}) from an air receiver blows air into the top of the hopper which drives the sand from the hopper through the sand slot down into the moulding chamber. The air in the chamber escapes through the small air vents. (middle) The sand is filling the chamber and the three cavities. (right) Finally the mould is squeezed and the mould is pressed out of the chamber ready for casting. The figure and the text are from PAPER [2]. 74

4.2 The progression of the flow front starts from the upper left going to the lower right. From the experimental video footage shot with the air pressure of 2.0 bar. The figure and text are taken from PAPER [2]. 75

4.3 The experimental progression of the sand pile flow front with respect to the eight times $t_1 - t_8$ for the compressed air pressures of 2.0 bar (black curve), 2.5 bar (red curve) and 3.0 bar (blue curve). The figure and text are taken from PAPER [2]. 75

4.4 (Left) From the green sand filling time of the four areas $A_1 - A_4$ (A_1 blue, A_2 red, A_3 black, A_4 green), four velocities ($v_1 - v_4$) can be calculated with the four selected time intervals $[t_0 \leq t \leq t_2, t_2 \leq t \leq t_4, t_4 \leq t \leq t_6, t_6 \leq t \leq t_8]$. (Right) From the four points an illustration of the velocities (v_1, v_2, v_3, v_4) are assumed to vary linearly in time with a constant final velocity of v_4 . The figure is from PAPER [2] and the chamber sections were applied for an approximation of the time filling dependent vertical velocity in PAPER [2]. 77

4.5 The six filling times $t_1 - t_6$ are found from the filling of the three boxes (t_2, t_4, t_6) and the three cavities (t_1, t_3, t_5). The magnitude of the velocity has been plotted with a scaling of 0-16 m/s. The figure is from PAPER [2] and a similar figure was also made in PAPER [1]. 80

4.6 Simulation of the compressed air pressure of 2.0 bar. (Left) From PAPER [1] with 2-D simulations having a constant inlet velocity and particle diameter sizes of 4 mm and 2 mm. (Right) From PAPER [2] with the time dependent velocities and the particle diameter size of 2 mm. 81

4.7 The simulated filling times $t_1 - t_6$ for the coefficient of restitution values. 82

4.8 The simulated filling times $t_1 - t_6$ for the rolling resistance and the cohesion values. 83

4.9 The simulated filling times $t_1 - t_6$ for different velocity distributions. 84

- 4.10 From the left to the right, (left) The simulations 2-D (red line) and 3-D (blue line) versus the experiment for 2.5 bar. (Right) The simulations 2-D (red line) and 3-D (blue line) versus the experiment for 3.0 bar for the entrance of the six times. The two figures and the text are from PAPER [2]. 85
- 4.11 The figures from the left to the right: The experimental video footage of the compressed air pressure of 2.0 bar, the 2-D constant velocity simulation (PAPER [1]), the 2-D linear interpolation velocity simulation and lastly the 3-D linear interpolation velocity from PAPER [2]. The figures and text are from PAPER [1] and from PAPER [2]. 86
- 4.12 The sensitivity and velocity analysis of the 2-D simulations of the compressed air pressure of 2.0 bar. 88
- 4.13 Flow contours obtained for the compressed air pressure of 2.0 bar: (left) The experimental video footage, (middle) the 3-D simulation $\mu_s = 0.50$, (right) the 2-D simulation $\mu_s = 0.50$. The experiments and simulations are all presented for the three selected times t_2 , t_4 and t_6 (from the upper figure to the lower figure). The magnitude of the velocity is plotted with a scaling of 0-16 m/s. The figure and text is from PAPER [2]. 89
- 4.14 Flow contours obtained for the compressed air pressure of 2.5 bar: (left) The experimental video footage, (middle) the 3-D simulation $\mu_s = 0.50$, (right) the 2-D simulation $\mu_s = 0.50$. The experiments and simulations are all presented for the three selected times t_2 , t_4 and t_6 (from the upper figure to the lower figure). The magnitude of the velocity is plotted with a scaling of 0-16 m/s. The figure and text is from PAPER [2]. 90
- 4.15 Flow contours obtained for the compressed air pressure of 3.0 bar: (left) The experimental video footage, (middle) the 3-D simulation $\mu_s = 0.50$, (right) the 2-D simulation $\mu_s = 0.50$. The experiments and simulations are all presented for the three selected times t_2 , t_4 and t_6 (from the upper figure to the lower figure). The magnitude of the velocity is plotted with a scaling of 0-16 m/s. The figure and text is from PAPER [2]. 90
- 4.16 The simulation for the three compressed air pressures 2.0 bar, 2.5 bar and 3.0 bar from the left to the right at (left), (middle), (right) the 2-D simulation is placed in the top and the 3-D simulation is placed in the bottom. (top) The 2-D simulation when the sand reaches the top of the chamber at $t=0.77$ (left), at $t=0.68$ (middle) and at $t=0.62$ (right). (bottom) The 3-D simulation when the sand reaches the top of the chamber at $t=0.95$ (left), at $t=0.72$ (middle) and at $t=0.73$ (right). The magnitude of the velocity is plotted with a scaling of 0-16 m/s. The figure and text is from PAPER [2]. 91

5.1	A photo of the chamber where the two cavities are placed on the lower left hand side on the pattern plate and the pattern plate is positioned on the Swing Plate side (SP). The sand shot start is indicated by the red light t_{start} and the flow behaviour of the green sand is monitored on the right hand side (PP side) with the 8 horizontal lines $l_1 - l_8$ equally spaced 50 mm apart. The air pressures are monitored by sensors in the air tank (light black cross), the shot valve (green cross), the hopper (black cross), the top of the chamber (red circle) and the bottom of the chamber (blue circle) where the sensors are listed from the top to the bottom.	94
5.2	(a) The simulated geometry, measurements and the areas applied for finding the particle flow rate and the particle inlet velocity. (b) The mesh and the air vent placements. The edited figures are from PAPER [3].	97
5.3	The filling times for case 6 - 7. The sand shot pressure is 1.5 bar in case 6 (black) and the pressure is 3.0 bar in case 7(blue).	98
5.4	The vertical inlet velocities for the simulations of case 6 - 7.	99
5.5	The pressure as a function of time shown in the positions listed from the top to the bottom: the air tank (black dotted line), the pressure shot valve (green), the hopper (black line), the pressure in the top of the chamber (red line) and in the bottom (blue line). The dotted black vertical lines is the filling times $t_0 - t_7$ of the chamber.	100
5.6	The experimental and simulation filling times of case 6 and case 7.	101
5.7	Case 6: The cavity masses as a function of time where $t_0 = 0.0$ s is the starting time on the x-axis.	103
5.8	Case 7: The cavity masses as a function of time where $t_0 = 0.0$ s is the starting time on the x-axis.	104
5.9	The time dependent velocity $v_y(t)$ simulation at time $t=0.50$ s. (Top) The velocity of the air phase. (Middle) The velocity of the particles. (Bottom) The experimental video footage at time $t=0.50$ s.	105
5.10	The time dependent velocity $v_y(t)$ simulation at time $t=0.50$ s. (Top) The velocity of the air phase. (Middle) The velocity of the particles. (Bottom) The experimental video footage at time $t=0.50$ s for case 6 where for case 7 the video footage is at time $t=0.48$ s (at $t=0.50$ s the photo was black).	106
A.1	The green sand mixture. The figure is from [8]	124
A.2	The recommended properties for the green sand when applied in the DISAMATIC process. The figure is from [8].	124
A.3	(A) Setup for methylene blue test and the reagent flask mixer. (B-D) results from the filter papers. The figure is from [9]	125
A.4	Calibration curve for methylene blue test with active bentonite contents of 11.9 %. The figure is from [9]	126
A.5	Figure showing graphical representation of the sieve analysis. The figure is from [9].	128
A.6	Showing the setup of crucibles inside the furnice.	130

B.1	The Anton Paar machine.	131
B.2	(Left) The Anton Paar machine seen from the side. (Middle) The cell where the propeller is positioned (this figure is edited from [6]).(Right) Illustration of the principle of the AP powder cell.	132
B.3	Pressure drop measurement over the green sand. The figure is from [6]. . .	134
B.4	Shear dependent behavior of green sand at different flow rates (viscosity vs. shear rate). The figure and text are from [6].	135
B.5	Shear stress vs. shear rate relationship for green sand at different flow rates. The figure and text are from [6].	135
B.6	The shear stress as a function of the shear rate. The figure is from [6]. . . .	136
C.1	Schematic illustration of green sand moulding from [6].	137
C.2	The fluidized bed setup. The figure is from [16].	138
C.3	A simple presentation of the relationship between the pressure drop and the inlet gas velocity. The relationship can roughly be estimated by two lines, with the first part being the linear interpolation of the increase in pressure and second part of the fluidization curve being the constant pressure ($\Delta P = \Delta P_{mf}$) as a straight line part occurring after the minimum fluidization (V_{mf}). The edited figure is originally from [17].	139
C.4	Low water contents: The minimum fluidization is found for (a) experiment 1 and (b) experiment 2 in the fluidized bed experiment. Each experiment was repeated 3 times with the colors blue, red and black for test 1 to test 3 subsequently. The points are the experiments, the line is a linear interpolation and the circle is the minimum fluidization point. Note the scaling on the x-axis is different from (a) experiment 1 to (b) experiment 2.	143
C.5	Medium water contents: The minimum fluidization is found for (a) experiment 3 and (b) experiment 4 for the fluidized bed test. Each experiment was repeated 3 times with the colors blue, red and black for test 1 to test 3 subsequently. The points are the experiments, the line is a linear interpolation and the circle is the minimum fluidization point.	144
C.6	High water contents: The minimum fluidization is found for (a) experiment 5 and (b) experiment 6 for the fluidized bed. Each experiment was repeated 3 times with the colors blue, red and black for test 1 to test 3 subsequently. The points are the experiments, the line is a linear interpolation and the circle is the minimum fluidization point.	145
C.7	Experiment 7: For compactability level of 38 % with different weight of 0.50 kg (blue), 0.75 kg (Red), 1.0 kg (Black) and 1.25 kg (Green). The dots are the results from the experiments, the mf is the point of minimum fluidization and the line is the linear interpolation of the first part (increase in pressure) and second part of the fluidization curve (straight part after the minimum fluidization).	146
C.8	Cohesive particles fluidization (left) versus non-cohesive particles fluidization (right). The figure is from www.anton-paar.com	147

List of Tables

1	List of used quantities.	xxvi
2.1	Results from the sand experiments in [9].	9
2.2	The green sand batch properties	14
2.3	The linear relationship between compactability and the density of the green sand is shown in Fig. 2.9. The fitted functions are presented here in the table.	15
2.4	(Ia) The ring shear test values, (IIa) the repose angle (α) calculated from the sand pile height and (IV) the compactability of the green sand pile. . .	29
2.5	The compactability, the wall yield locus results from the ring shear tests on the 8 batches of the green sand.	32
2.6	(Ic) The found values for the equation from eq. 2.5 shown in Fig. 2.26. . . .	34
2.7	A suggested relationship between repose angle and flowability which is from [18].	38
2.8	(IIa)-(IIc): Results from the sand pile and slumps tests	42
2.9	(V) The found values of the Young's modulus (E) from eq. 2.3.5.1.1 are shown as the slopes in Fig. 2.38. The standard deviation (std) is indicated by \pm std.	49
2.10	*(I)-(V): Results of the performed tests on the 8 batches of the green sand (I)-(V)	52
3.1	Results from the tests of the green sand in the PAPERS [2, 3]	60
3.2	Results from the tests of the green sand in the PAPERS [2, 3]	65
3.3	General material values for all the calibration simulations in PAPER [2](first column) and in PAPER [3](second column).	66
3.4	General material values and settings for the DEM model simulating the DISAMATIC process in the PAPERS [1](column 1), [3](column 2) for the rib chamber geometry and [3](column 3) for the cavity chamber geometry. .	70
4.1	The rolling resistance and static friction values in the parameter study. . . .	76
4.2	The coefficient of restitution ($e_n = e_t$) values in the paramter study.	79
4.3	The rolling resistance and cohesion values in the parameter study.	79
4.4	The horizontal velocity distribution in the parameter study.	79
4.5	The constant vertical velocity in the parameter study.	79

5.1	The experimental air vents settings in the chamber for the seven cases.	95
5.2	Mass in the cavities from the seven cases with respect to the experiments and the simulations. The number of repetitions of the sand shots and the compactability test are indicated by (n) and if (n=1) it is not written. The sign of \pm indicates the standard deviation σ around the mean μ in the following way $\mu \pm \sigma$	102
A.1	Results from the sieve analysis.	128
A.2	Input and output parameters from sieve analysis.	129
A.3	The results from the loss of ignition experiment.	130
A.4	Results from sand experiments	130
C.1	The green sand is tested for 7 individual fluidized bed experiments where 7 samples are made for determining the characteristic of the corresponding fluidized bed experiments. For each sample the compactability and density is repeated 5 times and for the water contents 3 times. Fluidized bed experiment number 7 is where the weight is changed in the bed. Note that $\pm std$ means the interval of plus to minus of the standard deviation.	141
C.2	The green sand is tested for 7 individual fluidized bed experiments. Fluidized bed experiment number 7 is where the weight is changed in the bed. Note that $\pm std$ means the interval of plus to minus of the standard deviation around the average value of the three experiments (except experiment 7).	142
C.3	The green sand fluidized bed experiment number 7.	147

List of symbols

Table 1: List of used quantities.

Quantity	Symbol
Test values	Symbol
Density	ρ
Density of green sand after 3 rammings	ρ_3
Density of green sand after 10 rammings	ρ_{10}
Uni-axial compression strength	σ_{max}
Youngs modulus from the uni-axial test	E
The linearized yield locus angle (RST-SX)	ϕ_{lin}
The effective angle of friction (RST-SX)	ϕ_e
The angle of internal friction at steady-state flow (RST-SX)	ϕ_{sf}
Flowability (RST-SX)	FFc
Yield limit (RST-SX)	σ_c
Sand pile height (sand pile experiment)	h_p
Slump length (slump experiment)	l_p
DEM parameters	Symbol
Solid density of the chamber wall	ρ_{wall}
DEM particle density	ρ_{DEM}
Green sand DEM particle radius	[r, R]
Green sand DEM particle diameter	[d, D]
Particle-particle static friction coefficient	$\mu_{s,p-p}$
Particle-wall static friction coefficient	$\mu_{s,p-w}$
Particle-particle cohesion value	W_{p-p}
Particle-wall cohesion value	W_{p-w}
Particle-particle rolling resistance	$\mu_{r,p-p}$
Particle-wall rolling resistance	$\mu_{r,p-w}$
Youngs modulus for the green sand	E_p
Youngs modulus for the chamber wall	E_w
Poisson ratio	ν
Coefficient of restitution particle-particle	e_n
Coefficient of restitution particle-wall	e_t
Gravity	\mathbf{g}
The simulation time step	Δt
Air phase parameters	Symbol
Kinematic viscosity	ν
Dynamic viscosity	η
Sand shot overpressure	P_{start}

Chapter 1

Introduction

This chapter introduces the thesis: Numerical simulation of flow and compression of green sand. The DISAMATIC process is presented first in section 1.1 together with the applied material green sand. Earlier research in the field of testing green sand, sand casting and simulations are presented in section 1.2 and followed by the main objectives of the thesis presented in section 1.3. Finally an overview of the thesis is given in section 1.4.

1.1 The DISAMATIC process

The DISAMATIC process is used to manufacture green sand molds for metal casting. These molds are used for typical sand casting components (parts) like e.g. brake disks, differential cases and steering knuckles for the automotive industry. The DISAMATIC molding process is illustrated in Fig. 1.1, showing how the chamber is filled with green sand during the sand shot.

The air overpressure of P_{start} is established in an air tank above the hopper and is used to blow the green sand from the hopper down into the molding chamber. The sand shot is followed by a squeezing step, where the sand is compacted to increase the density and build up strength in the sand mold before the casting process. The green sand is cohesive due to bentonite and water which together with the subsequent squeezing of the mold will result in a high compressive strength, sufficient tensile strength and a final stable mold. The green sand mixture typically contains: 3-4.5 % water, above 7 % bentonite, seal coal and other inactive fines around 2.5-4.0 % while the rest is quartz sand around 85-90 %.

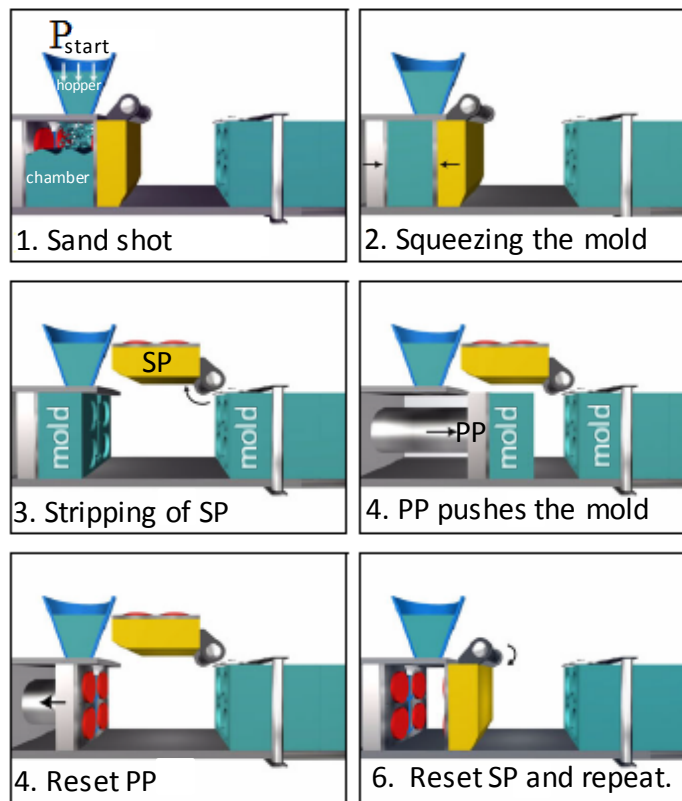


Figure 1.1: The DISAMATIC process: 1. The sand shot. 2. Squeezing the mold. 3. Moving the mold to the chamber front and stripping off the swing plate (SP). 4. Mold close-up where the pressure plate (PP) pushes the mold out of the molding chamber. 5. Stripping off the PP where the PP is stripped from the mold and returns to its starting position in the molding chamber. 6. Closing the molding chamber and repeating a new cycle. The edited figure and text are from [8].

1.2 Research in the field of green sand test, sand casting and simulations

It is important for the foundries to know the relationship between the input values for the sand mixture (active clay, dead clay, water content, sand casting settings) and the properties of the final cast part. Research has been conducted with experimental tests of green sand in [19] where a linear regression technique was applied to determine the relationship between the input values of the sand mixture, i.e active clay, dead clay, water content and each of the related output values of compactability, compressive strength, spalling strength and permeability. These four linear relationships for the dependent variables (output variables) compactability, compressive strength, spalling strength and permeability each had a high predictive capability due to a low R^2 value.

The plastic behaviour of the green sand which is also denoted flowability is important for obtaining a proper filling of the chamber and subsequently the solid mechanical properties are important for the final strength of the mold. This is problematic since these mechanical behaviours have an inverse relationship, e.g if the green sand is too dry then the green sand flowability will be very high and the strength of the mold will be low and vice versa at least for the wet green sand up to a certain water content level. The flowability of green sand was investigated in [20] with respect to confined compression and density from the relations in [21, 22]. The green sand flowability was investigated in [23] in which the sand was squeezed in a cylinder and the difference in the two force from two different heights was measured. The larger the difference in the two forces measured, the smaller the calculated flowability. Tri-axial tests have been performed on the green sand to obtain the yield locus in [24] and uni-axial compression tests were made for green sand in [25] where stress-strain curves were obtained and subsequently analyzed.

Continuum models as in [26] were designed to model cohesion-less granular material for silo simulations and in [27] the contributions of frictional and collisional-translational mechanisms were included in the model. Simulation of the sand casting process with a 2-D two-phase continuum model was presented in [28] studying the chamber flow. In [29] the core shooting process was simulated numerically in two and three dimensions with an Eulerian-Eulerian formulation of the two-phase flow. Recent research of the core shooting process was performed in [30] with a two-fluid model using a kinetic-frictional constitutive model. This model successfully modelled the core shooting process.

DEM has been used to simulate the lost foam process [31] a sand mold manufacturing process and DEM simulations of the green sand molding process have earlier been conducted by [32] with a particle diameter of 6.0 mm and moreover the squeezing process was simulated with DEM in [33].

Experiments which obtains well defined physical values seem to be limited to tri-axial tests, uni-axial compression tests or other compressions tests. In powder research the ring shear tester is a typical choice for investigating granular flow where the yield locus and

the flowability value can be found. The newly developed Anton Paar Powder Cell has recently been applied to investigate the fluidized viscosity of the green sand in PAPER [6]. The fluidization of the green sand is of great importance during the sand shot and in this context experiments on a DISAMATIC machine were performed with respect to the sand shot air overpressure in the tank and the air outlet settings in the chamber.

1.3 The main objectives of the thesis

The scientific goal of the project was to gain a basic understanding of how the flow and deposition of green sand should be characterized from experiments and subsequently modelled. Therefore experiments performed with the DISAMATIC process and corresponding simulations of the process that gave insights and proposals for improvements of the process were the main objective of this work.

The DISAMATIC process applies green sand which consists of quartz sand as the primary ingredient mixed with bentonite, which together with water coats the sand grains and thus allows the sand to bind together under compression. Thus, the internal forces control how well a complex mold chamber geometry can be filled especially if the green sand needs to pass narrow sections in the mold chamber geometry. The flow can stop prematurely in the narrow sections during the sand shot and this might prevent the mold from being completely filled. This could result in a too high variation in the material density, which directly influences the mold's thermal conductivity. The quality of the produced castings is directly affected by the material density of the mold and the variation of the density.

Hence, the main objective of thesis is to characterize the different determining mechanical behaviours of the green sand during the sand shot in the DISAMATIC process. The green sand is characterized mechanically by experiments, which are applied for calibration of the numerical model. The Discrete Element Method (DEM), a particle based method, is chosen as the numerical model simulating the granular structure of the green sand. Selected experiments testing the green sand mechanical behaviour were applied for calibrating the DEM model parameters for correct mechanical behaviour of the numerical model.

Special DISAMATIC chamber geometries were constructed to investigate the DISAMATIC process with respect to the flow and the deposition of green sand and DEM was used to simulate these geometries as well. Further investigations were performed with respect to the deposition of green sand using a special cavity design and testing different air vents settings in the chamber for transporting the green sand with an airflow in the chamber. The sand shot with the cavity design was simulated with DEM modelling the flow of the green sand combined with classical computational fluid dynamics (CFD) modelling the airflow in the chamber and the airflow through the air vents.

1.4 Thesis overview

The thesis consists of 6 chapters and 7 appended articles [1, 2, 3, 4, 5, 6, 7]. The topics of the chapters are:

Chapter 1: Introduction

This chapter gives a short introduction to the thesis by first describing the DISAMATIC process together with the green sand. Then earlier research in the field of green sand, sand casting and simulations are discussed, and this is followed by the main objectives of the thesis and lastly the thesis overview.

Chapter 2: Material characterization of the green sand

This chapter gives a general explanation of the used material (green sand) and its composition, qualitative behaviour, the material characterization and all the mechanical tests performed to characterize the green sand. Mechanical characterization with respect to the DISAMATIC process was performed together with experiments investigating the mechanical properties of the green sand and this is presented in the chapter too.

Chapter 3: The Discrete Element Method and calibration

This chapter presents the Discrete Element Method as well as its governing equations. This chapter also presents the calibration of the DEM model parameters together with the selected experiments, which were applied for the calibration procedure of the model parameters from the two PAPERS [2, 3].

Chapter 4: Simulating the rib chamber geometry

This chapter presents the flow dynamics of the sand shot experiments inside the rib chamber geometry together with the corresponding DEM simulations from the two PAPERS [1, 2]. A sensitivity study of several parameters' influence on the flow in the rib chamber geometry is presented too.

Chapter 5: Simulating the cavity chamber geometry

This chapter presents the flow dynamics of the sand shot inside the chamber with the special cavity design, which is investigated with both a DEM model and a combined CFD-DEM model in PAPER [3]. The CFD part of the latter which is used to simulate the air phase is presented as well.

Chapter 6: Conclusion and future work

The conclusions of the different investigations from this thesis are given in this chapter and the future perspectives of numerical modelling of the DISAMATIC process are discussed.

Appendix

Appendix A: The green sand composition.

Appendix B: Anton Paar Powder Cell tests of the green sand.

Appendix C: Fluidized bed tests of the green sand.

Chapter 2

Material characterization of the green sand

2.1 Introduction

In section 2.2 the green sand composition and its qualitative mechanical behaviour are presented. Simple tests of the green sand composition without taking into account the water content, are briefly explained in section 2.2.1 and further details of the tests are presented in appendix A. The general qualitative mechanical behaviour of the green sand are briefly discussed and presented in section 2.2.3.

Batches of green sand are prepared with water content and several tests are performed where these are used to characterize the mechanical behaviour of the green sand. The preparation of the green sand batches in a mixer and simple foundry tests are described in section 2.2.4. The results of the simple foundry tests are used to categorize the overall state of the batches with the water content and this is presented in section 2.2.5.

In section 2.3 a sequence of five stages in the DISAMATIC process has been identified and used for creating five mechanical categories denoted (1)-(5). These five categories describe the different mechanical conditions that the green sand experiences during the course of the DISAMATIC process. These five mechanical categories are also used to categorize the performed experiments in this project, which are also denoted (I)-(V). Each category is discussed separately with a corresponding literature review of experiments to test granular material, a description of the experiments performed, the results of the performed experiments on the batches and a separate short conclusion.

Finally, an overall conclusion is drawn from the five categories and for all the experiments performed on the batches in section 2.4 where the overall results for all the tests are listed in table 2.10.

2.2 The green sand

2.2.1 Green sand composition

First the green sand is prepared in a mixer before it is used in the DISAMATIC process where the composition of the green sand should be a homogeneous mixture. The mixer is described in section 2.2.4.1. The green sand mixture typically contains: 3-4.5 % water, above 7 % bentonite, seal coal and other inactive fines around 2.5-4.0 % and the rest is quartz sand around 85-90 %. The contents of the green sand mixture are illustrated below in Fig. 2.1.

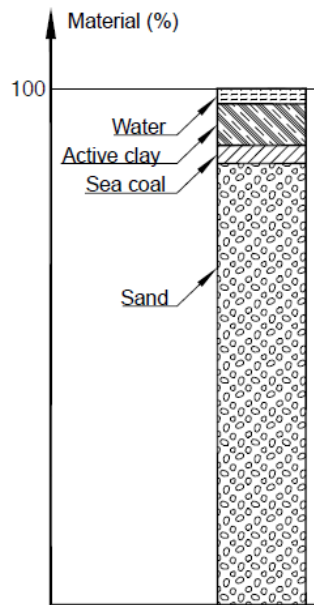


Figure 2.1: The green sand mixture. The figure is from [8].

2.2.2 Tests to determine the green sand composition

In order to make a fundamental characterization of the green sand composition, well known tests to determine the total content of fines, size distribution of green sand, active bentonite content and loss on ignition were performed in another master project [9] which used the same green sand as in the present project. The results of the tests are shown in table. 2.1 where a more detailed summary can be found in appendix A. The average grain size should not be too large thereby decreasing the metal penetration tendency especially under increasing metallostatic pressure. The size distribution of green sand can be seen in Fig. 2.2.

Table 2.1: Results from the sand experiments in [9].

Experiment on sand	Results	Range by Disa
Total fines content	less than 1.0 %	2.5 - 4.0
Average grain size	0.20 mm	0.14 - 0.28 mm
Active clay content	11.9 %	over 7 %
Loss of ignition	4.58 %	3.5 - 5.0 %

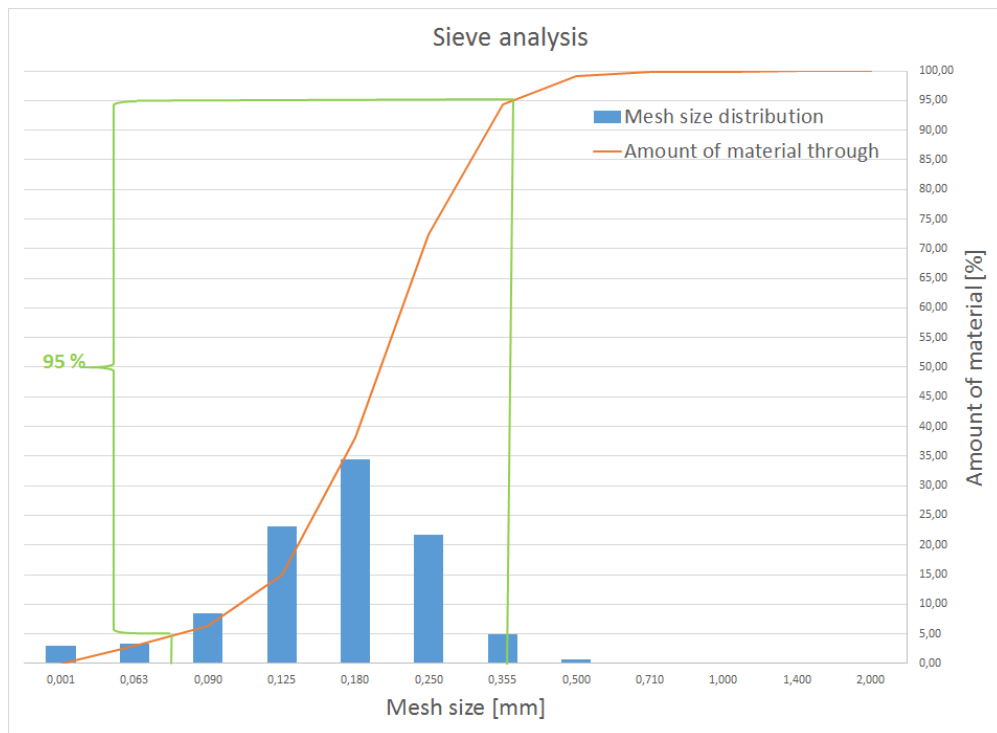
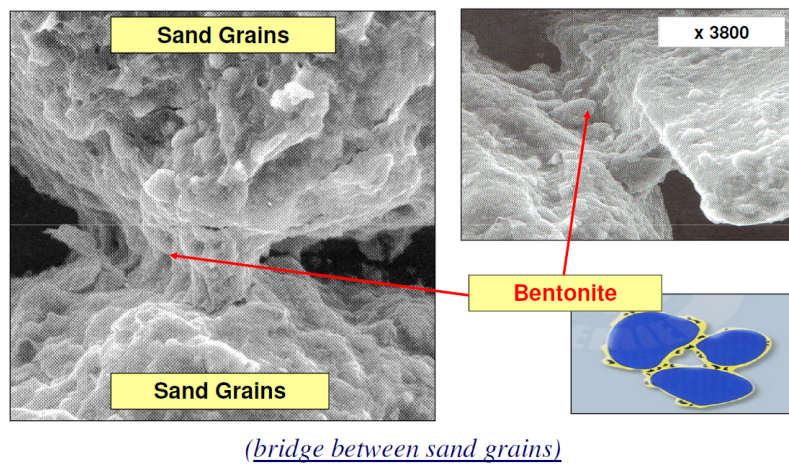


Figure 2.2: The size distribution of the green sand applied in the project. The figure is from [9].

2.2.3 Qualitative mechanical behaviour of the green sand

The mechanical properties of the green sand are important for the sand shot during filling of the chamber and finally for the quality of the squeezed mold. The flowability of the green sand is important when the sand flows down through the hopper filling the chamber with green sand during the shot. The flowability of green sand is mostly governed by the amount of water and bentonite. The wet bridges created by the bentonite make the sand grains stick together [10] which is shown in Fig. 2.3. The bentonite and water makes the green sand very cohesive and by squeezing the mixture it obtains a high green compressive strength, sufficient wet tensile strength and by that, it stabilizes the mold to acquire sufficient strength for the casting process.



(bridge between sand grains)

Figure 2.3: The wet bridges created in the bentonite from the water make the bentonite cohesive and thereby the sand grains will stick together. The pictures are from the slides in [10](<http://www.sut.ac.th/engineering/Metal/ru/GREEN20%20SAND.pdf>).

The quality of the final mold is affected by many factors, including the mixture of the quartz sand, the complexity of the mold chamber geometry and the compressed air pressure (P_{sand}) driving the flow of the green sand. The final mold must be homogeneous and stable [8, 34, 35]. Sufficient strength and solid mechanical properties of the mold are needed to withstand the load from the metallostatic pressure during filling of the liquid metal and afterwards the loads from the thermal contraction of the solidifying metal.

2.2.4 The green sand batch preparation and the simple foundry tests

The green sand batches constructed for the experiments are prepared in a mixer where the mixer and this is described in section 2.2.4.1. The simple foundry tests performed on the batches were constituted of the water content test which is described in section 2.2.4.2 and the compactability test which is described in section 2.2.4.3.

2.2.4.1 The green sand mixer

For each batch the green sand and the added water are prepared in a mixer to get the right homogeneous initial conditions for the experiments. The green sand is then filled into buckets for each batch, when the desired compactability value is reached for the 7 individual batches. The green sand was filled into sealed buckets to keep a constant water content during the testing of the batches. When the green sand tests are performed the



Figure 2.4: The mixer together with the bucket containing the homogeneously mixed green sand.

green sand is taken from the middle of the bucket for a more stable water content of the green sand and the plastic bag is closed afterwards. A dry batch of green sand where no water was added was created and denoted batch 7. This batch was not put into the mixer.

2.2.4.2 The water content test

The water content test is used to find the amount of water in the green sand. To find the



Figure 2.5: The heater applied for the water content test (left) and the scale (right).

water content in the green sand a heater is used together with a green sand sample with the weight of 50 g. The heater and the scale are shown in Fig. 2.5. The green sand sample is inserted in the heater for 15 minutes at the temperature range of 200-220°C and the weight is measured subsequently. The percentage of mass loss due to water vaporization is calculated according to,

$$\text{Water contents in \%} = \frac{50 \text{ g} - \text{Weight after heating}}{50 \text{ g}} \times 100\% \quad (2.1)$$

The water content tests were made on all the 8 batches of green sand and the results of the water content are presented in section 2.2.5.1 - 2.2.5.2.

2.2.4.3 The compactability test

The standard procedures for the compactability test is described by the American Foundry Society (AFS) [35] and the experimental setup is shown in fig. 2.6. The green sand was sieved before the compactability test was performed. The compactability test is used to characterize the overall condition of the green sand and it is performed similarly to a confined compression test and the value should be in the region of 34-44 %, [8]. The compactability tests were performed on the 7 batches of green sand except for the dry green sand in batch 7.

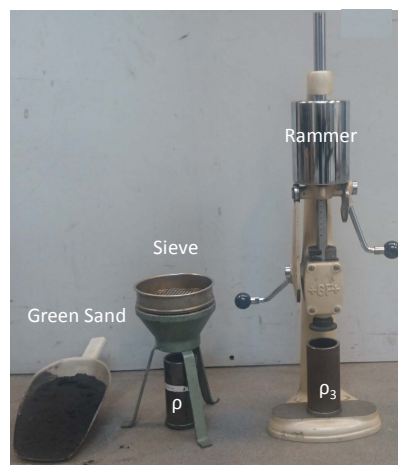


Figure 2.6: Green sand (left), is sieved into the cylinder and the density is found ρ (middle) and finally the ramming station is used to determine the compactability of the sand mixture by 3 rammings and the compacted density ρ_3 (right). The edited figure is originally from PAPER [2].

For the standard ramming a cylindrical tube was used to prepare a standard specimen sample of green sand. The initial green sand sample weight was measured before compaction and since the volume was known, the un-compacted density (ρ) and the compacted density (ρ_3) could be calculated. The ramming test was performed with the standard 3 strokes and the compacted density (ρ_3), was calculated from the compacted volume.

For three selected batches (3, 6, 8) all the compactability tests are plotted by the order of which the experiments were performed to see if the compactability level was constant over time.

Additional compactability tests were made with 10 strokes and the density was monitored for these special ramming tests (ρ_{10}). This test was repeated 7 times for each batch, and thereby an average of the density and the compactability was calculated for each ramming in the batch.

2.2.5 Results of the simple foundry tests

The 8 green sand batches were prepared for the fundamental characterization which was briefly described in the previous sections.

The compactability versus water contents is presented in section 2.2.5.1.

The water content over time is presented in section 2.2.5.2.

The density as a function of compactability results are presented in section 2.2.5.3.

The compactability of the consecutive tests made over time are presented in section 2.2.5.4.

The compactability as a function of 10 rammings results are presented in section 2.2.5.5.

Three of the eight batches are selected for further investigations as these were in the recommended region for the DISAMATIC process [8]: Low compactability (Batch 8), middle compactability (Batch 3) and high compactability (Batch 6).

2.2.5.1 Compactability versus water contents

The mechanical properties of green sand are investigated as a function of the compactability level (x) and water contents for the 8 tested batches. When the water content increases the compactability level increases as well and this is shown in Fig. 2.2.5.1 and in table 2.2. The dry sand from batch 7 has a low water content of 2.3% (the other green line) and this

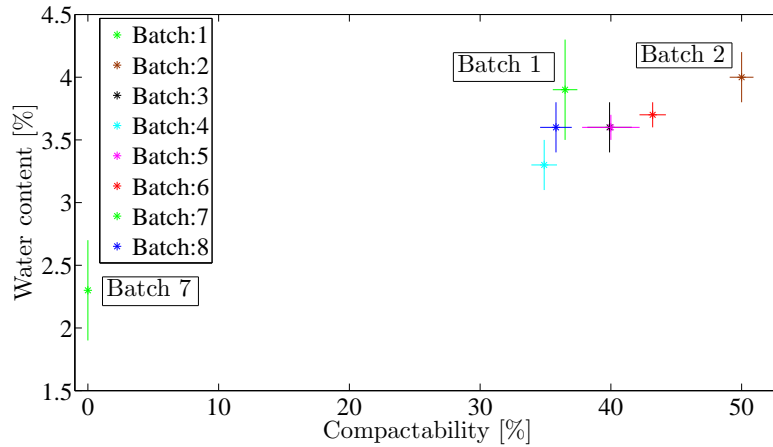


Figure 2.7: The water contents as a function of compactability of all the batches. The average value of the batches are shown with a cross and an individual color (green line used twice for batch 1 and batch 7). The standard deviations are shown for both the compactability and the water contents as a horizontal line and a vertical line respectively.

made it impossible to make the compactability test and consequently the compactability is set to 0 % with no standard deviation in this case. Batch 2 (The brown line) has a very high water content 4.0% and thereby also a very high compactability 50%. Batch 1 (green color) has a large average water content value of 3.9% when compared to the low average compactability value of 36.5 %. Substantial standard deviations occurred in the

water content tests especially for batch 1 (green line) where smaller standard deviations were observed for the other batches.

Table 2.2: The green sand batch properties

Test type	Batch number							
	1	2 (Wet)	3	4	5	6	7 (dry)	8
Water	3.9 ± 0.4	4.0 ± 0.2	3.6 ± 0.2	3.3 ± 0.2	3.6 ± 0.1	3.7 ± 0.1	2.3 ± 0.4	3.6 ± 0.2
Reps	n=6	n=14	n=13	n=12	n=11	n=12	n=9	n=15
3 ram	36.5 ± 0.94	50.0 ± 0.91	39.9 ± 1.70	34.9 ± 0.98	40.0 ± 2.20	43.2 ± 1.01	No	35.8 ± 1.21
Reps	n=14	n=13	n=17	n=14	n=15	n=13	n=7	n=15

2.2.5.2 Water content tests over time

The water content decreases as the water content tests progress with time for the three selected batches and this is shown in Fig. 2.8. Here the variance in the water content

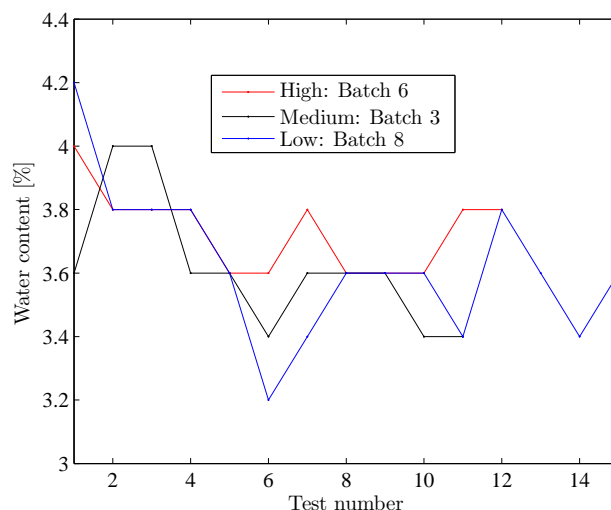


Figure 2.8: The water contents tests plotted in consecutive order for the high compactability (batch 6), the medium compactability (batch 3) and the low compactability (batch 8).

can be observed and some variance is expected due to the small mass of 50 g used for the water contents test and from the different green sand conditions in the buckets used for the individual batches.

2.2.5.3 The density as a function of compactability

All the $n=86$ compactability tests from the 7 batches (not batch 7) are shown in Fig. 2.9 where the density ρ_3 is plotted as a function of compactability. Linear relationships of the compactability versus non-compacted density (ρ) and the compactability versus compacted density (ρ_3) were made. The linear relationships listed in table 2.3 were made with MATLAB's fitting tool box which fits the curves with a standard least square algorithm.

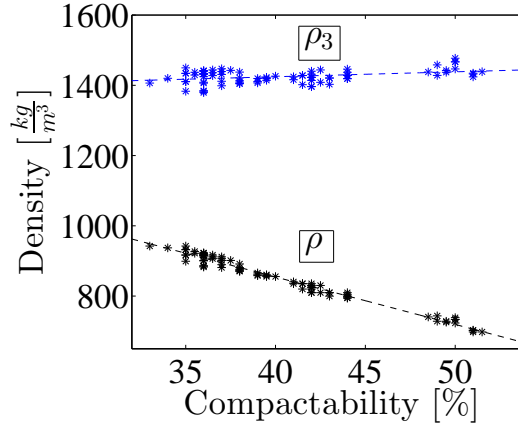


Figure 2.9: (IV) The density as a function of compactability where the compactability is in percentage % and the non-compacted density is denoted ρ and the compacted density is denoted ρ_3 with the units of $[\frac{kg}{m^3}]$.

Table 2.3: The linear relationship between compactability and the density of the green sand is shown in Fig. 2.9. The fitted functions are presented here in the table.

Density	A $[\frac{kg}{m^3 \times \%}]$	B $[\frac{kg}{m^3}]$	SSE	RSQ	Adj-RSQ	RMSE	dfe
ρ	-13.51	1395	8.7274×10^3	0.9780	0.9777	10.1930	84
ρ_3	1.404	1368	2.4313×10^4	0.1467	0.1365	17.0130	84

The linear relationship of the non-compacted density ρ as a function of compactability has a very high prediction capability indicated by the high root mean square value of $RSQ = 0.9780$ and the adjusted root mean square of $adj - RSQ = 0.9777$.

This means that for a certain compactability level (x) an estimate of the un-compacted density (ρ) can be predicted from the function fitted from the seven batches $\rho(x) = -13.51 \frac{kg}{m^3 \times \%} x + 1395 \frac{kg}{m^3}$ with good accuracy. The linear relationship found is obviously highly dependent on the green sand composition.

The function for the compacted density $\rho_3(x) = 1.404 \frac{kg}{m^3 \times \%} x + 1368 \frac{kg}{m^3}$ is fairly constant around the density of $1368 \frac{kg}{m^3}$ due to the small value of the slope found from the regression $1.404 \frac{kg}{m^3 \times \%}$. The prediction capability of the linear function is somewhat weak

which is indicated by the very small root mean square of $RSQ = 0.1467$ and the adjusted root mean square of $adj - RSQ = 0.1365$.

2.2.5.4 Compactability of the consecutive tests made over time

The compactability slightly decreases as the tests progresses with time, which is shown in Fig. 2.10. Some variance can be seen on the compactability with the progression of the tests over time. The three curves from the three batches can clearly be distinguished from each other and thereby these batches were a good choice to investigate. The compactability of the three batches are also in the region of $34\% \leq x \leq 44\%$ typically applied in the DISAMATIC process and suggested in [8].

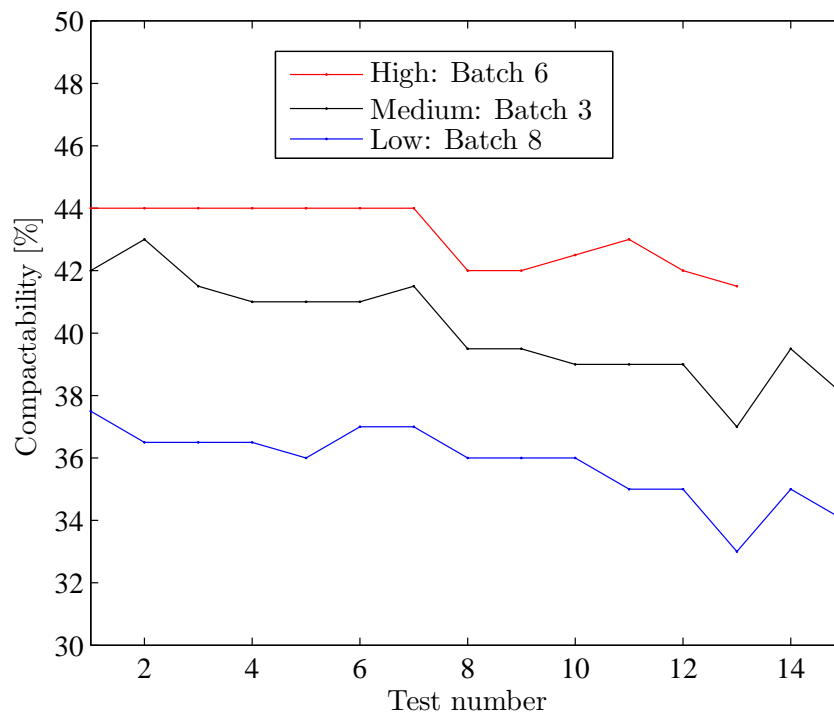


Figure 2.10: The compactability plotted for the consecutive tests for the three batches with high compactability batch 6 (red line), medium compactability batch 3 (black line) and low compactability batch 8 (blue line).

2.2.5.5 The density as a function of 10 rammings

The density as a function of compactability from the 10 rammings are shown in Fig. 2.11 for the three investigated compactability levels. The low compactability (red line, Batch 8), middle compactability (black line, Batch 3) and high compactability (blue line, Batch 6). The low compactability starts out having larger densities in the first 2-3 rammings where for the high compactability the density gets equal to the low and medium compactability at around 6-7 rammings and further on to the 10 rammings. This is due to the pores in the dry green sand (void fraction), which is low before compaction compared to the more wet sand with larger void fraction. For the high compactability the swelling of the bentonite together with the higher cohesion gives an initial lower density of the green sand.

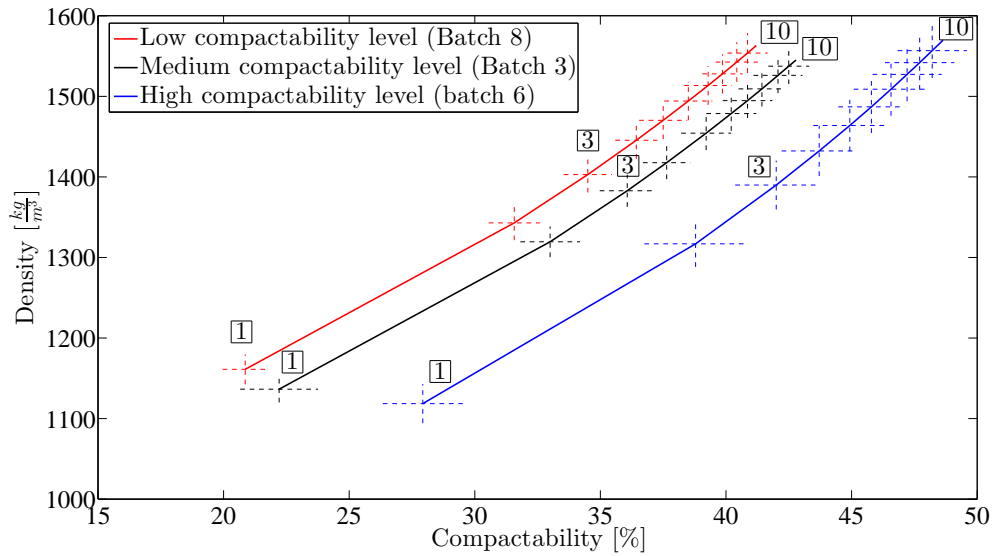


Figure 2.11: The density as a function of compactability with respect to the number of rammings 1-10. The first ramming starts from the left indicated by the number. The cross placed in the middle shows the average value of the batches with an individual color. The dotted lines are the standard deviations of compactability % as a horizontal line and the standard deviations of density $[\frac{kg}{m^3}]$ as a vertical line.

The tests results of the 10 rammings for all the batches are listed later in the overall table. 2.10.

2.2.6 Conclusion of the simple foundry tests

In general the compactability level increases when the water content increases too, which is due to the larger pores created by the wet bridges from the bentonite. Batch 1 could potentially be observed as an outlier due to the low compactability level as compared to the high water content. It should be noted that the water content and the compactability level decrease with time even though the green sand is stored in a plastic bag and a bucket.

The compactability test gives a better indication for the green sand as compared to the water content test due to the smaller standard deviation in relation to the size of the average value, together with the short time it takes to make a compactability test of around 30 s.

A linear function can be applied to describe the un-compacted density (ρ) as a function of the compactability level (x) with a great prediction capability. The linear relationship of the compactability level and un-compacted density is due to the swelling of the bentonite creating larger pores in the green sand (larger void fraction) with more water added. The compacted densities ρ_3 behave fairly constantly due to the small value of the slope found from the regression for the linear function although some randomness is indicated by the very small root mean square of $RSQ = 0.1467$ and the very small adjusted root mean square of $adj - RSQ = 0.1365$.

The 8 batches will be investigated next with additional experiments, which are typically not performed in a traditional foundry. These additional experiments are categorized from the five mechanical behaviours determined from the progress in the DISAMATIC process.

2.3 Five mechanical behaviours in the DISAMATIC process

The material characterization will be performed and numbered according to the order and the different mechanical conditions the green sand experiences during the DISAMATIC process. The five different conditions have been related to Mohr's circle for the mechanical analysis, which is illustrated in Fig. 2.12(Top).

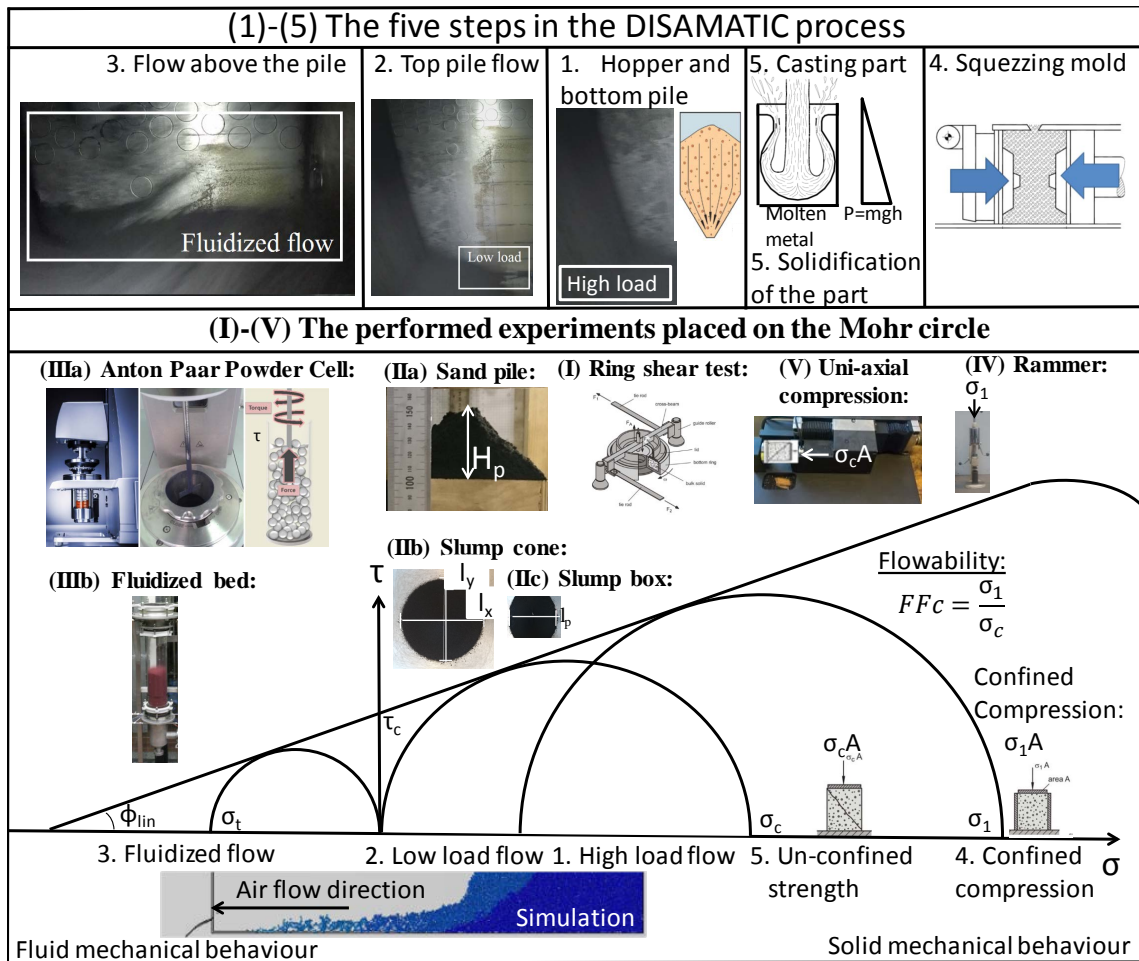


Figure 2.12: (Top) The sequence in the DISAMATIC process (1)-(5). (Middle) The performed experiments placed on the Mohr circle (I)-(V). (Bottom) The five names of the mechanical behaviours.

The purpose of the experiments in this chapter was to characterize and define the overall mechanical properties of the green sand for the five different mechanical conditions identified above. The experiments are denoted (I)-(V) which is illustrated in Fig. 2.12(middle) and the relationship to Mohr's circle is shown just below. The subdivision into the five different conditions in the DISAMATIC process and the five related experiments are discussed in the following sections:

Section 2.3.1 describes the high load flow region (1), which occurs for the green sand in the hopper and in the bottom of the pile in the chamber during the sand shot. The selected experiment investigating the high load flow region (I) on the batches is performed with a ring shear tester.

Section 2.3.2 describes the low load flow region (2), which occurs when the green sand is flowing on top of the sand pile in the chamber during the sand shot in the DISAMATIC process. The selected experiments investigating the low load flow region (II) on the batches are a sand pile experiment and two slump tests.

Section 2.3.3 describes the fluidized flow region (3), which occurs when the sand is transported along the chamber wall with an airflow and the flow at the absolute top of the sand pile in the chamber during the sand shot. The selected experiments investigating the fluidized flow region (III) are performed with the Anton Paar Powder Cell and a fluidized bed test.

Section 2.3.4 describes the confined compression (4) of the green sand during the squeezing of the green, which creates the final mold. The selected experiment investigating the confined compression (IV) on the batches is the compactability test. Note the compactability test was described earlier in section 2.2.4.3 and the results were shown in section 2.2.5 instead of section 2.3.4.

Section 2.3.5 describes the un-confined strength (5), which is required when the molten metal is poured into the final mold and subsequently when the metal solidifies. The selected experiment investigating the un-confined strength of the green sand (V) on the batches is the uni-axial compression test.

The five sections 2.3.1 - 2.3.5 have a common structure with a literature review of granular experiments, a short description of the performed experiments, the results and an analysis of the performed experiments on the batches and finally a short conclusion.

2.3.1 High load flow (1)

The high load flow occurs in the hopper during the sand shot and the flow in the lower part of the sand pile created in the chamber. In the high load flow the flowability of green sand is important and this was investigated in [20] with respect to the density as a function of pressure from the relations in [21, 22]. The green sand flowability was also investigated in [23] during the squeezing in a cylinder measuring the difference in the forces for two different heights in a cylinder. The larger the difference in forces the smaller the flowability value is. In [23] it was suggested that the green sand could be modelled as a yield stress material, although in [23] the physical behaviour was investigated in the high load flow transition to a solid mechanical behaviour. An analytical derivation based on the yield stress material with additional overpressure similar to when the sand enters the chamber was made in PAPER [4]. Experiments investigating high load flows for granular

material can be performed with the ring shear test to determine the yield locus and the yield stress. The yield locus together with the ring shear tests and the high load flow in the DISAMATIC process are illustrated in Fig. 2.13. In the high load flow region a direct shear test is also an option for testing the material properties and determining the yield stress (τ) of the granular material.

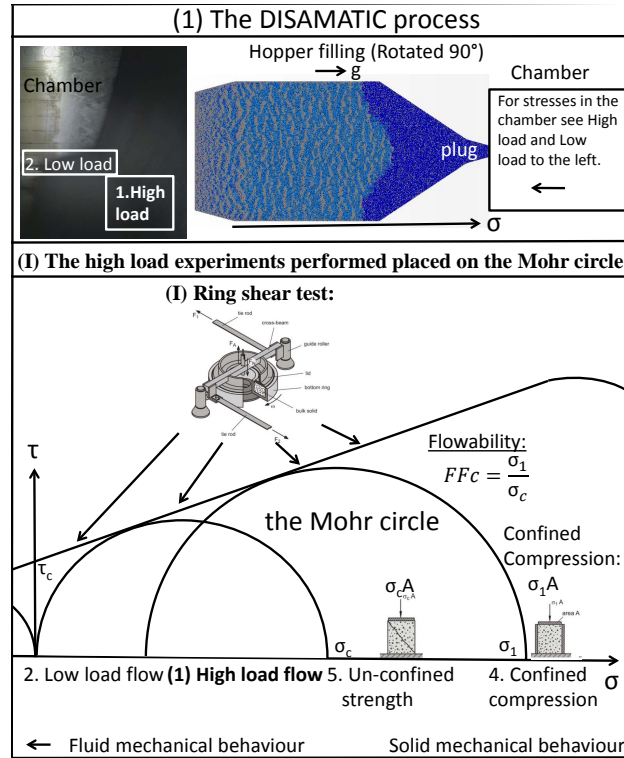


Figure 2.13: The high load flow in the DISAMATIC process and the ring shear test placed on the Mohr circle.

The ring shear tester is typically used for designing simple silos and hoppers for predicting the types of flow occurring in e.g. mass flow or funnel flow which is discussed further in [12]. The application of the yield locus with respect to approximating the pressures and arching in hoppers were discussed in [36]. Challenges in designing silos and hoppers applying silo design codes are discussed in [37]. The DISAMATIC process is very complex with respect to silo design since the green sand is blown from the hopper down into the chamber by the compressed air pressure (P_{sand}). To increase the complexity further after a mold is constructed a plug of cohesive green sand is created in the bottom of the hopper preventing the green sand from falling down before the next sand shot as illustrated in Fig. 2.13(Top right). The flowability has been investigated for many different materials with the ring shear testers as in e.g. [38, 39]. The flowability (FFc) found from a ring shear tester of the type RST-SX is explained in section 2.3.1.1.2 and is illustrated in Fig. 2.13. The ring shear test was performed on the green sand in the PAPERS [2, 3].

Mohr's circle

A force equilibrium can be applied at failure for a slice of bulk material which is illustrated in fig. 2.14(left). Mohr's circle represents the stresses from the major principle stress $\sigma_v = \sigma_1$ at $\alpha = 0^\circ$ to the minor principle stress $\sigma_h = \sigma_2$ at $\alpha = 180^\circ$ which are shown in fig. 2.14(right).

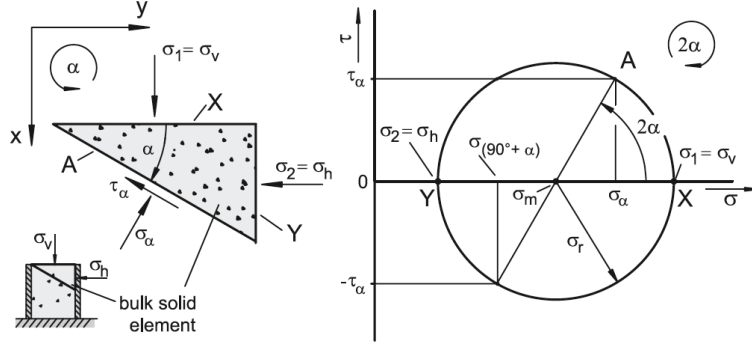


Figure 2.14: Mohr circle. The figure is taken from [11]

The normal stress on the Mohr's circle is given by,

$$\sigma = \cos(2\alpha) \frac{\sigma_v - \sigma_h}{2} + \frac{\sigma_v + \sigma_h}{2} \quad (2.2)$$

the shear stress on the Mohr's circle is given by,

$$\tau = \sin(2\alpha) \frac{\sigma_v - \sigma_h}{2} \quad (2.3)$$

Generally in bulk solid applications the major principle stress σ_1 will be in the vertical direction σ_v and the minor principle stress σ_2 will be in the horizontal direction σ_h due to gravity [12], which is also the case in this project. Mohr circles can be found with the ring shear tester, which is described in the next section 2.3.1.1.

2.3.1.1 High load flow experiments performed on the ring shear tester (I)

Several tests on the green sand were performed on the ring shear tester of the type RST-SX, which is described in [11] where the theory is more thoroughly explained in [12]. First the ring shear tests procedure is briefly explained and then the RST-SX is applied to find the yield locus, wall yield locus and compressibility of the granular material:

The yield locus and the internal friction angles are presented in section 2.3.1.1.1(Ia). The flowability (FFc) of the green sand together with the yield stress procedure are presented in section 2.3.1.1.2.

The wall yield locus procedure which obtains the wall friction angle is presented in section 2.3.1.1.3(Ib) with respect to the green sand-stainless steel plate interaction.

A standard compression test determining the density as a function of the pressure (P , $\rho(P)$) is presented in section 2.3.1.1.4(Ic).

Ring shear test procedure

The ring shear tester applies two stresses, first one in the vertical direction (σ) illustrated in Fig. 2.15(left). An additional shear stress is applied in the horizontal direction (τ) and this occurs when the lid on the top starts moving with the velocity of $v = 0.75 \text{ mm/min}$ which is illustrated in Fig. 2.15(right). The pressure in the vertical direction (σ) on the

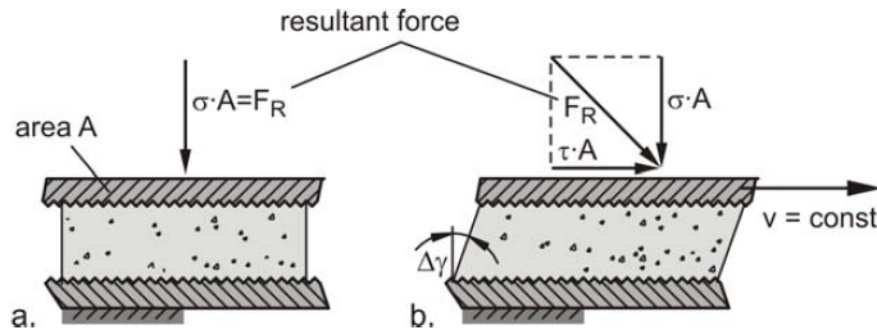


Figure 2.15: (Left) A vertical stress is applied and (right) additionally a shear stress is applied. The figure is from [11].

top of the sample can be varied to test different loading conditions.

The bulk sample is first prepared by applying a normal stress (σ_{pre}) together with the shear stress until a constant shear stress is reached (τ_{pre}) which is denoted pre-shear and is illustrated in Fig. 2.16(a). Afterwards the above-mentioned procedure is repeated now with a smaller normal stress (σ_{sh}) until the new constant shear stress is reached τ_{sh} . Then a point (σ_{sh}, τ_{sh}) can be plotted on the coordinate system of the shear stress versus normal stress which is illustrated in Fig. 2.16(b). The procedure can be repeated in order to construct more points which is shown from an experiment in Fig. 2.16(c) where the yield locus now can be constructed from the points obtained which is shown in Fig. 2.16(d).

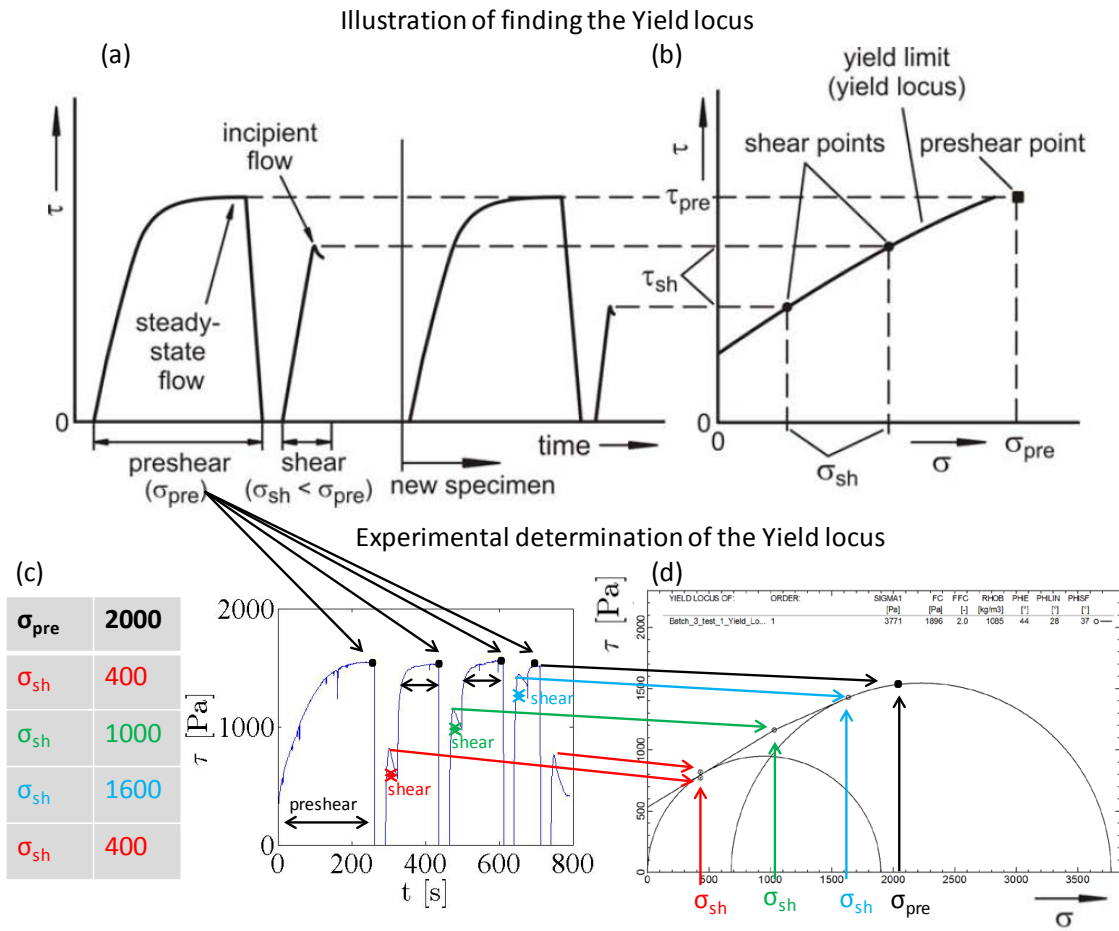


Figure 2.16: (a) The ring shear procedure illustrated. (b) Illustration of finding the yield locus. (c) Experimental procedure for finding the points. (d) The experimental determination of the yield locus. The figures in the top (a) and (b) are from [11].

2.3.1.1.1 Yield locus and the internal friction angles (Ia)

How the yield locus is obtained from the ring shear tester of the type RST-SX was discussed above and further details can be found in [12, 11]. When the yield locus is determined the consolidated sample (large circle with σ_1 and σ_2) and the unconsolidated sample (small circle with σ_c) can be found from the yield locus and they are illustrated in Fig. 2.17.

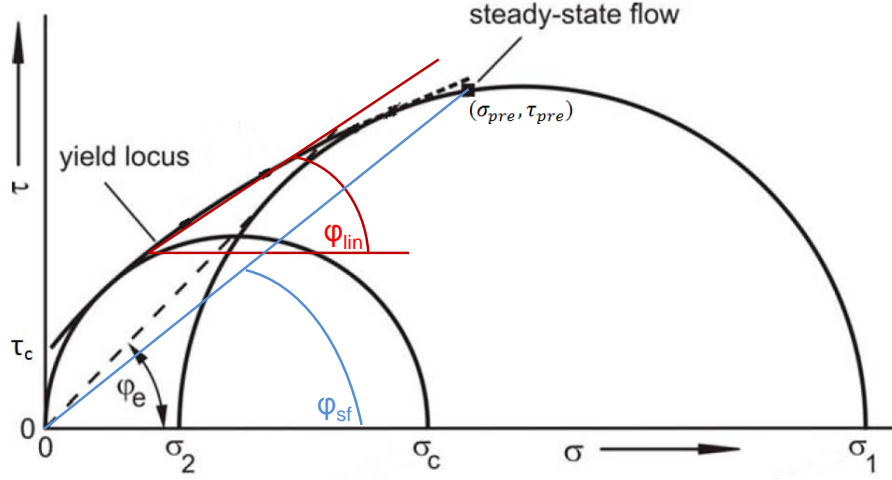


Figure 2.17: Yield locus and the three internal friction angles: φ_e (black dotted line) is the linearized yield locus angle, φ_{lin} (red line) is the effective angle of friction and φ_{sf} (blue line) the angle of internal friction at steady-state flow from the pre-shear point $(\sigma_{pre}, \tau_{pre})$. The normal stress is in the direction of the x-axis (σ) and the shear stress is in the direction of the y-axis (τ). The major principal stress is σ_1 and the minor principal stress σ_2 for the confined sample (large circle) and the major principal stress is σ_c for the unconfined sample (small circle). The cohesion value found from the ring shear tester of the material is denoted τ_c . Note the edited figure and text is from PAPER [2] and originally from [11] where the theory is from [12].

When the Yield locus is created the internal friction angles can also be found, i.e.:

The linearized yield locus angle, φ_{lin} .

The effective angle of friction, φ_e .

The angle of internal friction at steady-state flow, φ_{sf} .

These three internal friction angles and the cohesion of the material (τ_c) can be seen in Fig. 2.17.

The linearized yield locus, φ_{lin} is the tangent to both the Mohr stress circles defining σ_c and σ_1 . From the ratio of the shear stress, τ_{pre} to normal stress, σ_{pre} a sort of friction angle can be found from the angle of internal friction at steady-state flow, φ_{sf} from the pre-shear point, $\varphi_{sf} = \tan^{-1} \left(\frac{\tau_{pre}}{\sigma_{pre}} \right)$ and the effective internal friction angle, φ_e is defined as the ratio of the minor principal stress, σ_2 to the major principal stress, σ_1 at steady-state flow, $\sin(\varphi_e) = \frac{\sigma_1 - \sigma_2}{\sigma_1 + \sigma_2}$.

For poorly flowing bulk solids e.g. moist clay the effective angle of internal friction, φ_e can become large compared to the angle of internal friction at steady-state flow, φ_{sf} for the bulk solids layers that are sliding against each other as they do in a shear test during steady-state flow [12]. Thereby the angle of internal friction at steady-state flow, φ_{sf} and the linearized yield locus, φ_{lin} are used as indicators for the DEM model's particle-particle internal friction interval presented in chapter. 3. The cohesion of the material, τ_c is defined at the intersection with zero normal stress ($\sigma = 0$).

2.3.1.1.2 Flowability function from RST-SX

The flowability factor (FFc) is found from the major principal stress σ_1 divided by the unconsolidated sample stress σ_c where these stresses are illustrated in Fig. 2.17 and in Fig 2.18(left). The FFc is calculated the following way,

$$FFc = \frac{\sigma_1}{\sigma_c} \quad (2.4)$$

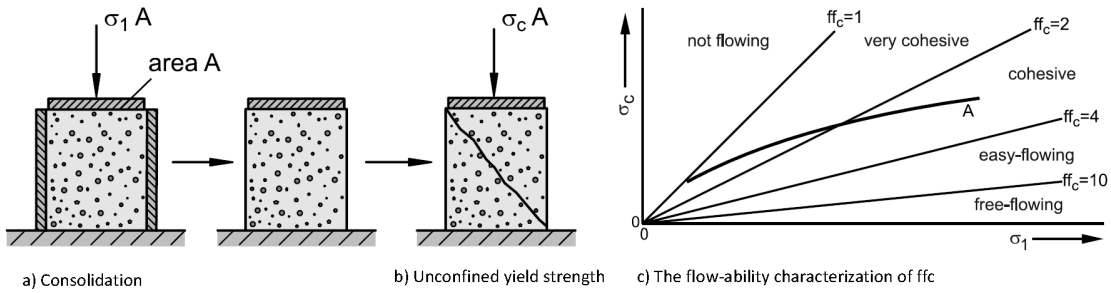


Figure 2.18: Flowability function. The figure is taken from [11].

The flowability factor (FFc) is illustrated as a function of the major principle stress σ_1 in Fig 2.18(right).

Note this is the same principle as the unconsolidated sample stress σ_c found from the uni-axial compression test performed in 2.3.5.1.1. Unfortunately σ_1 is unknown from the ramming procedure, which is used for the green sand sample preparation. In order to obtain the consolidation stress and subsequently finding the FFc value (flowability value) an confined compression test should have been made on the STM machine as in e.g. [40]. Unfortunately no tool was available which could measure σ_1 in the confined compression on e.g. the STM machine. Hence, the flowability was only determined by the ring shear tester.

2.3.1.1.3 Wall friction angle (Ib)

The wall yield locus is found by subjecting a bulk sample to decreasing normal loads (σ_{w1} , σ_{w2} , σ_{w3} , ...) and for each normal load the sample is sheared until a constant shear stress is reached τ_w , this is shown in Fig. 2.19(left). The subsequently found points (σ_w , τ_w) are shown in Fig. 2.19(right) and hereafter the sliding friction angle (φ_{wall}) is found from the slope of the points on the wall yield locus.

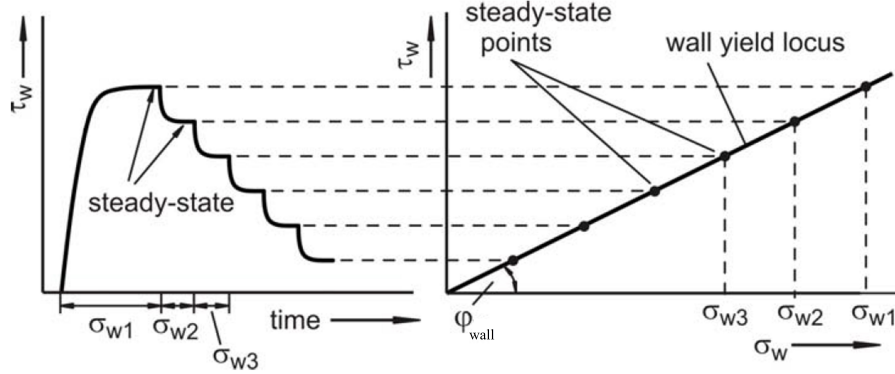


Figure 2.19: The selected normal loads (σ_{w1} , σ_{w2} , σ_{w3} , ...) and the shear stresses history, τ_w (left figure). The wall yield locus found from the steady-state points (right figure). Note the edited figures and text are from PAPER [2] and originally from [11] where the theory is from [12].

2.3.1.1.4 Compression test on the RST-SX (Ic)

Simple compression tests are made to determine the density as a function of the smaller compression stresses and fitted with a equation suggested in [21] which was earlier applied for green sand in [20], i.e.;

$$\rho(P) = \rho(0) + (\rho(\infty) - \rho(0)) e^{\frac{A-P}{B}} \quad (2.5)$$

the constants of A, B and $\rho(\infty)$ will be fitted by the Matlab regression toolbox using a least squares algorithm. The initial uncompressed green sand density $\rho(0)$ is known from the start of the experiment. Ten points of normal stresses which are distributed uniformly in the region of $\sigma = [1000Pa; 1000Pa + 2111Pa \times n; 20000Pa]$ were applied with $0 \leq n \leq 9$ to determine the three constants from eq. 2.5.

2.3.1.2 Results of high load flow test

The results of the high load flow tests which link to the hopper flow and the flow in the bottom of the sand pile during the DISAMATIC process are examined by the ring shear tester the following way:

The yield locus and the internal friction angles are presented in section 2.3.1.2.1 (Ia) and the flowability (FFc) and the yield stress τ_c are presented in section 2.3.1.2.2.

The wall yield locus is presented in section 2.3.1.2.3(Ib).

The density as a function of normal stress results is presented in section 2.3.1.2.4(Ic).

2.3.1.2.1 The yield locus (Ia)

First the yield locus of the dry green sand from batch 7 and the wet green sand from batch 2 with very high compactability are shown in Fig 2.20. The dry sand from batch 7 has a higher flowability FFc ($8.5 > 1.5$) and lower yield stress τ_c ($122 \text{ Pa} < 715 \text{ Pa}$) as compared to the wet green sand from batch 2. The friction angle of φ_{lin} is larger for the dry sand as compared to the wet green sand.

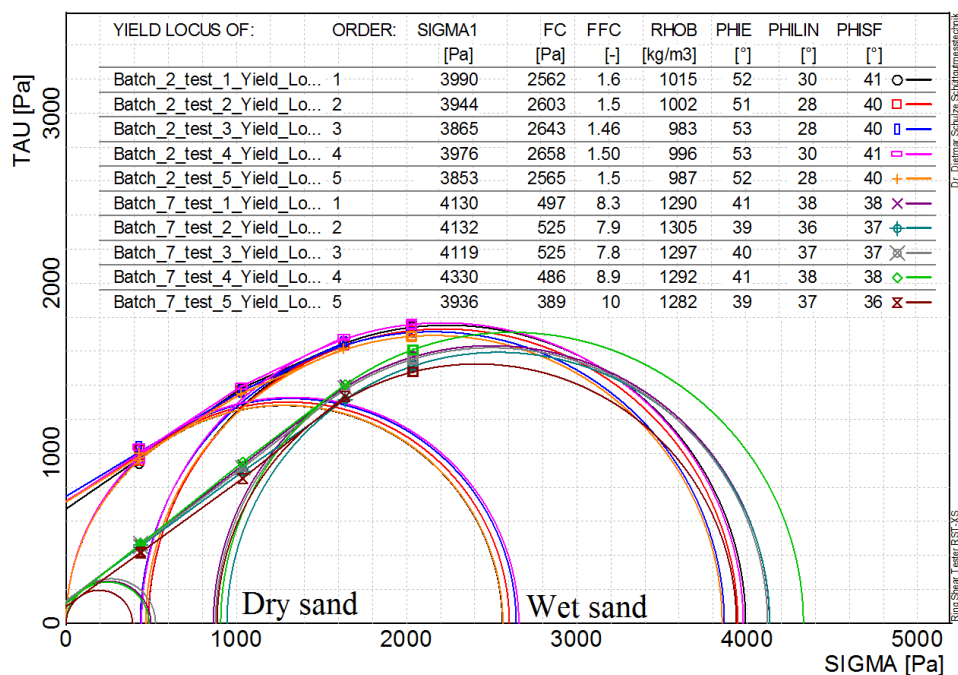


Figure 2.20: (Ia) The Mohr Coulomb circle for the wet green sand (batch 2) and the dry green sand (batch 7).

In table 2.4 the results of the internal friction angles together with the flowability are shown for all 8 batches.

The yield locus of the three selected batches:

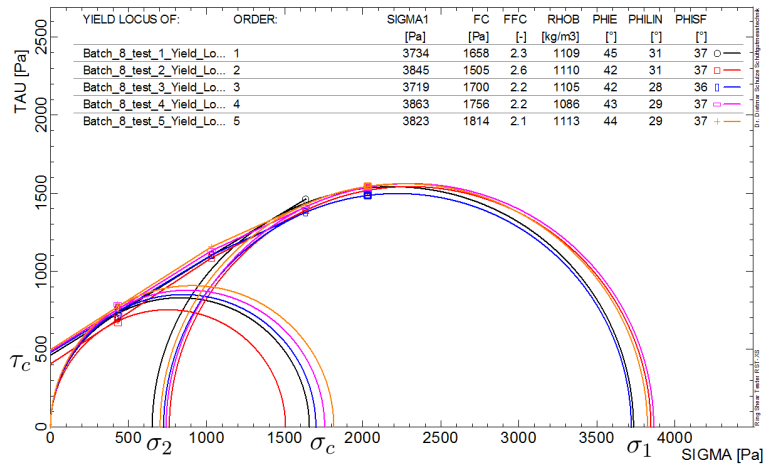
The yield locus is shown in Fig. 2.21 for the three investigated compactability levels, i.e.: Low compactability (a), middle compactability (b) and high compactability (c). In Fig. 2.21 for the low compactability level (a) the minor stresses σ_c are smaller than for the middle compactability (b) and high compactability (c). Due to the similar values of the major stresses σ_1 in all the three batches (a)-(c) the flowability value FFc for the low compactability (a) is larger than (b)-(c) as expected.

Table 2.4: (Ia) The ring shear test values, (IIa) the repose angle (α) calculated from the sand pile height and (IV) the compactability of the green sand pile.

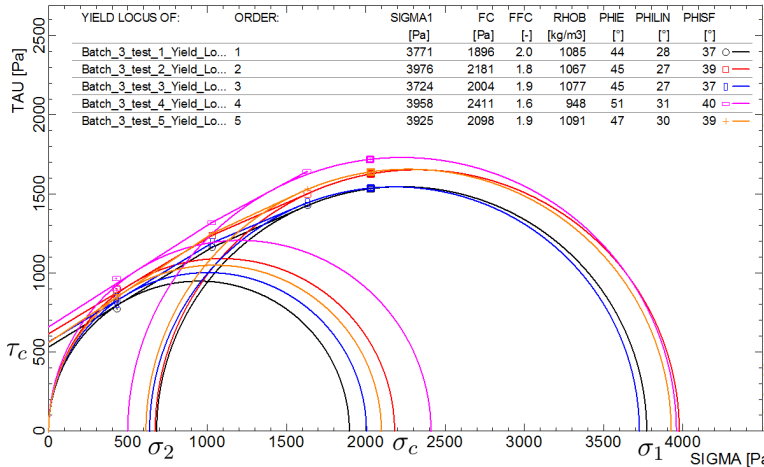
Test type	Batch number							
	1	2 (Wet)	3	4	5	6	7 (dry)	8
3 ram	36.5 ± 0.94	50.0 ± 0.91	39.9 ± 1.70	34.9 ± 0.98	40.0 ± 2.20	43.2 ± 1.01	No	35.8 ± 1.21
(Ia)								
φ_e	44.7 ± 1.46	52.0 ± 0.81	46.4 ± 2.70	44.6 ± 2.43	44.5 ± 1.57	45.6 ± 1.40	40.1 ± 0.92	43.1 ± 1.06
φ_{lin}	28.5 ± 0.55	28.7 ± 0.91	28.6 ± 1.63	30.6 ± 1.93	32.1 ± 2.83	28.4 ± 0.52	37.3 ± 0.96	29.5 ± 1.44
φ_{sf}	37.4 ± 0.51	40.4 ± 0.43	38.4 ± 1.38	38.0 ± 1.54	38.7 ± 1.10	38.2 ± 0.86	37.2 ± 0.90	36.9 ± 0.44
σ_c	539 ± 45.0	715 ± 26.5	586 ± 50.9	493 ± 32.9	446 ± 54.0	561.2 ± 37.0	122 ± 13.5	467 ± 36.0
FFc	2.0 ± 0.2	1.5 ± 0.0	1.8 ± 0.1	2.2 ± 0.1	2.4 ± 0.2	1.9 ± 0.1	8.5 ± 0.9	2.3 ± 0.2
Reps	n=3	n=5	n=5	n=5	n=5	n=5	n=5	n=5
α	37.9 ± 0.73	41.5 ± 1.62	38.1 ± 0.96	36.6 ± 1.04	36.3 ± 0.00	37.3 ± 0.49	30.8 ± 0.70	37.2 ± 1.29
Reps	n=3	n=3	n=3	n=3	n=3	n=3	n=3	n=3

The internal friction angles and the repose angle (IIa):

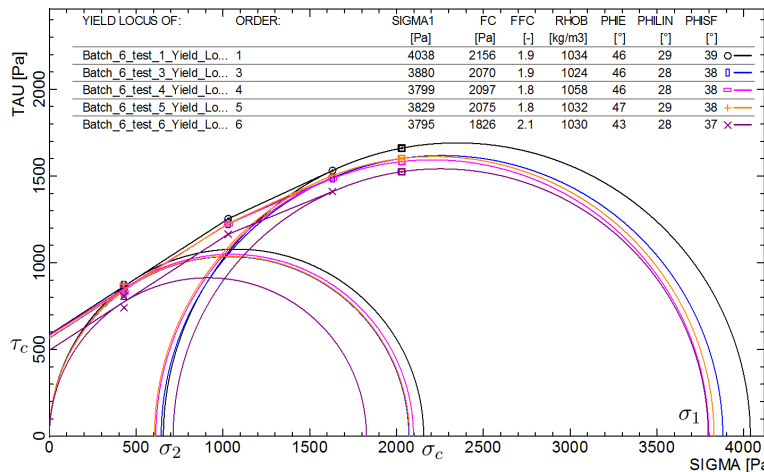
The internal friction angles (φ_e , φ_{sf} , φ_{lin}) from the yield locus are compared to, i.e.: (IIa) the sand pile repose angle (α). The internal angles found from the ring shear tester, which was described in section 2.3.1.1 are shown in table 2.4 and in Fig. 2.22. The internal friction angles of the linearized yield locus angle (φ_{lin}) were similar from batch to batch with values in the interval of 28° – 30°. The effective angle of (φ_e) was similar from batch to batch with values in the interval of 43° – 46°. The repose angle (α) is plotted as a function of compactability which is found from the height versus the width of the sand pile, which is explained later in section 2.3.2.1.1. The repose angles (α) are in good agreement with the angles of friction at steady state flow (φ_{sf}) with values in the region of 36° – 40°. The effective friction angle (φ_e) increases with the compactability level due to the increased cohesion σ_c from the additional water contents and this thereby also decreases the flowability (FFc) shown in Fig. 2.23 in the next section 2.3.1.2.1.



(a) Mohr circle: Low compactability (Batch 8)



(b) Mohr circle: Middle compactability (Batch 3)



(c) Mohr circle: High compactability (Batch 6)

Figure 2.21: (Ia) The Mohr Coulomb circles for the three selected batches.

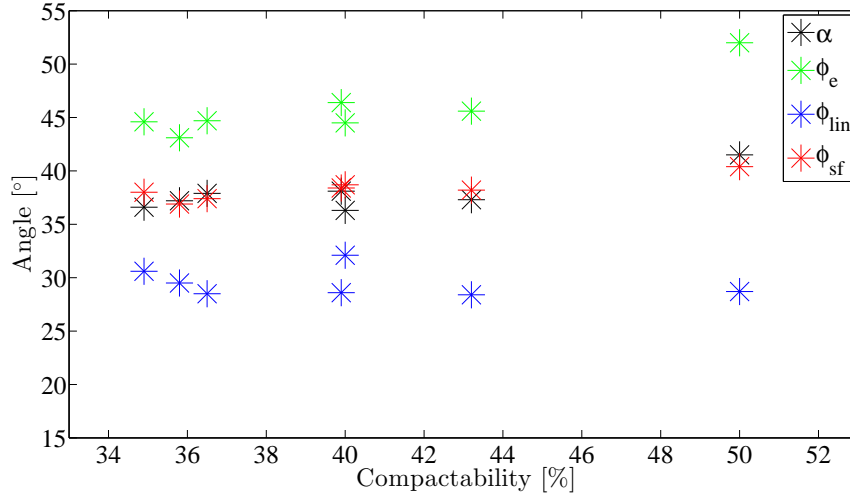


Figure 2.22: (Ia) The angles: the repose angle α (black dots), the effective angle of friction φ_e (green dots), the linearized yield locus angle φ_{lin} (blue dots), the angle of internal friction at steady-state flow φ_{sf} (red dots) as a function of the compactability.

2.3.1.2.2 The flowability (FFc) and the yield stress (τ_c)

The flowability and the yield stress are plotted together in Fig. 2.23 and also presented in table 2.4. The yield stress increases with the compactability (blue) whereas the flowability decreases (red). Especially for batch 2 (wet sand) which has a very large compactability level and thereby also a very high yield stress and a very low flowability (very cohesive) compared to all the other batches and for the dry sand the opposite is the case. Batch 5 has a large flowability value and a small yield stress value compared to the compactability value and thereby this could be considered as an outlier.

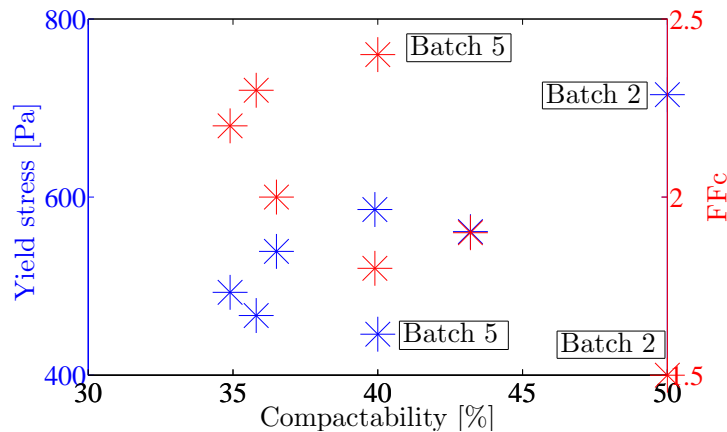


Figure 2.23: (Ia) The yield stress on the left y-axis (red) and the flowability (FFc) on the right y-axis (blue) as a function of the compactability on the x-axis.

2.3.1.2.3 The wall yield locus (Ib)

The wall yield loci are first shown for the dry green sand from batch 7 and for the wet green sand from batch 2 with very high compactability in Fig 2.24. The wall friction angle of $\varphi_{wall} = 19.8^\circ$ is larger for the wet green sand from batch 2 which means it slides less well than the dry green sand from batch 7 on the stainless steel with the wall friction angle of $\varphi_{wall} = 13.3^\circ$.

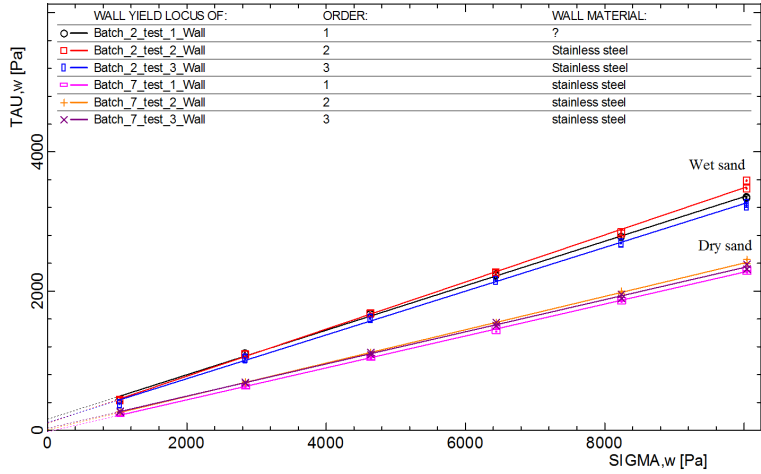


Figure 2.24: (Ib) The wall sliding friction for the wet green sand (batch 2) and dry green sand (batch 7).

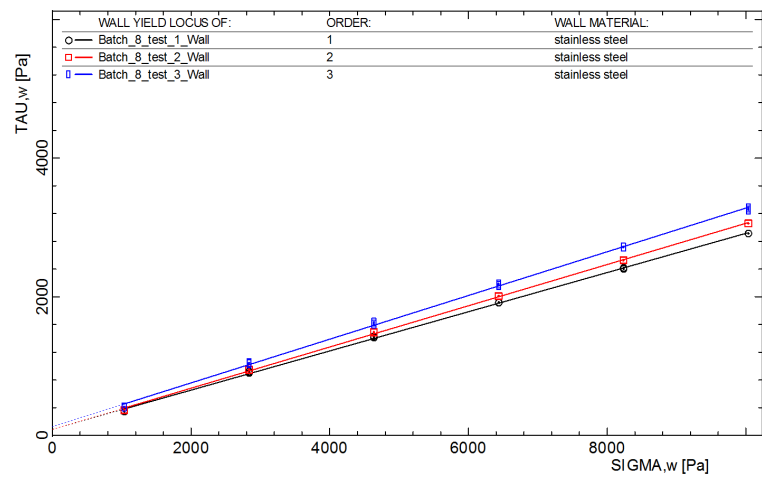
The wall yield locus of the three selected batches:

The wall yield locus is shown in Fig. 2.25 for the three selected compactability levels low compactability (a), middle compactability (b) and high compactability (c). The three batches have similar average values for the wall friction angle in the interval of $\varphi_{wall} = 18.1^\circ - 19.2^\circ$.

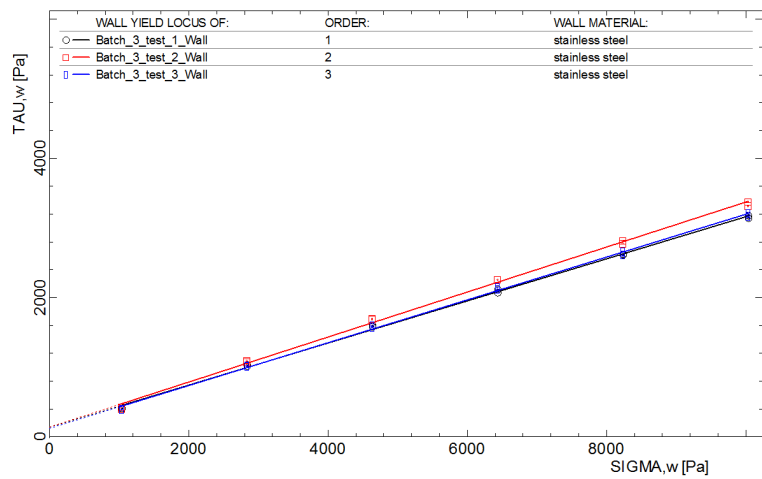
In table 2.5 all the wall friction angles are shown with the values being in the region of $\varphi_{wall} = 16.4^\circ - 19.2^\circ$ except for the dry sand (batch 7) which has a small angle of $\varphi_{wall} = 13.3^\circ$ and wet sand (batch 2) with a large angle of $\varphi_{wall} = 19.8^\circ$.

Table 2.5: The compactability, the wall yield locus results from the ring shear tests on the 8 batches of the green sand.

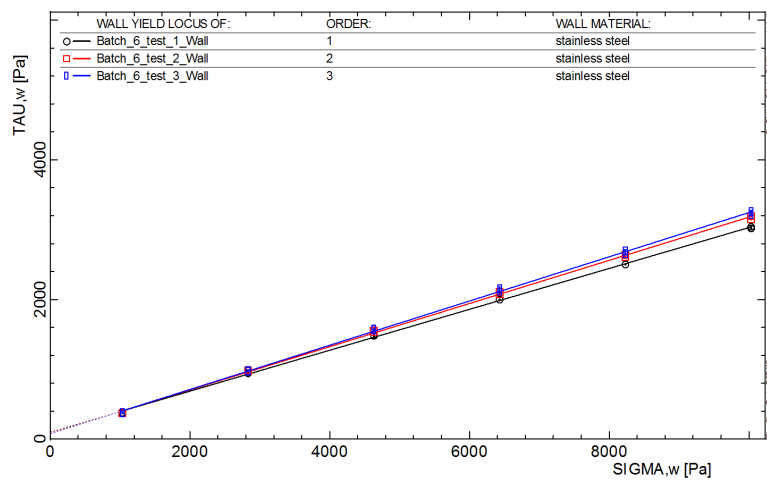
Test type	Batch number							
	1	2 (Wet)	3	4	5	6	7 (dry)	8
3 ram	36.5 ± 0.94	50.0 ± 0.91	39.9 ± 1.70	34.9 ± 0.98	40.0 ± 2.20	43.2 ± 1.01	No	35.8 ± 1.21
φ_{wall}	16.4 ± 1.74 n=3	19.8 ± 0.66 n=3	19.2 ± 0.58 n=3	19.0 ± 0.49 n=3	17.0 ± 0.93 n=3	18.3 ± 0.44 n=3	13.3 ± 0.56 n=3	18.1 ± 1.16 n=3



(a) Sliding friction: Low compactability(batch 8)



(b) Sliding friction: Middle compactability(batch 3)



(c) Sliding friction: High compactability (batch 6)

Figure 2.25: (Ib) The coulomb sliding friction for the three selected batches.

2.3.1.2.4 Compression tests of green sand (Ic)

The compression tests were done on the ring shear tester described in section 2.3.1.1.4 and the results are presented for the three selected batches. The density as a function of the compression stress is fitted by the equation in eq. 2.5, where the density function $\rho_{P=0} = \rho$ of zero compression is known initially from the measurements before the experiment. The max density $\rho(P = \infty)$ is found by MATLAB's fitting tool box which fits the curves with a standard least square algorithm and the three parameters that were fitted are A, B and $\rho_{P=\infty}$. The fitted curves are shown in Fig. 2.26 and the results are

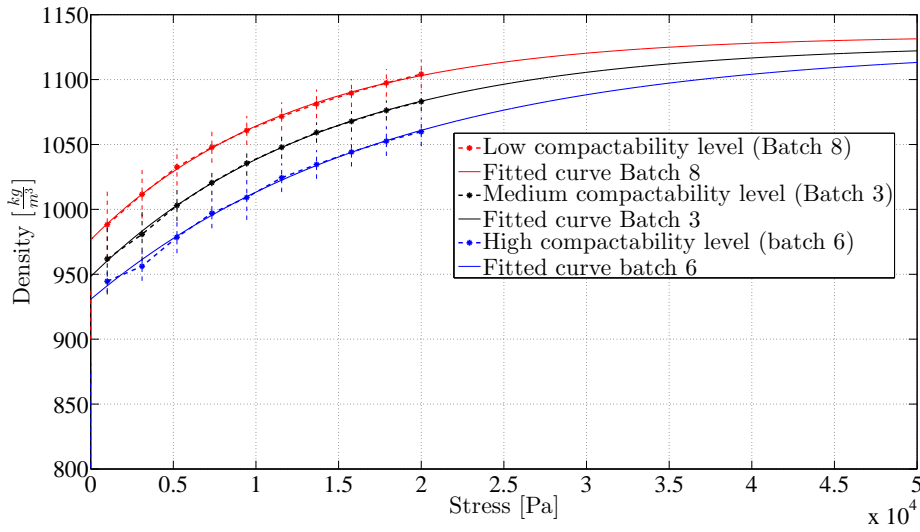


Figure 2.26: (Ic) The density as a function of stress found with the ring shear tester. The average value and the dotted line is the standard deviation of the density in $[\frac{kg}{m^3}]$.

listed in the table. 2.6, for the values of A, B and ρ_{max} .

Table 2.6: (Ic) The found values for the equation from eq. 2.5 shown in Fig. 2.26.

Compactability	A	B	$\rho(0)$	$\rho(P = \infty)$	SSE	RSQ	Adj-RSQ	RMSE	dfc
Low (b=8)	-3837	12320	919	1134	6.894	0.999	0.999	0.992	7
Medium (b=3)	-4967	14290	873.6	1128	9.520	0.999	0.999	1.166	7
High (b=6)	-7089	18130	837.4	1126	47.81	0.998	0.996	2.614	7

The function $\rho(P) = \rho(0) + (\rho(\infty) - \rho(0)) e^{\frac{A-P}{B}}$ predicts the density as a function of the compression stress with a good agreement to the experiment since the smallest root mean square value is $RSQ = 0.998$ and the adjusted root mean square value is $Adj - RSQ = 0.996$. Note, the function should only be applied for the normal stresses in the region where the experiment is performed ($0Pa \leq P \leq 20000Pa$) or maybe a little above as e.g. $P \leq 30000Pa$. Due to the small normal loads the maximum densities which were found $1120 - 1140 \frac{kg}{m^3}$ were small compared to the maximum densities found in the 10 ramming experiment of $1500 - 1600 \frac{kg}{m^3}$.

2.3.1.3 Conclusion of the high load flow experiments

In general the ring shear tester is typically applied for designing silos and the values can give an indication of the angle of the silo orifice which is suggested in [12]. The yield locus and the internal friction angles are typically combined with the wall yield locus (wall friction angle) to determine an optimal design of the geometry of the hopper and the hopper orifice (the orifice is the sand slot in the DISAMATIC process). The DISAMATIC process is very complex with respect to the high load flow behaviour occurring in the hopper when the green sand is driven from the hopper down into the chamber by the overpressure created in the air tank. The plug of green sand created above the sand slot is even more complex to investigate and thereby it has been difficult to apply the simple assumptions of the hopper design from e.g. [12] to the DISAMATIC process.

The internal friction angles of the linearized yield locus angle (φ_{lin}) were similar from batch to batch with values in the region of $28^\circ - 30^\circ$. The effective angle of (φ_e) were similar from batch to batch with values in the region of $43^\circ - 46^\circ$. The repose angles (α) are in good agreement with the angles of friction at steady state flow (φ_{sf}) with values in the region of $36^\circ - 40^\circ$.

The flowability decreased when the green sand became more wet and the opposite was the case for the dry green sand. The yield stress increased when the green sand became more wet and the opposite was the case for the dry green sand. The difference was especially observed for the dry sand (batch 7) that had a higher flowability FFc ($8.5 > 1.5$) and a lower yield stress τ_c ($122 Pa < 715 Pa$) as compared to the wet green sand (batch 2). The yield stress increases with increased compactability up to the tested level of around 50 % for batch 2. The high yield stress of 715 Pa for batch 2 indicates a more cohesive green sand, although it is found that the uni-axial compression test for batch 2, had the smallest uni-axial compression strength.

The wall friction angle increased when the green sand became more wet and the opposite was the case for the dry green sand. The wall friction angles determined were within the values of the region $\varphi_{wall} = 16.4^\circ - 19.2^\circ$ except for the dry sand (batch 7) which had a small angle of $\varphi_{wall} = 13.3^\circ$ and wet sand (batch 2) with a large angle of $\varphi_{wall} = 19.8^\circ$.

The density as a function of the normal stress proposed by [21] is in very good agreement with the normal compression versus density measurements found from the ring shear tester in the region of the normal stress tested.

2.3.2 The low load flow (2)

The low load flow is occurring when the green sand is freely flowing on the top of the sand pile created in the chamber during the DISAMATIC process and this is shown in Fig. 2.27(left). The low load flow can be characterized by tests such as (IIa) the sand pile and (IIb) the slump test finding the shapes expressed by the height and the length respectively, shown in Fig. 2.27(right). The height and shape of a pile are typically used to characterize materials as e.g. sand and subsequently to calibrate DEM models as in e.g. [2, 3, 41, 31, 5].

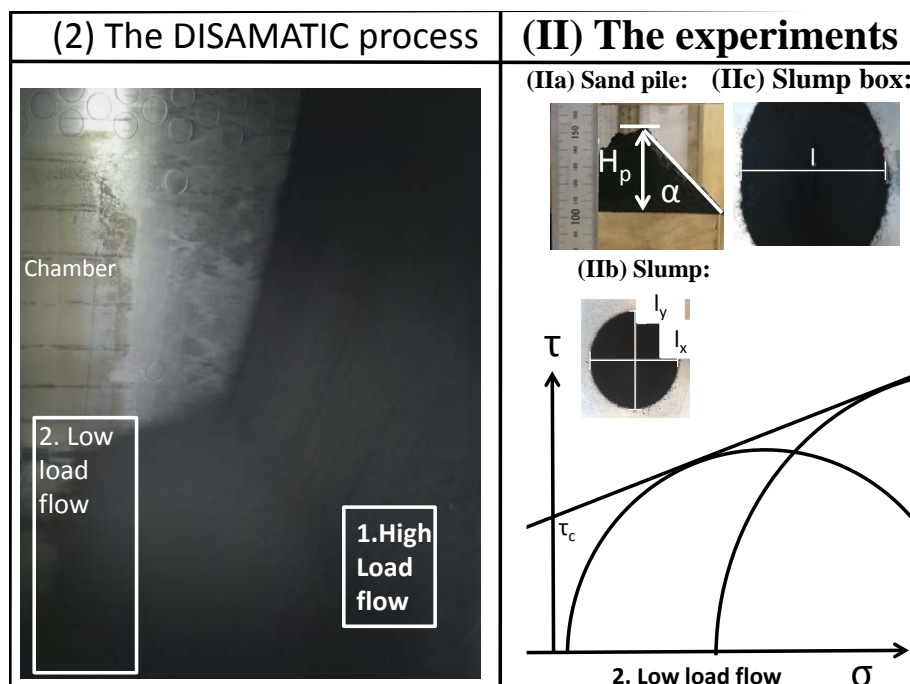


Figure 2.27: (Left side) The low load flow in the DISAMATIC process. (Right side) The performed experiments placed on the Mohr circle.

(II) The slump test is typically used for cement based materials and the cone tests are discussed in [42]. Here the cement-based materials' yield stress is measured using slump tests where stoppage tests measure the shape of a fresh material deposit after flow occurred. This measured geometrical value (slump, spread) is linked to a plastic yield stress value. Yield stress materials are discussed in [43, 44] where the material starts to flow when it exceeds the threshold described by the yield limit (τ_c). Yield stress materials come in many varieties such as concrete [45] and ceramic slurries [46]. An analytical solution was derived to determine the yield stress of a given material (i.e. a very fluid concrete also known as a self-compacting concrete) and this solution is discussed and simulated in the PhD thesis [47]. An additional overpressure was added in PAPER [4] to the analytical solution determining the yield stress and in PAPER [7] these solutions were non-dimensionlized.

2.3.2.1 The low load flow experiments (II)

2.3.2.1.1 The sand pile experiment (IIa)

A special hopper experiment was designed in the project shown in Fig. 2.28(left) where the experiment was designed to find the repose angle from the height of the sand pile above the box shown in Fig. 2.28(right). The sand pile test was made for investigating how the green sand flows during deposition on the box below the hopper, which is similar to the tests performed in [48]. The sand pile test has the low load flow behaviour similar to when the green sand is deposited on the top of the sand pile inside the DISAMATIC chamber.

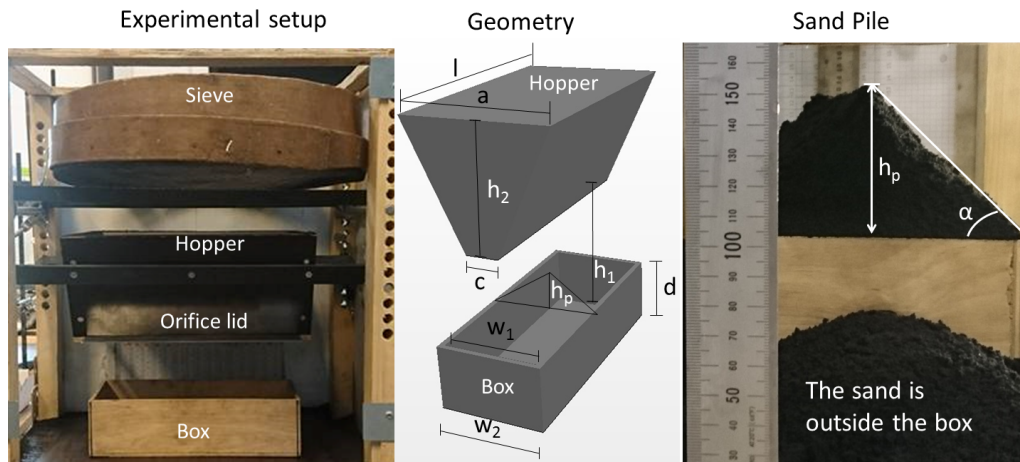


Figure 2.28: (Left) The hopper experiment can be seen with the sieve on the top, the hopper, orifice lid and finally the box in the bottom. (Middle) In the 3-D illustration the hopper measurement can be seen with the length $l=300$ mm, width of $a=180$ mm, orifice $c=40$ mm and the box measurements with the internal width $w_1=120$ mm, external width $w_2=134$, the height of the box $d=82$ mm, the measured height of the sand pile is denoted h_p and the drop height of $h_1=169$ mm and hopper height of $h_2=150$ mm. (Right) Sand pile experiment where the height h_p was found by a laser projected onto the ruler on the back. Note the box side and bottom thickness is 7 mm. The edited figure and text is originally from PAPER [2].

The hopper experiment and the geometry and all the dimensions of the hopper are illustrated in Fig. 2.28. The green sand is sieved down into the hopper. After the hopper is filled the orifice lid is opened for the final deposition of the green sand into the box. The final sand pile height h_p was found by a laser projected onto the ruler on the back and thereby the angle of repose can be calculated.

Repose angle

The angle of repose is used for characterization of granular material in this case from the sand pile height above the box. The larger the repose angle the lower the flowability and the more cohesive the material is which is categorized in table 2.7. The angle of repose

has some dependence on the test procedure in which the sand pile is created as e.g. sand pile created from a hopper onto a plate or sand pile created from a slump test discussed in [12]. The internal friction angles found from the ring shear test in section 2.3.1.1 are often compared to the repose angle and these angles are all presented in table 2.10 from the 8 batches. The repose angle α can be calculated from the sand pile height h_p and the external width of the box,

$$\alpha = \tan^{-1} \left(\frac{h_p}{\frac{w_2}{2}} \right) \quad (2.6)$$

Table 2.7: A suggested relationship between repose angle and flowability which is from [18].

Angle α	Flowability
25-30	Very free-flowing
30-38	Free-flowing
38-45	Fair-flowing
45-55	Cohesive
> 55	Very cohesive

2.3.2.1.2 The slump cylinder test (IIb)

A very simple slump cylinder test is designed for investigating the flowability properties of green sand and the green sand interaction on the steel plate. The standard cylinder specimen normally used in the compactability test is used for this test where the standard cylinder specimen has the dimensions of $H = 0.12 \text{ m}$ for the height and $D = 0.05 \text{ m}$ for the diameter. A flat steel plate was used under the box for contact with the green sand, the box was filled with green sand through the sieve shown in Fig. 2.29(left). The test was performed by lifting the tube rapidly, emulating an instantaneous wall opening in the simulation to finally find the slump diameter in Fig. 2.29(right). When the green sand slump has settled the two diameters orthogonal to each other (l_x, l_y) are measured and the average is calculated for the final slump length l_p . Note, that a metal plate resembling the DISAMATIC chamber is used under the standard specimen tube for having a proper metal plate-green sand contact. This test resembles the initial green sand hitting the bottom of the chamber and flowing outwards to the sides of the chamber.

2.3.2.1.3 Slump box test (IIc)

A slump test is designed with a box having the internal dimensions of height $H = 0.18 \text{ m}$, width $W = 0.134 \text{ m}$ and length $L = 0.313 \text{ m}$. A steel plate is used under the box for contact with the green sand. The box is filled with green sand through a sieve shown in Fig. 2.30(left) and afterwards the box is lifted rapidly and the green sand flows out to the sides and finally the length of the sand pile is measured (l_p) shown in Fig. 2.30(right).

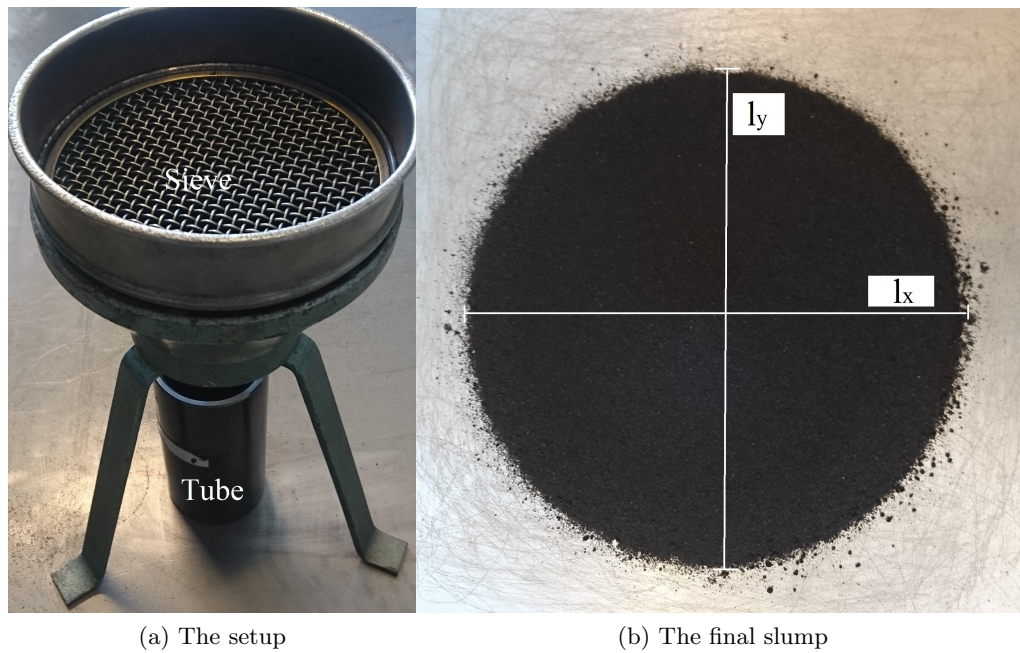


Figure 2.29: (a) The slump cylinder experiment setup. (b) The final slump where the two diameters of the sand pile is measured (denoted l_x , l_y) in orthogonal directions to each other.

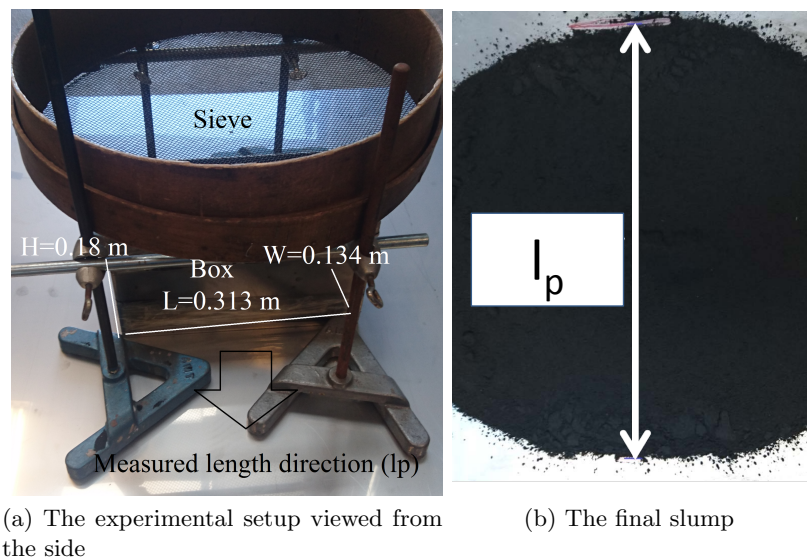


Figure 2.30: (a) The slump box experiment setup. (b) The final slump where the slump length l_p are measured

2.3.2.2 Results of the low load tests

The results of the low load tests which links to the flow on the top of the sand pile created in the chamber during the DISAMATIC process. The sand piles created with the sand pile experiment and slump tests are presented here:

(IIa) The sand pile test results are discussed in section 2.3.2.2.1.

(IIb) The slump cylinder results are discussed in section 2.3.2.2.2.

(IIc) The slump box results are discussed in section 2.3.2.2.3.

(IIa)-(IIc) Finally the sand pile heights and all the slump lengths are collected and presented in table 2.8.

2.3.2.2.1 Sand pile test (IIa)

The sand pile height (h_p) increases with higher compactability levels, which is shown in Fig. 2.31. For batch 2 the sand pile height ($h_p = 0.062m$) was higher as compared to all the other batches, which was due to the high compactability level of around 50 %. The flow-ability was small with the value of $FFc=1.5$, which was due to the very large cohesion that binds the sand grains together. For the dry sand in batch 7 then the sand pile height $h_p = 0.040m$ became smaller than all the other batches. Thereby batch 7 had a high flowability value of $FFc=8.5$, due to a smaller cohesion binding the sand grains together.

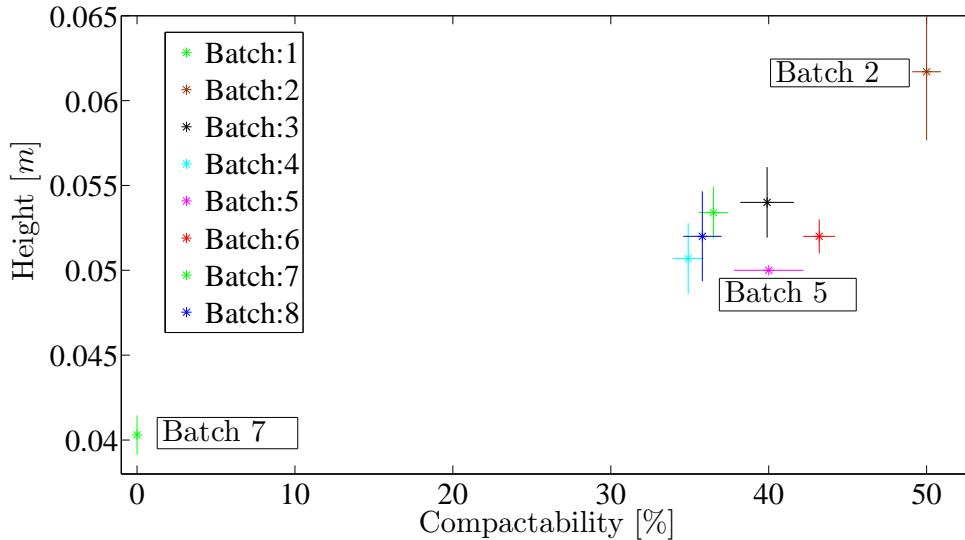


Figure 2.31: (IIa) The sand pile experiments average heights (h_p) for all the batches. The standard deviation for compactability is shown as a line in the horizontal direction and the standard deviation for the pile height is shown as a line in the vertical direction.

Batch 5 has a large compactability of 40 % when compared to the small sand pile height of $h_p = 50 \text{ mm}$, thereby this could be considered as an outlier as compared to the results of the other batches. Note that the results of the repose angles were presented in section 2.3.1.2.1 together with the internal friction angles found from the ring shear tester.

2.3.2.2.2 Slump cylinder test (IIb)

The governing trend of the slump test is that slump lengths decreases when the compactability increases which is shown in Fig. 2.32. For the wet green sand from batch 2

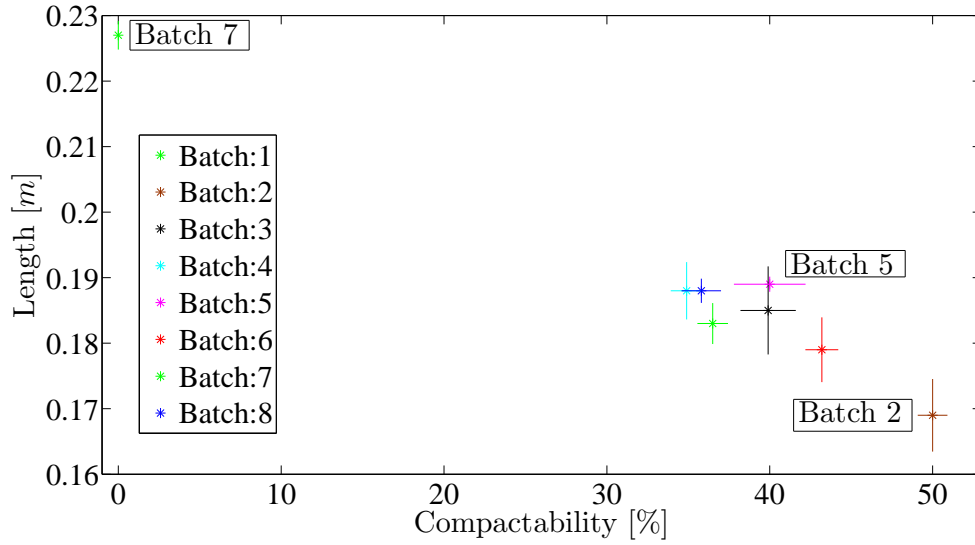


Figure 2.32: (IIb) The slump cylinder lengths (l_p) for all the batches. The standard deviation for compactability is shown as a line in the horizontal direction and the standard deviation for the slump length is shown as a line in the vertical direction.

with the high compactability level, then the slump length $l_p = 0.17 m$ became shorter when compared to all the other batches and this was due to the very cohesive wet green sand. The opposite is the case for the more freely flowing dry green sand from batch 7, which had a long slumb length of $l_p = 0.23 m$ and a small flowability value of $FFc=1.5$. Batch 5 had a large compactability value of 40 % compared to having the second longest slump length of $h_p = 0.19 m$, thereby it could be considered an outlier with respect to this test.

2.3.2.2.3 Slump box test (IIc)

The governing trend of the slump box test is that the lengths decrease when the compactability increases shown in Fig. 2.33. For wet green sand batch 2 with the high compactability level then the slump box length ($l_{p, 2-D} = 0.47 m$) became shorter compared to all the other batches. The opposite is the case for the dry green sand batch 7 which was very free flowing with the longest slumb box length of $l_{p, 2-D} = 0.62 m$ when compared to all the other batches. For batch 1 the box slump length was somewhat short $l_{p, 2-D} = 0.49 m$ when compared to the compactability level but note that only one repetition was performed in this slump box test. In general the larger the sand pile height becomes the shorter the slump length, which is due to the increased cohesion of the sand grains from the larger amount of water added shown in table 2.8.

2.3.2.3 Conclusion of the low load flow experiments

The sand pile height and the angle of repose increase with increased compactability. The sand pile becomes less conical together with larger clusters of sand particles (clumps) for an increased water content (larger compactability). The dry green sand pile height (Batch 7) was smaller compared to all the other batches, due to the smaller cohesion of the sand grains.

The slump length decreases as the compactability increases. The wet green sand batch had the shortest slump length whereas the dry green sand batch had the longest slump length as expected. A similar behaviour was experienced for the slump box test as for the slump cylinder test. In general, the larger the sand pile height, the shorter the slump length, which is due to the increased cohesion of the sand grains from the larger amount of water added.

Batch 5 had a large compactability level compared to the short sand pile height and the two long slump lengths. Batch 5 (purple color) also had the second largest flowability value $FFc=2.4$ shown in table 2.4, which is larger than expected when compared to the high compactability value, which was the third largest out of all the 8 batches. This could be due to the difference of the green sand condition in the buckets although the green sand mechanical behaviour should be very similar from bucket to bucket. Therefore batch 5 could be considered as an outlier with respect to these tests.

2.3.3 Fluidized flow (3)

The fluidized flow occurs when the green sand is transported by the airflow along the chamber wall or transported in the very top of the sand pile by the air flow which is illustrated in Fig. 2.34.

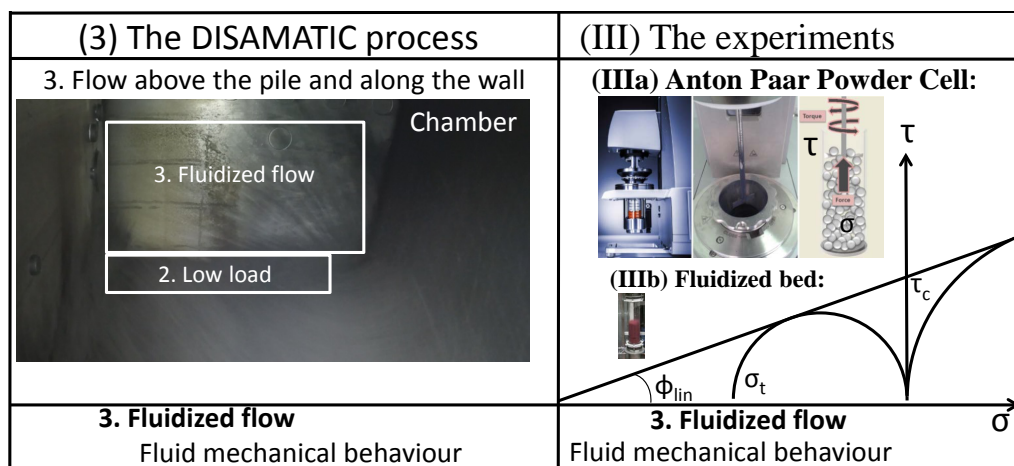


Figure 2.34: (Left) The low load flow in the DISAMATIC process. (Right) The performed experiments placed on the Mohr circle. (Bottom) The simulation showing the fluidized flow of the DEM particles on the left side.

Fluidized flow and pneumatic transport of solids are discussed in [49] and experiments were performed on a fluidized bed and on the newly developed Anton Paar Powder Cell for investigating the fluidized viscosity in PAPER [6].

2.3.3.1 Fluidized flow experiments (III)

2.3.3.1.1 The Anton Paar Powder Cell (IIIa)

The Anton Paar Powder Cell is used to investigate the fluidized viscosity which is discussed further in appendix B and in PAPER [6]. The air flow was kept fixed at different rates while the rotating velocity of the stirring blade was increased. The relationship of the viscosity, the air flow rate and the rotating velocity of the stirring blade could then be found.

2.3.3.1.2 The Fluidized bed (IIIb)

A standard fluidized bed test for finding the values of the pressure drop due to the drag force on the green sand and the minimum fluidization velocity with respect to the water content was performed in appendix C. The pressure drop and the minimum fluidization with respect to the mass of green sand was also tested for one batch of green sand.

2.3.3.2 Result and conclusion of the fluidized flow experiments (3)

The fluidized flow experiments were performed on different green sand batches and are therefore also presented separately in appendix B and in appendix C.

2.3.3.2.1 The Anton Paar Powder Cell (IIIa)

In PAPER [6] it was found that the green sand flow behaves like a shear thinning fluid, in which the viscosity is reduced by increasing the shear rate. The viscosity of the green sand is decreased by increasing the air flow rate. The results are discussed further in appendix B and in PAPER [6].

2.3.3.2.2 The Fluidized bed (IIIb)

In appendix C it was found that the overall trend is that the minimum fluidization velocity increases with the water content since the sand surface area decreases, due to the bonding of the individual sand grains into a collection of sand grains forming clusters. This suggested that green sand with a high compactability level of around 43-44 % is harder to fluidize and probably it is also harder to transport and fill the narrow passages with green sand in the chamber geometry during the sand shot, although the sand dries out fast when the green sand is transported by the air. For the detailed conclusions of the fluidized bed test, see appendix C.

2.3.4 The confined compression (4)

The mold squeezing is illustrated in Fig 2.12(right top) together with the tests performed that investigate the solid mechanical behaviour of the green sand confined compression (right middle). The mold squeezing has its solid mechanical behaviour more precisely described by the yield locus of a granular material which is explained in [50].

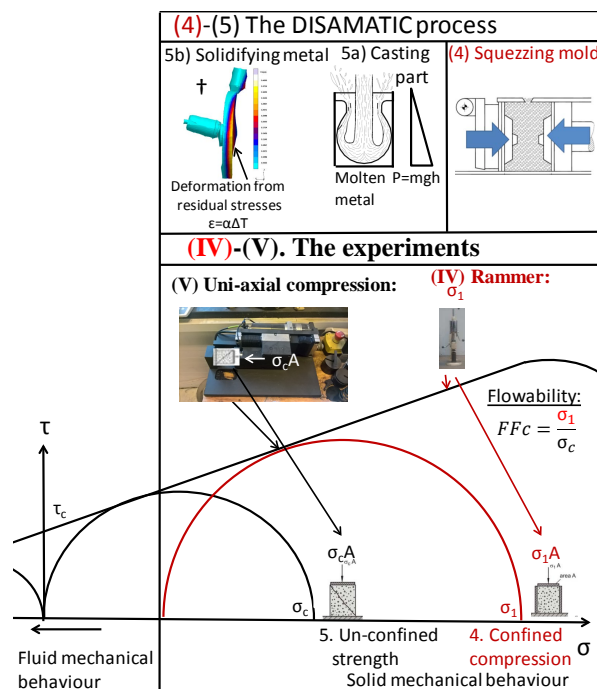


Figure 2.35: (Top) (4) Squeezing of the mold (confined compression) and (5) casting of the part and (un-confined strength) which is the solid mechanical behaviour of DISAMATIC process. (Bottom) The experiments performed in the project placed on the Mohr circle where (IV) the rammer creates a sample of green sand (confined compression). This sample is inserted into the STM machine performing (V) the uni-axial compression test (un-confined strength). The figure † in the left corner shows the deformation of a parts due to residual stresses and the figure is from [13].

The confined compression of the green sand is typically tested with the compactability test, which is discussed in [35, 8].

2.3.4.1 The confined compression experiments (IV)

2.3.4.1.1 The compactability test (IVa)

The compactability test is applied for investigating the confined compression of the green sand. Note that the compactability test was described earlier in section 2.2.4.3 and the results were shown in section 2.2.5 instead of section 2.3.4.

2.3.5 The un-confined strength (5)

In Fig. 2.35(left top corner) the mold filling occurs with the molten metal exerting a metallostatic pressure the mold during casting. It is important that the mold can withstand this metallostatic pressure together with the initial pouring of the metal into the mold (5a). During solidification, the solidifying metal contracts and the mold material has to withstand the load until the cast material has obtained sufficient stability to keep the shape of the design (5b).

The flowability (FFc) was illustrated in Fig. 2.35 and was found earlier from the ring shear tester. The flowability could also be found in the solid mechanical region with a compression machine, which could measure the confined compression strength followed by the unconfined compression strength. In [19] a regression model was applied to determine the relationship between the input value of the sand mixture, i.e active clay, water content to the related output values compactability, green compressive strength, spalling strength and permeability. This relationship was developed on a data set collected from a DISAMATIC foundry. Tri-axial tests have been performed on green sand to obtain the yield locus in [24]. Uni-axial compression tests were performed on green sand where the stress-strain curves were analyzed in [25].

2.3.5.1 The un-confined strength experiments (V)

2.3.5.1.1 Uni-axial compression on the STM machine (Va)

A compression test is a well known experiment for green sand, which is explained in [35] and the stress-strain curves were analyzed in e.g. [25]. The uni-axial compression strength of the green sand is tested on a strength testing machine described in [14] and the machine is shown in Fig. 2.36. The uni-axial compression tests is used to find the maximum strength (σ_{max}) of the compressed green sand sample prepared by 3 rammings to have a length and diameter of 0.05 m. In Fig. 2.37 the maximum stress is denoted σ_{max} . Depending on the height of the mold the compression strength should be increased for a mold height around 50 cm and the compression strength should be around $\sigma_{max} = 19 - 23 \frac{N}{cm^2}$ which is suggested in [8]. In seven out of the eight batches (not on the dry batch number 7) the uni-axial compression test was performed with seven repetitions for each batch.

The strain-stress curves:

A sample of green sand with the length of L=50 mm and diameter of 50 mm is prepared from the standard rammer (2.2.4.3). The correct mass of green sand is calculated from the known compactability value to get the desired length of the sample. This is not always exactly 50 mm and the initial starting point of the STM machine is hard to set to exactly zero strain $\epsilon \approx 0$. An algorithm is thereby constructed aligning and moving all the stress-strain curves' maximum stress point to the same position for each individual batch. This was done in the following way:

- (1) For each individual batch the smallest strain was found where the maximum stress σ_{max} occurred out of the seven repetitions in the specific batch.
- (2) For the individual batch all the maximum stresses from the experiments are repositioned to the same strain value.

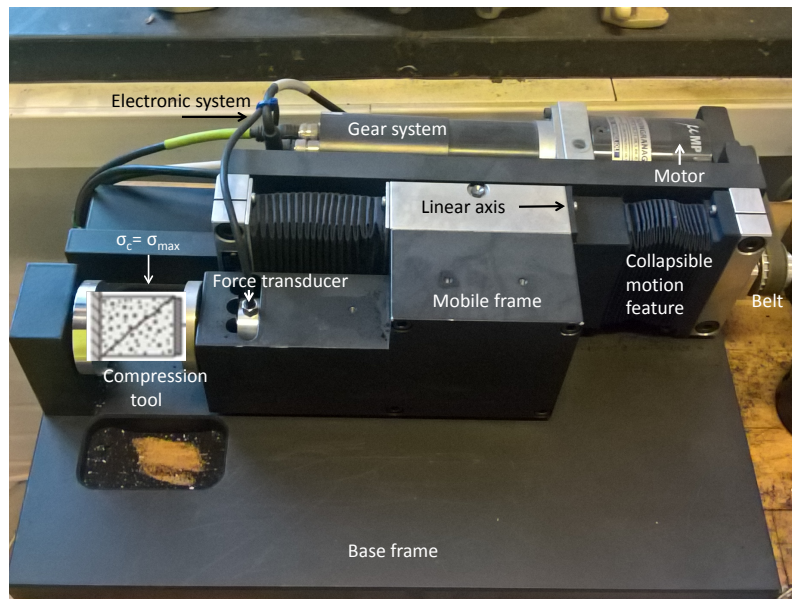


Figure 2.36: The strength testing machine with the parts identified. A similar figure was first originally presented in [14].

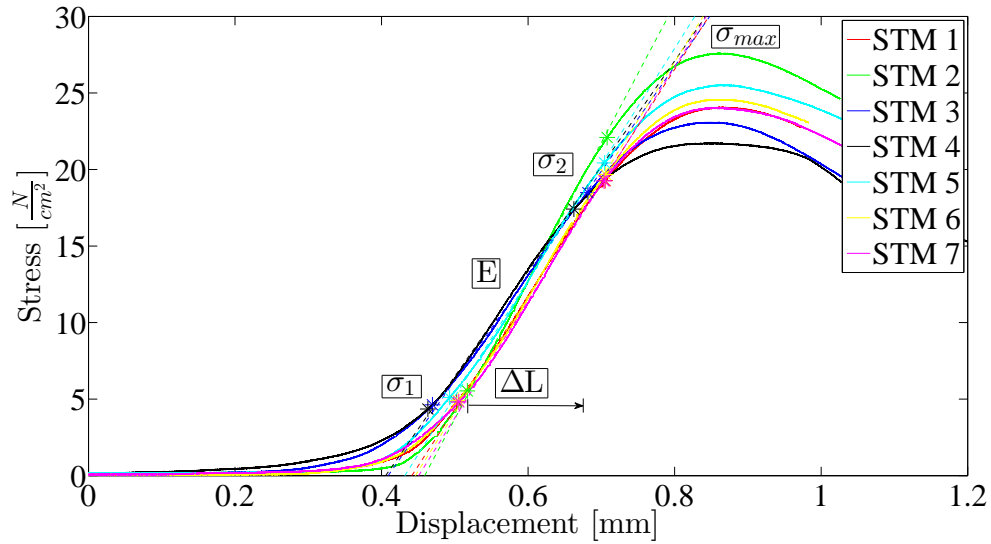


Figure 2.37: Stress-strain curves made on the STM machine for one batch. The x-axis is the displacement with the units of [mm] and the y-axis is the stress with units of [$\frac{N}{cm^2}$]

tioned to the smallest strain value found in (1), thereby repositioning the 6 other repetitions maximum stress to (1).

(3) This algorithm was applied for all the 7 batches where the uni-axial compression tests

were performed.

The linear intervals are determined to be in the stress range of $\sigma_1 = \max(\sigma_c) \times 20\% < \sigma_c < \max(\sigma_c) \times 80\% = \sigma_2$ and the linear intervals is illustrated by the arrow pointing to the right in Fig. 2.37. This method was also applied in [25] for determining the slope after failure. For the linear region the Young's modulus of the sample is calculated as the slope in the region as,

$$\sigma = E\epsilon \quad (2.7)$$

Where σ is the stress on the material subjected to the strain of $\epsilon = \frac{\Delta L}{L_0}$ where $L_0 = L - L_{\sigma_1}$ is the initial sample length assumed to be 50 mm minus the displacement found at the stress σ_1 . Hence, displacement above ϵ_1 , is monitored as the displacement ϵ in the linear region.

2.3.5.2 Results of unconfined strength experiments (V)

2.3.5.2.1 Results of the uni-axial compression test

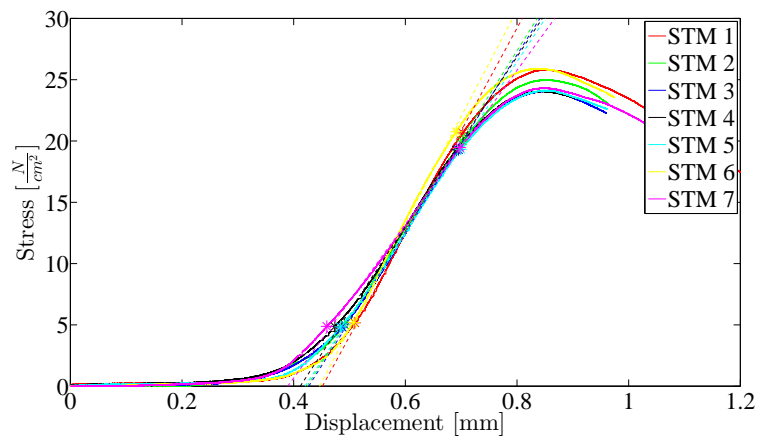
The compression strength and stiffness are shown in Fig. 2.38 for the three investigated compactability levels. The low compactability level (a), middle compactability level (b) and high compactability level (c). The stiffness is found from the slope of the linear region by MATLAB's fitting tool box which fitted the curve with a standard least square algorithm.

The results of the compression strength σ_{max} and the Young's modulus (E) for the three investigated batches are given in table. 2.9. The Young's modulus had similar values with a maximum difference smaller than 6 % for the three selected batches. The variance indicated by the standard deviation was an order of magnitude $\times 10$ smaller than the Young's modulus. The behaviour was very close to linear as indicated by the adjusted root mean square which was close to 1 for all the tests where the smallest average of the adjusted root mean squares was $0.9988 \pm (\text{Average(Adj-RMSQ)})$ and with a very small standard deviation of 4.8693×10^{-4} .

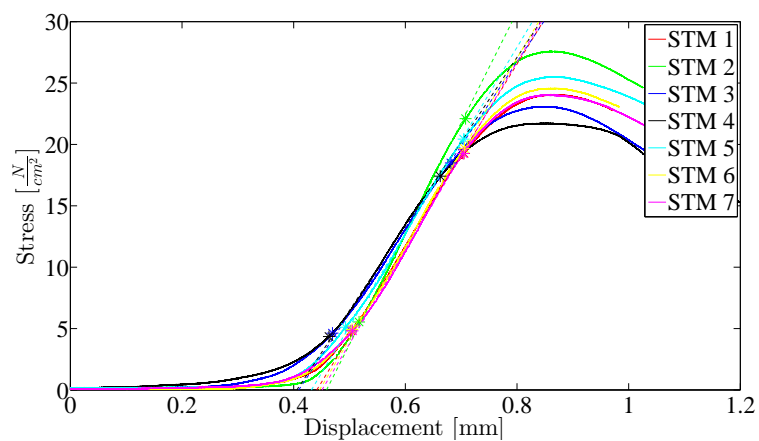
Table 2.9: (V) The found values of the Young's modulus (E) from eq. 2.3.5.1.1 are shown as the slopes in Fig. 2.38. The standard deviation (std) is indicated by \pm std.

Batch	E \pm std [Pa]	Average(Adj-RMSQ) \pm std	$\sigma_{max} \pm$ std [Pa]
Low (b=8)	$3.7 \times 10^7 \pm 4.2 \times 10^6$	$0.9988 \pm 4.8693 \times 10^{-4}$	24.8 ± 0.82
Medium (b=3)	$3.8 \times 10^7 \pm 3.6 \times 10^6$	$0.9988 \pm 3.5461 \times 10^{-4}$	24.4 ± 1.85
High (b=6)	$3.6 \times 10^7 \pm 4.6 \times 10^6$	$0.9990 \pm 3.9404 \times 10^{-4}$	23.4 ± 1.37

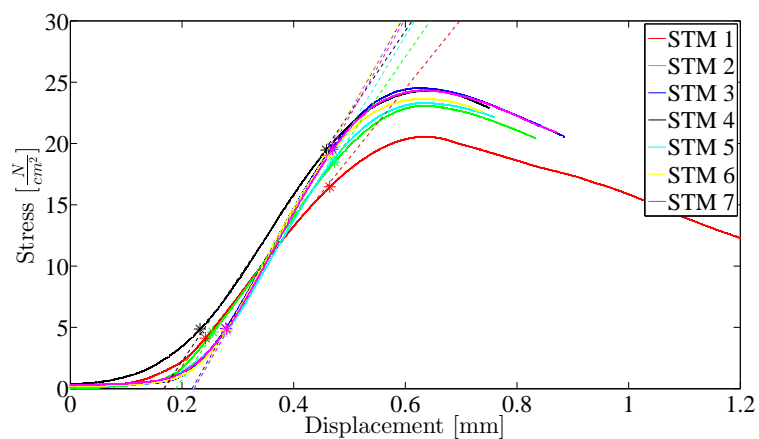
The linear regions and failure points occurred for larger strains at the low compactability level compared to the higher compactability level. The failure point is larger and has a smaller standard deviation for the low compactability level of $24.8 \pm 0.82 Pa$.



(a) Compression test: Low compactability (Batch 8)



(b) Compression test: Middle compactability (Batch 3)



(c) Compression test: High compactability (Batch 6)

Figure 2.38: (V) The compression tests for the three selected batches.

The compression strength (σ_{max}) and Young's modulus (E) for all the batches are given in table. 2.10(not the dry sand batch number 7).

2.3.5.3 Conclusion of the un-confined compression strength experiment

Based on the uni-axial compression test it was found that the stiffness and the uni-axial compression strength of the green sand were similar for all the batches. The strain-stress slope is close to constant in the selected area suggesting an elastic region for the green sand sample. The uni-axial compression strength and stiffness were significantly smaller for the wet green sand batch (batch 2) compared to the other batches.

2.4 Overall conclusion of all the experiments

The overall conclusion of the tests in the five mechanical categories (1)-(5) for the tests performed in the five regions (I)-(V) are:

All the results of the experiments for all the 8 batches are summarized in a table 2.10 placed on the next page. The compactability test values followed the water content tests values e.g. when the water content increased the compactability increased too. When the compactability increased the sand pile height became higher, the slump lengths became shorter and the yield stress limit became larger which was found from the ring shear tester. Batch 5 could be seen as an outlier, due to the results of high compactability level and the low flowability value from the ring shear tester, the low sand pile height and the long sand pile lengths from the two slump tests. An Instron machine (a more complex compression machine) investigating the compression of green sand could be an obvious choice for investigating the flowability value (FFc) of green sand under the solid mechanical regime with a controlled confined compression and a controlled uni-axial compression for comparison with the ring shear tester's flowability value.

The density as a function of the normal stress from [21] could be applied with the yield stress limit found from the ring shear tester to simulate the sand shot mold filling with a continuum model. The fluidized viscosity was found from the Anton Paar Powder Cell in appendix B and this combined with the ring shear tester could potentially be enough to calibrate e.g. a Herschel-Buckley model to simulate the sand shot. Thereby the test results can in general give indications of the green sand material properties and the results can be applied for calibrating and inserting physical values in models simulating the sand shot as e.g. STAR-CCM+, ANSYS or FLOW-3D. The knowledge and the physical values from the selected experiments are applied to calibrate the DEM model which is explained in the next chapter 3. The calibrated DEM model is later used to simulate the behaviour of the green sand in the sand shot in the following chapters 4 and 5.

Table 2.10: *(I)-(V): Results of the performed tests on the 8 batches of the green sand (I)-(V)

Tes type	Batch number							
	1	2 (Wet)	3	4	5	6	7 (dry)	8
Water	3.9 ± 0.4	4.0 ± 0.2	3.6 ± 0.2	3.3 ± 0.2	3.6 ± 0.1	3.7 ± 0.1	2.3 ± 0.4	3.6 ± 0.2
Reps	n=6	n=14	n=13	n=12	n=11	n=12	n=9	n=15
3 ram	36.5 ± 0.94	50.0 ± 0.91	39.9 ± 1.70	34.9 ± 0.98	40.0 ± 2.20	43.2 ± 1.01	No	35.8 ± 1.21
(Ia)-(Ic)								
φ_e	44.7 ± 1.46	52.0 ± 0.81	46.4 ± 2.70	44.6 ± 2.43	44.5 ± 1.57	45.6 ± 1.40	40.1 ± 0.92	43.1 ± 1.06
φ_{lin}	28.5 ± 0.55	28.7 ± 0.91	28.6 ± 1.63	30.6 ± 1.93	32.1 ± 2.83	28.4 ± 0.52	37.3 ± 0.96	29.5 ± 1.44
φ_{sF}	37.4 ± 0.51	40.4 ± 0.43	38.4 ± 1.38	38.0 ± 1.54	38.7 ± 1.10	38.2 ± 0.86	37.2 ± 0.90	36.9 ± 0.44
σ_c	539 ± 45.0	715 ± 26.5	586 ± 50.9	493 ± 32.9	446 ± 54.0	561.2 ± 37.0	122 ± 13.5	467 ± 36.0
FFc	2.0 ± 0.2	1.5 ± 0.0	1.8 ± 0.1	2.2 ± 0.1	2.4 ± 0.2	1.9 ± 0.1	8.5 ± 0.9	2.3 ± 0.2
Reps	n=3	n=5	n=5	n=5	n=5	n=5	n=5	n=5
φ_{wa}	16.4 ± 1.74	19.8 ± 0.66	19.2 ± 0.58	19.0 ± 0.49	17.0 ± 0.93	18.3 ± 0.44	13.3 ± 0.56	18.1 ± 1.16
	n=3	n=3	n=3	n=3	n=3	n=3	n=3	n=3
(IIa) (IIc)								
h_p	53.4 ± 1.52	61.7 ± 4.04	54.0 ± 2.08	50.7 ± 2.08	50.0 ± 0.00	52.0 ± 1.00	40.3 ± 1.15	52.0 ± 2.65
α	37.9 ± 0.73	41.5 ± 1.62	38.1 ± 0.96	36.6 ± 1.04	36.3 ± 0.00	37.3 ± 0.49	30.8 ± 0.70	37.2 ± 1.29
Reps	n=3	n=3	n=3	n=3	n=3	n=3	n=3	n=3
l_p [mm]	183 ± 3.13	169 ± 5.54	185 ± 6.72	188 ± 4.38	189 ± 1.15	179 ± 4.94	227 ± 2.19	188 ± 1.85
Reps	n=5	n=5	n=5	n=5	n=5	n=5	n=5	n=5
$l_{p,2}$	490	469 ± 8.54	499 ± 16.9	524 ± 9.02	522 ± 3.00	498 ± 10.8	621 ± 7.81	521 ± 12.5
Reps	n=1	n=3	n=3	n=3	n=3	n=3	n=3	n=3
(IV)								
3 ram	36.5 ± 0.94	50.0 ± 0.91	39.9 ± 1.70	34.9 ± 0.98	40.0 ± 2.20	43.2 ± 1.01	No	35.8 ± 1.21
ρ	896 ± 15.4	723 ± 17.0	852 ± 21.0	926 ± 15.5	842 ± 21.2	806 ± 21.2	1.21 × 10 ³ ± 11.3	917 ± 12.1
ρ_3	1.41 × 10 ³ ± 23.0	1.45 × 10 ³ ± 17.0	1.42 × 10 ³ ± 7.24	1.43 × 10 ³ ± 23.5	1.40 × 10 ³ ± 22.3	1.42 × 10 ³ ± 17.0	No	1.43 × 10 ³ ± 12.2
Reps	n=14	n=13	n=17	n=14	n=15	n=13	n=7	n=15
10 ram	43.0 ± 2.25	53.8 ± 0.45	46.6 ± 0.93	40.6 ± 0.48	46.6 ± 0.90	48.9 ± 0.24	No	41.5 ± 0.41
ρ_{10}	1.60 × 10 ³ ± 65.0	1.59 × 10 ³ ± 13.0	1.57 × 10 ³ ± 8.80	1.56 × 10 ³ ± 6.42	1.55 × 10 ³ ± 12.1	1.56 × 10 ³ ± 5.96	No	1.55 × 10 ³ ± 3.01
Reps	n=6	n=5	n=7	n=7	n=7	n=7	n=0	n=7
(V)								
σ_{STM}	26.0 ± 0.33	19.3 ± 0.92	24.4 ± 1.85	26.1 ± 0.67	25.1 ± 2.07	23.4 ± 1.37	No	24.8 ± 0.81
$E = [Pa]$	3.6 × 10 ⁷ ± 3.4 × 10 ⁶	2.5 × 10 ⁷ ± 3.1 × 10 ⁶	3.8 × 10 ⁷ ± 3.6 × 10 ⁶	3.6 × 10 ⁷ ± 3.0 × 10 ⁶	4.0 × 10 ⁷ ± 5.4 × 10 ⁶	3.6 × 10 ⁷ ± 4.6 × 10 ⁶	No	3.7 × 10 ⁷ ± 4.2 × 10 ⁶
Reps	n=7	n=7	n=7	n=7	n=7	n=7	n=0	n=7

Chapter 3

The Discrete Element Method and its calibration

3.1 Introduction

The Discrete Element Method (DEM) is chosen as the numerical model in the PAPERS [1, 2, 3] due to the discrete structure of the method which simulates the granular nature of the green sand. The DEM method uses a rolling resistance model to emulate the non-spherical quartz sand particles' resistance to rolling as well as a cohesive model to emulate the binding of the quartz sand particles from the bentonite in the PAPERS [2, 3]. The ring shear tester is used to obtain the static friction coefficients for the DEM model. A sand pile experiment was used to investigate the simple mechanical behaviour of green sand from the measured height. From this height the DEM model is also calibrated with respect to obtaining the values of the particle-particle rolling resistance and obtaining the particle-particle parameter value in the cohesive model. Additionally the density is adjusted to the loose green sand density and the slump experiments are applied to calibrate the particle-wall rolling resistance in PAPER [3].

This chapter summarizes the PAPERS [1, 2, 3] with the following topics:

The general work in the field of the DEM is presented in section 3.2 together with the governing equations for the DEM model.

Research with respect to general calibration of the DEM method together with the calibration procedure applied in this project is presented in section 3.3.

A short conclusion of this chapter is presented in section 3.4.

3.2 Introduction to DEM in general

A general review of the theoretical foundation was published in [51] and applied in [52] where a comparison of different frequently used DEM contact models were presented in [53]. DEM is gaining popularity as the computational power available to researchers increases and with the introduction of parallel computing in DEM, the method is starting

to be used for granular flow [54] since it has been possible to perform larger scale DEM simulations [55]. Newly developed codes based on the GPU framework are under development as e.g. [56] for realistic simulation of sand behaviour. The GPU framework in [57] was used for simulations of mill charge in [58] making the use of the GPU for faster simulations of millions of non-spherical particles.

3.2.1 The numerical model applied

The commercially available software STAR-CCM+ [15] and the parallel computing capabilities in this software were used for the simulations in the PAPERS [1, 2, 3]. In DEM the velocity is decomposed into a normal and tangential direction, as originally proposed by [59] and shown in Fig. 3.1. The Hertz-Mindlin contact model is chosen due to its ability to find the normal and tangential stiffness from real material parameters. Hertzian contact mechanics is used in the normal direction of impact [60] and a simplified Mindlin model is used in the tangential direction of impact [61], from which the non-linear damping can be derived. The non-linear damping model was tested in Refs. [62], [63]. The selected model for rolling resistance is the constant torque method first developed by [64] and tested in [65]. The cohesion model selected is the Johnson-Kendall-Roberts (JKR) model described in [66].

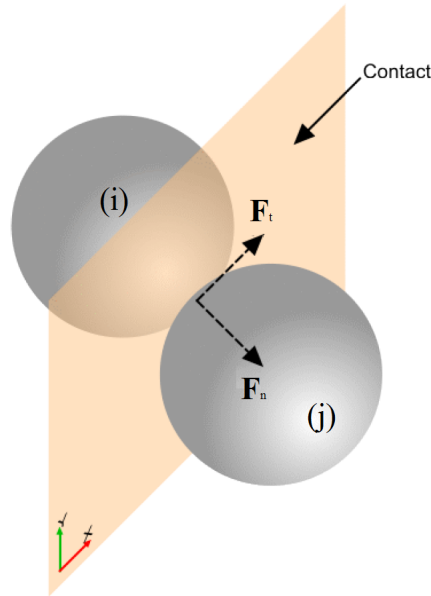


Figure 3.1: Particle i-th impact with particle j-th where the velocity is decomposed into a normal \vec{F}_n and tangential direction \vec{F}_t . The edited figure is from [15]

3.2.1.1 Particle kinematics

The notation applied for describing the equations applied in DEM is from [67], where the two particles in contact are denoted $\{i, j\}$ positioned at $\{\vec{r}_i, \vec{r}_j\}$ and the velocities

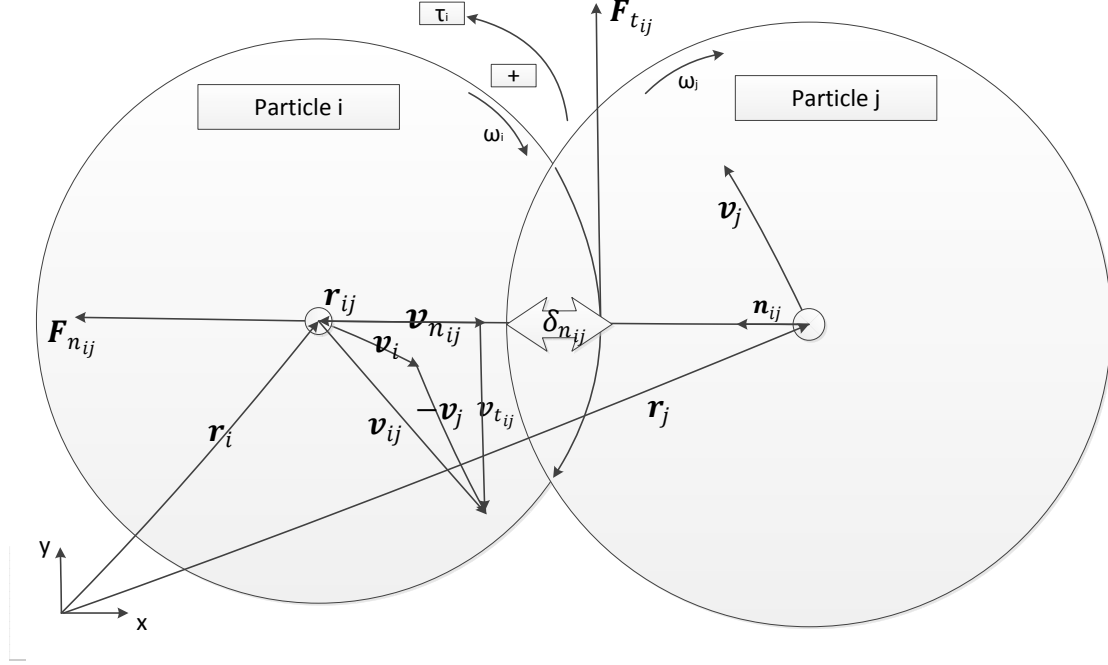


Figure 3.2: Particle i – th impact with particle j – th , the force exerted on the i – th particle in the normal direction is $\vec{F}_{n_{ij}}$ and in the tangential direction is \vec{T}_i^{tot} . The edited figure is from PAPER [1].

$\{\vec{v}_i, \vec{v}_j\}$ and finally the angular velocities of $\{\vec{\omega}_i, \vec{\omega}_j\}$ which are illustrated in Fig. 3.2. The distance between the two particles is denoted $r_{ij} = \|\vec{r}_i - \vec{r}_j\|_2$, the position vector from particle j to i is $\vec{r}_{ij} = \vec{r}_i - \vec{r}_j$ and the normal overlap δ_{ij} is

$$\delta_{ij} = (R_i + R_j) - r_{ij} = 2R - r_{ij}, \quad (3.1)$$

Since all the particles have the same radius and physical properties $(R_i + R_j) = 2R$ for the particle-particle interaction. The relative normal velocity is

$$\vec{v}_{n_{ij}} = (\vec{v}_{ij} \cdot \vec{n}_{ij}) \vec{n}_{ij}, \quad (3.2)$$

where $\vec{n}_{ij} = \vec{r}_{ij}/r_{ij}$ is the unit normal vector onto the contact plane. The relative tangential velocity is

$$\vec{v}_{t_{ij}} = \vec{v}_{ij} - \vec{v}_{n_{ij}} - (\vec{\omega}_i R_i + \vec{\omega}_j R_j) \times \vec{r}_{ij}, \quad (3.3)$$

3.2.1.2 Normal contact force

The normal force acting on the particles then becomes

$$\vec{F}_{n_{ij}} = \vec{n}_{ij} k_n \delta_{ij}^{\frac{3}{2}} - N_{n_{ij}} \vec{v}_{n_{ij}} + \vec{F}_{coh_{ij}} \quad (3.4)$$

$N_{n_{ij}}$ is the normal non-linear damping coefficient and $F_{coh_{ij}}$ is the cohesion. The stiffness in the normal direction can be found as,

$$K_n = \frac{4}{3}E_{eq}\sqrt{R_{eq}} \quad (3.5)$$

where the equivalent Youngs modulus is given by $E_{eq} = \frac{1}{\frac{1-\nu_i^2}{E_i} + \frac{1-\nu_j^2}{E_j}} = \frac{E}{2(1-\nu^2)}$ and the equivalent radius $R_{eq} = \frac{1}{\frac{1}{R_i} + \frac{1}{R_j}} = \frac{R}{2}$. Damping in the normal direction is defined as,

$$N_{n_{ij}} = \frac{4}{3}\sqrt{(5K_n M_{eq})}\delta_{n_{ij}}^{\frac{1}{4}}N_{n,damp} \quad (3.6)$$

The damping coefficient is equal to $N_{n,damp} = 1$ if $C_{rest} = 0$ otherwise

$$N_{n,damp} = \frac{-\ln(e_n)}{\sqrt{\pi^2 + \ln(e_n)^2}} \quad (3.7)$$

and the coefficient of restitution (COR) is formally defined as $e_n = -\frac{v_{in}}{v_{out}}$, where v_{in} is the velocity in the normal direction before impact and v_{out} is after and the equivalent mass is given by $M_{eq} = \frac{1}{\frac{1}{M_i} + \frac{1}{M_j}} = \frac{M}{2}$.

The cohesion $\vec{F}_{coh_{ij}}$ selected is the Johnson-Kendall-Roberts (JKR) model with the factor -1.5, where the particle-particle constant cohesion force in the normal direction is defined as

$$\vec{F}_{coh_{ij}} = -1.5\pi R_{min}W\vec{n}_{ij} \quad (3.8)$$

$R_{min} = R$ is the minimum radius of contact, W is the cohesion parameter with the units of $[\frac{J}{m^2}]$.

3.2.1.3 Tangential contact force

The tangential force on particle i from particle j can be found as,

$$\vec{F}_{t_{ij}} = K_t \frac{\vec{t}_{ij}}{\|\vec{t}_{ij}\|_2} \delta_{t_{ij}}^{\frac{3}{2}} - N_{t_{ij}}\vec{v}_{t_{ij}} + \vec{T}_{rol_{ij}} \quad (3.9)$$

The tangential stiffness is defined as $K_t = 8G_{eq} = \sqrt{R_{eq}\delta_{n_{ij}}}$ and the equivalent shear modulus as $G_{eq} = \frac{1}{\frac{2(2-\nu_i)(1+\nu_i)}{E_i} + \frac{2(2-\nu_j)(1+\nu_j)}{E_j}} = \frac{E}{4(2-\nu)(1+\nu)}$. The $N_{t_{ij}}$ is the tangential non-linear damping coefficient in the tangential direction is defined as,

$$N_{t_{ij}} = \frac{4}{3}\sqrt{(5K_t M_{eq})}N_{t,damp} \quad (3.10)$$

$N_{t,damp}$ is defined as

$$N_{t,damp} = \frac{-\ln(e_t)}{\sqrt{\pi^2 + \ln(e_t)^2}} \quad (3.11)$$

where the coefficient of restitution (COR) is formally defined as $e_t = -\frac{\vec{\omega}_{in}}{\vec{\omega}_{out}}$, where v_{in} is the angular velocity before impact and v_{out} is after impact. The rolling resistance for the particle-particle interaction used is the constant torque method, defined as,

$$\vec{T}_{rol_{ij}} = -\frac{\omega_{rel}}{|\omega_{rel}|} \mu_r R_{eq} |F_{n_{ij}}^{\vec{}}| \quad (3.12)$$

The relative angular velocity between the two particles is defined as $\vec{\omega}_{rel} = \vec{\omega}_i - \vec{\omega}_j$ and the torque from the rolling resistance is $\vec{T}_{rol_{ij}}$.

Note that there is a maximal tangential force due to Coulomb's law,

$$\|\mu_s \vec{F}_{n_{ij}}\|_2 < \|\vec{F}_{t_{ij}}\|_2 \quad (3.13)$$

the particle-particle static friction coefficient is denoted $\mu_{s,p-p}$ and particle-wall static friction coefficient is denoted $\mu_{s,p-w}$.

3.2.1.4 Summing the forces

The total resultant force on particle i is then computed by summing the contributions of all particles j with which it currently interacts, thus:

$$\vec{F}_i^{tot} = m_i \vec{g} + \sum_j \left(\vec{F}_{n_{ij}} + \vec{F}_{t_{ij}} \right) \quad (3.14)$$

where \vec{g} is the acceleration due to gravity. The total torque acting on particle i is given by

$$\vec{T}_i^{tot} = -R_i \sum_j \vec{n}_{ij} \times \vec{F}_{t_{ij}} \quad (3.15)$$

From these two expressions the acceleration, velocity, position and rotation, are calculated by Newton's second law, numerically for each time step.

3.2.1.5 Maximum time step

The maximum time step is found from taking into account the smallest value of the following three options: The first time constraint, δt_1 is the Rayleigh wave velocity [68, 69, 15]. The second constraint, δt_2 on the time step is that it takes at least 10 time-steps for the particle to move the full length of the radius. The third constraint on the time steps is δt_3 , which is the duration of impact of two perfectly elastic spheres with the Hertz contact theory derived by Timoshenko [70] and finally a dynamic time-step calculation takes the smallest value of the three times $\delta t = \min(\delta t_1, \delta t_2, \delta t_3)$, where in practice δt_1 is typically the limiting factor [15].

3.3 Calibrating the DEM model for applications

DEM simulations are widely used in many different research fields for materials as rocks, soils, powders and sand grains because DEM can simulate the discrete behaviour of these materials properly [71]. Thereby DEM simulations are also widely used for simulating many different mechanical behaviours as e.g. high load flows, low load flows, fluidized flows and solid mechanical behaviours for materials with discrete behaviour. Calibration of DEM models with subsequent applications is discussed more generally in [51, 52, 72, 73] and will be discussed in the next sections 3.3.1-3.3.4.

In section 3.3.1 the high load flow is discussed and in section 3.3.1.1 the ring shear tester is applied for finding the static friction coefficients for the DEM model.

In section 3.3.2 the low load flow is discussed and in section 3.3.2.1 a sand pile experiment and a slump test are applied for calibrating the cohesion and rolling resistance values for the DEM model.

3.3.1 Simulating the high load flow regime (1)

DEM simulations of the Schulze ring shear tester have been made in [74] where the particle shape, the cohesion and the static friction were investigated with respect to the resulting tangential pre-shear stress and the peak value (τ_{pre}). In [75] a sensitivity analysis was performed applying DEM to simulate a Schulze ring shear tester where several material input parameters' effect on the resulting tangential pre-shear stress was simulated. The tangential pre-shear stress had an asymptotic dependence from the particle-particle static friction ($\mu_{s,p-p}$) up to the value of $\mu_{s,p-p} < 0.70$ and a linear dependence on the peak stress was found from the parameters rolling friction ($\mu_{r,p-p}$) and Young modulus (E).

In [76] a direct shear test was used to calibrate the internal friction angle together with a compression test, which was used to find the particle stiffness for the DEM model and finally the DEM model was applied to simulate earth moving equipment. Recent simulations were performed in [77] where the effect of the DEM particle shape was investigated by simulating the crushed rock particles. The rock particles were tested with a confined compression test, which was used to determine the particle stiffness and a direct shear test, which was applied to determine the particle-particle static friction coefficient. The shape of the rock was emulated by three sets of representative DEM particle shapes applying 2, 4 and 8 spheres. The particle-particle static friction coefficient was varied to see the effect on the shear box test and the repose angle. In [77] it was concluded that the direct shear test was better than the angle of repose for calibrating the particle-particle static friction coefficient. Finally the calibrated model with the clump composed of 8 particles simulated a hopper discharge and an Anchor pull-out successfully.

3.3.1.1 Calibrating the DEM model at the high load flow

The first calibration step of the DEM model is from a Schulze ring shear tester of the type RST-SX described in [12] and applied in chapter 2. The ring shear tester starts with compressing the green sand and subsequently shearing to steady state flow, which is when a constant shear stress is reached, this procedure emulates the high load flow region. Due to the compression of the particles while shearing it is assumed that the flow is mostly governed by sliding and thereby the static friction coefficients are obtained in this way similar to the direct shear test in [77]. The ring shear tester was applied in the PAPERS [2, 3] to obtain the particle-particle static friction coefficient ($\mu_{s,p-p}$) as well as the particle-wall static friction coefficient ($\mu_{s,p-w}$). The ring shear tester was applied to obtain a suitable interval for the static friction coefficients for the DEM model in PAPER [2]. In PAPER [3] the ring shear test values were directly applied as shown in Fig. 3.3.

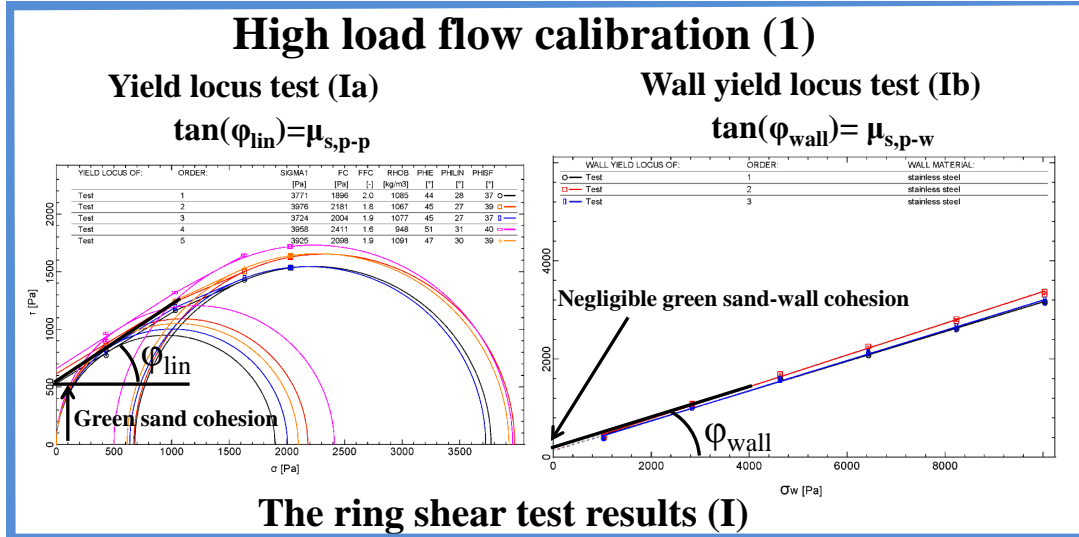


Figure 3.3: Calibrating the DEM model at high load flow (1).

Note the green sand cohesion is calibrated from a sand pile experiment for the low load flow region (2), which is described in section 3.3.2.1.1 and the green sand-wall cohesion is assumed to be negligible.

3.3.1.1.1 The particle-particle static friction coefficient

In PAPER [3] the ring shear test is used to find the linearized yield locus angle, φ_{lin} which is used for obtaining the particle-particle static friction coefficient $\tan(\varphi_{lin}) = \mu_{s,p-p}$ for the DEM model. In PAPER [2] the linearized yield locus angle was used for indicating the value of the particle-particle static friction coefficient.

3.3.1.1.2 The particle-wall static friction coefficient

In the PAPERS [2, 3] the particle-wall static friction ($\mu_{s,p-w}$) is obtained from the wall yield locus by $\tan(\varphi_{wall}) = \mu_{s,p-w}$.

3.3.1.2 Results from high load calibration

The ring shear test results from the PAPERS [2, 3] are summarized in table. 3.2.

Table 3.1: Results from the tests of the green sand in the PAPERS [2, 3]

The experimental results found in PAPER [2]			
Material properties	Average	Std	Repetitions
Particle-particle static friction coefficient $\mu_{s,p-p}$	$\tan(28.6^\circ) \approx 0.54$	$\pm 1.60^\circ$	5
Particle-wall static friction coefficient $\mu_{s,p-w}$	$\tan(19.2^\circ) \approx 0.35$	$\pm 1.33^\circ$	18
The experimental results found in PAPER [3]			
Material properties	Average	Std	Repetitions
Particle-particle static friction coefficient $\mu_{s,p-p}$	0.57	± 0.04	90
Particle-wall static friction coefficient $\mu_{s,p-w}$	0.33	± 0.02	26

3.3.1.2.1 The particle-particle static friction coefficient

In PAPER [2] the values from the ring shear test was $\mu_{s,p-p} = 0.54$ where the value chosen for the simulations were $\mu_{s,p-p} = 0.50$ for a 2-D simulation and a 3-D simulation. The value of $\mu_{s,p-p} = 0.75$ was applied for a 2-D simulation.

Note that in PAPER [2] the particle-particle static friction of $\mu_{s,p-p} = 0.50$ and $\mu_{s,p-p} = 0.75$ were compared when simulating the DISAMATIC process for the sand shot air overpressure of 2.0 bar where small deviations of less than 10 % (section 4.5.1.2) were found on the filling times and the difference in the qualitative flow behaviour were virtually undetectable.

In PAPER [3] the ring shear test is used to obtain the linearized yield locus angle, φ_{lin} which is used directly to calculate the particle-particle static friction coefficient the following way $\tan(\varphi_{lin}) = \mu_{s,p-p} = 0.57$ for the DEM model.

3.3.1.2.2 The particle-wall static friction coefficient

In PAPER [3] the values from the ring shear test obtained the value of $\mu_{s,p-w} = 0.33$ and in PAPER [2] the ring shear test value was $\mu_{s,p-w} = 0.35$.

3.3.2 Simulating the low load flow regime (2)

Several articles have been presenting work on investigating the repose angle and the pile shape with DEM models typically investigating parameters as e.g. the particle shape, the rolling resistance and the static friction coefficient as in [31, 48, 78]. The low load flow can be characterized by tests such as the repose angle of a sand pile and the slump test finding the shapes expressed by the height and the length, respectively. The height and shape of a pile is typically used to characterize materials as e.g. sand or cement and subsequently the experiments are used to calibrate e.g. DEM models as in [5, 41, 31].

It is stated in [71] that the macroscopic shear behaviour of cohesive granular materials can be characterized by the Mohr-Coulomb failure criterion which was shown in Fig. 3.3(left) with respect to the ring shear test experiment in chapter 2. A contact model with adhesive elasto-plastic three-dimensional non-spherical particles were implemented in [40] and this model was applied in [79] and discussed further in section 3.3.4. One of the first and most often used cohesion contact model implemented in DEM [15] is the Johnson-Kendall-Roberts (JKR) model described in [66] and the equation can be found in eq. 3.8. This cohesion model was applied in the PAPERS [2, 3] to simulate the cohesive nature of the bentonite in the green sand.

3.3.2.1 Calibrating the DEM model at the low load flow region

The low load experiments (IIa)-(IIb) performed on the green sand are thoroughly explained in chapter 2 and shown in Fig. 3.4(right).

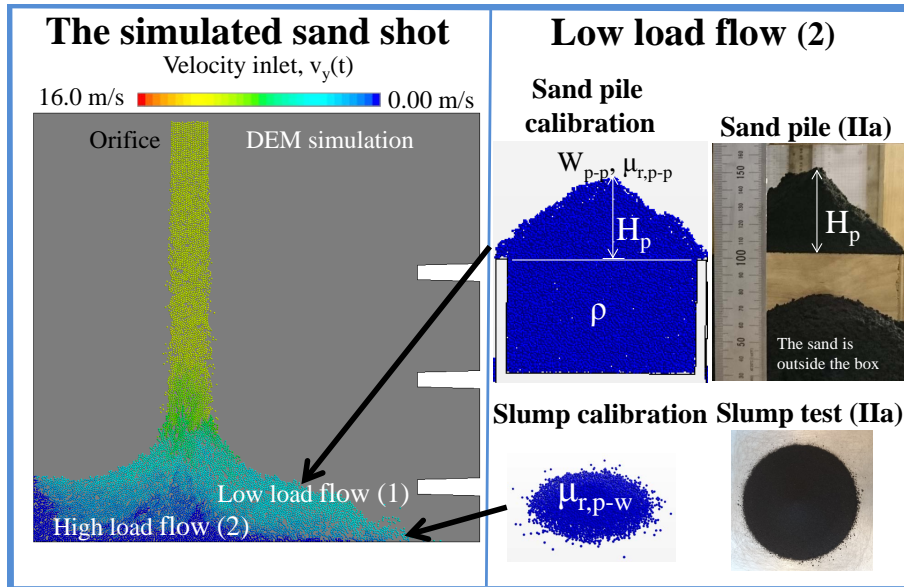


Figure 3.4: The low load flow calibration (2).

In the PAPERS [2, 3] where the green sand is loosely flowing in the low load flow region, the DEM model is calibrated from the sand pile height with respect to the particle-particle

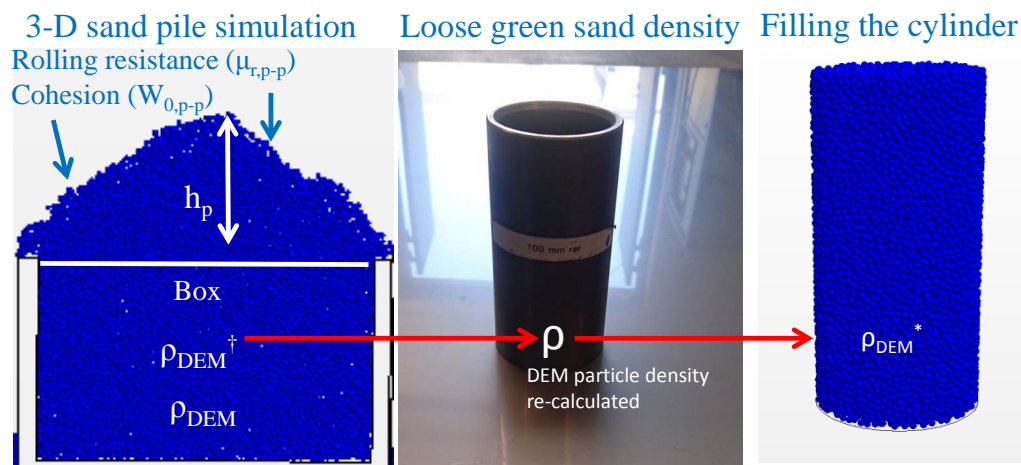


Figure 3.5: (left) The sand pile and the density inside the box for the 3-D simulation ρ_{DEM} . (Middle) The density inside the standard tube. (Right) The re-calculated density in the slump simulation. The edited figure to the left are originally from PAPER [2].

interaction which is described in section 3.3.2.1.1.

Additionally in PAPER [3] the density is re-calculated which is described in section 3.3.2.1.2. The slump test is applied for calibrating the particle-wall rolling resistance interaction, which is described in section 3.3.2.1.3.

The DEM model calibrations from the sand pile and slump test are accepted when the simulation results are less than a standard deviation away from the mean of the experimental values for the sand pile height and for the slump length.

3.3.2.1.1 The DEM calibration from the sand pile experiment

In the PAPERS [2, 3] when the sand pile is simulated it is assumed that the particles are mostly rotating and the particle resistance to rolling is described with eq. 3.12 together with the cohesion in eq. 3.8. The DEM model is calibrated by a sand pile experiment for the rolling resistance of the particle-particle interaction ($\mu_{r,p-p}$) and the particle-particle cohesion value (W_{p-p}) with respect to the height (h_p) of the sand pile above the box, which is shown in Fig. 3.4(Top right). The simulation is started by filling the hopper in the top with a random injector and afterwards when the hopper is filled the orifice is opened instantly. The green sand is then deposited from the hopper down into the box where the height above the box h_p is found. Finally the height in the simulation is found from the highest placed particle.

3.3.2.1.2 Re-calculating the DEM particle density from the cylinder

In PAPER [3] the simulated bulk density inside the box (ρ_{DEM}) is obtained and this is shown in Fig. 3.5(left). The simulated density is compared to the bulk density of the

loosely poured un-compacted green sand (ρ) in the cylinder before the compactability test, which is shown in Fig. 3.5(middle). The density measured from the standard tube specimen is used to re-calculate the density of the initial DEM particle ρ_{DEM}^\dagger to ρ_{DEM}^* in the following way,

$$\rho_{DEM}^* \approx \rho_{DEM}^\dagger \frac{\rho}{\rho_{DEM}} \quad (3.16)$$

Thus the subsequent slump calibration has the correct simulated bulk density shown in Fig. 3.5(right). The small change of the adjusted density will be assumed to have negligible effect of the simulated sand pile height h_p and the simulated particle configuration in the box, which was shown in Fig. 3.4(Top right). Hence, the particle-particle rolling resistance and particle-particle cohesion values are assumed to be correctly calibrated and these values are then applied in the next simulations together with the re-calculated density.

3.3.2.1.3 DEM calibration from the slump cylinder experiment

The slump experiment is performed by lifting the tube rapidly in order to emulate the instantaneous wall opening in the simulation to finally find the slump diameter. The standard specimen tube is a cylinder with the measurements of $H = 0.12$ m for the height and $D = 0.05$ m for the diameter. When the green sand slump has settled the two diameters orthogonal to each other (l_x, l_y) are measured and the average is calculated for the final slump length l_p . The slump simulation is executed with the obtained parameter values from the earlier calibrations ($\mu_{s,p-p}, \mu_{s,p-w}, \mu_{r,p-p}, W_{p-p}$). The obtained adjusted DEM particle density (ρ_{DEM}^*) is applied together with the density ρ from the standard specimen cylinder tube before ramming by injecting the number of particles into the slump simulation the following way,

$$N \approx \frac{\rho \frac{D^2}{2} H \pi}{\rho_{DEM}^* \frac{4}{3} (R)^3 \pi} \quad (3.17)$$

To get a fast and correct filling of the standard specimen tube in the simulation, the particles are injected with a max packing injector with the particles later being perturbed for creating a random packing effect with a normally distributed velocity (v_x, v_y, v_z) with the average velocity of $\mu = 0.0 \frac{m}{s}$ and the standard deviation of $\sigma = 2.0 \frac{m}{s}$ and with the cut off velocities of ($|v_x| \leq 1.5 \frac{m}{s}, |v_y| \leq 1.0 \frac{m}{s}, |v_z| \leq 1.5 \frac{m}{s}$) for the injector.

The slump experiment is shown in Fig. 3.6(top) and the slump simulation together with an illustration of the slump length algorithm are shown in Fig. 3.6(bottom). The slump length is used to calibrate the rolling resistance of the particle-wall interaction $\mu_{r,p-w}$. The cohesion of the particle-wall interaction was found to be negligible from the ring shear test.

The slump experiment is calibrated based on the slump length algorithm described in PAPER [5]:

(1) Finding the slump length by moving in the opposite directions from the middle of the sand pile outwards to the ends of the pile by moving from particle to particle. This is done

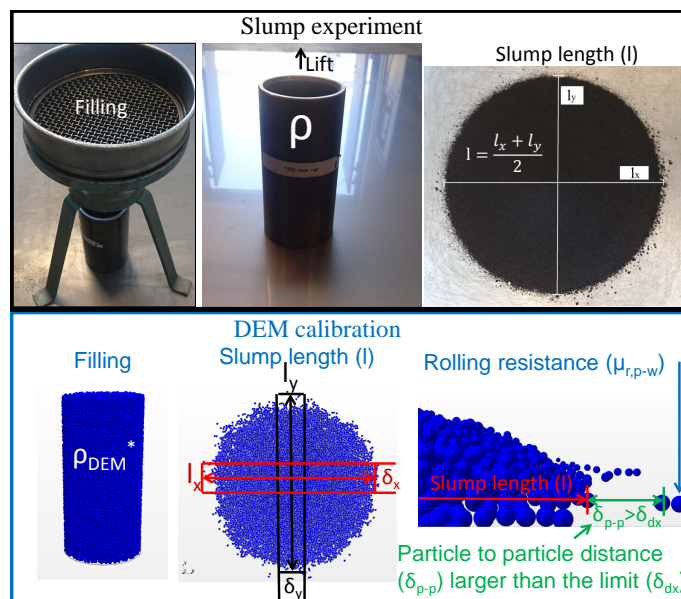


Figure 3.6: (Top) The slump cylinder experiment. (Bottom) The simulation of the slump cylinder test and an illustration of the slump length algorithm.

in two orthogonal directions getting the lengths l_x and l_y , which is shown in Fig. 3.6(bottom middle).

(2) The 4 pile ends are then defined as when the next neighbouring particle distance δ_{p-p} (center to center distance) is larger than three times the diameter of the particle $\delta_{p-p} > \delta_{dx} = 3D$ which is illustrated in Fig. 3.6(bottom right).

(3) The length of the slump is defined by the particle to particle distance in each opposite direction from pile end to pile end taking into account the radius of the end particles, this algorithm is illustrated in Fig. 3.6(bottom middle).

(4) The search width of the length algorithm is shown in Fig. 3.6(bottom middle) that only takes the particles into account which are inside the two orthogonal search widths of δ_x in the x-direction and δ_y in the y-direction. The two orthogonal directions indicated by the red box for the x-direction with the slump length of l_x and the black box for the y-direction with the slump length of l_y .

(5) Finally the slump length of the simulation is the average of the lengths in the two directions $l_p = \frac{l_x + l_y}{2}$.

The search width of the algorithm orthogonal to the length direction is set to the length of 4 times the particle diameter ($\delta y < \pm 2D$) thereby the width of the "orthogonal band" is set to $\delta_x = \delta_y = 0.016$ m. The slump diameter algorithm for the particle to particle connecting distance has the length of $\delta_{dx} = 6R = 0.008$ m, where R is the radius of the DEM particle.

3.3.2.2 Results of the experiments and the DEM calibrations

Experimental results applied for the DEM calibrations

In table 3.2 the experimental results are listed for the PAPERS [2, 3].

Table 3.2: Results from the tests of the green sand in the PAPERS [2, 3]

The experimental results found in PAPER [2]

Material properties	Average	Std	Data points
Particle-particle static friction coefficient $\mu_{s,p-p}$	$\tan(28.6^\circ) \approx 0.54$	$\pm 1.60^\circ$	n=5
Particle-wall static friction coefficient $\mu_{s,p-w}$	$\tan(19.2^\circ) \approx 0.35$	$\pm 1.33^\circ$	n=18
Sand pile height h_p	54 mm	4 mm	n=3
Average loose density ρ	$832 \frac{kg}{m^3}$	$\pm 11 \frac{kg}{m^3}$	n=14
Average maximum density ρ_{10}	$1557 \frac{kg}{m^3}$	$\pm 8.8 \frac{kg}{m^3}$	n=7

The experimental results found in PAPER [3]

Material properties	Average	Std	Data points
Particle-particle static friction coefficient $\mu_{s,p-p}$	0.57	± 0.04	n=90
Particle-wall static friction coefficient $\mu_{s,p-w}$	0.33	± 0.02	n=26
Sand pile height h_p	52 mm	2 mm	n=15
Average loose density ρ_{Bulk}	$902 \frac{kg}{m^3}$	$\pm 30.0 \frac{kg}{m^3}$	n=27
Slump length l_p	186 mm	5.48 mm	n=50

General simulation settings for the DEM calibrations

Obtaining accurate DEM parameters to realistically simulate the DISAMATIC process is important but the small green sand average particle radius of approximately $R = 0.1 \text{ mm}$ makes a direct numerical simulation impractical due to the large number of particles required. However the complexity of cohesion properties of their combination of water and bentonite coats the quartz sand and also binds the quartz sand particles together creating larger clusters of particles. This indicates that the used particle size in the calculation should be somewhat closer to the selected size of $R=1 \text{ mm}$ in radius to represent a cluster of quartz sand particles for the PAPERS [2, 3]. In PAPER [1] the selected sizes of the radii are $R=1 \text{ mm}$ and $R=2 \text{ mm}$ to represent the cluster of quartz sand.

In table 3.4 typical values are chosen for the Poisson ratio (ν) and Young modulus (E) for the steel in the chamber wall and for the sand it is chosen to be of the same value as a similar material, brick (Fire Clay) in STAR-CCM+. The coefficient of restitution (e) is chosen to be very small and very close to the critical damping because of the high damping property of the bentonite coated green sand in the PAPERS [1, 2, 3].

The densities in the PAPERS [1, 2] were found from an approximated maximum density of the green sand applying the compactability test. In PAPER [3] the adjusted density for the DEM particle was calculated to have the value of $\rho_{DEM} = 1900 \frac{kg}{m^3}$.

Table 3.3: General material values for all the calibration simulations in PAPER [2](first column) and in PAPER [3](second column).

Material properties	PAPER [2]	PAPER [3]
Green sand particle radius, (R)	0.001 m	0.001 m
Solid density chamber wall (ρ_{wall})	7500 kg/m^3	7500 kg/m^3
Youngs modulus Green Sand, (E_p)	17000 MPa	17000 MPa
Youngs modulus chamber wall, (E_w)	200000 MPa	200000 MPa
Poisson ratio Green Sand, (ν)	0.3	0.3
Poisson ratio Chamber wall, (ν)	0.3	0.3
Coefficient of restitution particle-particle, (e_n)	0.01	0.01
Coefficient of restitution particle-wall, (e_t)	0.01	0.01
Gravity (g)	9.82 m/s^2	9.82 m/s^2
Density for 3-D DEM particle (ρ_{DEM})	2100 $\frac{kg}{m^3}$	1750 $\frac{kg}{m^3}$
Density for 2-D DEM particle (ρ_{DEM})	1720 $\frac{kg}{m^3}$	No 2-D model
Adjusted density for 3-D DEM particle (ρ_{DEM})	No	1900 $\frac{kg}{m^3}$
The particle-particle static friction ($\mu_{s,p-p}$)	[0.50, 0.75]	0.57
The particle-wall static friction ($\mu_{s,p-w}$)	0.33	0.35

Note the simulation settings in PAPER [1] are listed later in table. 3.4(first column) because no calibration was performed in this PAPER.

3.3.2.2.1 Results of the sand pile calibration

Based on the results in PAPER [2], which is shown in Fig. 3.7(blue dotted line) the selected parameter for the 2-D simulation of the DISAMATIC process is: particle-particle cohesion of $W_{p-p} = 0.5 J/m^2$, particle-particle rolling resistance of $\mu_{r,p-p} = 0.3$ (height of $h_p = 0.054m$). The corresponding parameters for the 3-D simulation of the DISAMATIC process in the rib chamber geometry is: The particle-particle cohesion of $W_{p,p} = 0.3 \frac{J}{m^2}$ and the particle-particle rolling resistance of $\mu_{r,p-p} = 0.3$ which is shown in Fig. 3.7(the square on the black dotted line).

In PAPER [3] the initial values of the DEM model used for the calibrations is the particle-wall rolling friction coefficient of $\mu_{r,p-w} = 0.4$, the density for DEM particle is (ρ_{DEM}) = 1750 $\frac{kg}{m^3}$ and the DEM particle radius is R=0.001 m. The simulation with $\mu_{r,p-p} = 0.4$ and $W_{p,p} = 0.3 \frac{J}{m^2}$ (blue dotted line) and $\mu_{r,p-p} = 0.2$ and $W_{p,p} = 0.5 \frac{J}{m^2}$ (red dot) both gives values of the height which is inside the standard deviation of the measured height showed in Fig. 3.8. The selected parameters are $\mu_{r,p-p} = 0.4$ and $W_{p,p} = 0.3 \frac{J}{m^2}$ because they give a more conically shaped sand pile, which was observed in the experiments.

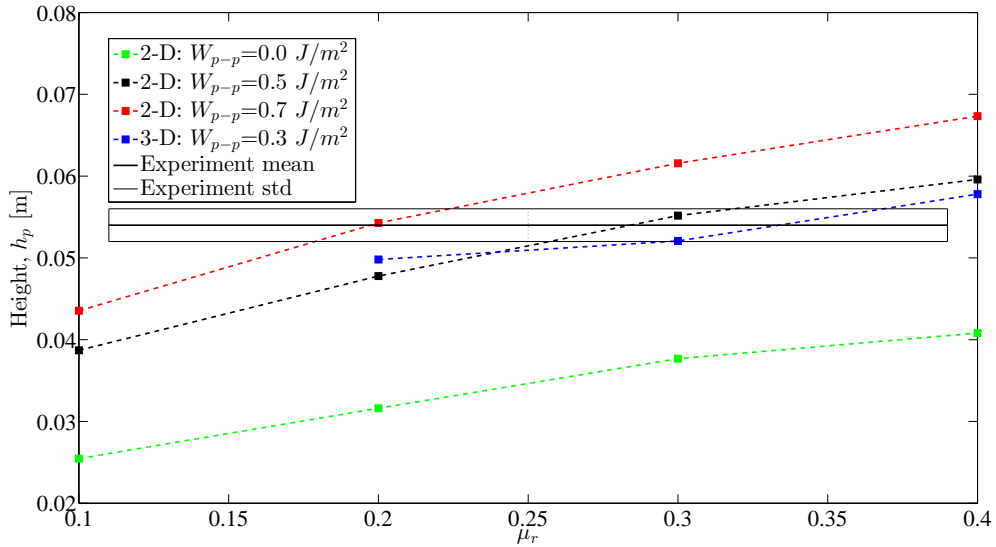


Figure 3.7: The height of the simulated sand pile (h_p) as function of the particle-particle rolling resistance ($\mu_{r,p-p}$). The black line is the mean height of the green sand pile experiment of $h_p = 0.054 \pm 0.002m$ with standard deviation of $\sigma = 0.002m$ (the two grey lines). The figure and the text are originally from article PAPER [2].

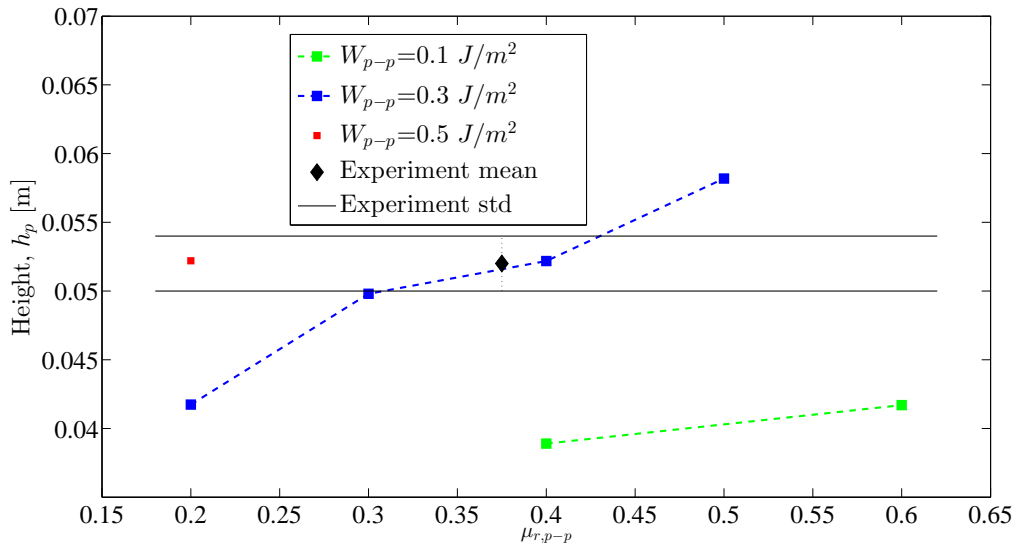


Figure 3.8: The height of the simulated sand pile (h_p) as function of the particle-particle rolling resistance ($\mu_{r,p-p}$). The black diamond is the mean height of the green sand pile experiment of $0.054 \pm 0.002m$ with the standard deviation of $\sigma = 0.002 m$ (black horizontal lines). The figure and the text are originally from PAPER [3].

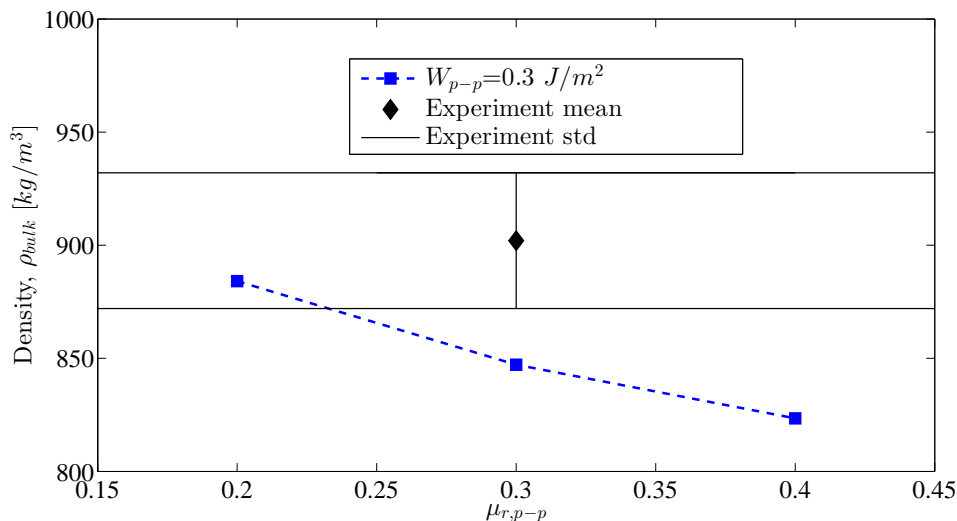


Figure 3.9: Plot of the density: The black diamond is the mean density of the green sand pile experiment of $902 \pm 30 \frac{kg}{m^3}$ with plus/minus the standard deviation of $\sigma = 30 \frac{kg}{m^3}$ (thin black line). The simulated density as a function of the particle-particle rolling resistance ($\mu_{r,p-p}$) with the DEM simulations settings having the cohesion value of $W_{p-p} = 0.3 \frac{J}{m^2}$ (blue dotted line).

3.3.2.2.2 Adjusted density for the DEM particle

In PAPER [3] the sand pile simulations were performed with the DEM particle density of $\rho_{DEM}^\dagger = 1750 \frac{kg}{m^3}$ and comparing these to the "loose" bulk density measured in the standard specimen tube which is shown in Fig. 3.9.

The particle density for the DEM simulation is $\rho_{DEM}^\dagger = 1750 \frac{kg}{m^3}$, which is too small for the selected h_p with the particle-particle value of $\mu_{r,p-p} = 0.4$ and $W_{p,p} = 0.3$. The re-calculated density $\rho_{DEM}^* = 1900 \frac{kg}{m^3}$ is found from eq. 3.16.

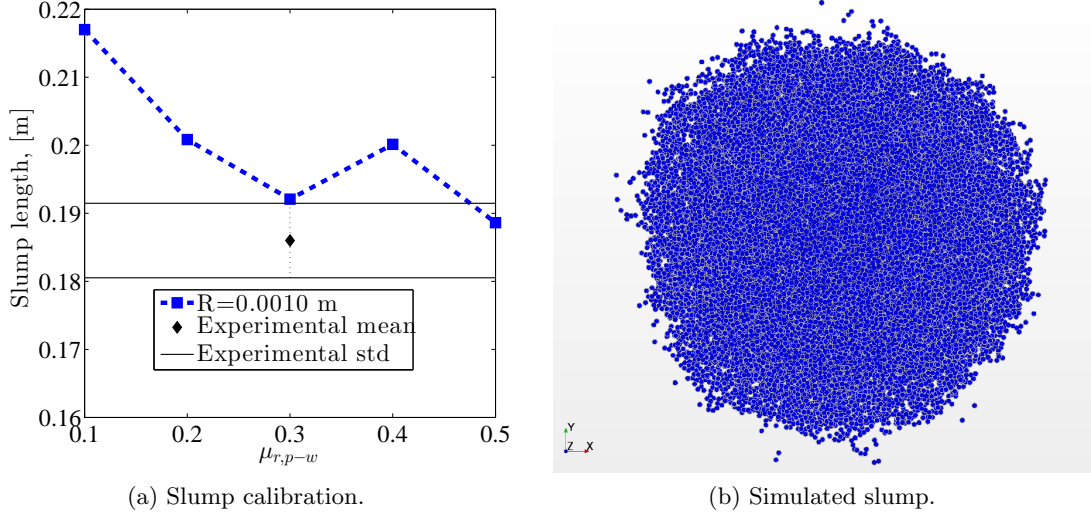


Figure 3.10: (a) The black diamond is the mean length (diameter) of the green sand slump experiment of 0.186 ± 0.00548 m with the standard deviation of $\sigma = 5.48$ mm (thin black line). The simulated slump length as a function of the particle-particle rolling resistance ($\mu_{r,p-p}$) with the DEM simulations settings having the cohesion value of $W_{p-p} = 0.3 \frac{\text{J}}{\text{m}^2}$ (blue dotted line). (b) The selected simulation with the particle-wall rolling resistance of $\mu_{r,p-w} = 0.5$.

3.3.2.2.3 Results of the slump length simulation

In PAPER [3] continuing the calibration with the found values from the sand pile experiment the found values of $\mu_{r,p-p} = 0.4$ and $W_{p,p} = 0.3 \frac{\text{J}}{\text{m}^3}$ are applied together with the re-calculated DEM particle density of $\rho_{DEM}^* = 1900 \frac{\text{kg}}{\text{m}^3}$ and the number of particles injected into the cylinder is found from eq. 3.3.2.1.3. The calibrated DEM model is determined by finding the particle-wall rolling resistance $\mu_{r,p-w}$ with less than a standard deviation away from the slump experiment l_p . The slump length result in the experiment is shown in Fig. 3.10(a) where the mean slump length l_p is the black diamond and standard deviation is indicated by the two black horizontal lines. The value for the particle-wall interaction with less than a standard deviation away from the experimental slump length is $\mu_{r,p-w} = 0.5$ and this is shown in Fig. 3.10(a) the dotted blue line and the simulation result is shown in Fig. 3.10(b).

3.3.2.3 Conclusion and summary of the calibrated DEM model

A summary is shown in table 3.4 of the parameter values used in the PAPERS [1],[2] and [3] for simulating the DISAMATIC process.

Table 3.4: General material values and settings for the DEM model simulating the DISAMATIC process in the PAPERS [1](column 1), [3](column 2) for the rib chamber geometry and [3](column 3) for the cavity chamber geometry.

Material properties	PAPER [1])	PAPER [2]	PAPER [3]
Solid densitychamber wall (ρ_{wall})	7500 kg/m^3	7500 kg/m^3	7500 kg/m^3
Youngs modulusGreen Sand, (E_p)	17000 MPa	17000 MPa	17000 MPa
Youngs moduluschamber wall, (E_w)	200000 MPa	200000 MPa	200000 MPa
Poisson ratioGreen Sand, (ν)	0.3	0.3	0.3
Poisson ratioChamber wall, (ν)	0.3	0.3	0.3
Coefficient of restitution particle-particle, (e_n)	0.01	0.01	0.01
Coefficient of restitution particle-wall, (e_t)	0.01	0.01	0.01
Gravity (g)	9.82 m/s^2	9.82 m/s^2	9.82 m/s^2
The simulation time step	$10^{-5}s$	$10^{-5}s$	$10^{-4}s$
3-D simulation settings			
Green sand particle radius, (R)	No	0.001 m	0.001 m
Density for the DEM particle (ρ_{DEM})	No	2100 kg/m^3	1900 kg/m^3
Particle-Particle static friction, ($\mu_{s,p-p}$)	No	[0.5, 0.75*]	0.57
Particle-Wall static friction, ($\mu_{s,p-w}$)	No	0.35	0.33
Particle-particle rolling resistance, ($\mu_{r,p-p}$)	No	0.3	0.4
Particle-particle rolling resistance, ($\mu_{r,p-w}$)	No	No	0.5
Particle-particle cohesion value, (W_{p-p})	No	$0.3 \frac{J}{m^2}$	$0.3 \frac{J}{m^2}$
2-D simulation settings			
Green sand particle radius, (R)	[0.001 m, 0.002 m]	0.001 m	No
Density for the DEM particle (ρ_{DEM})	1600 kg/m^3	1720 kg/m^3	No
Particle-Wall static friction, ($\mu_{s,p-w}$)	Table 4.1	0.35	No
Particle-Particle static friction, ($\mu_{s,p-p}$)	Table 4.1	[0.5, 0.75*]	No
Particle-particle rolling resistance, ($\mu_{r,p-p}$)	Table 4.1	0.3	No
Particle-particle rolling resistance, ($\mu_{r,p-w}$)	Table 4.1	See [2]*	No
Particle-particle cohesion value, (W_{p-p})	No	$0.5 \frac{J}{m^2}$	No
Particle-Wall cohesion value, (W_{p-w})	No	See [2]*	No

The ring shear tester was applied to obtain the static friction coefficients for the DEM model. The height of the sand pile was measured and from this the DEM model was calibrated. The calibration was performed with respect to obtaining the values in the rolling resistance as well as in the parameter value of the cohesive model. As expected, an increase in the value of the particle-particle rolling resistance increased the simulated sand pile height and an increase in the value of the particle-particle cohesion increased the height of the sand pile further. Increasing the cohesion changed the shape of the sand pile to become more uneven and higher as also seen in the experiments for the more wet green sand.

3.3.3 Simulating the fluidized flow regime (3)

A Simulation of the sand casting process with a two phase continuum model has earlier been presented in [28] and continuum models have been designed to model granular material as e.g. in [26, 27]. In [29] a multiphase model was applied to simulate a core shooting process numerically in two and three dimensions. The Lagrangian method of the Discrete Element Method was combined with Computational Fluid Mechanics which is typically denoted CFD-DEM and is often used to simulate fluidized beds as in [80, 81]. The newly developed Anton Paar Powder Cell was recently used to obtain the fluidized viscosity in PAPER [6]. Hence, the experiment has probably been used sparingly for calibration of e.g. CFD-DEM models. The fluidized viscosity obtained from the experiment, could be compared to the simulated value of the torque as a function of the airflow obtained from the CFD-DEM simulation and this is a potential way of calibrating the fluidized viscosity.

The DISAMATIC process was simulated with a DEM model in the PAPERS [1, 2] in the rib chamber geometry, which is discussed in chapter 4. In PAPER [3] a DEM model and a combined CFD-DEM model which simulated the air phase were applied. The simulated the chamber geometry in had a special cavity design and this is discussed in chapter 5 and in PAPER [3].

3.3.4 Simulating the solid mechanics regime (4)-(5)

The yield locus of a granular material is described in the field called soil mechanics and details can be found in e.g. [50] and computational modelling of the physics is described in e.g. [82, 83]. In [40] the relation of the confined compression to the unconfined compression strength (uni-axial compression) from experiments were simulated with DEM applying the software package EDEM with an adhesive elasto-plastic contact model with three dimensional non-spherical particles. This model achieved quantitative prediction of cohesive powder flow-ability (FFc) as described in e.g. [11, 12]. The framework of [40] was applied for calibrating the DEM model in [79] which simulated a cone penetration and an unconfined compression in cohesive solids showing that this framework is very suitable for simulating failure and solid mechanical behaviour. The squeezing process of green sand was simulated with DEM in [84] where the effect of the particle size distribution on the sand compacting behaviour was clarified by both the experiment and the simulation.

Commercial software such as Abacus is applying a continuum model based on the FEA approach for simulating solid mechanical behaviours as bending beams, mechanical loadings or uni-axial compression tests for yield stress materials. For the residual stresses in the mold during solidification simulating are introduced and described thoroughly in [85]. The commercial software MagmaSoft can simulate the molten metal filling of the mold and the subsequent solidification of the metal in the mold.

Compression pressures larger than the applied pressures in the DISAMATIC squeezing process occurs in the comminution process. The comminution process is the reduction of

solid materials particle size to smaller particle size by crushing, grinding, cutting, vibrating which is frequently simulated by DEM. DEM simulations applying a breakage model is applied to study a broad range of existing compression based crushers in [86]. In [87] the cracking phenomena of aggregates is investigated and with the help of DEM particle size distributions and liberation degrees of the comminution process can be predicted with high precision. A tumbling mills was simulated utilizing the GPU architecture for a faster simulation of 4 millions particles in the work of [58].

3.4 Conclusion

The parameters of the DEM model were found from the following experiments: A ring shear tester, a sand pile experiment and finally a slump test. The ring shear tester was applied to obtain the static friction coefficients for the DEM model. Although in PAPER [2] the particle-particle static friction of $\mu_{s,p-p} = 0.50$ and $\mu_{s,p-p} = 0.75$ were compared when simulating the DISAMATIC process for the sand shot air overpressure of 2.0 bar where small deviations of less than 10 % (section 4.5.1.2) was found on the filling times and the difference in the qualitatively flow behaviour were virtually undetectable.

The height of the sand pile was measured and from this the DEM model was calibrated. The calibration was performed with respect to obtaining the values in the rolling resistance as well as in the parameter value of the cohesive model in the PAPERS [2, 3]. As expected, an increase in the value of the particle-particle rolling resistance increased the simulated sand pile height and an increase in the value of the particle-particle cohesion increased the height of the sand pile further. Increasing the cohesion changed the shape of the sand pile to become more uneven and higher as also seen in the experiments for the more wet green sand. In PAPER [3] the density was adjusted to the loose green sand density and the slump experiments was applied to calibrate the DEM models particle-wall rolling resistance.

Next the calibrated DEM models are used to simulate the DISAMATIC process in the PAPERS [1, 2, 3], in chapter 4 and in chapter 5.

Chapter 4

Simulating the rib chamber geometry

4.1 Introduction

The flow dynamics of the sand shot inside the rib chamber geometry was investigated with a DEM model in the two PAPERS [1, 2] and the investigated themes are briefly summarized here:

First the DISAMATIC process and the rib geometry is presented in section 4.2.

Monitoring the green sand flow in the rib geometry with video footage and the chamber filling times are presented in section 4.3.

The simulation setup for the DISAMATIC process is presented in section 4.4 for the two PAPERS [1, 2] where an additional sensitivity study is presented in section 4.4.3.

The results of the simulations are presented in section 4.5 with respect to the chamber filling times in section 4.5.1 and the qualitative flow behaviour in section 4.5.2.

Finally a short conclusion of this chapter is presented in section 4.6.

4.2 The rib chamber geometry and the DISAMATIC process

The DISAMATIC process in the rib chamber geometry is illustrated in Fig. 4.1. The reference geometry has three ribs at one side of the chamber reaching the end of the chamber in both sides perpendicular to the inlet flow direction from the sand slot, shown in Fig. 4.1. The compressed air creates an overpressure P_{start} in the top of the hopper which drives the flow of the sand down into the chamber. The ribs become obstacles for the sand flow and as a result some of the cavities inside the ribs may not be sufficiently filled and the density is hence typically lower in the cavity regions. This type of shadow effect from the ribs is more pronounced in the upper region of the reference geometry. Similarly the geometry of the cast part and the casting system can make the moulding process complicated due to obstacles such as ribs that deflect the sand flow causing shadowing effects around the cavities of the mould.

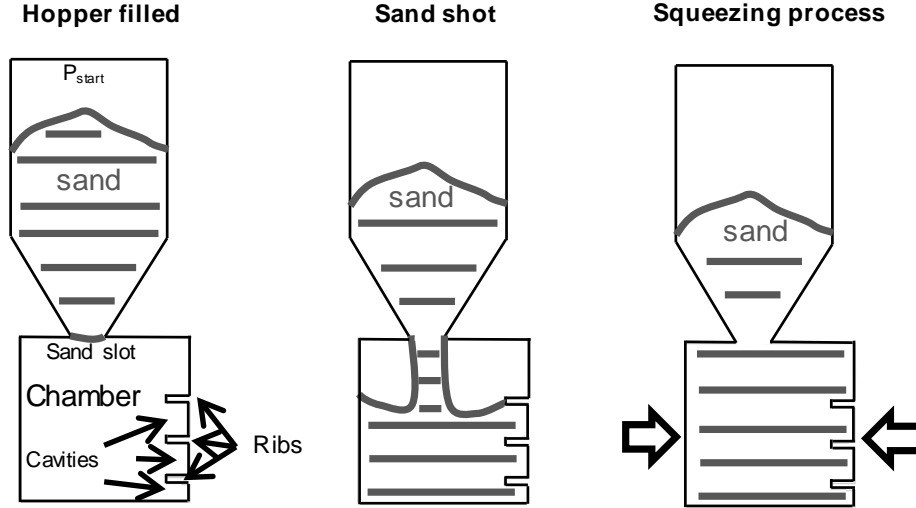


Figure 4.1: (left) The sand shot starts when the compressed air (P_{start}) from an air receiver blows air into the top of the hopper which drives the sand from the hopper through the sand slot down into the moulding chamber. The air in the chamber escapes through the small air vents. (middle) The sand is filling the chamber and the three cavities. (right) Finally the mould is squeezed and the mould is pressed out of the chamber ready for casting. The figure and the text are from PAPER [2].

4.3 Monitoring the DISAMATIC experiments

In Fig. 4.2, the progression of the sand shot in the chamber can be followed and the shape of the sand pile can be seen for the compressed air pressure of $P_{start} = 2.0\text{bar}$. Eight filling times are defined and denoted $t_1 - t_8$, where the times t_1 , t_3 , t_5 and t_7 denote when the sand pile reaches cavity 1, 2, 3 and 4 respectively. The times t_2 , t_4 and t_6 denote when the sand pile reaches the bottom corners of ribs 1, 2 and 3 respectively and t_8 when the mould chamber is completely full. The video images at these eight times are shown for 2.0 bar in Fig. 4.2, where the geometric configuration in the DISAMATIC process is shown Fig. 4.1. The experimental video footage was captured with a Go-pro camera positioned in the right hand side top corner of the mould chamber (facing downwards on the flow around the ribs and cavities). The recorded sand shot pressures in the successive trials were 2.0 bar, 2.5 bar and 3.0 bar. The times $t_1 - t_8$ for all three experiments can be seen in Fig. 4.3. In this figure it is evident that varying the air pressure affects the flow pattern. The filling times for completion of the sand shots were $t_8=0.74$ s for 2 bar (black curve), $t_8=0.65$ s for 2.5 bar (red curve) and $t_8=0.64$ s for 3 bar (blue curve). In PAPER [2] the filling times of $t_1 - t_8$ and the shape of the area filled with green sand in the mould were used in the following sub-section to fit the four vertical inlet velocities and particle flow rates for the sand slot in the DEM simulations of the DISAMATIC process.

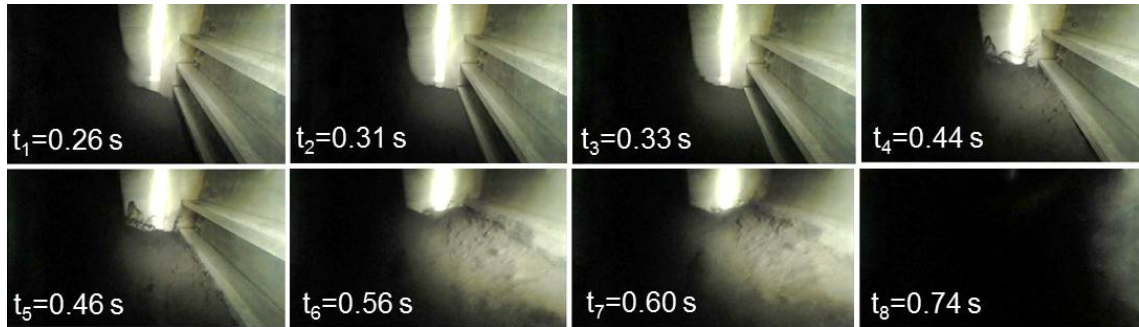


Figure 4.2: The progression of the flow front starts from the upper left going to the lower right. From the experimental video footage shot with the air pressure of 2.0 bar. The figure and text are taken from PAPER [2].

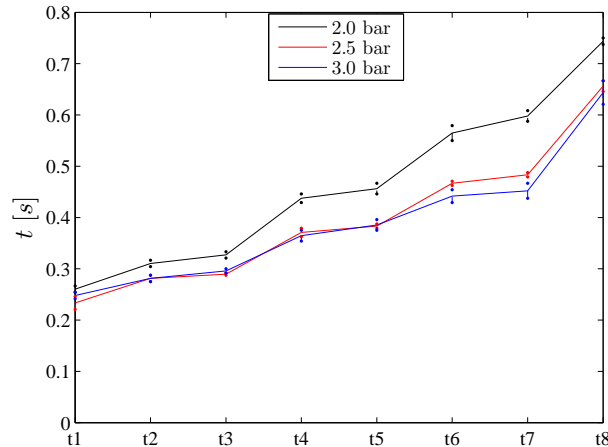


Figure 4.3: The experimental progression of the sand pile flow front with respect to the eight times $t_1 - t_8$ for the compressed air pressures of 2.0 bar (black curve), 2.5 bar (red curve) and 3.0 bar (blue curve). The figure and text are taken from PAPER [2].

4.4 Simulation settings for the DISAMATIC process

The simulation settings of the DEM model for simulating the DISAMATIC process are presented in the following way:

The calculation of the inlet velocities and the particle flow rates are presented in section 4.4.1 together with the parameter settings for the DEM model in the two PAPERS [1, 2]. To simulate the stochastic behaviour of the granular flow a normally distributed random fluctuation was added on the inlet velocity and this is presented in section 4.4.2.

The additional sensitivity study settings is presented in section 4.4.3.

The filling times for the simulations are defined in section 4.4.4.

4.4.1 Calculating the inlet velocity and the particle flow rate

4.4.1.1 The constant particle velocity and particle flow rate

In the study of PAPER [1] considered a constant particle inlet velocity of $6 \frac{m}{s}$ and the constant particle flow rate was calculated the following way:

The flow rate is calculated from the particle diameter e.g. $d=0.004$ m, the filling time of $t_f=1.05$ s, the assumed packing fraction of 0.75 and the total area of the mould which is $A = 0.25 m^2$ and finally this gives the flow rate of $\frac{0.75 \times 0.25 m^2}{(0.004 m)^2 \pi 1.05 s} = 14210 \frac{particles}{s}$ and for the diameter of 0.002 m it gives $568490 \frac{particles}{s}$.

4.4.1.1.1 The sensitivity study

In PAPER [1] a sensitivity study were performed on the following parameters shown in table. 4.1 and the unchanged parameters are listed in table. 3.4(first column).

Table 4.1: The rolling resistance and static friction values in the parameter study.

Simulation	$\mu_{s,p-p}$	$\mu_{r,p-p}$	$\mu_{s,p-w}$	$\mu_{r,p-w}$	Diameter
1	0.8	0.6	0.8	0.6	4 mm
2	0.8	0.9	0.8	0.9	4 mm
3	1	0.6	1	0.6	4 mm
4	1	0.9	1	0.9	4 mm
5	0.8	0.6	0.8	0.6	2 mm
6	0.8	0.9	0.8	0.9	2 mm
7	1	0.6	1	0.6	2 mm
8	1	0.9	1	0.9	2 mm

4.4.1.2 The time dependent velocity

In PAPER [2] a time dependent velocity was applied for a more accurate simulation of the chamber filling. An illustration of the geometry of the chamber is shown in Fig. 4.1. The mould chamber has three ribs mounted on the fixed pattern plate forming four cavities positioned on the right hand side. The cross section in the middle of the chamber perpendicular to the ribs were imported as a CAD file and subsequently selected for a 2-D simulation and a 3-D slice simulation. The 2-D cross section can be seen in Fig. 4.4 (left). The sand enters the chamber at the intersection between the hopper and chamber which is denoted as the sand slot. The dimension of the chamber is $W \cdot H \cdot D = 0.48m \times 0.50m \times 0.60m$ and the sand slot has a width of $W_s = 0.04 m$ and a depth of 0.54 m which is centred at the middle of the chamber depth.

The flow is modelled as a 2-D section placed in the middle of the chamber depth. The 3-D slice simulation has a depth of 0.04 m placed around the middle of the chamber depth and applying a periodic boundary in the z-direction (depth direction). The sand slot particle inlet velocity and particle flow rate were estimated by using the filling times of the different

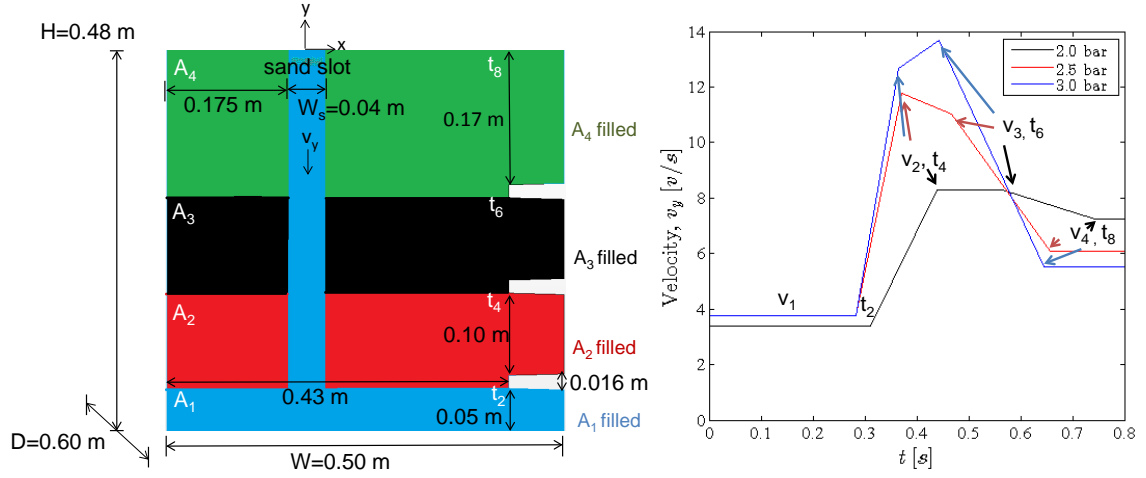


Figure 4.4: (Left) From the green sand filling time of the four areas $A_1 - A_4$ (A_1 blue, A_2 red, A_3 black, A_4 green), four velocities ($v_1 - v_4$) can be calculated with the four selected time intervals [$t_0 \leq t \leq t_2, t_2 \leq t \leq t_4, t_4 \leq t \leq t_6, t_6 \leq t \leq t_8$]. (Right) From the four points an illustration of the velocities (v_1, v_2, v_3, v_4) are assumed to vary linearly in time with a constant final velocity of v_4 . The figure is from PAPER [2] and the chamber sections were applied for an approximation of the time filling dependent vertical velocity in PAPER [2].

parts of the mould chamber from the video footage. A time dependent velocity was incorporated in PAPER [2] ($v_y(t)$). The sand slot inlet velocity, $v_y(t)$ in the DEM simulations is fitted from the experimental video footage cf. e.g., Fig. 4.4 with respect to the filling times t_2, t_4, t_6, t_8 . The four inlet velocities (v_1, v_2, v_3, v_4) are calculated from the four filled areas ($A_1 - A_4$) divided by the filling times of the four areas ($t_2, t_4 - t_2, t_6 - t_4, t_8 - t_6$) and the sand slot width (W_s). The velocities (v_1, v_2, v_3, v_4) are assumed to vary linearly in time with a constant final velocity of v_4 , cf. Fig. 4.4 (right). The particle flow rate (particles/s) is obtained from the sand slot velocity by the area of the sand slot, the ideal particle packing fraction (hexagonal packing fraction) and the radius of the particle.

4.4.1.2.1 The calibrated DEM model

In PAPER [2] the DEM model was calibrated from experiment to obtain the rolling resistance, cohesion, static friction coefficients and assuming a 2 mm particle diameter. The calibration of the parameters can be found in chapter 3 where the applied values for the simulation of the DISAMATIC process can be found in table 3.4(second column).

4.4.2 The particle velocity distribution

In PAPER [1] and in PAPER [2] the initial particle velocity in the vertical direction is given by the sand slot inlet velocity ($v_y(t)$) adding a normally distributed random fluctuation with a zero mean and a standard deviation of $0.1 \frac{m}{s}$ with a cut off value of $\pm 0.2 \frac{m}{s}$.

A similar perturbation is added to the horizontal velocity ($v_x(t)$) with a mean of $0.0 \frac{m}{s}$ and with a maximum fluctuation of $\pm 1.0 \frac{m}{s}$. The fluctuations emulate the random nature of the green sand flow in the chamber.

4.4.3 The 2-D sensitivity study

In this chapter the additional sensitivity study is applying the time dependent inlet velocity and the time dependent particle flow rate described in section 4.4.1.2 from PAPER [2] when simulating the sand shot with the compressed air pressure of 2.0 bar. The parameters which are not changed in the sensitivity study has the calibrated values shown earlier in 3.4(second column) from PAPER [2].

4.4.3.1 The sensitivity study of the DEM model parameters

The filling times of the rib chamber geometry together with qualitative flow behaviour are investigated with respect to the parameters: The coefficient of restitution, the rolling resistance and the cohesion value.

4.4.3.1.1 The coefficient of restitution

The coefficient of restitution ($e_n = e_t$) parameter values are listed in table 4.2. The coefficient of restitution ($e_n = e_t$) is tested where the normal direction is equal to the tangential direction for the impact of particle-particle and particle-wall interaction. The coefficient of restitution simulates the energy dissipation of the particles on impact where e_n simply is the relationship of the before and after impact velocity in the normal direction.

4.4.3.1.2 The rolling resistance and the cohesion value

The rolling resistance ($\mu_{r,p-p}, \mu_{r,p-w}$) and the cohesion value (W_{p-p}, W_{p-w}) parameter values are listed in table 4.3. The rolling resistance and cohesion value are both tested for the particle-particle effect and the particle-wall effect. The rolling resistance simulates non-spherical nature of the green sand and the particles resistance to rolling and the cohesion value simulates the cohesive nature of the green sand from when it is bonded by the wet bentonite.

4.4.3.2 The sensitivity study of the inlet velocity

The filling times of the rib chamber geometry together with qualitative flow behaviour are investigated with respect to the horizontal velocity and vertical velocity.

4.4.3.2.1 The horizontal velocity distribution

The horizontal velocity distributions are investigated with the values listed in table 4.4.

Table 4.2: The coefficient of restitution ($e_n = e_t$) values in the parameter study.

Simulation	$e_n = e_t$
1	0.001
2	0.500
3	0.900

Table 4.3: The rolling resistance and cohesion values in the parameter study.

Simulation	$\mu_{r,p-p}$	W_{p-p}
1	0.1	0.1
2	0.8	0.8
Simulation	$\mu_{r,p-w}$	W_{p-w}
3	0.1	0.1
4	0.5	0.5

Table 4.4: The horizontal velocity distribution in the parameter study.

Simulation	std $\frac{m}{s}$	cut of $\pm \frac{m}{s}$
1	0.050	0.5
2	0.075	0.2
3	0.100	0.2
4	0.250	2.0
5	0.500	2.0

Table 4.5: The constant vertical velocity in the parameter study.

Simulation	$\frac{m}{s}$
1	4
2	5
3	6
4	8

4.4.3.2.2 The vertical velocity

The vertical velocity investigations are made with the different constant velocities shown in table 4.5. The constant flow rate is calculated by the method described in PAPER [1] and in section 4.4.1.1 where the filling time t_f is obtained from the selected constant velocity v , in the following way $t_f = \frac{A}{v \times W_s}$.

4.4.4 Definition of the filling times for the DEM simulation

4.4.4.1 The particle arrival times

In PAPER [1] the particle arrival times were found in a more complex way than in PAPER [2]. The particle arrival times is defined as a starting time and an ending time for each of the filling times $t_1 - t_6$. The starting time for the interval, is when the flow front reaches the red line and the ending time of the interval is when the bulk flow of the flow front has reached the red line. The starting time of the interval is when the loosely packed particles reach into the cavities and ending time of the interval is when the bulk flow or closely packed particles reach the cavities. The starting times of t_2 , t_4 and t_6 intervals are when the flow front reaches the bottom edge of rib 1, 2 and 3 subsequently. Here the starting times of the time intervals are again, when the loosely packed particles hit the bottom edge of the rib. The ending time of t_2 , t_4 and t_6 intervals are again defined as when the closely packed particles reach the bottom edge rib in the time step.

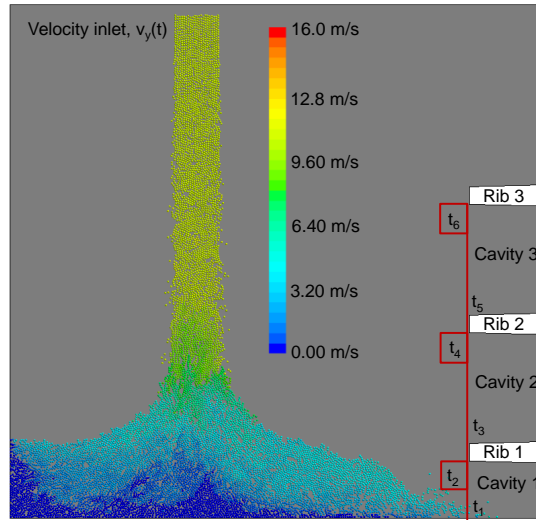


Figure 4.5: The six filling times $t_1 - t_6$ are found from the filling of the three boxes (t_2 , t_4 , t_6) and the three cavities (t_1 , t_3 , t_5). The magnitude of the velocity has been plotted with a scaling of 0-16 m/s. The figure is from PAPER [2] and a similar figure was also made in PAPER [1].

4.4.4.2 The filling time

In PAPER [2] the filling times $t_1 - t_8$ are measured in the experiments, but only $t_1 - t_6$ are defined for the simulations as seen in Fig. 4.5, the filling time intervals are defined as when a particle crosses the red lines and goes into the boxes (t_2 , t_4 , t_6)(the red boxes have the area of $100mm^2$) and goes into the cavities (t_1 , t_3 , t_5).

4.5 Results of the simulations and the experiments

The simulation results are compared to the experimental results in the following way: The filling times for the simulations and the experiments are compared in section 4.5.1. The qualitative flow behaviour for the simulations and the experiments are compared in section 4.5.2.

4.5.1 The filling times $t_1 - t_6$

The filling times are investigated in the following way:

The filling times of the constant velocity from PAPER [1] are compared to the time dependent velocity from PAPER [2] in section 4.5.1.1.

The filling times for the additional sensitivity study are presented in section 4.5.1.2.

The filling times from PAPER [2] for the "higher compressed air pressures" of 2.5 bar and 3.0 bar are presented with respect to the 2-D DEM model and 3-D DEM model in section 4.5.1.3.

4.5.1.1 The constant velocity versus time dependent velocity.

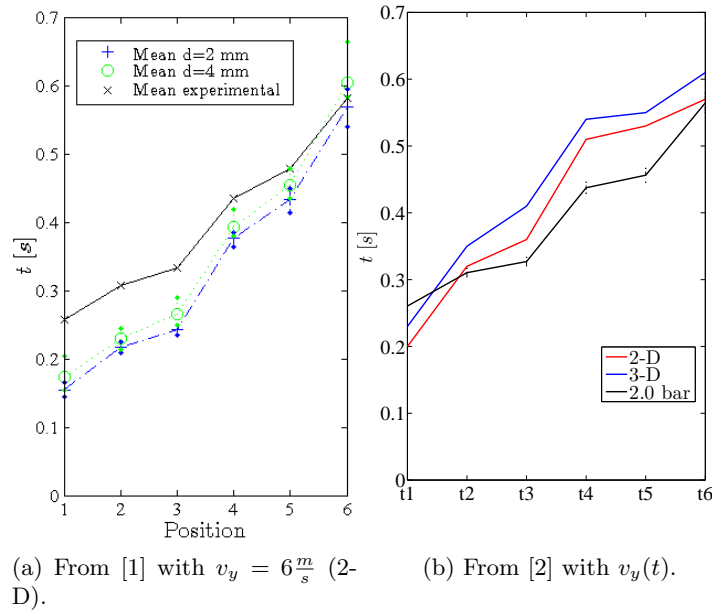


Figure 4.6: Simulation of the compressed air pressure of 2.0 bar. (Left) From PAPER [1] with 2-D simulations having a constant inlet velocity and particle diameter sizes of 4 mm and 2 mm. (Right) From PAPER [2] with the time dependent velocities and the particle diameter size of 2 mm.

The filling times ($t_1 - t_6$) presented in PAPER [1] are compared to the filling times from PAPER [2] in Fig. 4.6 for the compressed air pressure of 2.0 bar. The simulated filling

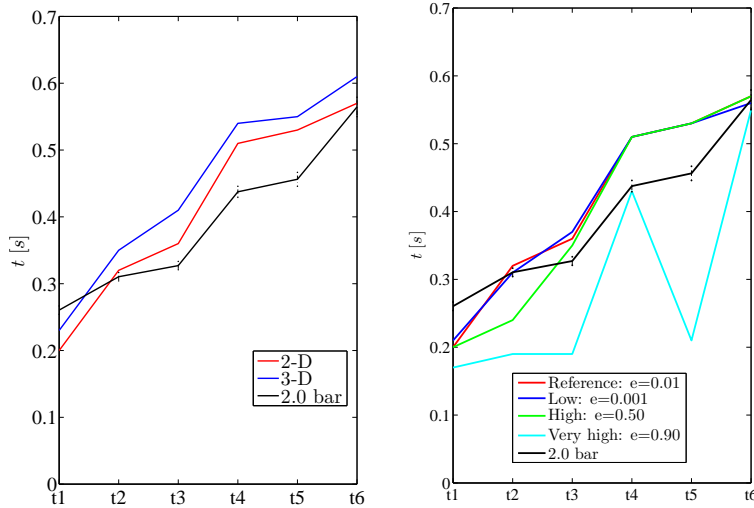
times of $(t_1 - t_6)$ from Fig. 4.6 (left) are compared to Fig. 4.6 (right) where the linear velocity interpolation $v_y(t)$ from PAPER [2] is in better agreement with the experimental values than the constant velocity from PAPER [1]. The simulated filling times of $(t_1 - t_6)$ from [2] with the compressed air pressure of 2.0 bar are generally in good agreement with the experimental values with small differences for the filling of t_1 and $t_4 - t_5$ as shown in Fig. 4.6(right). In general the simulated filling time of t_1 is too slow due to the overestimated vertical inlet velocities in the simulations when compared to the experiment.

4.5.1.2 The 2-D sensitivity study

The settings for the sensitivity study were presented in section 4.4.3 for simulating the compressed air pressure of 2.0 bar and the results of the filling times are presented in the following sections 4.5.1.2.1-4.5.1.2.3.

4.5.1.2.1 The coefficient of restitution (e)

The sensitivity study of the coefficient of restitution with respect to particle-particle and particle-wall are shown in Fig.4.7(right). The results of changing the coefficient of restitution are not effecting the simulated filling times significantly when compared to the experimental results and the simulations from PAPER [2] which are shown in Fig.4.7(left). Except for the very high coefficient of restitution $e = 0.90$ that makes individual particles bounce earlier into the box that monitors the filling time, although the overall qualitative flow behaviour is very similar to the reference simulation shown later in Fig. 4.12.



(a) The 2-D and 3-D simulation from [1]. (b) Coefficient of restitution study (e).

Figure 4.7: The simulated filling times $t_1 - t_6$ for the coefficient of restitution values.

4.5.1.2.2 The sensitivity study of the rolling resistance and the cohesion value

The sensitivity study of the rolling resistance and the cohesion with respect to the particle-particle and the particle-wall interaction are shown in Fig. 4.8. In Fig. 4.8(left) the particle-particle sensitivity analysis simulated in 2-D for the compressed air pressure of 2.0 bar predicts the filling times well. The low particle-particle interaction (blue line) gives the best agreement with the experimental filling times although later in Fig. 4.12 it can be seen that the qualitative behaviour is less similar to the experiment than the reference simulation (red line). The high particle interaction gives slower filling times in Fig. 4.8(left) but gives the best qualitative behaviour when comparing to the experiment, which are shown later in Fig. 4.12.

In Fig. 4.8(right) the particle-wall sensitivity analysis simulated in 2-D for the compressed air pressure of 2.0 bar predicts filling times with a deviation less than 5.0 % of the reference simulation (blue line) in PAPER [2]. The differences of the qualitative flow behaviour are almost undetectable and this is shown later in Fig. 4.12.

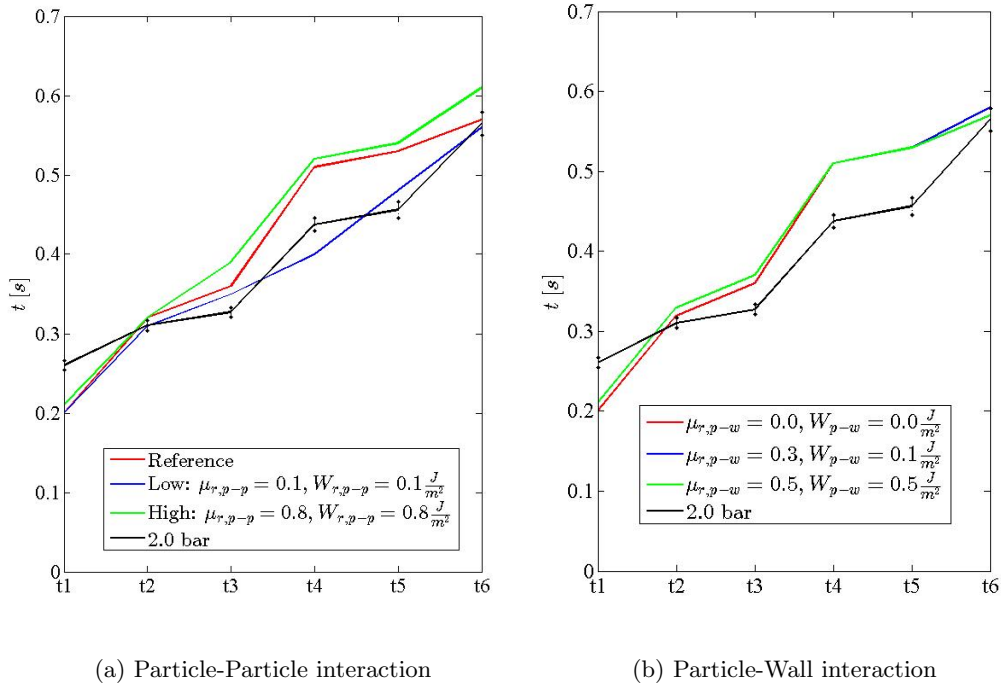
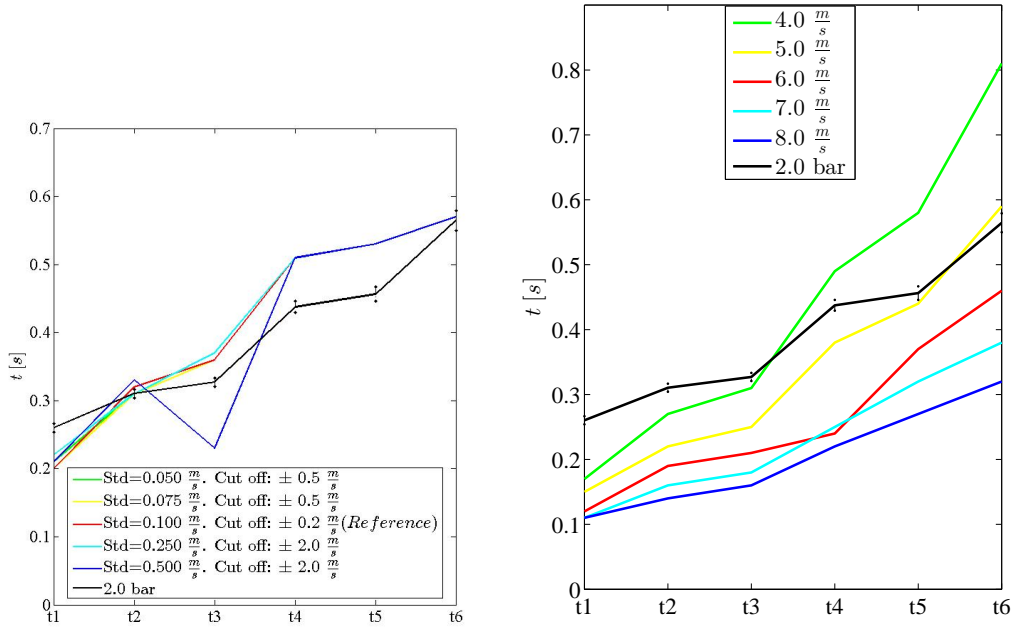


Figure 4.8: The simulated filling times $t_1 - t_6$ for the rolling resistance and the cohesion values.

4.5.1.2.3 The sensitivity study of the inlet velocity

Changing the velocity distribution in the horizontal direction in smaller intervals has virtually no influence on the filling times unless the standard deviation is chosen to become as large as $std = 0.5 \frac{m}{s}$ (blue line) shown in Fig. 4.9 (left). This deviation is only detected in one of the filling times t_3 .



(a) Investigating the horizontal velocity.

(b) Investigating the vertical velocity.

Figure 4.9: The simulated filling times $t_1 - t_6$ for different velocity distributions.

For the overall sensitivity analysis of the 2-D simulations with respect to the DEM model parameters when simulating the compressed air pressure of 2.0 bar, large parameter changes are needed to see significant changes in the filling times ($t_1 - t_6$).

Where the velocity in the vertical direction is observed to be of the greatest importance for the filling times which is shown in Fig. 4.9(right). For the increased vertical velocity the filling times obviously become shorter. The first filling time (t_1) is still too fast in the simulation for the smallest vertical velocity of $4 \frac{m}{s}$ and it can be seen in the experimental times that the particle flow rate and particle velocity is increasing with time (time dependent) due to the intersection of the $4 \frac{m}{s}$ simulation and the experiment at the time of around t_3 .

4.5.1.3 The compressed air pressures of 2.5 bar and 3.0 bar

Finally the filling times of the compressed air pressure of 2.5 bar and 3.0 bar were also investigated in PAPER [2] and are presented in Fig. 4.10. The simulated filling times of ($t_1 - t_6$) from PAPER [2] are in general in good agreement with the experimental values with small differences in the filling of t_1 and $t_4 - t_5$ as shown in Fig 4.10.

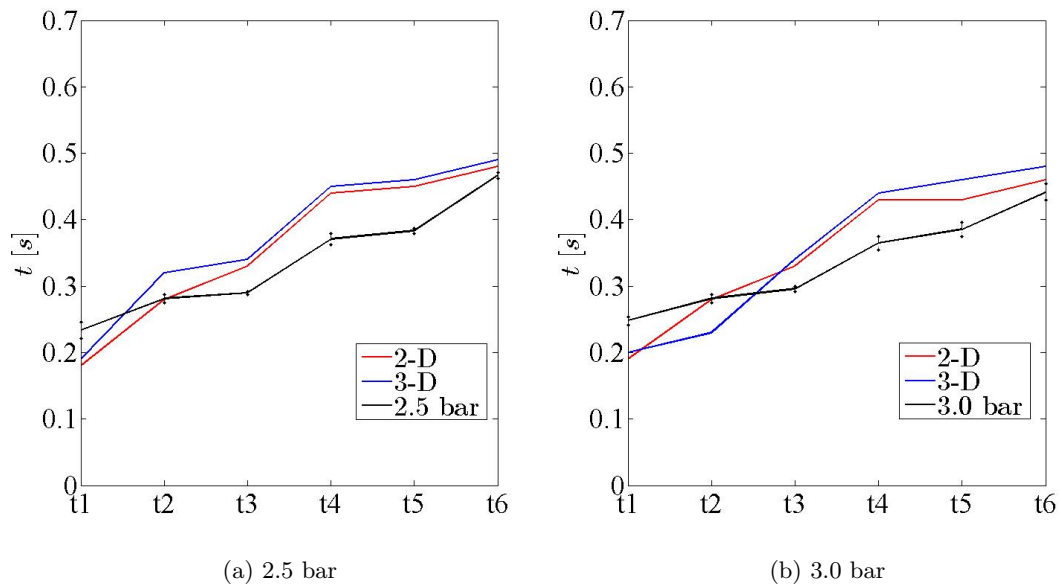


Figure 4.10: From the left to the right, (left) The simulations 2-D (red line) and 3-D (blue line) versus the experiment for 2.5 bar. (Right) The simulations 2-D (red line) and 3-D (blue line) versus the experiment for 3.0 bar for the entrance of the six times. The two figures and the text are from PAPER [2].

4.5.2 The qualitative flow behaviour

The qualitative flow behaviour is investigated in the following way:

The qualitative flow behaviour of the constant velocity from PAPER [1] are compared to the time dependent velocity from PAPER [2] in section 4.5.2.1.

The qualitative flow behaviour for the additional sensitivity study are presented in section 4.5.2.2.

The qualitative flow behaviour from the PAPER [2] for the compressed air pressures of 2.0 bar, 2.5 bar and 3.0 bar are presented with respect to the 2-D DEM model and 3-D DEM model in section 4.5.2.3.

4.5.2.1 The results of the constant velocity versus the time dependent velocity

The flow behaviour in Fig. 4.11 is similar to the experiment for the filling time of t_2 . The length of the constant velocity simulation filling time is too short $t_2 = 0.23$ for PAPER [1] as compared to the experiment filling time $t_2 = 0.32$.

The filling time fits better for PAPER [2] with the filling time of $t_2 = 0.32$ for the 2-D simulation and with the filling time of $t_2 = 0.35$ for the 3-D simulation are close to the experiment filling time $t_2 = 0.32$.

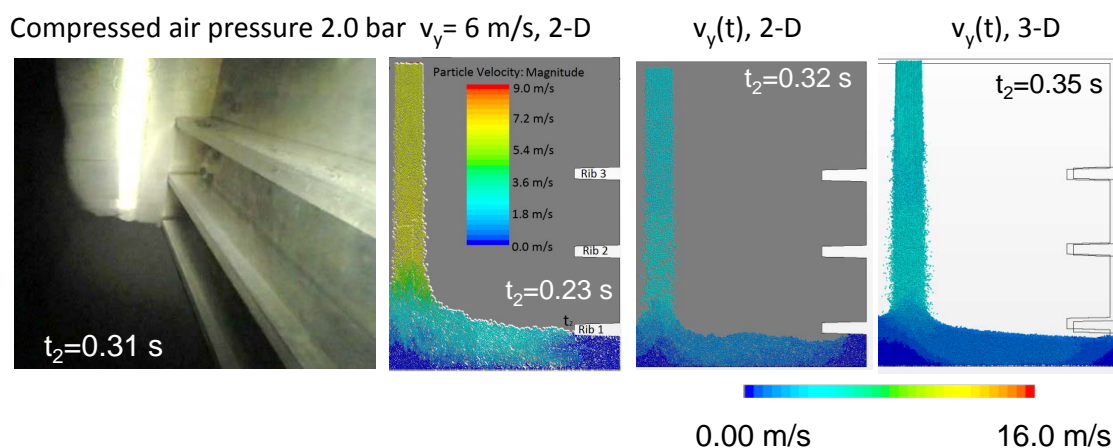


Figure 4.11: The figures from the left to the right: The experimental video footage of the compressed air pressure of 2.0 bar, the 2-D constant velocity simulation (PAPER [1]), the 2-D linear interpolation velocity simulation and lastly the 3-D linear interpolation velocity from PAPER [2]. The figures and text are from PAPER [1] and from PAPER [2].

4.5.2.2 The results of the 2-D sensitivity study

The flow dynamics of particle-particle sensitivity analysis for the 2-D simulations with the model from PAPER [2] applied for the selected compressed air pressure of 2.0 bar can be seen in Fig. 4.12. It can be seen that the reference simulation has good agreement with nearly all the other simulations with respect to the filling time of $t_6 = 0.55 - 0.58$ s except $\mu_{r,p-p} = 0.8$, $W_{p-p} = 0.8 \frac{J}{m^2}$ with the time $t_6 = 0.61$ s.

The results shown in Fig. 4.12(next page) are explained here:

In the first row of Fig. 4.12: The reference simulation flow behaviour from PAPER [2] is in good agreement with the simulations of $\mu_{r,p-p} = 0.1$, $W_{p-p} = 0.1 \frac{J}{m^2}$ with respect to the filling time although an increased vertical slushing is observed around the top rib. The larger energy dissipation of $\mu_{r,p-p} = 0.8$, $W_{p-p} = 0.8 \frac{J}{m^2}$ can be observed in the decreased slushing in the vertical direction actually with better agreement to the experiment and the bulk density is lower, which is due to the large pores which can be observed in the simulated particle arrangement.

In the second row of Fig. 4.12: The flow behaviours are very similar to the reference simulation even for the large coefficient of restitution of $e = 0.9$ where the particles are more scattered, which is due to the particles are obviously bouncing more. Changing the particle-wall parameters values ($\mu_{r,p-w}$, W_{p-w}) were virtually undetectable in the qualitative flow behaviour and this was also observed in PAPER [2].

In the third row of Fig. 4.12: For the simulation with the standard deviation of $std = 0.5 \frac{m}{s}$ in the horizontal direction it is seen that the particles in the jet are more spread but surprisingly the flow is in remarkable good agreement with the reference simulation.

In the last row of Fig. 4.12: Finally changing the velocity in the vertical direction together with the flow rate gives different flow behaviour, where increasing the velocity gives more slushing and a more pronounced flow profile with respect to the vertical direction and obviously shorter filling times too.

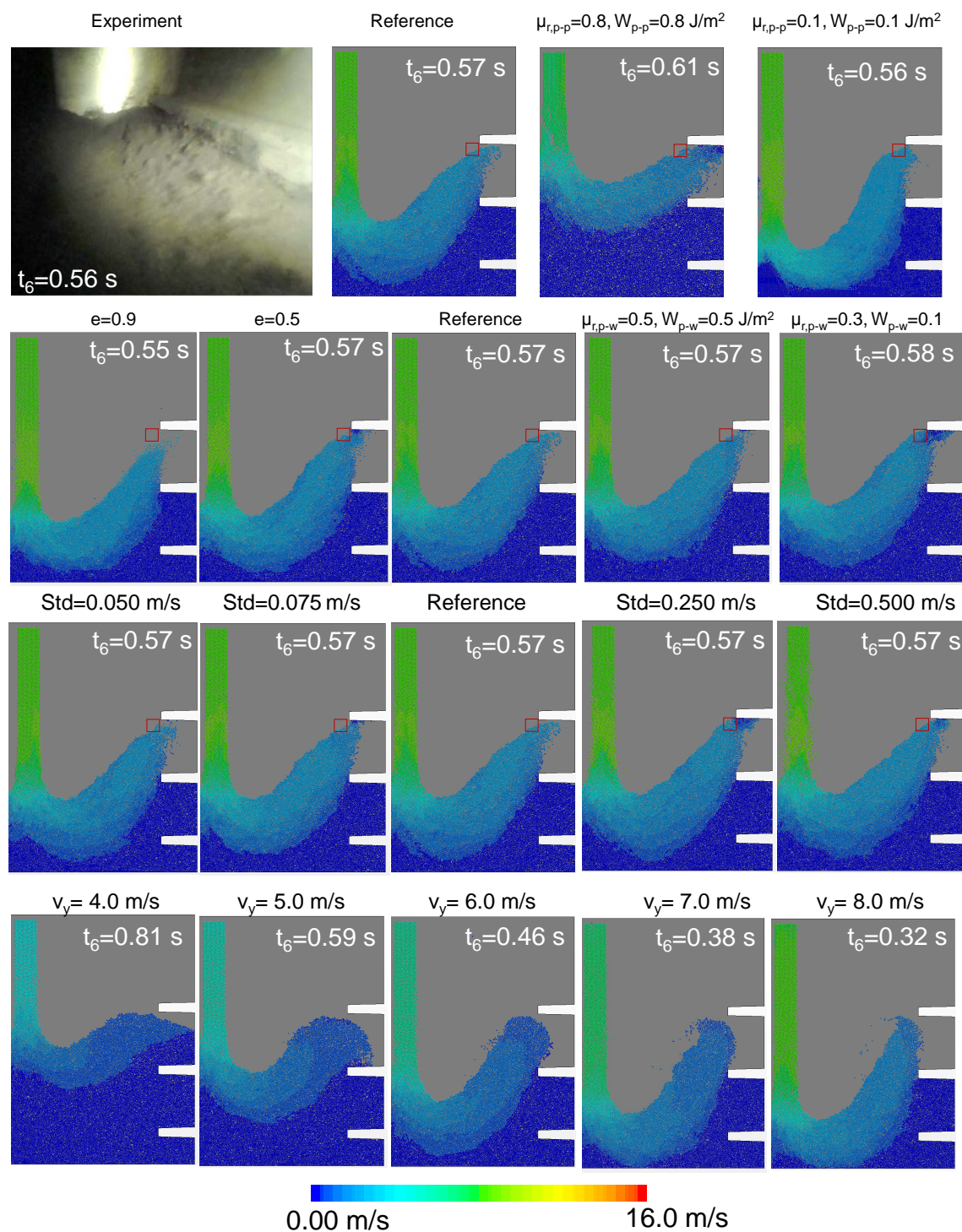


Figure 4.12: The sensitivity and velocity analysis of the 2-D simulations of the compressed air pressure of 2.0 bar.

4.5.2.3 The results of the time dependent velocity for the 2-D model versus the 3-D model

The results from PAPER [2] are presented in Fig. 4.13 to Fig. 4.15 with respect to the following compressed air over-pressures of 2.0 bar, 2.5 bar and 3.0 bar. The simulations show similar behaviour and filling times (t_2 , t_4) as the corresponding video footage rear wall profile for the three compressed air pressures. The filling time of t_4 is consistently longer for the simulations than the experiment. Generally the sand is observed to move more dynamically in the vertical direction for both the 2-D and 3-D simulations as compared to the experiments, which results in stronger curvature of the flow front. Note in chapter 5 the curvature of the flow front found in the combined CFD-DEM simulations are less pronounced, which is due to the simulated air phase dispersed the DEM particles more in the horizontal direction.

For the 2-D simulations the particle-particle static friction coefficient of $\mu_{s,p-p} = 0.75$ had virtually the same qualitative behavior as $\mu_{s,p-p} = 0.50$ in PAPER [2].

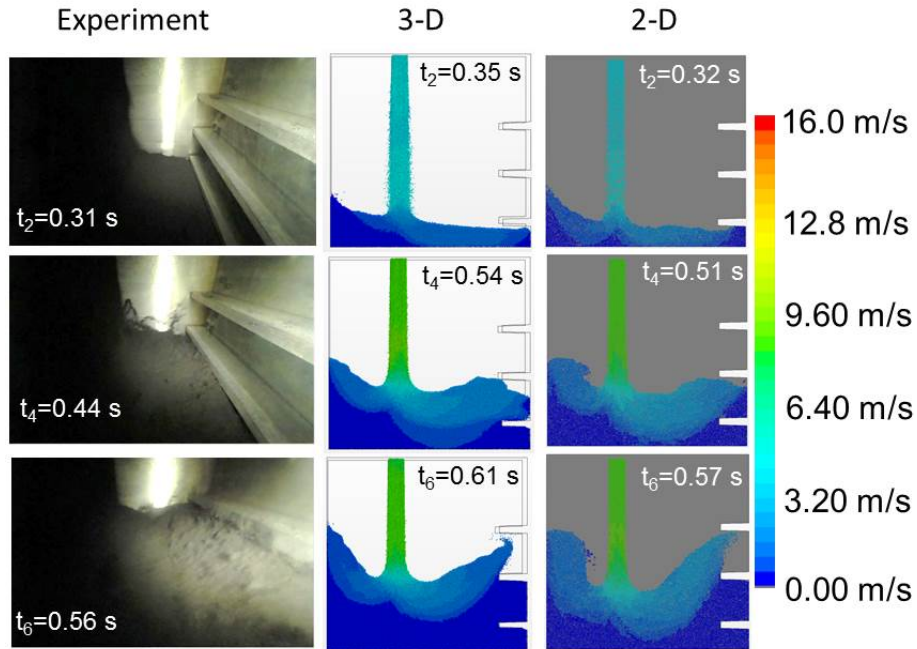


Figure 4.13: Flow contours obtained for the compressed air pressure of 2.0 bar: (left) The experimental video footage, (middle) the 3-D simulation $\mu_s = 0.50$, (right) the 2-D simulation $\mu_s = 0.50$. The experiments and simulations are all presented for the three selected times t_2 , t_4 and t_6 (from the upper figure to the lower figure). The magnitude of the velocity is plotted with a scaling of 0-16 m/s. The figure and text is from PAPER [2].

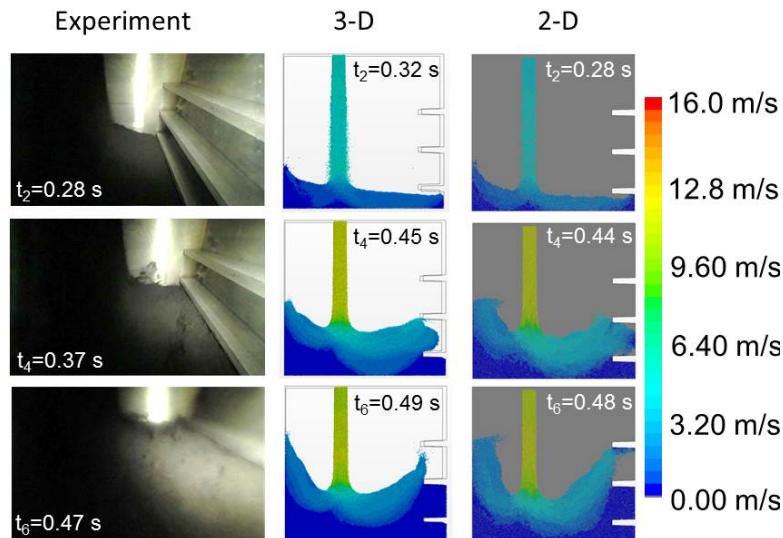


Figure 4.14: Flow contours obtained for the compressed air pressure of 2.5 bar: (left) The experimental video footage, (middle) the 3-D simulation $\mu_s = 0.50$, (right) the 2-D simulation $\mu_s = 0.50$. The experiments and simulations are all presented for the three selected times t_2 , t_4 and t_6 (from the upper figure to the lower figure). The magnitude of the velocity is plotted with a scaling of 0-16 m/s. The figure and text is from PAPER [2].

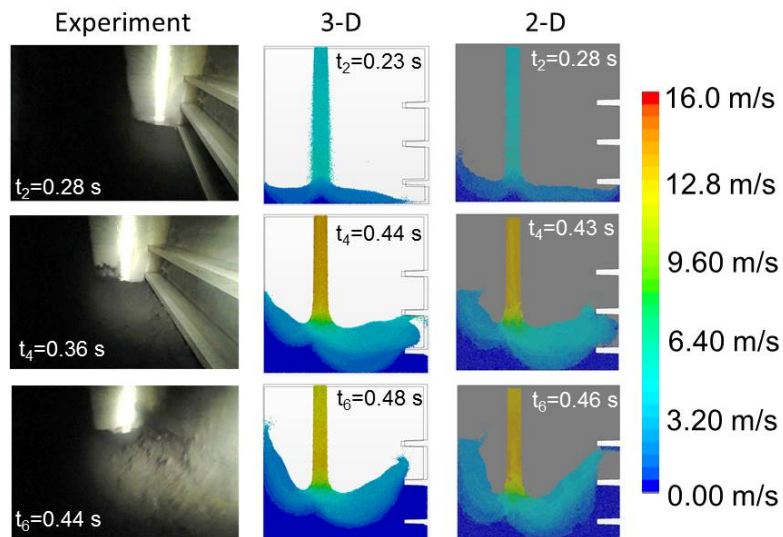


Figure 4.15: Flow contours obtained for the compressed air pressure of 3.0 bar: (left) The experimental video footage, (middle) the 3-D simulation $\mu_s = 0.50$, (right) the 2-D simulation $\mu_s = 0.50$. The experiments and simulations are all presented for the three selected times t_2 , t_4 and t_6 (from the upper figure to the lower figure). The magnitude of the velocity is plotted with a scaling of 0-16 m/s. The figure and text is from PAPER [2].

4.5.2.3.1 Filling the top part of the rib chamber geometry

In Fig. 4.16 the dynamics of the filling in the top of the chamber is investigated for the different air pressures. A slower deposition of the green sand in the larger top cavity can be seen in Fig. 4.16 for the 3-D simulations compared to the 2-D simulations. For 3.0 bar (Fig. 4.16 to the right) the 2-D simulation has more energy than the corresponding 3-D simulation, especially for later times where the green sand interferes with the jet coming from the sand slot. The larger vertical velocity of the 2-D simulations is due to the alignment of the particle contact interaction in the plane and thereby the 3-D simulations predict longer filling times than the corresponding 2-D simulations. In general a larger scatter of particles is observed in the 3-D simulations than in the 2-D simulation, due to the extra degrees of freedom [58]. The 2.0 bar simulation shows a lesser chaotic flow front compared to the simulated air pressures of 2.5 bar and 3 bar where the sloshing upwards at the two sides is more pronounced cf. Fig. 4.16.

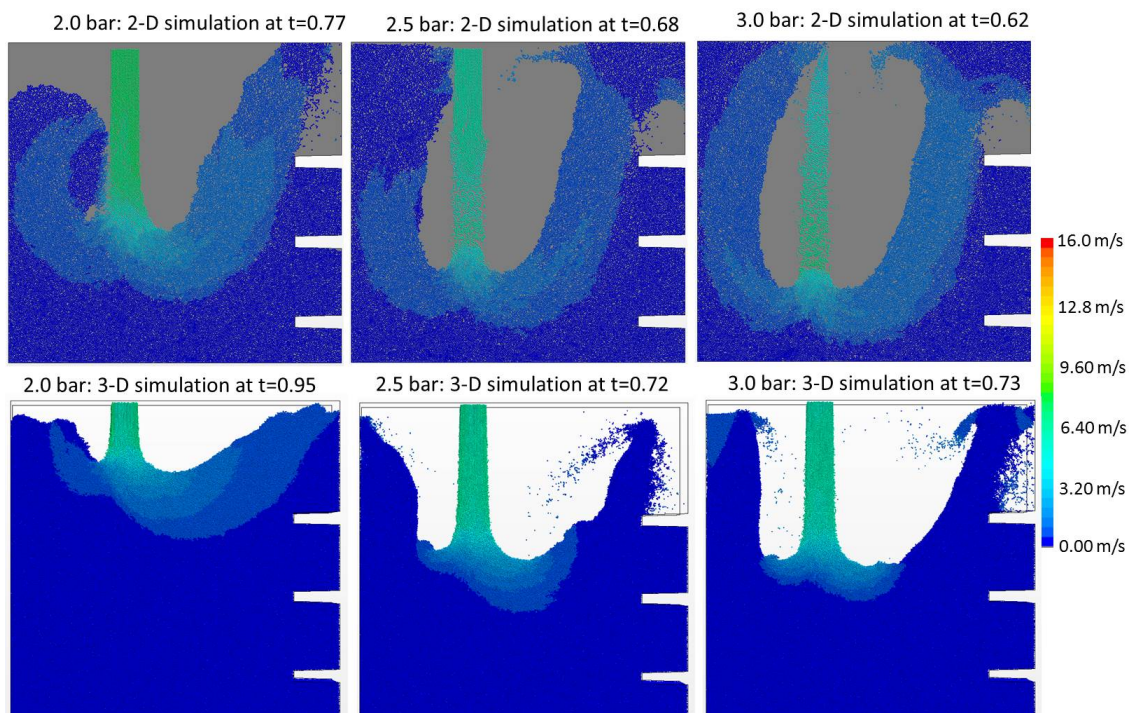


Figure 4.16: The simulation for the three compressed air pressures 2.0 bar, 2.5 bar and 3.0 bar from the left to the right at (left), (middle), (right) the 2-D simulation is placed in the top and the 3-D simulation is placed in the bottom. (top) The 2-D simulation when the sand reaches the top of the chamber at $t=0.77$ (left), at $t=0.68$ (middle) and at $t=0.62$ (right). (bottom) The 3-D simulation when the sand reaches the top of the chamber at $t=0.95$ (left), at $t=0.72$ (middle) and at $t=0.73$ (right). The magnitude of the velocity is plotted with a scaling of 0-16 m/s. The figure and text is from PAPER [2].

4.6 Conclusion

In PAPER [2] the calculated time intervals ($t_1 - t_6$) from the simulations are in good agreement with the three experiments. The dynamic flow behaviour of the particles in the simulations are generally similar to that of the sand shot in the DISAMATIC process. More specifically, with a well-selected coefficient of restitution, flow rate, damping coefficient, rolling resistance and static friction coefficient, it is possible to simulate the experimental video footage very well. When the model is calibrated the flow rate and the velocity are obviously the most important factors for the flow dynamics during the filling of the chamber. In PAPER [2] the increased scattering in the simulation results also might be due to a smaller selected cohesion value of the 3-D simulations compared to the 2-D simulations. Although differences are seen from 2-D to the 3-D simulation the results remains in good agreement and the fast execution of 2-D simulations can still be used for parameter studies in simple geometries.

The sensitivity analysis of the 2-D simulations suggested that the flow rate and particle velocity are of greater importance than most of the other parameters especially if the parameters are chosen in physically reasonable intervals as found by the calibration in PAPER [2]. A sensitivity study of the particle-wall interaction parameters were performed and it was found that the quantitative and qualitative behaviours are virtually the same as the reference 2-D DISAMATIC simulation. Thereby these particle-wall parameters are of less importance for simulating the DISAMATIC process.

It is found that the geometrical configuration as well as the applied compressed air pressure is highly affecting the filling pattern of the mould. More specifically, the lower compressed air pressure of 2.0 bar gives a slower deposition of green sand in general and in the top cavities in particular. The compressed air pressure and thereby the green sand velocity is of great importance especially for the filling of the top part of the mould. Generally the sand is observed to move more dynamically in the vertical direction for both the 2-D and 3-D simulations as compared to the experiments, which resulted in a stronger curvature of the flow front. In the next chapter 5 the curvature of the flow front found in the combined CFD-DEM simulations are less pronounced, which is due to the simulated air phase dispersed the DEM particles more in the horizontal direction.

Chapter 5

Simulating the cavity chamber geometry

5.1 Introduction

In PAPER [3] a special setup in the chamber was designed with two cavities on the left hand side each having a narrow gap for testing the ability of green sand to enter the two cavities in the sand shot. The cavities are designed to quantify the mass of green sand locally deposited in the cavities. In Fig. 5.1 the sand shot start t_{start} is indicated by the red light at the moment when the valve opens where the air overpressure P_{start} in the air tank creates an airflow into the hopper. The airflow drives the sand vertically down from the hopper through the sand slot into the chamber filling the mold chamber and the two cavities. The air pressures are monitored by sensors in the air tank, the shot valve, the hopper, the top of the chamber and the bottom of the chamber.

Seven process times are monitored during the sand shot, these seven times are obtained when the flow front reaches the lines $l_1 - l_7$ and they are denoted $t_1 - t_7$, where the time t_0 is defined as when the sand enters the chamber shown in Fig. 5.1. The seven filling times were used to calculate the particle inlet velocity and the particle flow rate for the simulated sand shot. In PAPER [3] additional filling times were monitored by cameras placed inside the cavities and cavity filling times were applied to compare with the simulated mass in the two cavities as a function of time.

The deposition of green sand in the two cavities is also investigated with respect to the air pressure and ventilation of the chamber. In PAPER [3] three different air vents settings have been tested in the sand shot to evaluate the effects on the cavity fillings and the flow in the chamber. The sand shot was simulated by the discrete element method (DEM) combined with computational fluid dynamics (CFD) to compare with the experimental results. In this chapter two different air over pressures having the same air vent settings are tested and compared to the simulated results.

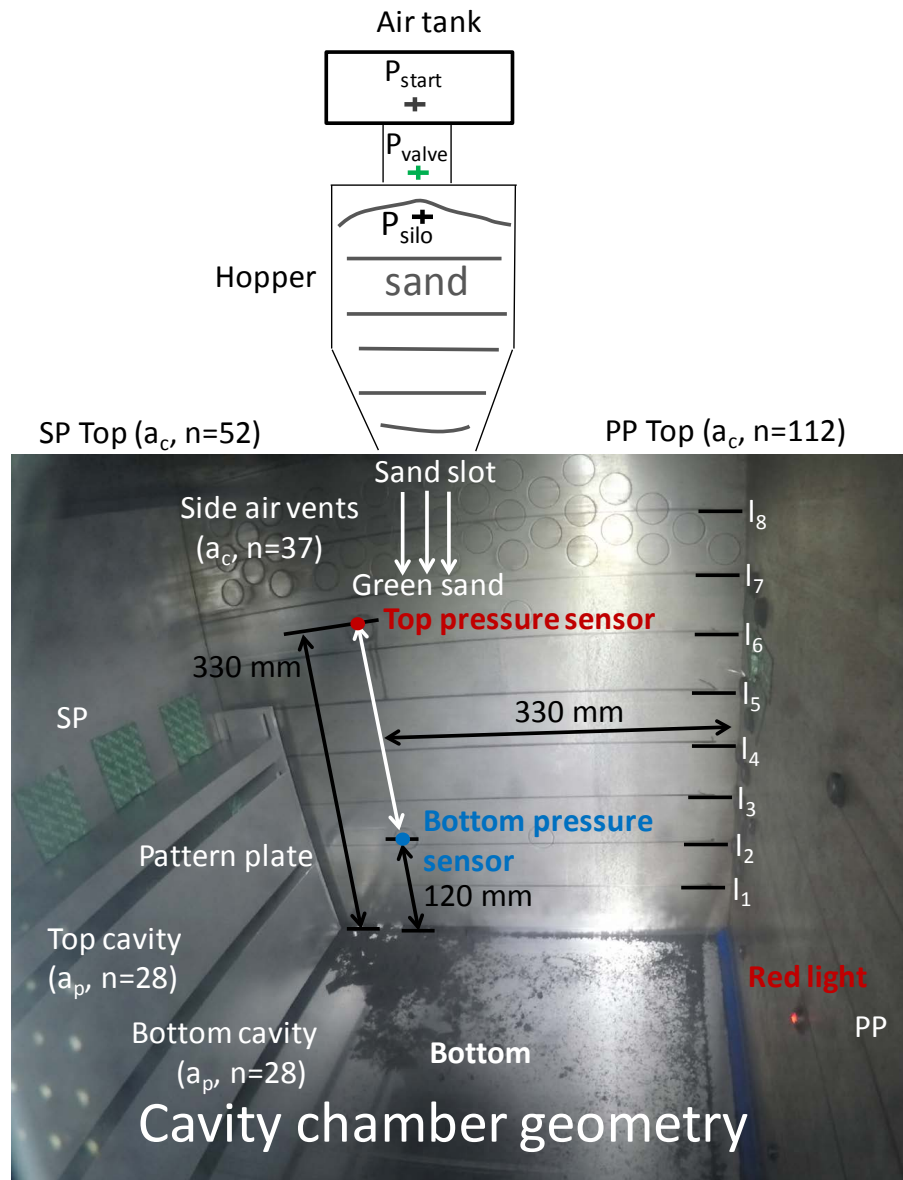


Figure 5.1: A photo of the chamber where the two cavities are placed on the lower left hand side on the pattern plate and the pattern plate is positioned on the Swing Plate side (SP). The sand shot start is indicated by the red light t_{start} and the flow behaviour of the green sand is monitored on the right hand side (PP side) with the 8 horizontal lines $l_1 - l_8$ equally spaced 50 mm apart. The air pressures are monitored by sensors in the air tank (light black cross), the shot valve (green cross), the hopper (black cross), the top of the chamber (red circle) and the bottom of the chamber (blue circle) where the sensors are listed from the top to the bottom.

Table 5.1: The experimental air vents settings in the chamber for the seven cases.

Case	1, 4 - 7	2	3
SP top air vents opened (a_c)	52	0	52
PP air vents, opened (a_c)	112	112	112
Pattern plate air vents opened (a_p)	28·2	28·2	14·2
Side air vents opened (n)	37·2	32·2	37·2
Total opened air vents ($a_c + a_p$)	294	232	266
Experimental repetitions	7	3	3

5.1.1 Settings of the air vents

There are 238 air vents of the type a_c placed in the chamber where 112 air vents are placed at the top of the PP chamber side shown in Fig. 5.1(PP top), 52 air vents are placed at the top of the SP side shown in Fig. 5.1(SP top) and 2×37 air vents are placed on the chamber sides in Fig. 5.1(Side air vents). On the pattern plate shown in Fig. 5.1 inside each cavity 28 air vents of the type (a_p) are placed. Details of the two air vent types physical behaviour and their specific positions were presented in PAPER [3]. Three different air vents settings are used for case 1 - 3 and the settings are listed in table 5.1. Case 1 is defined as the normal air vent setting which is defined as when all the air vents are opened and this setting is used for case 4 - 7 too. In this chapter the seven cases are investigated and presented:

Case 1: The normal setting of the air vents for the sand shot with the air overpressure of $P_{start} = 2.0$ bar. Simulations of case 1 were presented in PAPER [3].

Case 2: The sand shot has an overpressure of $P_{start} = 2.0$ bar where 62 out of the 238 air vents of the type a_c in the chamber are blocked. Simulations of case 2 were presented in PAPER [3].

Case 3: Sand shot with the overpressure of $P_{start} = 2.0$ bar where 14 air vents of the type a_p are blocked in each cavity on the pattern plate. Simulations of case 3 were presented in PAPER [3].

Case 4: The normal setting of the air vents for the sand shot with the air overpressure of $P_{start} = 2.0$ bar and using dry green sand.

Case 5: The normal setting of the air vents for the sand shot with the air overpressure of $P_{start} = 2.0$ bar and using wet green sand.

Case 6: The normal setting of the air vents for the sand shot with the air overpressure of $P_{start} = 1.5$ bar. Simulations of case 6 are presented in this chapter too.

Case 7: The normal setting of the air vents for the sand shot with the air overpressure of $P_{start} = 3.0$ bar. Simulations of case 7 are presented in this chapter too.

5.2 Governing equations

5.2.1 Governing equation and the Discrete Element Method

The Discrete Element Method and the governing equations for the method were presented in chapter 3 together with the calibration of the DEM model and the calibrated values for the DEM model were listed in table 3.4(third column) used in this chapter and in PAPER [3].

5.2.2 Governing equation for the air phase

The air phase is described by the Navier-Stokes equations these equations are all based on a Eulerian description. The low air pressures (P) measured in the chamber during the sand shot and the corresponding low air velocities (\mathbf{v}_g) make the assumption of the air phase being an incompressible fluid valid for small values of the Mach number $Ma \leq 0.3$. Then the continuity equation becomes,

$$\rho_g \frac{\partial}{\partial t} (\epsilon_g) + \rho_g \nabla \cdot (\epsilon_g \mathbf{v}_g) = 0 \quad (5.1)$$

where ϵ_g is the air volume fraction found from $\epsilon_g = \frac{V_g}{V_g + V_s}$ where V_g is the volume of the air phase and V_s is the volume of solid phase. The Navier-Stokes equations for the incompressible air phase are,

$$\rho_g \frac{\partial}{\partial t} (\epsilon_g \mathbf{v}_g) + \rho_g \nabla \cdot (\epsilon_g \mathbf{v}_g \mathbf{v}_g) = -\epsilon_g \nabla P + \epsilon_g \rho_g \mathbf{g} - \nabla \cdot (\epsilon_g \boldsymbol{\tau}_g) - \mathbf{I}_f \quad (5.2)$$

where $\rho_g = 1.18415 \frac{\text{kg}}{\text{m}^3}$ is the density of the air phase, $\mathbf{g} = [0, -9.82, 0] \frac{\text{m}}{\text{s}^2}$ is gravity and the shear stress on the air is $\boldsymbol{\tau}_g$ where the air is assumed to be a Newtonian fluid with the dynamic viscosity of $\mu = 1.85508 \cdot 10^{-5} \text{ Pa} \cdot \text{s}$. The two-way coupling between the air phase and the solid phase is enforced via the inter-phase momentum transfer of \mathbf{I}_f due to the drag on the solid phase.

5.2.2.1 The inter-phase momentum transfer

A source smoothing method is applied for the inter-phase momentum transfer of \mathbf{I}_f , which averages the momentum transfer from larger parts of the mesh to the solid phase stabilizing the simulations to run faster and converge. The drag force on the solid phase is,

$$\mathbf{F}_D = -\frac{1}{8} \pi d^2 \rho_g C_d (\mathbf{v}_g - \mathbf{u}) |\mathbf{v}_g - \mathbf{u}| \quad (5.3)$$

where \mathbf{u} is the velocity of the solid phase and $\frac{1}{4} \pi d^2$ is the reference area equal to the projected area of the sphere with the diameter of d . The interaction of the solid phase with the air phase is described by the Schiller-Naumann drag model,

$$C_d(Re_p) = \begin{cases} \frac{24}{Re_p} (1 + 0.15 Re_p^{0.687}), & Re_p \leq 10^3 \\ 0.44, & Re_p > 10^3 \end{cases} \quad (5.4)$$

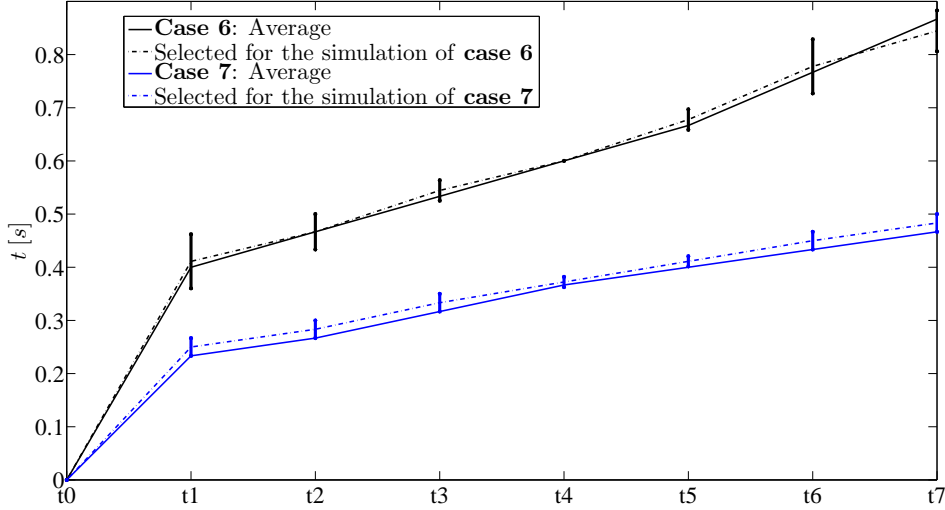


Figure 5.3: The filling times for case 6 - 7. The sand shot pressure is 1.5 bar in case 6 (black) and the pressure is 3.0 bar in case 7 (blue).

an elongated air channel with a pressure outlet shown in Fig. 5.2(b). The simulation air vent settings were derived and explained in PAPER [3]. Case 6 and case 7 use the normal air vent settings for the simulations as in case 1 from PAPER [3].

5.3.2 Boundary condition for the granular flow

The experimental filling times of $t_0 - t_7$ are shown in Fig. 5.3 for the two different cases, case 6 - 7. For each of the two cases an experiment is selected for the simulation and these times are plotted with the two full lines in Fig. 5.3. From the filling times $t_1 - t_7$ and the areas $A_1 - A_7$ the inlet flow rate and the inlet velocities of the DEM particles can be found from the procedure described in PAPER [3] where the seven applied areas $A_1 - A_7$ are shown in Fig. 5.2(a). The found vertical inlet velocities are shown in Fig. 5.4 and due to the spikes in the time dependent velocity of $v_y(t)$ from case 7 a two - step velocity $v_{2y}(t)$ was chosen to remove the spikes. The derivation of the velocities are also described in PAPER [3].

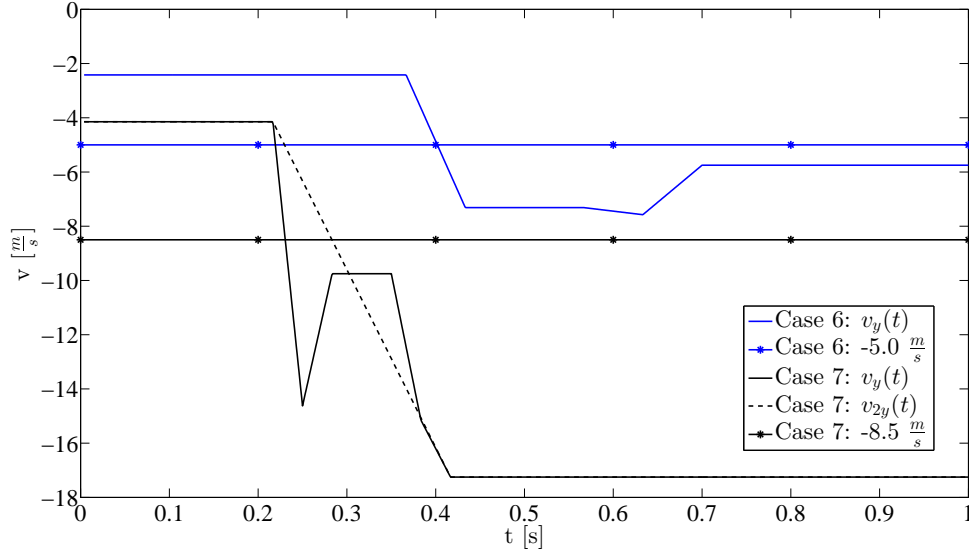


Figure 5.4: The vertical inlet velocities for the simulations of case 6 - 7.

5.4 Results of the DISAMATIC process and simulations

5.4.1 The experimental measured air pressures and the filling times

Measurements from the different pressure sensors are plotted as a function of time together with the filling times in case 6 and case 7 for the selected experiments which are shown in Fig. 5.5. The chamber pressure in case 7 was significantly larger than in case 6 as expected. The air pressure builds up in the hopper (black line) in the start of the sand shot as the pressure decreases in the air tank (black dotted line). The pressure in the hopper starts to decrease after t_1 when the green sand has reached the bottom line l_1 . The duration of time from t_0 to t_1 is longer than the subsequent next time intervals t_1 to t_2 . The shorter times intervals are due to an increase in the pressure difference between the hopper and the chamber, which subsequently increases the velocity of the green sand flowing into the chamber. Case 7 has shorter filling times compared to case 6 and at the end of the sand shot the chamber pressure increases significantly in case 7 with a maximum chamber pressure obtained at around the time of 0.85 s.

In PAPER [3] the same behaviour was observed for the experiments and the measured pressure in the chamber. The air tank air overpressure in PAPER [3] was 2.0 bar which is in between case 6 (1.5 bar) and case 7 (3.0 bar) and therefore the chamber pressure was in between case 6 and case 7 too.

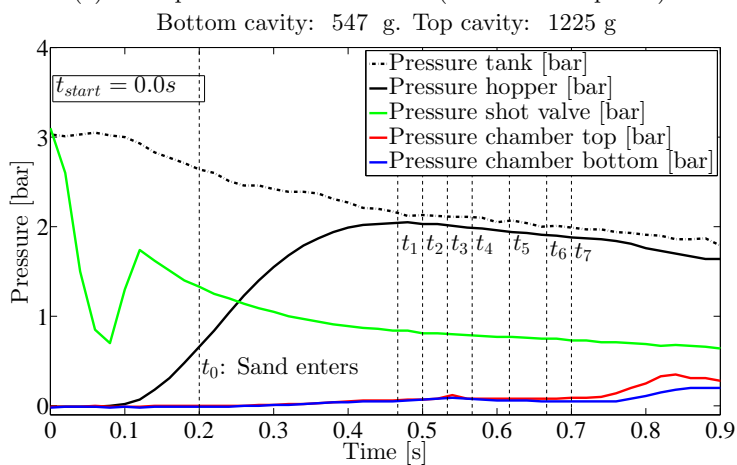
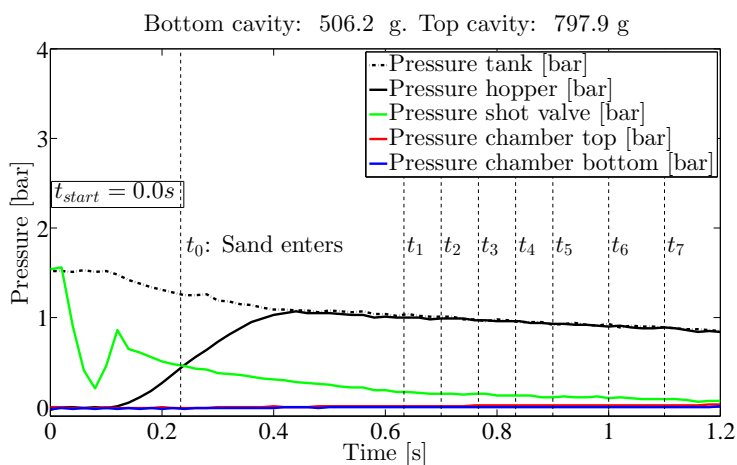


Figure 5.5: The pressure as a function of time shown in the positions listed from the top to the bottom: the air tank (black dotted line), the pressure shot valve (green), the hopper (black line), the pressure in the top of the chamber (red line) and in the bottom (blue line). The dotted black vertical lines is the filling times $t_0 - t_7$ of the chamber.

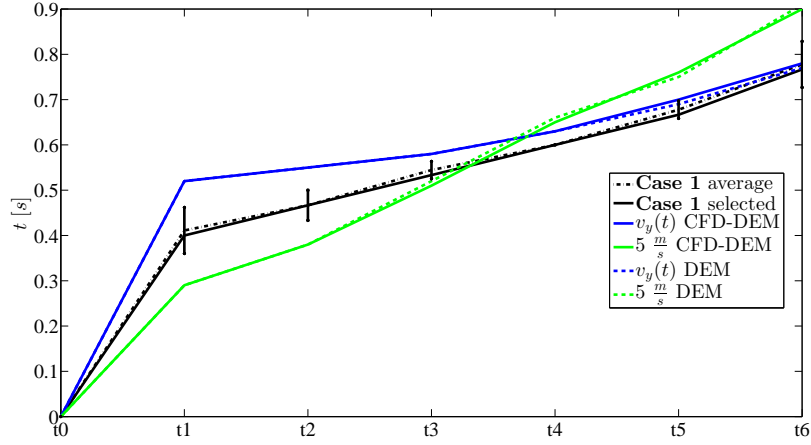
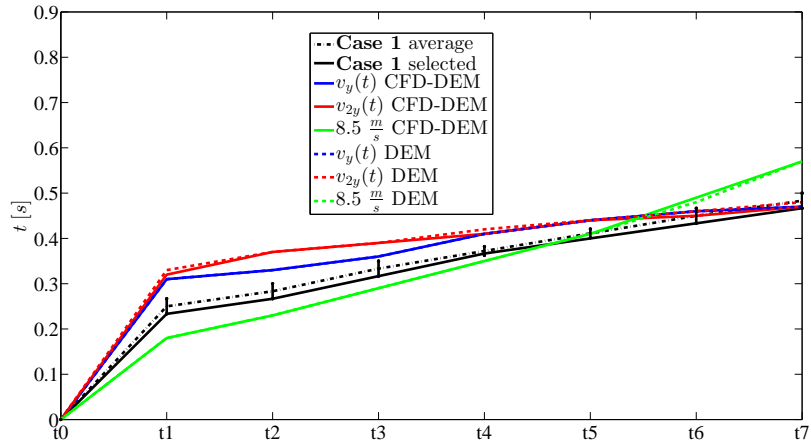
(a) Case 6: 1.5 bar for the fillings times of $t_0 - t_6$.(b) Case 7: 3.0 bar for the fillings times of $t_0 - t_7$.

Figure 5.6: The experimental and simulation filling times of case 6 and case 7.

5.4.2 The simulated filling times

In Fig. 5.6 it is shown that the simulated filling times are in good agreement with the experimental results of case 6 and case 7. In the experiments, case 6 had longer filling times compared to case 7 due to the higher air overpressure in the sand shot and this behaviour was also observed in the simulations. The time dependent velocities first filling time, t_1 was too long as when compared to the experiment for both cases. The constant velocities first filling time, t_1 was too short as when compared to the experiment for both cases. In PAPER [3] the same behaviour was observed for the experimental filling times and the simulated filling times. The air tank air overpressure in PAPER [3] was 2.0 bar which is in between case 6 (1.5 bar) and case 7 (3.0 bar) and therefore the filling times were in between case 6 and case 7 too.

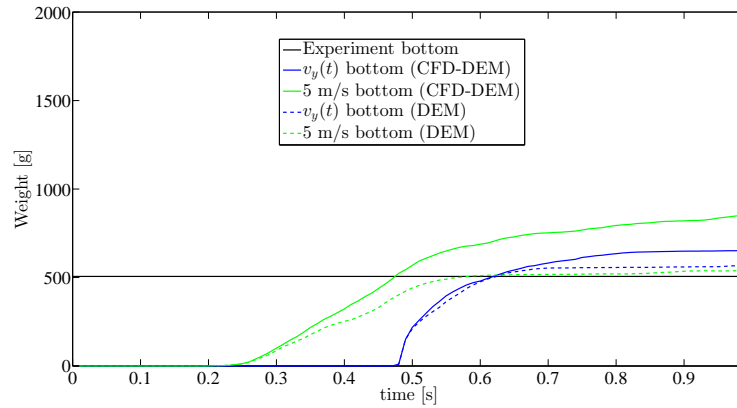
5.4.3 Sand deposited in the two cavities

The mass of green sand in the cavities for the DISAMATIC experiments and the simulations are listed in table. 5.2(left) for all the seven cases. The green sand densities and the compactabilities are listed in table. 5.2(right) for all the seven cases.

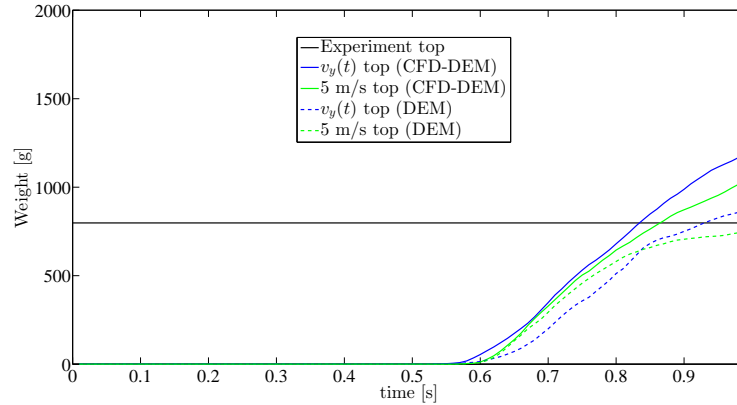
Table 5.2: Mass in the cavities from the seven cases with respect to the experiments and the simulations. The number of repetitions of the sand shots and the compactability test are indicated by (n) and if (n=1) it is not written. The sign of \pm indicates the standard deviation σ around the mean μ in the following way $\mu \pm \sigma$.

Case	Sand shot	Bottom cavity [g]	Top cavity [g]	$\rho_{sand} = [kg/m^3]$	Compaca [%]
1	2.0 bar (n=7)	593 \pm 189	961 \pm 237	920 \pm 50.1	34 \pm 3.5 % (n=18)
1	2.0 bar (selected)	792	1118		
1	$v_y(t)$ CFD-DEM	1753	1817		
1	$v_{2y}(t)$ CFD-DEM	1758	1786		
1	$5 \frac{m}{s}$ CFD-DEM	1782	1719		
1	$7 \frac{m}{s}$ CFD-DEM	1787	1782		
1	$v_y(t)$ DEM	582	918		
1	$v_{2y}(t)$ DEM	696	864		
1	$5 \frac{m}{s}$ DEM	568	586		
1	$7 \frac{m}{s}$ DEM	734	893		
2	2.0 bar (n=3)	933 \pm 215	1220 \pm 72.5	970 \pm 19.7	31 \pm 0.7 % (n=9)
2	2.0 bar (selected)	1100	1284		
2	$v_y(t)$ CFD-DEM	1830	1882		
2	$v_{2y}(t)$ CFD-DEM	1846	1852		
2	$5 \frac{m}{s}$ CFD-DEM	1801	1851		
2	$7 \frac{m}{s}$ CFD-DEM	1819	1842		
2	$v_y(t)$ DEM	618	1363		
2	$v_{2y}(t)$ DEM	673	1159		
2	$5 \frac{m}{s}$ DEM	557	586		
2	$7 \frac{m}{s}$ DEM	770	934		
3	2.0 bar (n=3)	623 \pm 47.7	687 \pm 30.2	937 \pm 28.6	33 \pm 1.9 % (n=9)
3	2.0 bar (selected)	674.8	721		
3	$v_y(t)$ CFD-DEM	1723	1872		
3	$v_{2y}(t)$ CFD-DEM	1562	1590		
3	$5 \frac{m}{s}$ CFD-DEM	1607	1333		
3	$7 \frac{m}{s}$ CFD-DEM	1657	1684		
3	$v_y(t)$ DEM	1008	1774		
3	$v_{2y}(t)$ DEM	823	832		
3	$5 \frac{m}{s}$ DEM	595	569		
3	$7 \frac{m}{s}$ DEM	605	790		
4	2.0 bar (n=3)	810 \pm 284	1070 \pm 326	966 \pm 29.0	31 \pm 2.2 % (n=9)
5	2.0 bar (n=3)	396 \pm 37.7	667 \pm 42.0	814 \pm 14.5	41 \pm 1.7 % (n=9)
6	1.5 bar (n=3)	676 \pm 216	894 \pm 84	915 \pm 17.9	34 \pm 1.0 % (n=9)
6	1.5 bar (selected)	506	798		
6	$v_y(t)$ CFD-DEM	651	1189		
6	$5 \frac{m}{s}$ CFD-DEM	852	1033		
6	$v_y(t)$ DEM	572	869		
6	$5 \frac{m}{s}$ DEM	538	749		
7	3.0 bar (n=3)	701 \pm 143	1340 \pm 337	875 \pm 34.8	38 \pm 2.4 % (n=9)
7	3.0 bar (selected)	725	1072		
7	$v_y(t)$ CFD-DEM	1821	1889		
7	$v_{2y}(t)$ CFD-DEM	1812	1895		
7	$8.5 \frac{m}{s}$ CFD-DEM	1793	1832		
7	$v_y(t)$ DEM	1091	1801		
7	$v_{2y}(t)$ DEM	1028	1812		
7	$8.5 \frac{m}{s}$ DEM	993	929		

Case 7 with the air pressure of 3.0 bar gave the largest average mass of green sand in the top cavity of 1340 g and third largest average mass of green sand in the bottom cavity of 701 g. In Case 2 with the chamber air vents blocked the bottom cavity was filled with the largest average mass of green sand of 933 g and the top cavity was filled with the second largest average mass of green sand of 1220 g. Comparing case 2 to case 4 (normal air vent setting) with equivalent green sand properties for the density and compactability, the cavities were still better filled for case 2 as expected. The smallest mass in the cavities were found for case 5 because the wet green sand had the lowest flowability properties, the lowest fluidization properties and the lowest density and thereby gave problems for the sand flowing through the narrow entrance into the two cavities. The simulations of



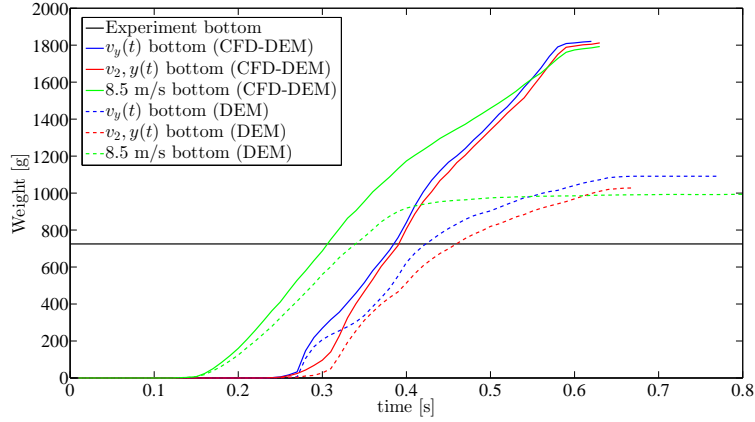
(a) The bottom cavity



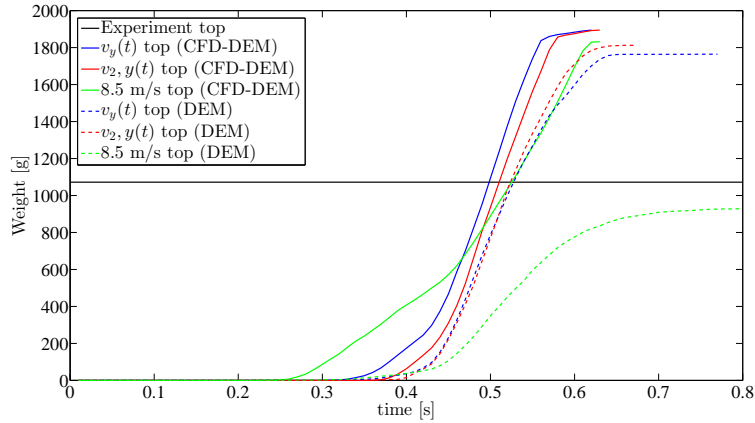
(b) The top cavity

Figure 5.7: Case 6: The cavity masses as a function of time where $t_0 = 0.0$ s is the starting time on the x-axis.

case 6 were in good agreement with the experiments for the mass in the cavities due to the lower simulated air pressures in the chamber. The simulated velocity of the air phase was slower in case 6 and thereby the simulated mass in the cavities for case 6 was similar for the DEM model as the values from the CFD-DEM model were and these are shown in Fig. 5.7. Due to the high chamber pressures in case 7 the simulated air velocities were very large too and thereby the mass in the cavities were overestimated for the CFD-DEM



(a) The bottom cavity



(b) The top cavity

Figure 5.8: Case 7: The cavity masses as a function of time where $t_0 = 0.0$ s is the starting time on the x-axis.

model when compared to the experiment shown in Fig. 5.8. The DEM model in case 7 predicted the mass in the cavities with better agreement to the selected experiment. The DEM model in case 7 overestimated the top cavity mass as compared to the experimental results, except for the constant velocity of $8.5 \frac{m}{s}$. The CFD-DEM simulated results of case 1 - 2 from PAPER [3] are shown in Fig. 5.9 and case 7 is shown in Fig. 5.10(right). These three simulations overestimated the mass in the cavities as when compared to case 6 shown in Fig. 5.10(left). For the cases 1, 2 and 7 the simulated air velocities in the cavities were around $15 - 30 \frac{m}{s}$ as compared to case 6 where the cavity air velocities were around $5 - 8 \frac{m}{s}$. When comparing case 1 to case 2 in Fig. 5.9(middle) the particles have greater velocities and a more pronounced particle jet when the particles entered the bottom cavity in case 2. When comparing the simulations to the experiments shown in Fig. 5.9 and shown in Fig. 5.10 all the simulations were in good agreement with the experiments with respect to the sand pile shape at time $t=0.50$ s in the sand shot.

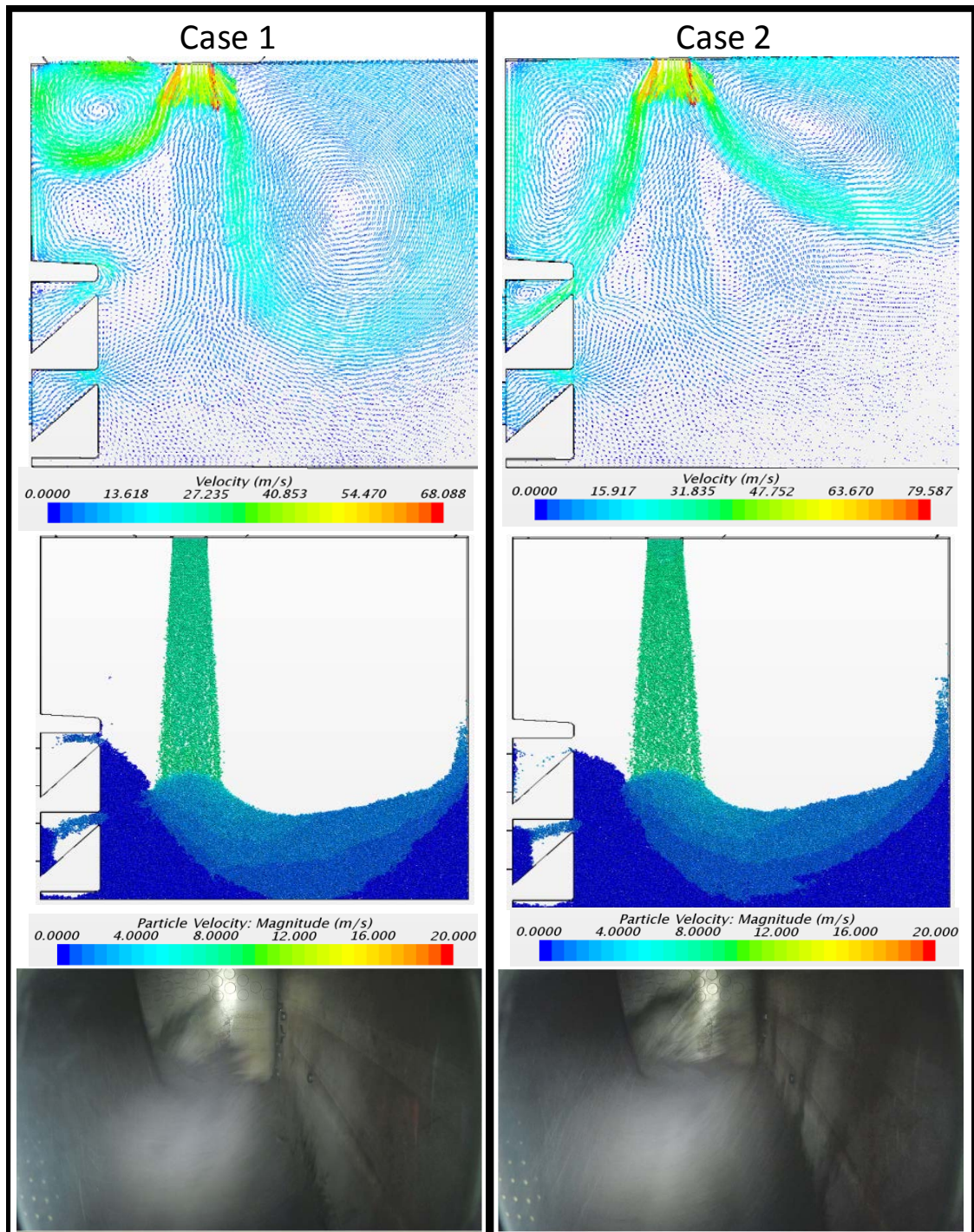


Figure 5.9: The time dependent velocity $v_y(t)$ simulation at time $t=0.50$ s. (Top) The velocity of the air phase. (Middle) The velocity of the particles. (Bottom) The experimental video footage at time $t=0.50$ s.

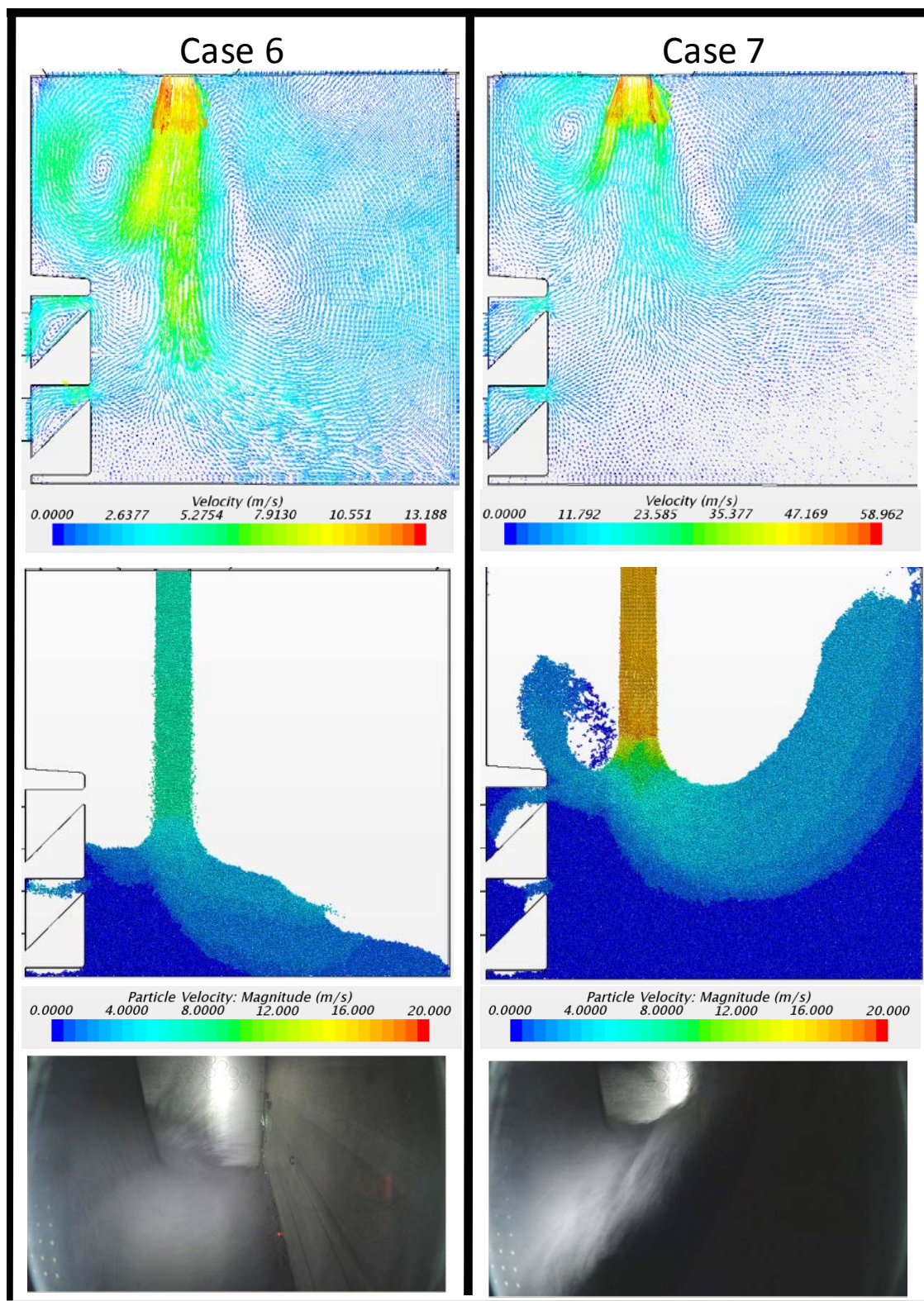


Figure 5.10: The time dependent velocity $v_y(t)$ simulation at time $t=0.50$ s. (Top) The velocity of the air phase. (Middle) The velocity of the particles. (Bottom) The experimental video footage at time $t=0.50$ s for case 6 where for case 7 the video footage is at time $t=0.48$ s (at $t=0.50$ s the photo was black).

5.5 Conclusion

In the present chapter the sand shot in the DISAMATIC process was investigated for the air vent settings, the air overpressure and the green sand condition and these settings abilities to deposit the mass of green sand into the two cavities. In this chapter the air overpressure of 1.5 bar (case 6) and the air overpressure of 3.0 bar (case 7) were simulated and the results were compared to the experiments. Whereas in PAPER [3] three different air vent settings (case 1 - 3) with the air overpressure of 2.0 bar were simulated with respect to the mass of green sand deposited in two cavities and compared to experimental results.

5.5.1 The experiments

In case 2 the air vents were blocked in the chamber for an enhanced local airflow through the cavities and as expected the mass in the two cavities were among the largest. Decreasing the number of air vents in the cavities as done in case 3 decreased the deposited mass of green sand in the cavities as compared to case 2. The largest mass in the top cavity was observed in case 7 which had the largest air pressure in the chamber especially at the last part of the sand shot. Hence, the air stream transported more green sand into the top cavity at the last part of the sand shot. The sand shot could be performed with a large air pressure of 3.0 bar as in case 7 combined with the chamber air vents blocked as in case 2 for an additional increased airflow through the cavities. Thereby the mass of green sand in the cavities are expected to become even larger due to the increased local airflow through the cavities.

Larger mass in the cavities were also observed in case 4 as expected due to the less cohesive dry green sand having a higher flow-ability, higher fluidization properties and a higher density. Smaller masses in the cavities were also observed in case 5 as expected due to the wet cohesive green sand having a lower flow-ability, lower fluidization properties and a lower density.

The pressure difference between the air tank and the hopper, which drives the green sand from the hopper down into the chamber is important. Secondly the air pressure difference between the chamber and the surroundings, which drives the sand outwards to the mold geometry is important too. The larger these two air pressure differences are the larger the velocity of the green sand flow becomes. The larger the velocity of the green sand flow up to a certain velocity, the larger the green sand mass deposited in the two cavities for this geometry are expected to become.

5.5.2 The simulations

With the chosen particle flow rates and particle velocities it was possible to simulate the qualitative flow behaviour and the final mass of green sand in the cavities. Larger inlet velocities for the DEM particles increased the final mass in the cavities of the investigated

rib geometry. The following conclusions are partially from PAPER [3] and from this chapter.

In PAPER [3] the CFD-DEM simulations show larger masses in the cavities as compared to the experimental results due to the airflow in the simulations still drags the particles into the cavities at the end of the sand shot. The side air vents could not be simulated due to the running time of the number of DEM particles when simulating a larger part of the chamber and thereby the volume of air that exits the cavities is correspondingly overestimated. In case 3 the CFD-DEM simulations were in better agreement with the selected experiment due to the lower air inlet pressure in the simulations which gave subsequently lower air velocities through the cavities. Close predictions of the mass of the green sand in the cavities were accomplished by the DEM simulations however with a tendency to underestimate the mass. The CFD-DEM simulations predict the cavity filling times better as compared to the DEM simulations although the CFD-DEM simulations still show too long filling times for the cavities as compared to the experiments.

In this chapter the high chamber pressures in case 7 and thereby the subsequent simulated air velocity in the CFD-DEM model was very large too and therefore the masses in the cavities were overestimated as compared to experiments and the DEM simulations. The simulations of case 6 were in better agreement with the experiments for the mass in the cavities due to the lower simulated air pressures in the chamber. Therefore the simulated mass in the cavities for case 6 were more similar for the CFD-DEM model when compared to the experimental cavity masses and also when compared the DEM model cavity masses.

Chapter 6

Conclusion and future Work

This chapter presents the conclusion of the material characterization of the green sand from the experiments and subsequently how selected experiments were used to calibrate the numerical model, thereby preparing the model to simulate the process. The conclusion of experiments performed on the DISAMATIC machine and the simulations of these experiments are presented too. Finally future perspectives in the field of the sand casting process and simulating the process are given.

6.1 The material characterization of green sand

The material characterization was performed with respect to five different mechanical conditions of the green sand found in the DISAMATIC process. The purpose of the experiments was to characterize and define the overall mechanical properties of the green sand during the following five conditions: High load flow (1), low load flow (2), fluidized flow (3), confined compression (4) and the unconfined compression (5).

The high load flow was investigated with a ring shear tester where the flowability decreased when the green sand became more wet and the opposite was the case for the dry green sand. The yield stress increased when the green sand became more wet and the opposite behaviour was the case for the dry green sand. The density as a function of the normal stress proposed by [21] was found to be a good predictor for the relationship of these two variables.

The low load flow was investigated with a sand pile experiment where the sand pile height increased when the green sand was wet and the opposite was the case for the dry green sand. The sand pile shape became more uneven when the green sand was wet and for the dry green sand the sand pile shape became more conically shaped. The two slump tests decreased in spread length when the green sand was wet and the opposite was the case for the dry green sand.

The fluidized flow was investigated with a fluidized bed test and the Anton Paar Powder

Cell. The fluidized bed test found the dry green sand to have better fluidization properties as compared to the wet green sand. The Anton Paar Powder Cell found the green sand to behave like a shear thinning fluid, in which the viscosity is reduced by increasing the shear rate and the viscosity of the green sand also behaved like a shear thinning fluid when the airflow rate was increased in PAPER [6].

The confined compression test was performed with the compactability test, in which the compactability was found to increase when the green sand water content increased, which was due to the larger pores in the green sand created from the wet bridges.

The un-confined compression test was performed as a uni-axial test which was used to obtain the stiffness and the un-confined compression strength of the green sand. The found values for stiffness and strength were in good agreement with all the performed tests on the green sand batches, except for the "very wet" green sand batch number 2 where the values were significantly smaller as compared to the other batches. Note that this batch was above the recommended compactability value with respect to using the green sand in the DISAMATIC process.

6.2 Calibration of the DEM model

The Discrete Element Method (DEM) was chosen as the numerical model since the discrete nature of the method simulates the granular nature of the green sand with good agreement. The DEM model used a rolling resistance model to emulate the non-spherical quartz sand particles' resistance to rolling and used a cohesive model to emulate the binding of the quartz sand particles from the bentonite.

The parameters used in the DEM model were found from the following experiments: A ring shear tester, a sand pile experiment in the PAPERS [2, 3] and additionally a slump test in PAPER [3]. The ring shear tester was applied to obtain the static friction coefficients for the DEM model. The height of the sand pile was measured and from this the DEM model was calibrated. The calibration was performed with respect to obtaining the values in the rolling resistance as well as in the parameter value of the cohesive model. As expected, an increase in the value of the particle-particle rolling resistance increased the simulated sand pile height and an increase in the value of the particle-particle cohesion increased the height of the sand pile further. Increasing the cohesion changed the shape of the sand pile to become more uneven and higher as also seen in the experiments for the more wet green sand.

In PAPER [3] the density was adjusted to that of the loose green sand and a slump experiments was applied to calibrate the DEM models with respect to the value of the particle-wall rolling resistance. For a small value of this the particles rolled further away from the sand pile slump as compared to larger values as expected.

6.3 The sand shot and the simulations

In the PAPER [2] a 2-D DEM model and a 3-D slice DEM model were applied to simulate the DISAMATIC process' dynamic flow behaviour with good agreement with the experiments performed in the rib geometry. The dynamic flow behaviour of the particles in the simulations was generally similar to that of the sand shot in the DISAMATIC process. More specifically, with a well selected coefficient of restitution, flow rate, damping coefficient, rolling resistance and static friction coefficient it is possible to simulate the experimental video footage very well. When the model is calibrated the flow rate and the velocity are obviously the most important factors for the modelling flow dynamics during the filling of the chamber.

Although differences are seen from the 2-D to the 3-D slice simulation the results remain in good agreement and the fast execution of 2-D simulations can still be used for parametric studies in simple geometries. Hence it was decided to perform a 2-D sensitivity analysis in PAPER [1] and an additional sensitivity study in chapter 3. The two sensitivity analyses of the 2-D simulations suggested that the particle flow rate and the particle velocity are of greater importance than most of the other parameters especially if the parameters are chosen in physical reasonable intervals as found by the calibration in the PAPERS [2, 3].

A sensitivity study of the particle-wall interaction parameters were performed in PAPER [2] and it was found that the quantitative and qualitative behaviour were virtually the same as the reference 2-D DISAMATIC simulation. Hence, these particle-wall parameters are of less importance for simulating the DISAMATIC process.

In chapter 5 it was found that the pressure difference between the air tank and the hopper, which drives the green sand from the hopper down into the chamber, is important. Moreover, the air pressure difference between the chamber and the surroundings, which drives the sand outwards to the mold geometry is important as well. The larger these two air pressure differences, the larger the velocity of the green sand flow.

In PAPER [3] and in chapter 5 for the cavity geometry, it was found that with special air tank pressures and with special air vents settings, the mass of the green sand in the cavities could be increased. Hence, by increasing the local airflow through the cavities during the sand shot, the mass in the cavities were found to be increased as well. A 3-D slice with a combined CFD-DEM model was applied to simulate a slice of the DISAMATIC process where the dynamic flow behaviour showed good agreement with the experiments. The combined CFD-DEM simulations predicted a larger mass in the cavities compared to the experimental results. This was most probably due to an enhanced airflow at the end of the simulated sand shot, which dragged more particles into the cavities. The side air vents could not be simulated, due to the increased CPU time of the number of DEM particles when simulating a larger part of the chamber. Hence, the volume of air that exits the cavities are correspondingly overestimated in the 3-D CFD-DEM slice simulations and

therefore the predicted mass in the cavities were overestimated as well. Close predictions of the mass of the green sand in the cavities were accomplished by the DEM simulations with a tendency to underestimate the mass.

Conclusively, it can be stated that the experiments performed on the Ferrofos foundry with the special designed cavity geometry as well as the simulations gave very useful insights into the DISAMATIC process and how to improve the process in the future.

6.4 Future work

Experiments

A plug of green sand is created in the sand slot due to the cohesion in the sand mixture after the sand shot. The plug prevents the sand from falling down into the chamber in-between sand shots. The initial acceleration of the green sand and removing the plug probably decrease the initial velocity of the green sand entering the chamber and probably decrease the pressure build up in the chamber in the initial part of the sand shot too. The smaller mass in especially the bottom cavity is most likely due to the small velocity of the green sand and the low chamber pressure in the initial part of the sand shot. Hence, a sand slot closing mechanism that opens when the pressure in the hopper is equal to the air tank pressure could be suggested in a future design, since this might imply a higher initial green sand velocity and a larger chamber pressure in the initial phase of the sand shot. This closing mechanism could also make it possible to start the next sand shot while the mould was being squeezed or pushed out, saving production time. Moreover, such closing mechanism could potentially create a strong plug of green sand during the pressure build up in the hopper thus preventing the green sand from leaving the sand slot during the sand shot.

Simulations

Simulating the sand shot with half of the mold geometry including the side air vents and using a symmetry boundary in the middle of the geometry could give a more correctly simulated airflow in the combined CFD-DEM model. This is because the airflow towards the sides would be included and subsequently this would decrease the airflow through the cavities due to the air now could escape in the sides. Hence, the decrease in airflow through the cavities would decrease the mass in the cavities too, for a more correct prediction when using the combined CFD-DEM model.

In the future it could be interesting to simulate the hopper during the sand shot to instigate the flow in it and the flow through the sand slot (hopper orifice) thereby simulating the inlet particle flow rate and the inlet particle velocity versus the experimental inlet behaviour of the green sand in the DISAMATIC process.

Currently new and potentially faster CFD-DEM frameworks as the CUDA platform run-

ning on a GPU are being developed [58, 57]. This framework could potentially run faster CFD-DEM calculations on normal laptop graphics cards with millions of particles as compared to a CPU based framework. Further out in the future, simulating the individual non-spherical quartz sand particle shapes and size distribution together with a suitable cohesion model would be interesting, but at the current moment it is not possible.

Future calibration of the DEM model with respect to solid mechanical behaviour combined with fluidization behaviour could be interesting. Calibrating the DEM model with an uni-axial compression test or the ring shear tester for the solid mechanical region combined with the fluidized viscosity from the Anton Paar Powder Cell for obtaining a "full range calibration of the CFD-DEM model" could be made. With this full range calibration it would be possible to simulate the sand shot correctly and subsequently simulate the squeezing process correctly after the sand shot and hopefully this could be accomplished in one simulation.

The sand shot in the DISAMATIC process could also be modelled in a continuum framework where the ring shear tester could give indications of the solid mechanical behaviour of the green sand and the Anton Paar Powder Cell could give indications of the fluidized viscosities of the green sand.

Bibliography

- [1] E. Hovad, P. Larsen, J. H. Walther, J. Thorborg, and J. H. Hattel. Flow dynamics of green sand in the disamatic moulding process using discrete element method (dem). *IOP Conference Series: Materials Science and Engineering*, 84(1):012023, 2015.
- [2] E. Hovad, J. Spangenberg, P. Larsen, J.H. Walther, J. Thorborg, and J.H. Hattel. Simulating the disamatic process using the discrete element method a dynamical study of granular flow. *Powder Technology*, 303:228 – 240, 2016.
- [3] E. Hovad, J. Spangenberg, P. Larsen, J.H. Walther, J. Thorborg, and J.H. Hattel. Cavity prediction in sand mould production applying the disamatic process. *To be submitted to Powder Technology in 2017*.
- [4] E. Hovad, J. Spangenberg, P. Larsen, J. Thorborg, and J. H. Hattel. An analytical solution describing the shape of a yield stress material subjected to an overpressure. *AIP Conference Proceedings*, 1738(1), 2016.
- [5] Jon Spangenberg, Rolands Cepuritis, Emil Hovad, George W. Scherer, and Stefan Jacobsen. Shape effect of crushed sand filler on rheology: A preliminary experimental and numerical study. *Rilem State of the Art Reports*, pages 193–202, 2016.
- [6] J. Masoud, J. Spangenberg, E. Hovad, R. Comminal J. H. Hattel, K. I. Hartmann, and D. Schuutz. Rheological characterization of green sand flow. *Proceedings of the ASME 2016 International Mechanical Engineering Congress and Exposition*, 2016.
- [7] E. Hovad, J. Spangenberg, P. Larsen, J. Thorborg, and J. H. Hattel. An non-dimensionlized analytical solution describing the shape of a yield stress material subjected to an overpressure. *Report*, 2016.
- [8] DISA Industries A/S. DISA 231/DISA 231 Var. Sand Moulding System Instructions for Use. (9157), 2013.
- [9] Kristjan Kristjansson. Dimensional control in casting. 8 2016. Supervisor: Kamran Mohaghegh, Postdoc.
- [10] U. Ittipon. Technical presentation green sand mold-ing management. *Suranaree University of Technology*, (<http://www.sut.ac.th/engineering/Metal/ru/GREEN20%20SAND.pdf>), 2011.

- [11] Dietmar Schulze. Flow properties of powders and bulk solids. pages 1–21, 2006.
- [12] Dietmar Schulze, Jrg Schwedes, and John W. Carson. Powders and bulk solids: Behavior, characterization, storage and flow. *Powders and Bulk Solids: Behavior, Characterization, Storage and Flow.*, pages 1–511, 2008.
- [13] Nikolaj Kjelgaard Vedel-Smith. Spot feeding spheroidal graphite iron with exothermic and insulating ram-up sleeves in vertically parted moulds. *PHD-Thesis from Danish Technical University of Denmark (DTU)*, 2015.
- [14] Ugochukwu Chibuzoh Nwaogu, K. S. Hansen, and Niels Skat Tiedje. Design and production of a novel sand materials strength testing machine for foundry applications. *International Foundry Research*, 64(2), 2012.
- [15] STAR-CCM+. *USER GUIDE STAR-CCM+, Version 8.02.* 2013.
- [16] Department of Chemical and Biochemical Engineering. Technical University of Denmark. Chemical and biochemical unit operations. exercise 7c, fluidized bed drying.
- [17] Lindsey C. Teaters and Francine Battaglia. On the computational modeling of unfluidized and fluidized bed dynamics. *Proceedings of the Asme International Mechanical Engineering Congress and Exposition - 2012, Vol 7, Pts A-d*, pages 2539–2546, 2013.
- [18] Henk G. Merkus and Gabriel M. H. Meesters. *Production, handling and characterization of particulate materials.* 2016.
- [19] Raghwendra Banchhor and S.K Ganguly. Modeling of moulding sand characteristics in disomatic moulding line green sand casting process. *Proceedings of BITCON-2015 Innovations For National Development. National Conference on: Innovations In Mechanical Engineering For Sustainable Development*, 2015.
- [20] Y Chang and H Hocheng. The flowability of bentonite bonded green molding sand. *Journal of Materials Processing Technology*, 113(1-3):238–244, 2001.
- [21] MM CARROLL and KT KIM. Pressure density equations for porous metals and metal powders. *Powder Metallurgy*, 27(3):153–159, 1984.
- [22] T SHEPPARD and HB MCSHANE. Strength of cold-pressed compacts. *Powder Metallurgy*, 23(3):120–125, 1980.
- [23] J. Bast. A new method for the measurement of flowability of green moulding sand. *Archives of Metallurgy and Materials*, 58(3):945–952, 2013.
- [24] J Frost and JM Hiller. The mechanics of green sand moulding. *AFS Trans*, 74:177–186, 1966.
- [25] Fred. W. Schuster. Scott M. Strobl. Using stress-strain curves to evaluate control clay bonded moldings sands.

- [26] David G Schaeffer. Instability in the evolution equations describing incompressible granular flow. *Journal of Differential Equations*, 66(1):19–50, January 1987.
- [27] P. C. Johnson and R. Jackson. Frictional collisional constitutive relations for granular materials, with application to plane shearing. *Journal of Fluid Mechanics*, 176:67–93, 03 1987.
- [28] J Wu, H Li, W Li, H Makino, and M Hirata. Two phase flow analysis of aeration sand filling for green sand molding machine. *International Foundry Research/Giessereiforschung*, 60(1):20–28, 2008.
- [29] B Winartomo, U Vroomen, A Buhrig-Polacek, and M Pelzer. Multiphase modelling of core shooting process. *International Journal of Cast Metals Research*, 18(1):13–20, 2005.
- [30] Chang-jiang Ni, Gao-chun Lu, Qing-dong Zhang, Tao Jing, Jun-jiao Wu, Lin-long Yang, and Qin-fang Wu. Influence of core box vents distribution on flow dynamics of core shooting process based on experiment and numerical simulation. *China Foundry*, 13(1):22–29, 2016.
- [31] J Rojek, F Zarate, CA de Saracibar, C Gilbourne, and P Verdot. Discrete element modelling and simulation of sand mould manufacture for the lost foam process. *International Journal for Numerical Methods in Engineering, Int. J. Numer. Methods Eng, Int J Num M, Int J Numer Meth Eng, Int J Numer Method Eng, Int J Numer Methods Eng, Internat. J. Numer. Methods Engrg*, 62(11):1421–1441, 2005.
- [32] H Makino, Y Maeda, and H Nomura. Computer Simulation of Various Methods for Green Sand Filling. *Transactions of American Foundry Society*, 110:1–9, 2002.
- [33] H Makino, Y Maeda, and H Nomura. Computer Simulation of Squeeze Molding Using the Distinct Element Method. *Transactions of American Foundry Society*, 109:1–7, 2001.
- [34] John Campbell. *Castings*. 2003.
- [35] American Foundry Society. *Mold and Core Test Handbook*. 2015.
- [36] Walker D.M. An approximate theory for pressures and arching in hoppers. *Chemical Engineering Science*, 22(22):486, 1967.
- [37] John Carson and David Craig. Silo design codes: Their limits and inconsistencies. *Procedia Engineering*, 102:647–656, 2015.
- [38] Marcus Ripp, Zewdu A. Debele, and Siegfried Ripperger. Determination of bulk flow property of tef flour and seed and design of a silo. *Particulate Science and Technology*, 33(5):494–502, 2015.

- [39] S. Behera, S. Das, Z. Hatvani, and M. H. Pahl. Flowability studies of bulk materials for design of hopper using a Jenike shear cell. *Powder Handling and Processing*, 14(2):96–101, 2002.
- [40] Subhash C. Thakur, John P. Morrissey, Jin Sun, J. F. Chen, and Jin Y. Ooi. Micromechanical analysis of cohesive granular materials using the discrete element method with an adhesive elasto-plastic contact model. *Granular Matter*, 16(3):383–400, 2014.
- [41] Andrew Phillip Grima and Peter Wilhelm Wypych. Discrete element simulations of granular pile formation: Method for calibrating discrete element models. *Engineering Computations*, 28(3):314–339, 2011.
- [42] N Roussel, C Stefani, and R Leroy. From mini-cone test to abrams cone test: measurement of cement-based materials yield stress using slump tests. *Cement and Concrete Research*, 35(5):817–822, 2005.
- [43] Prabhata K. Swamee and Nitin Aggarwal. Explicit equations for laminar flow of bingham plastic fluids. *Journal of Petroleum Science and Engineering*, 76(3-4):178–184, 2011.
- [44] Nicolas Roussel. The LCPC BOX: a cheap and simple technique for yield stress measurements of SCC. *Mat. Struct.*, 40:1789–1796, 2007.
- [45] J. Spangenberg, N. Roussel, J. H. Hattel, E. Sarmiento, and M. R. Geiker G. Zirculis. Patterns of gravity induced aggregate migration during casting of fluid concretes. *Cem. Concr. Res.*, 42:1571–1578, 2012.
- [46] M. Jabbari and J. Hattel. Bingham-plastic fluid flow model in tape casting of ceramics using two doctor blades—analytical approach. *Mater. Sci. Tech.*, 30:283–288, 2014.
- [47] Jon Spangenberg. Numerical modelling of form filling - with self-compacting concrete. *PHD-Thesis from Danish Technical University of Denmark (DTU)*, 2012.
- [48] Andrew Phillip Grima and Peter Wilhelm Wypych. Development and validation of calibration methods for discrete element modelling. *Granular Matter, Granul. Matter, Granul Matt, Granul Matter*, 13(2):127–132, 2011.
- [49] O. Molerus. Overview: Pneumatic transport of solids. *Powder Technology*, 88(3):309–321, 1996.
- [50] K. TERZAGHI. *THEORETICAL SOIL MECHANICS*. 1944.
- [51] H. P. Zhu, Z. Y. Zhou, R. Y. Yang, and A. B. Yu. Discrete particle simulation of particulate systems: Theoretical developments. *Chemical Engineering Science, Chem. Eng. Sci., Chem Eng Sc, Chem Eng Sci*, 62(13):3378–3396, 2007.
- [52] H. P. Zhu, Z. Y. Zhou, R. Y. Yang, and A. B. Yu. Discrete particle simulation of particulate systems: A review of major applications and findings. *Chemical Engineering Science, Chem. Eng. Sci., Chem Eng Sc, Chem Eng Sci*, 63(23):5728–5770, 2008.

- [53] Alberto Di Renzo and Francesco Paolo Di Maio. Comparison of contact-force models for the simulation of collisions in DEM-based granular flow codes. *Chemical Engineering Science*, 59(3):525–541, February 2004.
- [54] P W Cleary. Industrial particle flow modelling using discrete element method. *Engineering Computations*, 26:698–743, 2009.
- [55] Jens H. Walther and Ivo F. Sbalzarini. Large-scale parallel discrete element simulations of granular flow. *Engineering Computations*, 26(6):688–697, 2009.
- [56] Juan-Pierre Longmore, Patrick Marais, and Michelle M. Kuttel. Towards realistic and interactive sand simulation: A gpu-based framework. *Powder Technology*, 235:983, 2013.
- [57] Nicolin Govender, Daniel N. Wilke, and Schalk Kok. Blaze-demgpu: Modular high performance dem framework for the gpu architecture. *SoftwareX*, 2016.
- [58] Nicolin Govender, Raj K. Rajamani, Schalk Kok, and Daniel N. Wilke. Discrete element simulation of mill charge in 3d using the blaze-dem gpu framework. *Minerals Engineering*, 79:152–168, 2015.
- [59] P. A. Cundall and O. D. L. Strack. A discrete numerical model for granular assemblies. *Geotechnique*, 29(1):47–65, 1979.
- [60] Heinrich Hertz. Über die Berührung fester elastischer Körper. *Journal für die Reine und Angewandte Mathematik*, 1882(92):156–171, 1882.
- [61] Y TSUJI, T TANAKA, and T ISHIDA. Lagrangian numerical-simulation of plug flow of cohesionless particles in a horizontal pipe. *Powder Technology*, 71(3):239–250, 1992.
- [62] D. Zhang and W.J. Whiten. The calculation of contact forces between particles using spring and damping models. *Powder Technology*, 88(1):59 – 64, 1996.
- [63] Guoming Hu, Zhenyu Hu, Bin Jian, Liping Liu, and Hui Wan. On the determination of the damping coefficient of non-linear spring-dashpot system to model hertz contact for simulation by discrete element method. *Proceedings - 2010 Wase International Conference on Information Engineering, Icie 2010*, 3:5571553, 295–298, 2010.
- [64] YC Zhou, BD Wright, RY Yang, BH Xu, and AB Yu. Rolling friction in the dynamic simulation of sandpile formation. *Physica A-statistical Mechanics and Its Applications*, 269(2-4):536–553, 1999.
- [65] Jun Ai, Jian Fei Chen, J. Michael Rotter, and Jin Y. Ooi. Assessment of rolling resistance models in discrete element simulations. *Powder Technology*, 206:269–282, 2011.
- [66] K L Johnson. *Contact Mechanics*. 1985.

- [67] LE Silbert, D Ertas, GS Grest, TC Halsey, D Levine, and SJ Plimpton. Granular flow down an inclined plane: Bagnold scaling and rheology. *Physical Review E*, 64(5):051302, 051302/1–051302/14, 2001.
- [68] L. Rayleigh. On waves propagated along the plane surface of an elastic solid. *Proceedings of the London Mathematical Society, Proceedings of the London Mathematical Society, Proc London Math Soc, P Lond Math, P Lond Math Soc, Proc. Lond. Math. Soc. (3), Proc. London Math. Soc. (3), Proc. London Math. Soc.*, s1-17(1):4–11, 1885.
- [69] Leon M. Keer. Contact mechanics (k. l. johnson). *Siam Review, Siam Rev, Siam Rev Soc Ind Appl Math*, 29(2):332–333, 1987.
- [70] S. Timoshenko. Theory of elasticity. *McGraw-Hill Book Company*, 1951.
- [71] T. Tsuji, Y. Nakagawa, N. Matsumoto, Y. Kadono, T. Takayama, and T. Tanaka. 3-d dem simulation of cohesive soil-pushing behavior by bulldozer blade. *Journal of Terramechanics*, 49(1):37–47, 2012.
- [72] Michele Marigo and Edmund Hugh Stitt. Discrete element method (dem) for industrial applications: Comments on calibration and validation for the modelling of cylindrical pellets. *Kona Powder and Particle Journal*, 32(32):236–252, 2015.
- [73] Wenqi Zhong, Aibing Yu, Xuejiao Liu, Zhenbo Tong, and Hao Zhang. Dem/cfd-dem modelling of non-spherical particulate systems: Theoretical developments and applications. *Powder Technology*, 302:108–152, 2016.
- [74] Oleh Baran, Alfred DeGennaro, Enrique Rame, and Allen Wilkinson. Dem simulation of a schulze ring shear tester. *AIP Conference Proceedings*, 1145:409–412, 2009.
- [75] Tom A. H. Simons, Rouven Weiler, Stefan Strege, Sven Bensmann, Martin Schilling, and Arno Kwade. A ring shear tester as calibration experiment for dem simulations in agitated mixers: a sensitivity study. *Procedia Engineering*, 102:741–748, 2015.
- [76] C. J. Coetzee and D. N. J. Els. Calibration of discrete element parameters and the modelling of silo discharge and bucket filling. *Computers and Electronics in Agriculture*, 65(2):198–212, 2009.
- [77] C. J. Coetzee. Calibration of the discrete element method and the effect of particle shape. *Powder Technology*, 297:50–70, 2016.
- [78] R.N. Cunha, K.G. Santos, R.N. Lima, C.R. Duarte, and M.A.S. Barrozo. Repose angle of monoparticles and binary mixture: An experimental and simulation study. *Powder Technology*, 303:203–211, 2016.
- [79] Alvaro Janda and Jin Y. Ooi. Dem modeling of cone penetration and unconfined compression in cohesive solids. *Powder Technology*, 293:60–68, 2016.
- [80] Mikio Sakai and Seiichi Koshizuka. Large-scale discrete element modeling in pneumatic conveying. *Chemical Engineering Science*, 64(3):533–539, February 2009.

- [81] Mikio Sakai, Hiroyuki Takahashi, Christopher C. Pain, John-Paul Latham, and Jian-sheng Xiang. Study on a large-scale discrete element model for fine particles in a fluidized bed. *Advanced Powder Technology*, 23(5):673–681, September 2012.
- [82] A. Gens and D.M. Potts. Critical state models in computational geomechanics. *International Journal of Rock Mechanics and Mining Sciences and Geomechanics Abstracts*, 26(26):76, 1989.
- [83] H. A. Sheldon, A. C. Barnicoat, and A. Ord. Numerical modelling of faulting and fluid flow in porous rocks: An approach based on critical state soil mechanics. *Journal of Structural Geology*, 28(8):1468–1482, 2006.
- [84] Y Maeda, Y Maruoka, H Makino, and H Nomura. Squeeze molding simulation using the distinct element method considering green sand properties. *Journal of Materials Processing Technology*, 135(2-3):172–178, 2003.
- [85] Nini Pryds, Jesper Thorborg, Marek Lipinski, and Marc Schneider. *Fundamentals of Numerical Modelling of Casting Processes*. Polyteknisk Forlag, 2005.
- [86] Paul W. Cleary and Matthew D. Sinnott. Simulation of particle flows and breakage in crushers using dem: Part 1-compression crushers. *Minerals Engineering*, 74:178–197, 2015.
- [87] W Schubert, M Khanal, and J Tomas. Impact crushing of particle-particle compounds - experiment and simulation. *International Journal of Mineral Processing*, 75(1-2):41–52, 2005.
- [88] Thomas G Mezger. *The Rheology Handbook*. Hannover: Curt R Vincentz Verlag, pages 27–28, 2006.
- [89] Daizo Kunii, Octave Levenspiel, and Howard Brenner. *Fluidization engineering*. Elsevier Science and Technology, 1991.

Appendix A

The green sand composition

A.1 Introduction

In this appendix the green sand are described and the general tests of the green sand without changing the water contents are performed. The tests in this appendices was performed in the master thesis [9] and several parts and figures are taken from the master thesis. The thorough details about how the tests were performed can be found in the guideline [8].

The tests performed are:

- A description of the green sand mixture in section A.2.
- Determination of active bentonite contents in section A.3.
- Total contents of fines in section A.4.
- Size distribution of green sand in section A.5.
- Loss on ignition in section A.6.

A.2 The green sand mixture and general sand properties

The green sand mixture typically contains: 3-4.5 % water, around 5-8 % bentonite, seal coal and other inactive fines around 2.5-4.0 % and the rest is quartz sand around 85-90 % shown in Fig. A.1. The green sand consists of quartz sand as the primary ingredient, mixed with bentonite which together with water coats the quartz sand and it binds the green sand together. This binding of the green sand gives e.g. high green compression strength, high wet tensile strength, stabilize the mould cavity to acquire a strong mould for casting the metal. This makes the green sand very cohesive and strong when the mould is finally squeezed. Before metal is casted in the moulds, the green sand is prepared in a mixer. The quality of the final mould is affected by many factors, including the mixture of the quartz sand, the complexity of the mould chamber geometry and the compressed air pressure driving the flow of the green sand where the final mould must be homogeneous and stable [8, 34, 35]. The recommended properties for the green sand are shown in Fig. A.2.

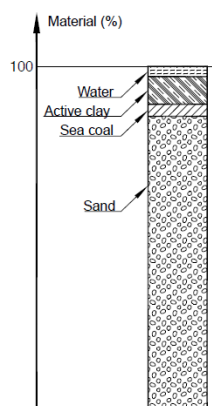


Figure A.1: The green sand mixture. The figure is from [8]


	SAND PROPERTIES FOR DISA VERTICAL MOULDING MACHINES					
	Mould height 400		480 ≤ mould height < 600		600 ≤ mould height < 1050	
Average sand grain size (washed)	0.14-0.28 DIN	AFS 110-60	0.14-0.22 DIN	AFS 110-70	0.14-0.18 DIN	AFS 110-80
Grain size distribution	3-4 sieves for 90% grains					
Green compression strength	16-21 N/cm ²	23-30 psi	19-23 N/cm ²	27-33 psi	22-25 N/cm ²	31-36 psi
Green tensile strength	>2 N/cm ²	>2.8 psi	> 2.2 N/cm ²	>3.1 psi	>2.5 N/cm ²	> 3.5 psi
Spalling strength	>3 N/cm ²	>4.3 psi	> 3.3 N/cm ²	>4.7 psi	>3.8 N/cm ²	>5.4 psi
Wet tensile strength	>0.20 N/cm ²	>0.3 psi	>0.22 N/cm ²	>0.32 psi	>0.25 N/cm ²	>0.35 psi
Permeability	≥60					
Compactability	40% ± 2%					
Moisture content	Adjusted until a compactability of 40% ± 2% is obtained					
Active clay content (MB)	>7%			>8%		
AFS clay content	2.5 to 4% higher than active clay					
Loss on ignition	3.5 to 5%			3.5 to 7.5%		
Temperature	≤ 40°C (≤ 104°F)					

Figure A.2: The recommended properties for the green sand when applied in the DISAMATIC process. The figure is from [8].

A.3 Determination of active bentonite contents

This test aims to find the active bentonite contents in % contained in the green sand which was applied in this project. Here the results of the methylene blue test will be briefly presented and some parts are copied from [9, 8]. This experiment is made by the use of methylene blue solution and the active clay capacity to absorb the blue methylene solution. The methylene blue solution is added at a rate of 2 ml each time to the green sand in the reagent flask mixer shown in Fig. A.3(a). Afterwards a drop from the flask is put on the paper and the colour is observed shown in Fig. A.3(b-d). When the colour on

the paper changes from a blue circle to a blue circle which has a bluish-green halo then the saturation starts to occur in Fig. A.3(b) blue drop number 17.

Now when the halo appears for the first time the procedure is followed from the guidelines in [8]:

”Stir for another two min. without adding further methylene-blue, and check to see if the bluish-green halo disappears. If the bluish-green halo disappears, add another 1 ml of methylene-blue and stir for two minutes. Then place a drop on the filter paper. Continue this process until the bluish-green halo around the dark blue spot reappears. The final stage has now been reached, and a calibration curve for the clay sample in question can be drawn up”.

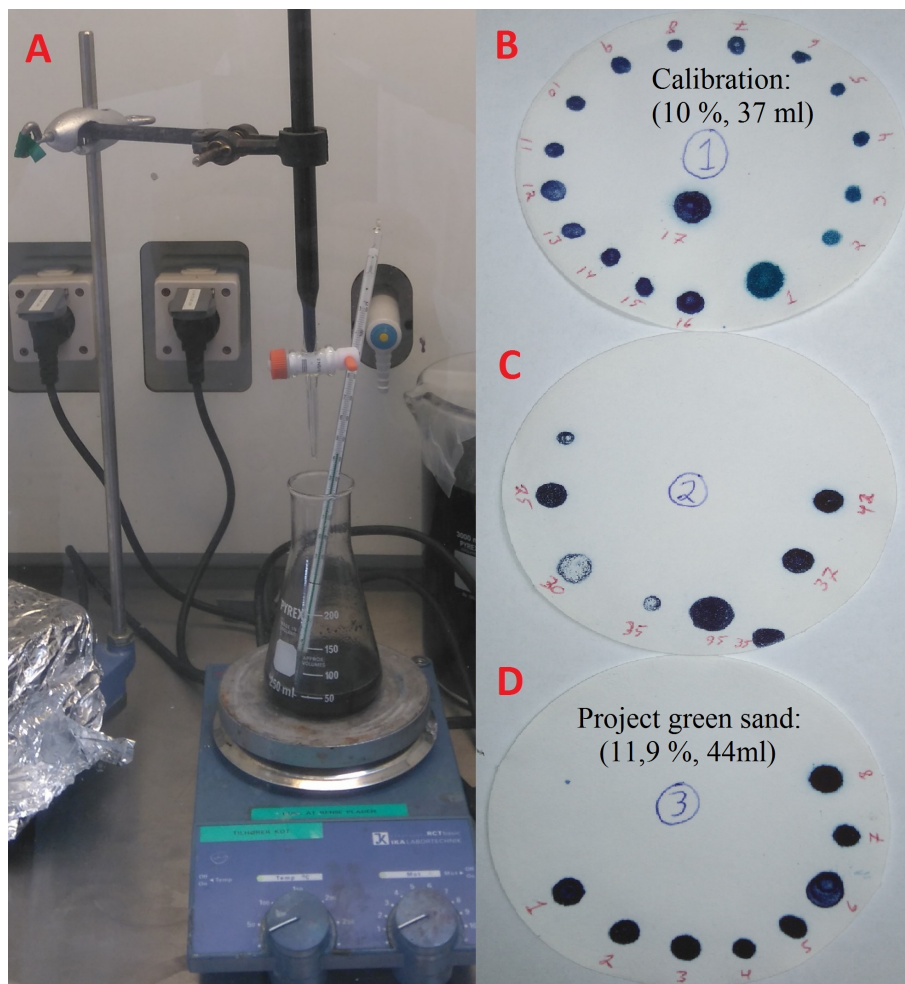


Figure A.3: (A) Setup for methylene blue test and the reagent flask mixer. (B-D) results from the filter papers. The figure is from [9]

The amount of methylene blue solution added is monitored and a point of the curve can be found. First the determination of the calibration curve takes place for a sand/clay mixture containing 10 % of bentonite to find the base point on the curve (10 %, y [ml]). The result of sand/clay mixture containing 10 % of bentonite was 37 ml methylene blue solution, giving the first point on the curve (10 %, 37 ml) shown in A.3(B). The calibration curve can now be plotted as a line starting at point of origin (0 %, 0 ml) and going through the calibration point (10 %, 37 ml). The second saturation point is from the green sand used in the project, this saturation point was at (x %, 44 ml) shown in A.3(D). From the calibration curves linear relationship of the added blue methyl solution gives:

- **The contents of active bentonite in the green sand used in this project was around 11.9 %.**

Where the recommended contents of active bentonite measured by the Methylene Blue test is suggested to be around 7 %-8 % in [8].

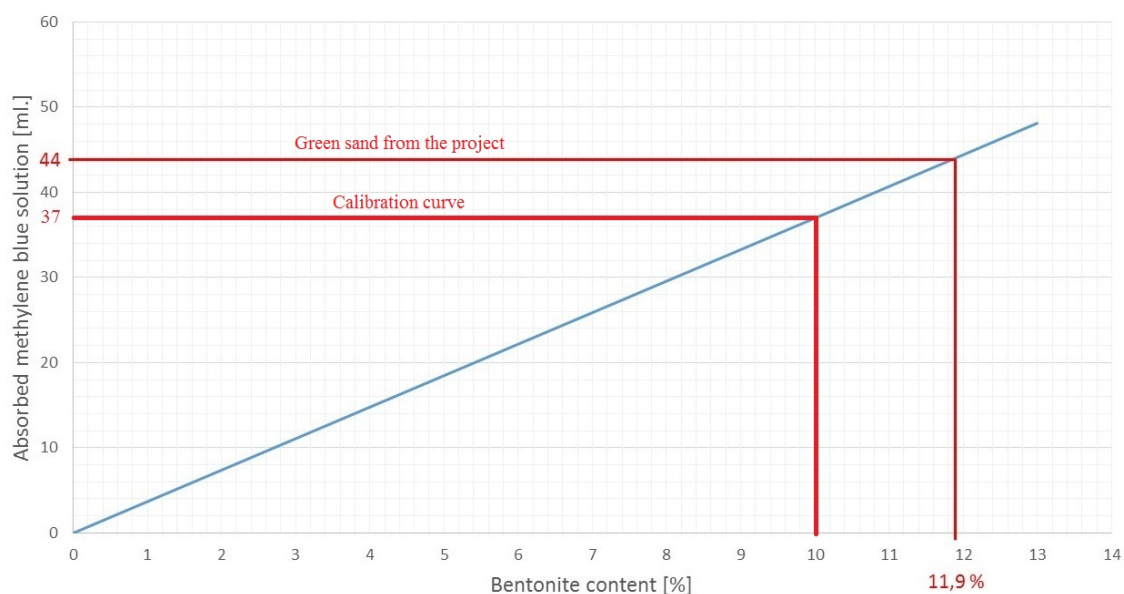


Figure A.4: Calibration curve for methylene blue test with active bentonite contents of 11.9 %. The figure is from [9]

A.4 Total contents of fines

The DISA manual states ([8]) that all contents smaller than 0.02 mm is identified as fine material. In this experiment all fine material is washed away from the sand. The total contents of fines are made up of the inactive fines together with the active bentonite found in section A.3.

This experiment was run as stated in [8] with the wet screen method with the application of two batches. The two batches are started with 50 gr and after the washing the weight was 44 gr. thereby the fraction of fine contents was 12%. Note that the accuracy of this test is only ± 0.5 gr. ($\pm 1\%$). The two green sand samples were then combined and used in the following sieve analysis A.5. The active bentonite test in section A.3 was close to 12% it is likely that the inactive fines constitute less than 1.0% of the green sand, while the DISA manual recommends a 2.5 - 4.0 % of inactive fines.

A.5 Particle size distribution with a sieve analysis

The sieve analysis test is made to determine the average grain size and the distribution of the sand and the test was originally conducted in [9]. The weight of sand specimen used was roughly 88 g for more details of the value for each sieve, see in the table. A.1 and the explanation of the columns in table A.5.

- Col. 1, shows sieve sizes (shown in DIN standard).
- Col. 2, the weighing results of each fraction in grams.
- Col. 3, percentage of each individual fraction calculated in relation to the total weight.
- Col. 4, cumulative percentage of each fraction when the weight is considered as 100%.
- Col. 5, conversion factors which are inversely proportional with the mesh size of the preceding sieve.
- Col. 6, product of figures from column 3 and column 5. Explained in [8]

Now the average grain size can be calculated by using formula (A.1).

$$AGS = \frac{100}{Sum_{Prod.}} \quad (A.1)$$

Where $Sum_{Prod.} = 496.40$ is the total from col. 6. in table. A.1 and AGS is the average grain size of 0.20 mm, note the average grains size is in this case good. This is important since the probability of metal penetration between sand grains increases with increasing average grain size especially as the ferrostatic pressure height increases [8].

A Graphical representation of the sieve analysis is illustrated in figure A.5 which shows that the green sand is distributes between 4 - 5 sieves, while [8] recommends distribution between 3 - 4 sieves for a good dense packing of the green sand.

To determine the sand distribution, calculation of uniformity was made by using the

Col. 1	Col. 2	Col. 3	Col. 4	Col. 5	Col. 6
Sieve [mm]	[g]	Individual %	Cumulative %	Factor	-
2.00	0.00	0.00	100.00	0.40	0.00
1.40	0.00	0.00	100.00	0.50	0.00
1.00	0.09	0.10	99.90	0.70	0.07
0.71	0.11	0.13	99.77	1.00	0.13
0.50	0.52	0.60	99.17	1.40	0.84
0.36	4.27	4.89	94.28	2.00	9.78
0.25	19.01	21.78	72.50	2.80	60.98
0.18	30.01	34.38	38.12	4.00	137.53
0.13	20.22	23.17	14.95	5.70	132.05
0.09	7.44	8.52	6.43	8.00	68.19
0.06	2.98	3.41	3.01	11.40	38.92
0.00	2.63	3.01	0.00	15.90	47.91
Total	87.283	100	-	-	496.40

Table A.1: Results from the sieve analysis.

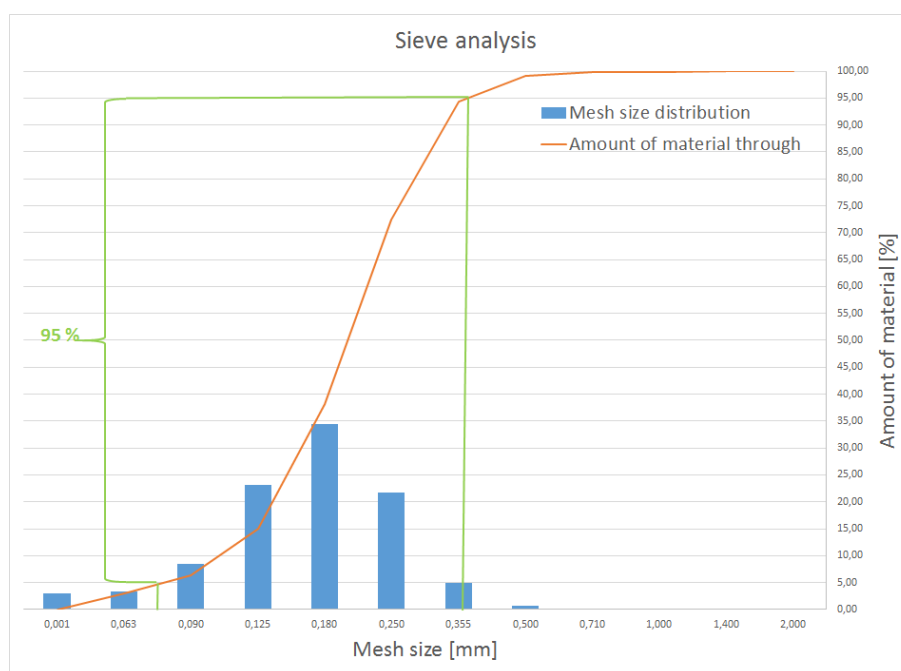


Figure A.5: Figure showing graphical representation of the sieve analysis. The figure is from [9].

average grain size (AGS), and the purpose is to eliminate the coarsest material ($1.33 * \text{AGS}$), and the finest material ($0.67 * \text{AGS}$), on the cumulative distribution curve. Calcula-

lation reveal that the coarsest material is over 0.268 mm and the finest material is under 0.135 mm.

A.5.1 Summarized results of the tests performed until now

Parameters are summarized in Table A.2.

Weight of specimen	100.1 gr.
Weight of specimen after wash	87.28 gr.
Weight of fines	12.82 gr.
Fine contents	12.80 %
Calculation of average grain size	0.20 mm
Estimated uniformity	60

Table A.2: Input and output parameters from sieve analysis.

The DISA application manual ([8]) states that uniformity of molding sand should be kept at 60 - 80 and therefore it can be stated that the sand is close to having a low uniformity.

A.6 Loss on ignition test

The loss of ignition test determines the amount of combustible materials in the green sand, this includes carbonaceous materials, residual core binders and crystallized water. The testing procedure used can be seen in the [8]. Originally there were 4 specimen tests made, two from the buckets taken from the experiments in Borup (sample nr. 1 and nr. 2) and two from the big silo bags in DTU foundry (sample nr.3 and nr.4), this was done to see if the same results would be found in both cases and if the two samples can be treated as same. Unfortunately one of the samples from DTU got destroyed as the crucible used could not withstand the heat and broke (sample 4). The sand at DTU was taken earlier in time from the Borup foundry and was used for earlier experiments. The specimens were numbered from 1 - 4 and inserted into the furnace, starting with nr. 2 and 3, and then 1 and 4. Samples are shown in clockwise order in figure A.6 starting with sample 1 bottom left.

The loss on ignition is calculated the following way

$$W_2 = 20g + W_1 \quad (\text{A.2})$$

Where the weight of crucible is W_1 and the weight of sample after ignition is W_3 and the percentage is calculated

$$\text{Loss on ignition in \%} = (W_2 - W_3) \times 5 \quad (\text{A.3})$$

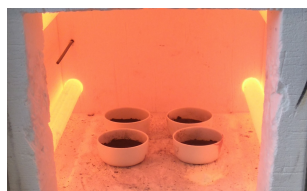


Figure A.6: Showing the setup of crucibles inside the furnace.

Sample	1 (Borup)	2 (Borup)	3 (DTU)	4 (DTU)
Weight of crucible (w1)	37.588	37.200	37.765	37.541
Weight of crucible after heating (w2)	36.674	36.283	36.861	Broken
Loss of weight (w)	0.914	0.917	0.904	Broken
Loss of ignition	4.57 %	4.58 %	4.52 %	Broken

Table A.3: The results from the loss of ignition experiment.

Results from the experiment can be seen in table A.3. The loss on ignition in the sample is 4.58 % while the DISA manual states that loss on ignition should be kept between 3.5 and 5.0 %, depending on production program.

A.7 Results and conclusion

Test of the total contents of fines, particle size distribution and bentonite contents on the green sand used in this PhD project were done in [9] and further information can be found in this manual [8] about green sand test, green sand mixture, green sand properties, settings of the DISAMATIC etc.

Experiment on sand	Results	Range by Disa
Total fines contents	less then 1,0 %	2,5 - 4,0
Average grain size	0,20 mm	0,14 - 0,28 mm
Uniformity of sand	60	60 - 80
Active clay contents	11,9 %	over 7 %
Loss of ignition	4,58 %	3,5 - 5,0 %

Table A.4: Results from sand experiments

Appendix B

Anton Paar Powder Cell tests of the green sand

B.1 Introduction

The Anton Paar Powder cell is constructed for investigating **(IIIa)** fluidized flows as compared to the ring shear tester that is constructed for **(I)** high load flow region transition to low load flow region occurring in e.g. silo design. The Anton Paar Powder Cell is a rheometer combined with a fluidized bed and the Anton Paar machine is shown in Fig. B.1. This machine is an appropriate choice for investigating the more freely flowing fluidized green sand that occurs in the DISAMATIC chamber during the sand shot. The more freely flowing fluidized green sand occurs at the top of the sand pile and when the green sand sand is sloshed up the chamber sides and for the flow in the top of the sand pile during the sand shot.

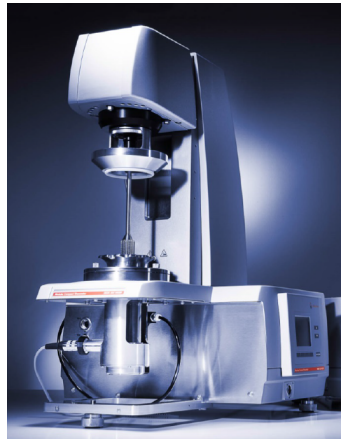


Figure B.1: The Anton Paar machine.

The fluidized rheological properties were investigated in [6] with the focus on charac-

terizing the flow properties of green sand with respect to viscosity. The characterization is carried out with a state-of-the-art device that allows for viscosity measurements while an air stream is forced through the granular material.

For further information about the Anton Paar Powder cell see www.anton-paar.com.

B.2 The experiment

All measurements were carried out on a MCR 502 (Anton Paar, Ostfildern, Germany) rheometer with the powder cell seen in Fig. B.2 (middle), in a profiled cylinder according to standard liquid rheological tests (DIN 53019 , and ISO 3219) [88, 6].

A pressure drop test and a rheology test (viscosity as a function of the shear- and flow rate) were performed and are illustrated in Fig. B.2 (right). In the pressure drop test, the device increases the rate of the air flow that is introduced from vents below the sample and detects the volumetric flow rates that causes a pressure drop in the cell. The drop indicates the minimum volumetric flow that is needed to fully fluidize the sample, i.e. every particle is surrounded by air and a homogeneous powder bed is created. This test was carried out with a sample volume of 80 mL (104.4 gr). Note that general fluidization theory together with simple fluidized bed tests are explained in appendix C.

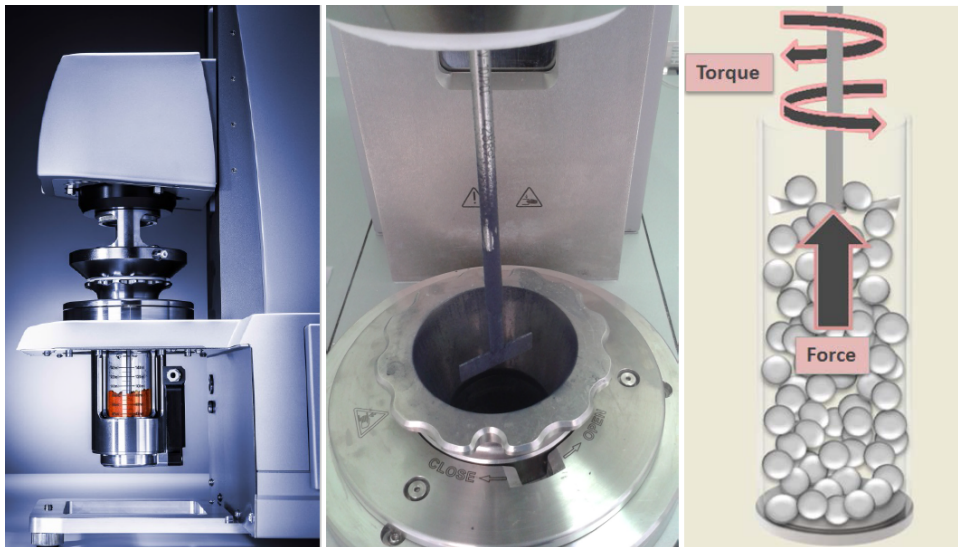


Figure B.2: (Left) The Anton Paar machine seen from the side. (Middle) The cell where the propeller is positioned (this figure is edited from [6]).(Right) Illustration of the principle of the AP powder cell.

In the rheology test, the air flow was kept fixed at different rates while the rotating velocity of the stirring blade was increased. At the same time, the torque was continuously measured in order to back-out the apparent viscosity. This test was carried out with a

sample volume of 90 mL (114 gr) and before every measurement the sample was fully fluidized in a sample preparation step.

B.3 Results

In [6] first the standard fluidized bed test is shown in Fig. B.3 where the full fluidization is found at the air flow rate around $10 \frac{L}{s}$ together with the incipient flow found at the air flow rate around $5.0 \frac{L}{s}$. The full fluidization was investigated further in appendix C with respect to different compactabilities and different amount of green sand added in the fluidized bed.

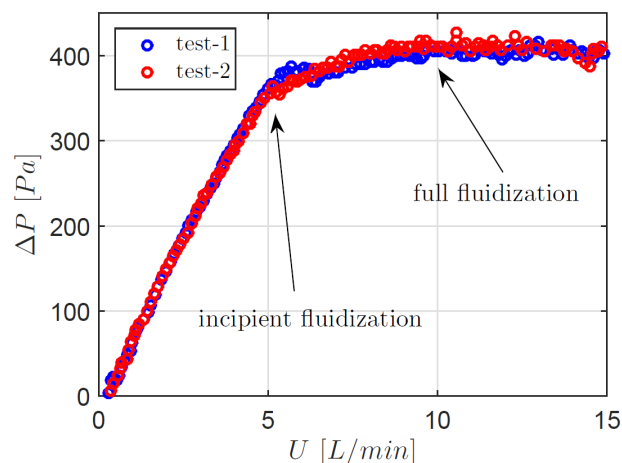


Figure B.3: Pressure drop measurement over the green sand. The figure is from [6].

In Fig. B.4 it can be seen that the viscosity decreases as the flow rate increases. Shear thinning behaviour occurs especially when the air flow rate is above $2 \frac{L}{s}$. For the air flow rate of $0 \frac{L}{s}$ and $2 \frac{L}{s}$ shear thinning behaviour start to occur from the shear rate of $10^{-1} \frac{1}{s}$. In fig. B.5 for the black lines it can be seen that the viscosity decreases as the flow rate increases for the same rotation speeds. Thereby shear thinning also occurs as a function of the air flow rate.

In Fig. B.6 the shear rate as a function of the shear stress, the shear stress decreases as the air flow rate increases. If the shear stress is interpolated back to zero the material will have a yield stress threshold which was also found with the ring shear tester.

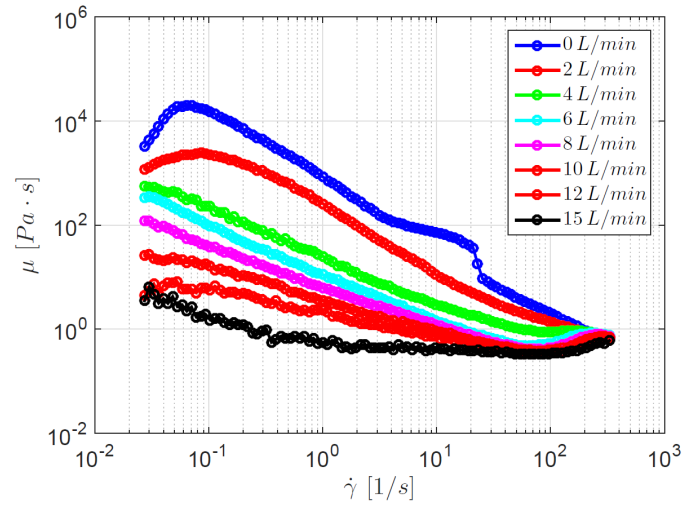


Figure B.4: Shear dependent behavior of green sand at different flow rates (viscosity vs. shear rate). The figure and text are from [6].

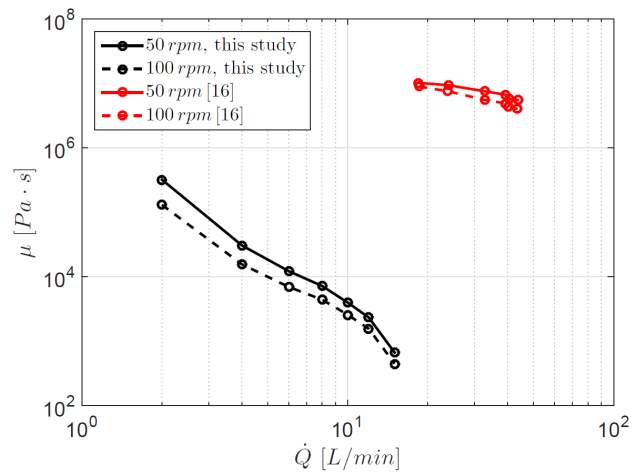


Figure B.5: Shear stress vs. shear rate relationship for green sand at different flow rates. The figure and text are from [6].

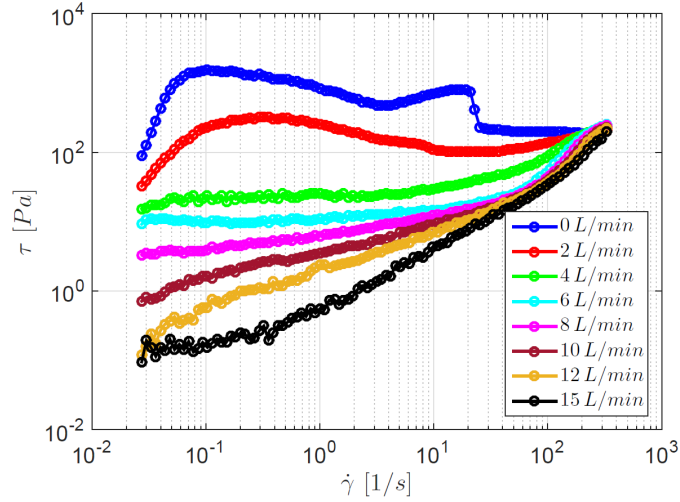


Figure B.6: The shear stress as a function of the shear rate. The figure is from [6].

B.4 Conclusion

The conclusions of Anton Paar powder cell experiments from [6] are;

- The green sand flow behaves like a shear thinning fluid, in which the viscosity is reduced by increasing the shear rate.
- The viscosity of the green sand also behaves like a shear thinning fluid when the air flow rate is increased.
- A yield limit in the shear stress-shear rate curve for the green sand can be found and this yield point decreases with increasing flow rate. This yield stress point can also be found with the ring shear tester and this was done in chapter 2.
- These information can be used as a tabular data or apply function fitting for conducting continuum based CFD simulations together with the values from the ring shear tests of the yield limit and density as function of normal stress. A Herschel-Buckley model could be a good choice although other models exist as the 2-phase continuum model such as [26, 27].
- The Anton Paar test could also be interesting to applied for calibrating the discrete element method especially the parameters as e.g. the young modulus, the coefficient of restitution, the rolling resistance and the cohesion for investigating the energy dissipation of the model and obviously the drag force also. The smaller size of the Anton Paar Powder Cell gives it better possibility for simulating the correct particle size with a DEM model compared to the typically larger fluidized beds and which makes larger parameter sweeps possible.

Appendix C

Fluidized bed tests of the green sand

C.1 Introduction to fluidization

The fluidization properties are investigated with a fluidized bed at Department of Chemical and Biochemical Engineering Technical University of Denmark with the following guidelines from [16]. The minimum fluidizing velocity and the bed pressure drop over the fluidized green sand are determined. The reason for this fluidization investigation is that the air flow from the air tank drives the green sand from the hopper down into the chamber in the DISAMATIC process. Fluidization properties are also of particular importance for the DISAMATIC process when the green sand is transported and fluidized by the air flow in the chamber shown in Fig. C.1. Thereby fluidization properties of green sand are important for the DISAMATIC process overall.

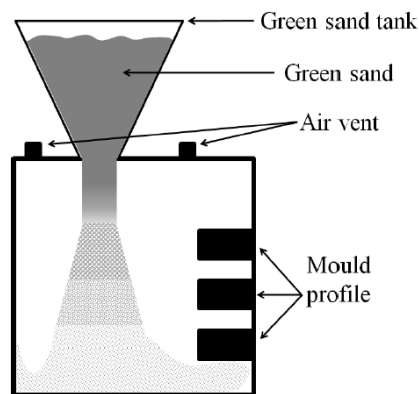


Figure C.1: Schematic illustration of green sand moulding from [6].

C.1.1 The fluidization equipment

The fluidized bed is shown in fig. C.2 consists of two cylindrical sections made of QVF glass with the diameter of $d_{bed} = 100mm$ in the bottom and the diameter of the freeboard which is the top cylinder $d_{freeboard} = 150mm$ respectively and each having a 500 mm length. The bed (bottom cylinder) is connected with the freeboard (top cylinder) by a conical expansion in stainless steel placed in the middle.

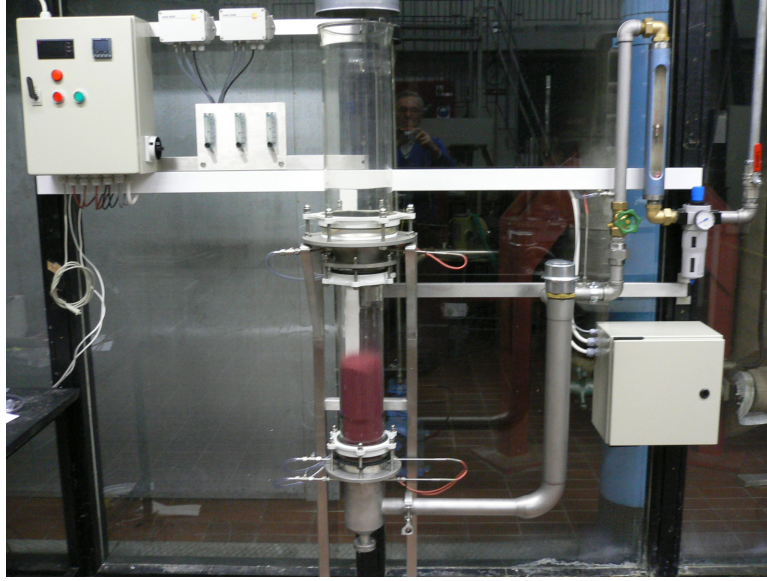


Figure C.2: The fluidized bed setup. The figure is from [16].

The air is released from the windbox placed in the bottom of the bed and subsequently the differential pressure Δp across the bed is recorded.

C.2 Fluidization theory

The following terms are investigated with respect to the gas fluidization of the particles:

- Superficial velocity: Gas velocity V_s in $[m/s]$ (actual temperature and average pressure) in the bed calculated as if no particles are present. The fluidizing velocity V_s with unit of $[\frac{m}{s}]$ in the middle of the bed is,

$$V_s = \frac{W}{3600A\rho_g} \quad (C.1)$$

where W is the mass per time of the inlet gas in kg/h and A is the bed area in m^2 .

- The density of air ρ_g is calculated as,

$$\rho_g = \frac{353 \left(1 + \frac{\Delta P_{Bed}}{2}\right)}{T_{Bed} + 273C^\circ} \quad (C.2)$$

where T_{Bed} is the bed temperature in degrees Celsius [C°], ρ_g is the gas density in [kg/m^3] and ΔP_{Bed} is the bed pressure drop in [bar]. Note the formula assumes that the outlet of the bed is at atmospheric pressure.

- The minimum velocity, V_{mf} : The fluidizing velocity in a bed at the onset of fluidization where the static bed starts to get fluidized. The onset of fluidization occurs when the drag force of the gas moving upwards equals the weight of the particles, i.e.

$$\Delta P_{mf} = H_{mf} (1 - \epsilon_{mf}) (\rho_p - \rho_g) g \quad (C.3)$$

where ΔP_{mf} is the pressure drop across the bed height H_{mf} , ϵ is the voidage, g is the gravity, ρ is the density and index "mf" relates to minimum fluidization, ρ_p is the particle density and ρ_g is the gas density.

- A simplified fluidization curve can be seen in fig. C.3 illustrating the value of minimum fluidization and the two linear regions and further discussion of the fluidization curve can be found in the book [89]. The minimum fluidization pressure loss should in theory be equal the pressure of the sand over the fluidized bed area $P_{sand} = \frac{mg}{A}$.

$$\Delta P_{mf} \approx P_{sand} = \frac{mg}{A} \quad (C.4)$$

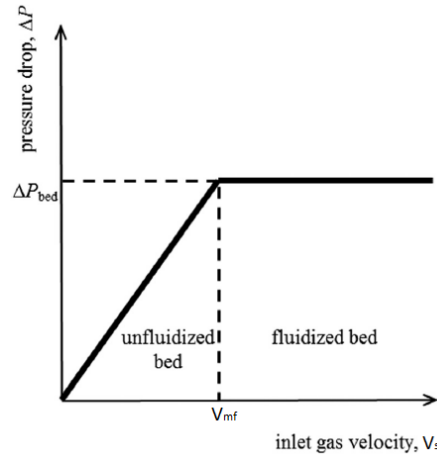


Figure C.3: A simple presentation of the relationship between the pressure drop and the inlet gas velocity. The relationship can roughly be estimated by two lines, with the first part being the linear interpolation of the increase in pressure and second part of the fluidization curve being the constant pressure ($\Delta P = \Delta P_{mf}$) as a straight line part occurring after the minimum fluidization (V_{mf}). The edited figure is originally from [17].

C.2.1 Algorithm for detecting minimum fluidization velocity (v_{mf}) and the constant pressure drop (ΔP_{mf}).

An algorithm is designed to find the two linear regions shown in fig. C.3. The constant pressure drop (ΔP_{mf}) can be found above the minimum fluidization velocity (v_{mf}) which was determined by the pressure drop found from the average of the last 10 experimental points with the largest air velocities occurring in the tests. The slope of the fluidization curve is approximately linear in this region.

The minimum fluidization velocity (v_{mf}) is found when the pressure exceeds the "constant" pressure drop ΔP_{mf} . Then two simple linear interpolations are made connecting the two lines for each individual test. Where the constant pressure region is a constant line ($v_{mf} \leq v$) and this is connected with the slope calculated by the point under the minimum velocity ($v < v_{mf}$) with the constraint that the slope should end in $(x, y) = (v_{mf}, \Delta P_{mf})$ for attaining a continuous function.

C.3 Results of the experiment

Fluidization experiments are made for 7 different green sand batches with different water contents added and thereby also different compactability levels were attained.

The first 1-6 fluidized bed experiments were done with 1 kg of green sand where the minimum fluidization velocity (v_{mf}) is found. The number 7 fluidized bed experiment found the minimum fluidization for 4 different amount of green sand added to the fluidized bed from 0.5 kg to 1.25 kg with an interval of 0.25 kg.

The green sand characteristics for the 7 fluidized bed experiments can be seen in table. C.1.

Table C.1: The green sand is tested for 7 individual fluidized bed experiments where 7 samples are made for determining the characteristic of the corresponding fluidized bed experiments. For each sample the compactability and density is repeated 5 times and for the water contents 3 times. Fluidized bed experiment number 7 is where the weight is changed in the bed. Note that $\pm std$ means the interval of plus to minus of the standard deviation.

Sample	Compactability (%)	Water contents (%)	Green sand density [$\frac{kg}{m^3}$]	Sieved
1	Dry sand	2.97 ± 0.06	$119 \times 10 \pm 19.3$	No
2	32 ± 0.8	3.17 ± 0.23	934 ± 8.36	Yes
3	34 ± 0.6	3.29 ± 0.34	920 ± 11.0	Yes
4	37 ± 0.4	3.52 ± 0.41	870 ± 5.45	Yes
5	43 ± 0.9	3.69 ± 0.24	793 ± 10.4	Yes
6	44 ± 0.7	3.63 ± 0.05	784 ± 6.42	Yes
7	38 ± 0.3	3.30 ± 0.11	908 ± 9.01	Yes

C.3.1 Experiment 1-6

The fluidization curves for the fluidized bed 1-6 experiments can be seen in fig. C.4, fig. C.5 and fig. C.6. The minimum fluidization velocity is detected when the pressure drop in the experiments (points) exceeds an average pressure drop determined by the constant pressure drop. The results of the minimum fluidization velocities, initial slope of the fluidization curves and constant pressure drop values are listed in table. C.2.

The minimum fluidization increases with the water contents and the pressure drops are similar for the experiment 1 up to experiment 6 as expected. In the start of the fluidization experiment a high pressure drop is seen for a low air velocity seen in fig. C.6 at the left top corner. This is due to rat-holes (channelling of the air) which are created through the green sand in the bed afterwards a normal fluidization curve is created. The minimum fluidization for the high water contents is detected after the rat-holes occurred and the green sand was fluidized properly, this could properly have been due to a lower water content. Fluidization of cohesive material is illustrated later in Fig. C.8(left).

Table C.2: The green sand is tested for 7 individual fluidized bed experiments. Fluidized bed experiment number 7 is where the weight is changed in the bed. Note that $\pm std$ means the interval of plus to minus of the standard deviation around the average value of the three experiments (except experiment 7).

Experiments	$v_{mf} [\frac{m}{s}]$	$\Delta P_{mf} [Pa]$	Slope $\frac{\Delta P}{V_s}$	Compactability (%)
1	0.30 ± 0.08	944 ± 6.62	$931 \times 10^{-3} \pm 161 \times 10^{-3}$	Dry sand
2	0.38 ± 0.05	$107 \times 10 \pm 132$	$829 \times 10^{-3} \pm 265 \times 10^{-3}$	32 ± 0.8
3	0.39 ± 0.05	$101 \times 10 \pm 2.27$	$710 \times 10^{-3} \pm 265 \times 10^{-3}$	34 ± 0.6
4	0.42 ± 0.11	$106 \times 10 \pm 140$	$893 \times 10^{-3} \pm 261 \times 10^{-3}$	37 ± 0.4
5	0.61 ± 0.11	$103 \times 10 \pm 8.45$	$123 \times 10^{-2} \pm 275 \times 10^{-3}$	43 ± 0.9
6	0.66 ± 0.19	$103 \times 10 \pm 16.4$	$965 \times 10^{-3} \pm 260 \times 10^{-3}$	44 ± 0.7
7	0.55 ± 0.12	table C.3	$640 \times 10^{-3} \pm 221 \times 10^{-3}$	38 ± 0.3

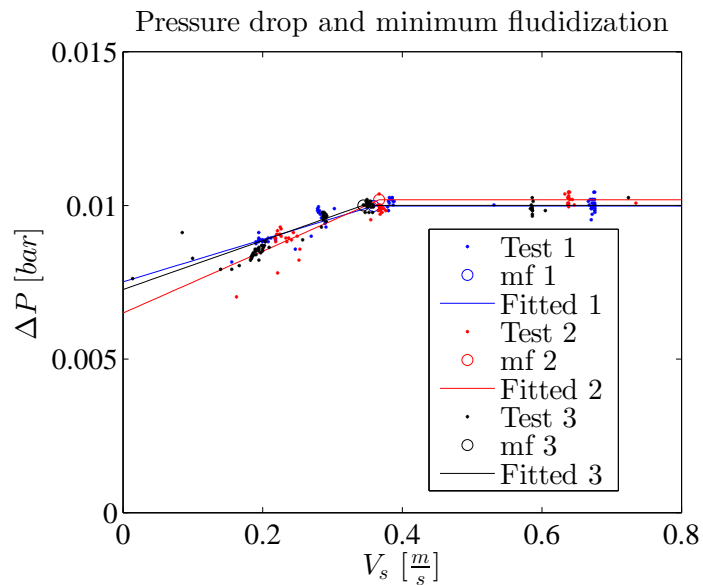
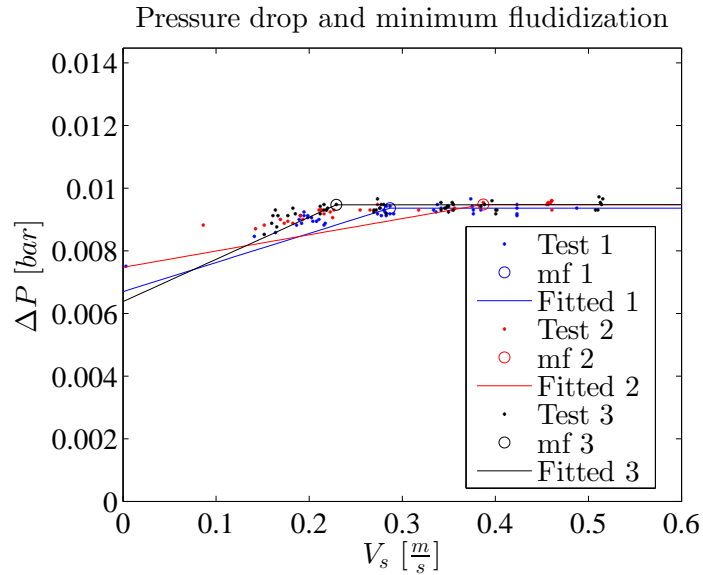


Figure C.4: Low water contents: The minimum fluidization is found for (a) experiment 1 and (b) experiment 2 in the fluidized bed experiment. Each experiment was repeated 3 times with the colors blue, red and black for test 1 to test 3 subsequently. The points are the experiments, the line is a linear interpolation and the circle is the minimum fluidization point. Note the scaling on the x-axis is different from (a) experiment 1 to (b) experiment 2.

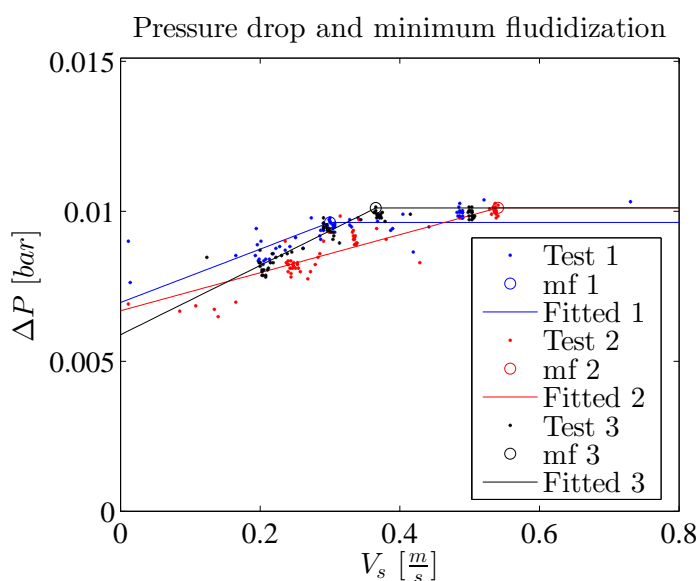
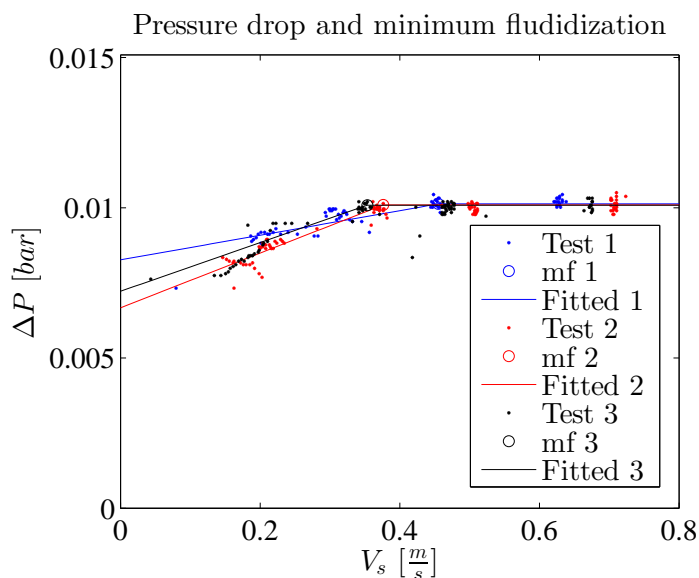


Figure C.5: Medium water contents: The minimum fluidization is found for (a) experiment 3 and (b) experiment 4 for the fluidized bed test. Each experiment was repeated 3 times with the colors blue, red and black for test 1 to test 3 subsequently. The points are the experiments, the line is a linear interpolation and the circle is the minimum fluidization point.

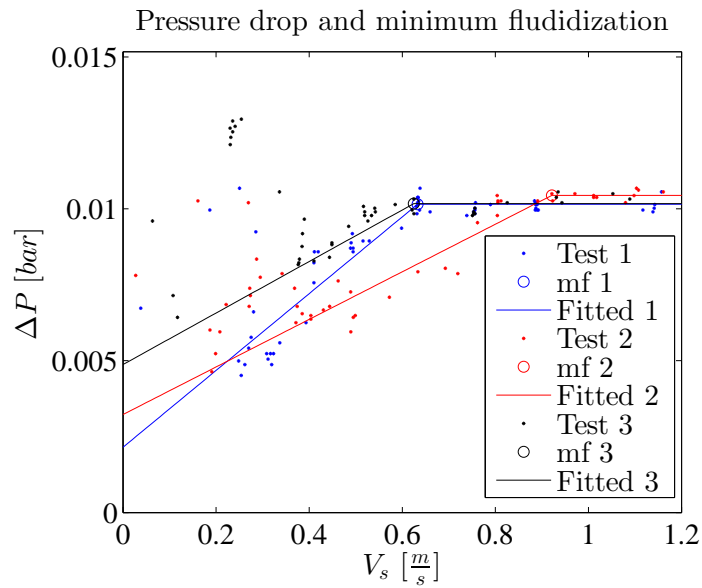
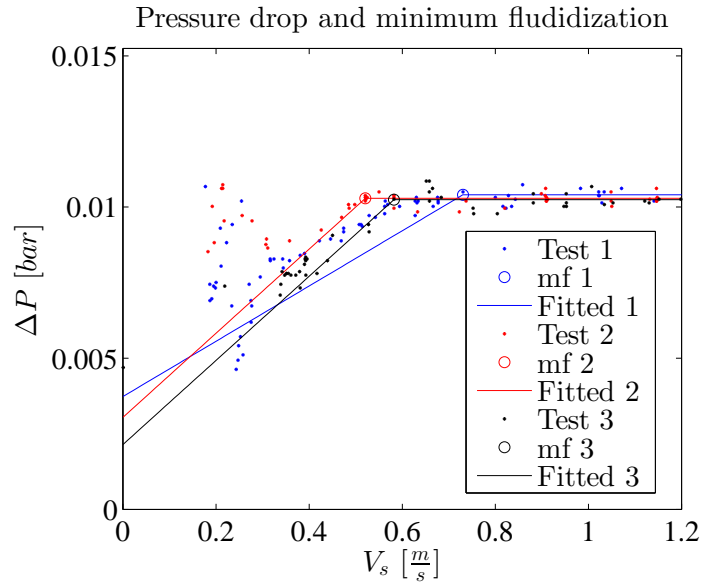


Figure C.6: High water contents: The minimum fluidization is found for (a) experiment 5 and (b) experiment 6 for the fluidized bed. Each experiment was repeated 3 times with the colors blue, red and black for test 1 to test 3 subsequently. The points are the experiments, the line is a linear interpolation and the circle is the minimum fluidization point.

C.3.2 Experiment number 7

The investigated minimum fluidization velocities when the amount of green sand are changed in the fluidized bed is shown in fig. C.7. The pressure drop should be sized

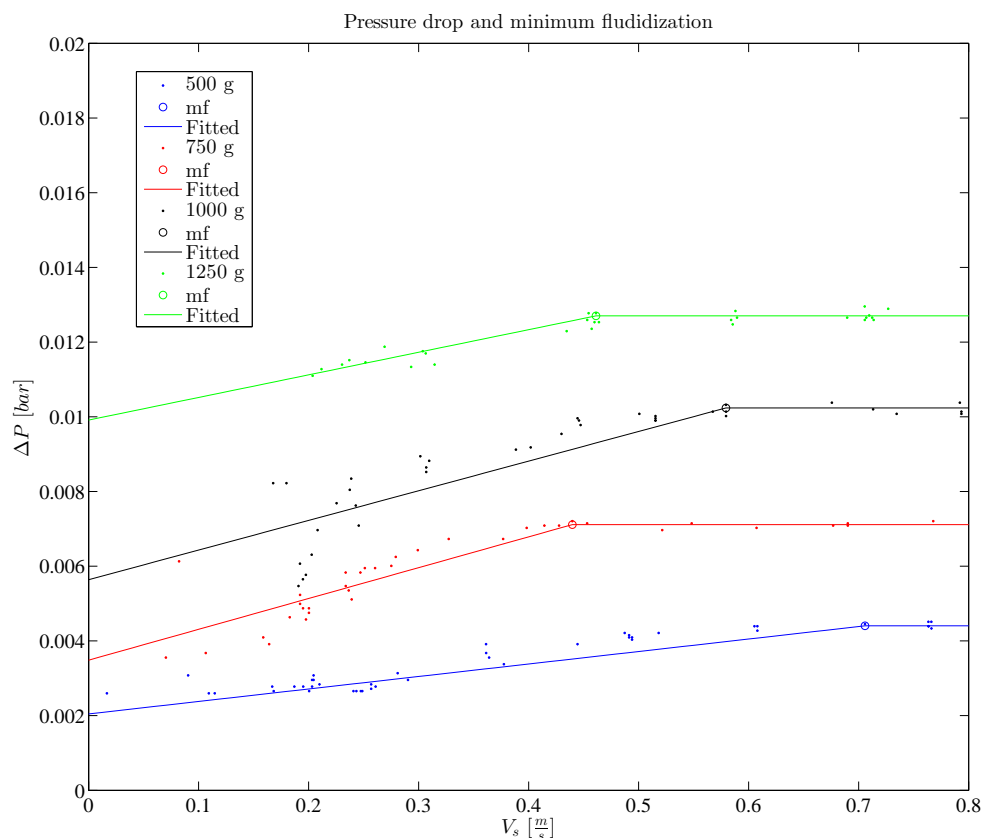


Figure C.7: Experiment 7: For compactability level of 38 % with different weight of 0.50 kg (blue), 0.75 kg (Red), 1.0 kg (Black) and 1.25 kg (Green). The dots are the results from the experiments, the mf is the point of minimum fluidization and the line is the linear interpolation of the first part (increase in pressure) and second part of the fluidization curve (straight part after the minimum fluidization).

according to the amount of green sand added which is shown in table. C.3. The pressure drop relation with respect to the weight fits well when larger amount of green sand are added to the fluidized bed which is around 1 kg as recommended in the guidelines. The pressure from the weight of the sand on the fluidized bed area should in theory be equal to the pressure loss from eq. C.2, but here the pressure loss is smaller and only reaches 80-85 % for test 1-6 and test 7 for 1 kg and 1.25 kg.

Table C.3: The green sand fluidized bed experiment number 7.

Experiment	v_{mf} [$\frac{m}{s}$]	ΔP_{mf} [Pa]	$P_{sand}=mg/A$ [Pa]	$\frac{P_{sand}}{P_{mf}}$	$\frac{P_{mf}}{P_{sand}}$	Slope $\frac{\Delta P}{V_s}$
0.50 kg	0.71	440	623	1.42	0.66	334×10^{-3}
0.75 kg	0.44	711	936	1.32	0.76	825×10^{-3}
1.00 kg	0.60	102×10	125×10	1.23	0.82	794×10^{-3}
1.25 kg	0.46	127×10	156×10	1.23	0.82	605×10^{-3}

C.4 Conclusion

The overall trend is that the minimum fluidization velocity increases with the water contents since the sand surface area decreases due to the binding of the individual green sand grains into particle clumps that also are heavier. This is illustrated in Fig. C.8.

This suggested that green sand with a compactability level of around 43-44 % is harder to fluidized and properly it is also harder to transport and fill the narrow passages with green sand in the mold geometry during the sand shot.

For low to medium water contents green sand from experiment 2, experiment 3, experiment 4 and experiment 7 the minimum fluidization lies mostly in the interval of around $0.35\text{-}0.45 \frac{m}{s}$.

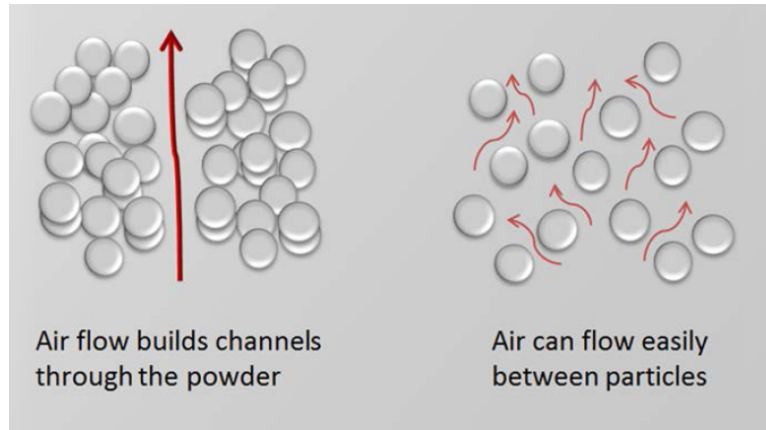


Figure C.8: Cohesive particles fluidization (left) versus non-cohesive particles fluidization (right). The figure is from www.anton-paar.com.

For experiment 7 with medium water content and compactability it can be more loosely suggested that the minimum fluidization for all the tests 0.50 kg-1.25 kg has the minimum fluidization velocity from $0.44\text{-}0.50 \frac{m}{s}$. Since the algorithm needs the pressure to be

equal or larger to the constant pressure drop for the large air velocities when detecting the minimum fluidization velocity, this could potentially predict the the minimum fluidization velocity to large.

When different amount of green sand are added in the fluidized bed the pressure drop behaves as expected at least when an minimum amount of green sand are applied to the fluidized bed (0.5 kg). The pressure from the weight of the sand on the fluidized bed area should in theory be equal to the pressure loss from eq. C.2, but here the pressure loss is smaller and only reaches 80-85 % for test 1-6 and test 7 for 1 kg and 1.25 kg. This could be due to the green sand is still hitting the bottom of the bed or gets stuck to the side wall.



Flow Dynamics of green sand in the DISAMATIC moulding process using Discrete element method (DEM)

Hovad, Emil; Larsen, P.; Walther, Jens Honore; Thorborg, Jesper; Hattel, Jesper Henri

Published in:

I O P Conference Series: Materials Science and Engineering

DOI:

[10.1088/1757-899X/84/1/012023](https://doi.org/10.1088/1757-899X/84/1/012023)

Publication date:

2015

Document Version

Publisher's PDF, also known as Version of record

[Link to publication](#)

Citation (APA):

Hovad, E., Larsen, P., Walther, J. H., Thorborg, J., & Hattel, J. H. (2015). Flow Dynamics of green sand in the DISAMATIC moulding process using Discrete element method (DEM). I O P Conference Series: Materials Science and Engineering, 84, [012023]. DOI: 10.1088/1757-899X/84/1/012023

General rights

Copyright and moral rights for the publications made accessible in the public portal are retained by the authors and/or other copyright owners and it is a condition of accessing publications that users recognise and abide by the legal requirements associated with these rights.

- Users may download and print one copy of any publication from the public portal for the purpose of private study or research.
- You may not further distribute the material or use it for any profit-making activity or commercial gain
- You may freely distribute the URL identifying the publication in the public portal ?

If you believe that this document breaches copyright please contact us providing details, and we will remove access to the work immediately and investigate your claim.

Flow Dynamics of green sand in the DISAMATIC moulding process using Discrete element method (DEM)

This content has been downloaded from IOPscience. Please scroll down to see the full text.

2015 IOP Conf. Ser.: Mater. Sci. Eng. 84 012023

(<http://iopscience.iop.org/1757-899X/84/1/012023>)

View [the table of contents for this issue](#), or go to the [journal homepage](#) for more

Download details:

IP Address: 192.38.67.115

This content was downloaded on 01/07/2015 at 12:19

Please note that [terms and conditions apply](#).

Flow Dynamics of green sand in the DISAMATIC moulding process using Discrete element method (DEM)

E Hovad^{1,3}, P Larsen³, J H Walther¹, J Thorborg^{1,2} and J H Hattel¹

1 Department of Mechanical Engineering, Technical University of Denmark (DTU)

2 MAGMA Giessereitechnologie GmbH, Kackertstr. 11, 52072 Aachen, Germany

3 DISA Industries A/S, Højager 8, 2630 Taastrup, Denmark

E-mail: emilh@mek.dtu.dk

Abstract. The DISAMATIC casting process production of sand moulds is simulated with DEM (discrete element method). The main purpose is to simulate the dynamics of the flow of green sand, during the production of the sand mould with DEM. The sand shot is simulated, which is the first stage of the DISAMATIC casting process. Depending on the actual casting geometry the mould can be geometrically quite complex involving e.g. shadowing effects and this is directly reflected in the sand flow during the moulding process. In the present work a mould chamber with “ribs” at the walls is chosen as a baseline geometry to emulate some of these important conditions found in the real moulding process. The sand flow is simulated with the DEM and compared with corresponding video footages from the interior of the chamber during the moulding process. The effect of the rolling resistance and the static friction coefficient is analysed and discussed in relation to the experimental findings.

1. Introduction

The DISAMATIC process is extensively used in casting of metal parts for the automotive industry for making breaking disks, crank shafts, engine blocks etc. In order to ensure a high quality of the components, it is important to control the manufacturing process of the mould, so that it is homogeneous and stable. A short explanation of the DISAMATIC process for manufacturing of the mould, is given in [1]. The following figure 1, is an illustration of the sand shot in the mould chamber. The flow dynamics of the sand shot inside the mould chamber is investigated with DEM and compared to the video footage, capturing the flow dynamics in the real mould chamber. The sand shot is driven by air pressure, initializing the flow of sand from the hopper above, into the chamber below. The sand fills out the mould geometry in the chamber at around the time 1 s.

Hence, the focus of the present work is on the sand shot and how this first part of the moulding process can be modelled numerically with the DEM, in this study only the sand phase is investigated. The first period of the sand shot 0.6 s is investigated, where the space underneath the three “ribs” is filled with green sand (see figure 3). Earlier research has been done, using DEM to simulate the sand flow [2] as well as the subsequent squeezing process [3] in the application of green sand moulding. Obtaining the right DEM parameters to realistically simulate the process is important, but at the same time also quite challenging [4]. This especially goes for the green sand material properties due to the small particle size around 0.2 mm as well as for the description of adhesion. The latter is often neglected in DEM simulations and this is also the case for the present work.



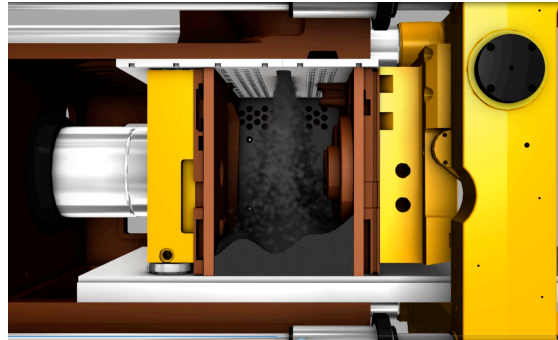


Figure 1. The sand shot, the sand coming from the hopper down into the chamber. The simulation of the sand shot is the topic of the present work.

DEM has also been used to simulate the lost foam process [5], where it was suggested that the rolling resistance and the Coulomb sliding friction are the most important parameters for the flow behaviour in this process. The fitting of rolling resistance and sliding friction parameters was studied in [4], in which different experimental tests were used for calibration. Particle scaling is frequently needed in the discrete element method [6], in this study two different particle sizes are used for the simulations.

2. Discrete element method (DEM).

DEM has received increased attention the last decade and the general application areas of the method can be found in e.g. [7]. A general review of the method’s theoretical foundation is also given by [8] and a comparison of different frequently used DEM models was made by Di Renzo et. Al [9]. With the advancement in computational power and the introduction of parallel computing in DEM, the method also seems to be convenient for granular flow [10] and [11]. The commercial software STAR-CCM+ has been used for the 2-D simulations.

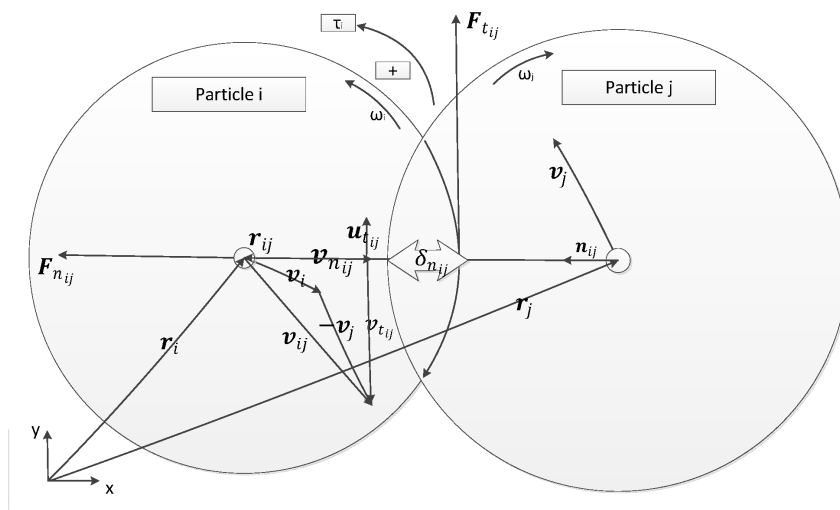


Figure 2. Particle i-th impact with particle j-th, the force exerted on the i-th particle in the normal direction is $F_{n_{ij}}$ and in the tangential direction is $F_{t_{ij}}$.

In figure 2, the impact distance $r_{ij} = \|\mathbf{r}_{ij}\|_2$ of the spherical i-th particle center of mass (\mathbf{r}_i) is found by the spherical particle j-th center of mass (\mathbf{r}_j) as

$$\mathbf{r}_{ij} = \mathbf{r}_i - \mathbf{r}_j \quad (1)$$

In DEM there is a normal direction ($\mathbf{n}_{ij} = \frac{\mathbf{r}_{ij}}{r_{ij}}$). The relative velocity of the two particles is

$$\mathbf{v}_{ij} = \mathbf{v}_i - \mathbf{v}_j$$

decomposed to a velocity in the normal direction ($\mathbf{v}_{n_{ij}}$) and a velocity in the tangential ($\mathbf{v}_{t_{ij}}$) to find the elastic force from the “spring” and the viscous damping force from the “dashpot” [11][12]. The normal velocity is given by

$$\mathbf{v}_{n_{ij}} = (\mathbf{n}_{ij} \cdot \mathbf{v}_{ij})\mathbf{n}_{ij} \quad (2)$$

The tangential velocity vector is defined as

$$\mathbf{v}_{t_{ij}} = \mathbf{v}_{ij} - \mathbf{v}_{n_{ij}} - (\boldsymbol{\omega}_i R_i + \boldsymbol{\omega}_j R_j) \times \mathbf{n}_{ij} \quad (3)$$

The normal displacement is $\delta_{n_{ij}} = \|\mathbf{v}_{n_{ij}}\|_2 \Delta t$ and the tangential displacement vector $\mathbf{u}_{t_{ij}}$ is found by integration of the tangential velocity $\frac{d\mathbf{u}_{t_{ij}}}{dt} = -\mathbf{v}_{t_{ij}}$

The simplified Hertz-Mindlin (H-MDNs) force model with non-linear damping is used [13] [14] [15] and now that the displacements has been found the normal interaction force can be found

$$\mathbf{F}_{n_{ij}} = \mathbf{n}_{ij} K_n \delta_{n_{ij}}^{3/2} - N_n \mathbf{v}_{n_{ij}} \quad (4)$$

The tangential interaction force

$$\mathbf{F}_{t_{ij}} = \mathbf{u}_{t_{ij}} K_t - N_t \mathbf{v}_{t_{ij}} \quad (5)$$

K_n is the normal stiffness and K_t is the tangential stiffness, note that N_n is the normal and N_t the tangential non-linear damping model [13].

There is a max tangential force due to the Coulomb’s law,

$$\|\mathbf{F}_{t_{ij}}\|_2 < \|\mu_s \mathbf{F}_{n_{ij}}\|_2 \quad (6)$$

μ_s is the static friction coefficient. Finally the total force on the particle is,

$$\mathbf{F}_i^{tot} = m_i \mathbf{g} + \sum_j (\mathbf{F}_{n_{ij}} + \mathbf{F}_{t_{ij}}) \quad (7)$$

The tangential forces give a final torque on the i-th particle,

$$\mathbf{T}_i = -R_i \sum_j (\mathbf{n}_{ij} \times \mathbf{F}_{t_{ij}}) \quad (8)$$

From this the acceleration, velocity and position is calculated by Newton second law, incrementally for each time step. The rolling resistance chosen is the Constant Torque Method first used by Zhou et. Al [16]. The relative rotation between the two particles is defined as $\boldsymbol{\omega}_{rel} = \boldsymbol{\omega}_i - \boldsymbol{\omega}_j$ and the Constant Torque Method is used to calculate the rolling resistance, defined as

$$\mathbf{T}_{rol} = -\frac{\boldsymbol{\omega}_{rel}}{|\boldsymbol{\omega}_{rel}|} \mu_r R_{eq} \mathbf{F}_{n_{ij}} \quad (9)$$

So the tangential force \mathbf{T}_i is counteracted by a torque from the rolling resistance \mathbf{T}_{rol} and the rolling resistance is μ_r .

3. Settings for the simulation

In the following figure 3, a simulation of the sand shot is shown with the green sand coming from top of the chamber with the flow rate and the initial velocity calculated from the experimental footage.

The flow rate is calculated by the circle diameter e.g. $d=0.004$ m, filling time 1.05 s, the assumed packing fraction of 0.75 and the total area of the mould which is 0.25 m^2 and finally this gives the flow rate $\frac{0.75 \cdot 0.25 \text{ m}^2}{(0.002 \text{ m})^2 \pi \cdot 1.05 \text{ s}} = 14210 \text{ particles/s}$. The diameter of 0.002 m gives the 56840 particles/s.

The particle velocity at the inlet is found by a simple 2-D bulk flow calculation based on the areas filling time of sand and orifice length from the actual chamber and experimental video footage.

This area has the height going to the third rib, $h = 0.3 \text{ m}$ (see figure 3) and the width of the chamber is $w = 0.48 \text{ m}$, then this area is $0.3 \text{ m} \cdot 0.48 \text{ m} = 0.144 \text{ m}^2$.

The orifice width is 0.04 m and the filling time of the area is around 0.6 s, so the average vertical velocity is estimated to be $v_y = \frac{0.144m^2}{0.04m \cdot 0.6s} = 6.0 \text{ m/s}$. For a more realistic velocity distribution a normal distribution is assumed around the calculated mean value and the standard deviations is given in table 1.

Table 1. The velocity distribution.

Direction	Mean value (m/s)	Standard deviation (m/s)	Velocity range	
			Min (m/s)	Max (m/s)
v_x	0	0.1	-0.1	0.2
v_y	-6.0	0.1	-5.8	-6.2

The time step is chosen to be $\Delta t=0.00001$ s, plots of the velocities are made for every 500 time step, corresponding to the time 0.005 s, 0.01 s, 0.015 s and 0.02 s etc.

Table 2. Material values for the simulation.

Material properties	Value
Solid density – green sand	1600 kg/m ³
Solid density – chamber wall	7500 kg/m ³
Young’s modulus – green sand	17000 MPa
Young’s modulus – chamber wall	200000 MPa
Poisson ratio – green sand	0.3
Poisson ratio – chamber side	0.3
Coefficient of restitution particle-particle	0.01
Coefficient of restitution particle-wall	0.01
Gravity	9.82 m/s ²

In table 2 typical values have been chosen for the Poisson ratio and Young modulus for the steel in the chamber wall. For the sand it is chosen to be the same value as a similar material, brick in STAR-CCM+. The sand in the mould has a density of 1200 kg/m³ after the sand shot and before squeezing. The density of “representative” sand particles is $\frac{1200 \text{ kg/m}^3}{0.75} = 1600 \frac{\text{kg}}{\text{m}^3}$, due to the packing fraction.

The coefficient of restitution is chosen to be very small and very close to critical damping. This is due to the high damping properties of the bentonite coated green sand and Young modulus have been suggested to be of less importance compared to the rolling resistance (equation (9)) and static friction coefficient (equation (6)), [5].

Table 3. Simulation parameters, where the rolling resistance is μ_r and the static friction coefficient is μ_s .

Diameter	μ_s	μ_r	Injection rate
4 mm	0.8	0.6	14210 particles/s
4 mm	0.8	0.9	14210 particles/s
4 mm	1	0.6	14210 particles/s
4 mm	1	0.9	14210 particles/s
2 mm	0.8	0.6	56841 particles/s
2 mm	0.8	0.9	56841 particles/s
2 mm	1	0.6	56841 particles/s
2 mm	1	0.9	56841 particles/s

In table 3, choosing different values for the rolling resistance and static friction coefficient simulates changing the flow ability of the particles. This way, the effect of changing the moisture and bentonite content in the “real” green sand can be simulated as this changes the flow ability.

4. Results of simulation and experiment

The result that will be presented show when the flow front passes underneath the three “ribs” into the three “cavities” at the right side wall, seen in the following figure 3. The flow front is hard to define and track exactly in DEM, so six times intervals t_1 - t_6 are constructed for the arrival of the particles at the six positions. These six times intervals t_1 - t_6 will be measured for the flow front for different parameter values of the rolling resistance, static friction coefficient and particle radius and will then be compared to the experimental results.

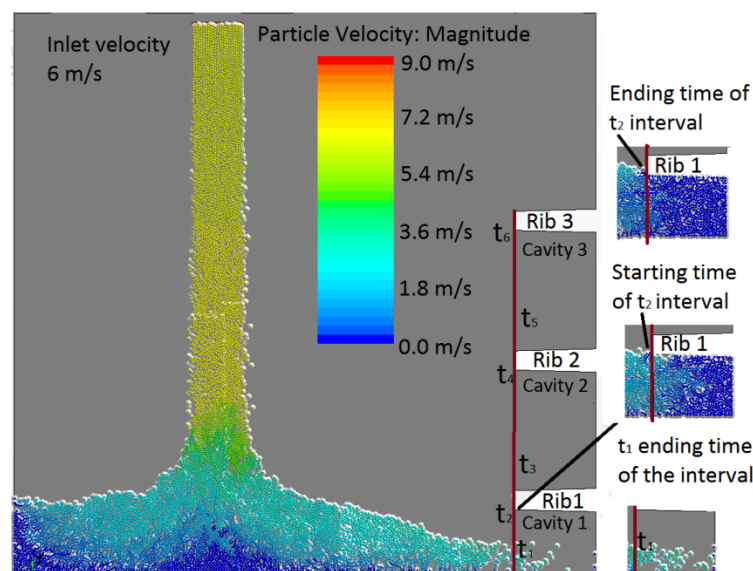


Figure 3. Tracking the front of the flow profile at the 6 different positions (t_1 - t_6). An example of interval start and end time is shown in the bottom right corner of the figure for the time interval denoted t_1 . An example of interval start and ending is shown in the right top of the figure for the time interval denoted t_2 . The magnitude of the velocity is plotted with a scaling of 0-9 m/s the scale going from minimum dark blue, 0 m/s to the maximum velocity red 9 m/s.

In figure 3, the starting time for the interval, is when the flow front reaches the brown line and the ending time of the interval is when the bulk flow of the flow front has reached the brown line. The flow reaches the “cavities” underneath the three “ribs”, when the particles cross the brown line into cavity 1 (t_1), cavity 2 (t_3) and cavity 3 (t_5). The starting time of the interval is when the “loosely packed particles” reach into the cavities and ending time of the interval is when the bulk flow or “closely packed particles” reach the cavities. The starting times of t_2 , t_4 and t_6 intervals are when the flow front reaches the bottom edge of rib 1, 2 and 3 subsequently. Here the starting times of the time intervals are again when the “loosely packed” particles hit the bottom edge of the rib in the time step. The ending time of t_2 , t_4 and t_6 intervals are again defined as when the “closely packed particles” reaches the bottom edge rib in the time step. The following table 4 will show all the intervals t_1 - t_6 for

the different simulations and selected plots will be made showing the flow profile passing the different positions and compared to the video footage.

Table 4. The six time intervals t_1 - t_6 , where each interval (start-end) indicates the period, when the flow front reaches the selected positions at the brown line. The experimental values are shown in the last row.

Simulations values	t_1 [s]	t_2 [s]	t_3 [s]	t_4 [s]	t_5 [s]	t_6 [s]
$\mu_r=0.6, \mu_i=0.8, 4$ mm	0.155-0.170	0.215-0.225	0.255-0.270	0.380-0.390	0.435-0.445	0.585-0.590
$\mu_r=0.9, \mu_i=0.8, 4$ mm	0.175-0.205	0.225-0.245	0.275-0.290	0.380-0.390	0.450-0.460	0.585-0.600
$\mu_r=0.6, \mu_i=1, 4$ mm	0.160-0.165	0.225-0.230	0.250-0.260	0.385-0.395	0.440-0.450	0.590-0.605
$\mu_r=0.9, \mu_i=1, 4$ mm	0.175-0.185	0.235-0.240	0.255-0.270	0.410-0.420	0.475-0.480	0.625-0.665
$\mu_r=0.6, \mu_i=0.8, 2$ mm	0.145-0.155	0.215-0.220	0.245-0.250	0.370-0.380	0.415-0.425	0.550-0.560
$\mu_r=0.9, \mu_i=0.8, 2$ mm	0.155-0.165	0.220-0.225	0.240-0.245	0.380-0.390	0.435-0.440	0.585-0.595
$\mu_r=0.6, \mu_i=1, 2$ mm	0.150-0.165	0.210-0.215	0.235-0.240	0.365-0.370	0.440-0.450	0.540-0.550
$\mu_r=0.9, \mu_i=1, 2$ mm	0.155-0.160	0.215-0.225	0.240-0.250	0.380-0.385	0.430-0.440	0.590-0.595
Experiment	0.254-0.262	0.304-0.313	0.325-0.342	0.429-0.441	0.467-0.492	0.575-0.591

In table 4, the different values for the six time intervals t_1 - t_6 are listed for the different simulations values and the experiment. A mean is calculated for each of the two diameters overall simulation times, this includes all the 4 times interval for each of the six columns with the times intervals t_1 - t_6 . Maximum and minimum times are also found from the 4 times interval for each of the six columns with the times intervals t_1 - t_6 . So for all the simulations with the diameter e.g $d=4$, a mean, maximum and minimum is calculated for each of the six time intervals t_1 - t_6 . The results from table 4 are depicted in figure 4, with the mean, maximum and minimum values plotted for the two diameters and the experiment.

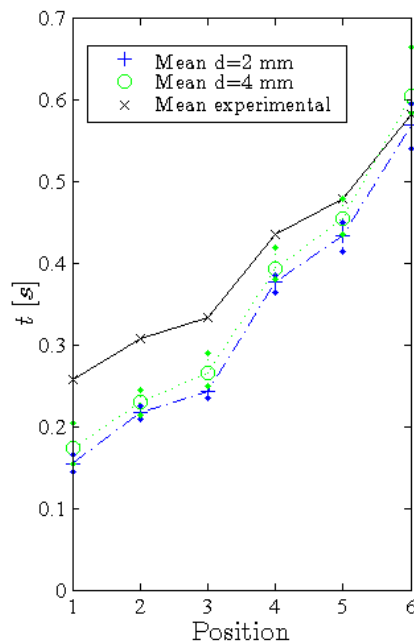


Figure 4. The mean, maximum and minimum times for t_1 - t_6 for all the simulations compared to the experiment. The solid black line is linear interpolation of the experimental mean; the cross is the actual value of the experimental mean. The circle is the mean of the diameter $d=4$ mm and the plus is the diameter $d=2$ mm. The green dots are the intervals minimum and maximum of the diameter 4 mm and the blue dots represents the diameter 2 mm.

In figure 4, the simulation of diameter 4 mm mean is occurring around 0.06 s earlier than the first times t_1 - t_3 from the experimental mean's and the difference narrows as the flow passes at the times t_4 - t_5 , at t_6 the simulations reached this point later than the experiment. Similarly dynamics occurs for the simulation of diameter 2 mm, where the mean is occurring around 0.08 s earlier compared to the experimental mean, for the first times t_1 - t_3 and the difference narrows as the flow passes at the times t_4 - t_5 and at the time t_6 the simulations are very close to the experimental value (difference 0.01). The larger diameters of 4 mm, have longer t_1 - t_6 times than the diameter of 2 mm. The specific simulation chosen is the diameter of 2 mm, rolling resistance $\mu_r=0.9$ and static friction coefficient $\mu_s=1$, because this simulation's qualitative flow dynamics is very similar to the experiment. In figure 5 (simulation) and figure 6 (experiment) the progression of the flow front at t_2 is presented and the results are compared. The flow profile of the experiment figure 6, shows a quite conical pile shape (free surface shape) and the simulation exhibits a very similar conical shaped flow profile, although the actual time of the occurrence (t_2) is somewhat different i.e. 0.1 s, as earlier mentioned.

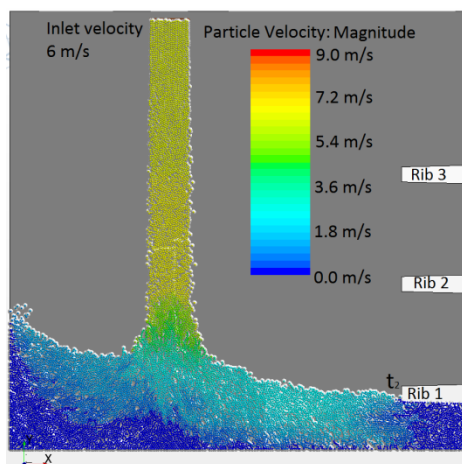


Figure 5. The simulation in the interval of t_2 plot taken at the time 0.225 s ($\mu_r=0.9$, $\mu_s=1$, 2 mm).



Figure 6. The experiment: t_2 at the time of 0.32 s, the contour of the flow profile can be seen on the rear wall.

5. Conclusion

The sand shot in the DISAMATIC process has been investigated with experimental video footage of the chamber and also simulated with DEM “representing” the sand particles. The dynamical flow properties of the green sand have been quantified by tracking the flow fronts arrival in six positions for the “ribbed” geometry. The Experimental video footage flow front and the DEM simulations flow front are compared for these six filling positions in the times (t_1 - t_6) and plotted together with mean, minimum and maximum values. Selected plot for a specific chosen simulation is compared with the experimental footage, when the flow fronts has reached the rib 1 bottom edge position (t_2) and these flow fronts profiles similarities is discussed.

The main findings of the discrete element method for modelling green sand flow during production of DISA moulds is presented below.

- The dynamic flow behaviour of the particles in the simulation is similar to the experiment
- The behaviour of the time intervals (t_1 - t_6) for the simulation is also similar to the experiment

- The flow ability changes to a more viscous flow with larger rolling resistance and static friction coefficient, resembling the behaviour of moisture and bentonite content in green sand
- With the correct particle velocity, flow rate, damping coefficient, rolling resistance and static friction coefficient it is possible to simulate the experimental video footage very well

The experimental data t_1 is slower with a time delay of 0.1 s for the diameter 2 mm and 0.8 s for the diameter 4 mm compared to these simulations, properly due to a non-constant flow rate in the inlet, especially overestimating the initial flow rate. In later studies the flow rate will be fitted more precisely with the experimental video footage and selected material values will also be tested experimentally. The density will also be measured from experiments and compared to the simulations. Overall it is possible to represent the flow quite well with a DEM model especially qualitative behaviors of the flow and for the different times t_1 - t_6 .

References

- [1] DISA Industries A/S 2013 DISA 231/DISA 231 Var. Sand Moulding System Instructions for Use
- [2] Makino H, Maeda Y and Nomura H 2002 Computer Simulation of Various Methods for Green Sand Filling *Trans. Am. Foundry Soc.* **110** 1–9
- [3] Maeda Y, Maruoka Y, Makino H and Nomura H 2003 Squeeze molding simulation using the distinct element method considering green sand properties *J. Mater. Process. Technol.* **135** 172–8
- [4] Grima A P and Wypych P W 2011 Discrete element simulations of granular pile formation: Method for calibrating discrete element models *Eng. Comput.* **28** 314–39
- [5] Rojek J, Zarate F, de Saracibar C A, Gilbourne C and Verdot P 2005 Discrete element modelling and simulation of sand mould manufacture for the lost foam process *Int. J. Numer. Methods Eng.* **62** 1421–41
- [6] Sakai M, Takahashi H, Pain C C, Latham J-P and Xiang J 2012 Study on a large-scale discrete element model for fine particles in a fluidized bed *Adv. Powder Technol.* **23** 673–81
- [7] Zhu H P, Zhou Z Y, Yang R Y and Yu A B 2008 Discrete particle simulation of particulate systems: A review of major applications and findings *Chem. Eng. Sci.* **63** 5728–70
- [8] Zhu H P, Zhou Z Y, Yang R Y and Yu a. B 2007 Discrete particle simulation of particulate systems: Theoretical developments *Chem. Eng. Sci.* **62** 3378–96
- [9] Di Renzo A and Di Maio F P 2004 Comparison of contact-force models for the simulation of collisions in DEM-based granular flow codes *Chem. Eng. Sci.* **59** 525–41
- [10] Cleary P W 2009 Industrial particle flow modelling using discrete element method *Eng. Comput.* **26** 698–743
- [11] Walther J H and Sbalzarini I F 2009 Large-scale parallel discrete element simulations of granular flow *Eng. Comput.* **26** 688–97
- [12] Cundall P A and Strack O D L 1979 A discrete numerical model for granular assemblies *Géotechnique* **29** 47–65
- [13] Tsuji Y, Tanaka T and Ishida T 1992 Lagrangian numerical simulation of plug flow of cohesionless particle in a horizontal pipe *Powder Technol.* **71** 239–50
- [14] Hertz H 1881 Über die Berührung fester elastischer Körper *J. für die reine und Angew. Math.* **171** 156–71
- [15] Mindlin R D and Deresiewicz H 1953 Elastic spheres in contact under varying oblique forces *Am. Soc. Mech. Eng. -- Trans. -- J. Appl. Mech.* **20** 327–44
- [16] Zhou Y C, Wright B D, Yang R Y, Xu B H and Yu a. B 1999 Rolling friction in the dynamic simulation of sandpile formation *Phys. A Stat. Mech. its Appl.* **269** 536–53



Contents lists available at ScienceDirect

Powder Technology

journal homepage: www.elsevier.com/locate/powtec

Simulating the DISAMATIC process using the discrete element method – a dynamical study of granular flow

E. Hovad^{a,c,*}, J. Spangenberg^a, P. Larsen^c, J.H. Walther^{a,d}, J. Thorborg^{a,b}, J.H. Hattel^a^a Department of Mechanical Engineering, Technical University of Denmark (DTU), Denmark^b MAGMA Giessereitechnologie GmbH, Kackerstr. 11, 52072 Aachen, Germany^c DISA Industries A/S, Højager 8, Høje Taastrup, 2630 Taastrup, Denmark^d Computational Science and Engineering Laboratory, ETH Zurich, CH 8092, Switzerland

ARTICLE INFO

Article history:

Received 4 May 2016

Received in revised form 26 August 2016

Accepted 15 September 2016

Available online 17 September 2016

Keywords:

Sand casting

Green sand

Granular flow

Discrete element method

DISAMATIC process

ABSTRACT

The discrete element method (DEM) is applied to simulate the dynamics of the flow of green sand while filling a mould using the DISAMATIC process. The focus is to identify relevant physical experiments that can be used to characterize the material properties of green sand in the numerical model. The DEM parameters describing the static friction coefficients are obtained using a ring shear tester and the rolling resistance and cohesion value is subsequently calibrated with a sand pile experiment. The calibrated DEM model is used to model the sand shot in the DISAMATIC process for three different sand particle flow rates as captured on the corresponding video footage of the interior of the chamber. A mould chamber with three ribs mounted on the fixed pattern plate forming four cavities is chosen as a reference geometry to investigate the conditions found in the real moulding process. The geometry of the cast part and the casting system can make the moulding process complicated due to obstacles such as ribs that deflect the sand flow causing “shadows effects” around the cavities of the mould. These dynamic effects are investigated by the qualitative flow dynamics and quantitative mould filling times captured in the video footage and simulated by the calibrated DEM model. Both two- and three-dimensional DEM models are considered and found to produce results in good agreements with the video footage of the DISAMATIC process.

© 2016 Elsevier B.V. All rights reserved.

1. Introduction

The DISAMATIC process produces moulds made of green sand for metal casting. These sand moulds are typically used for casting metal parts, such as brake disks, crank shafts and engine blocks used in the automotive industry. The DISAMATIC moulding process is illustrated in Fig. 1, showing how the chamber is filled with green sand. The compressed air creates an overpressure in the top of the hopper that drives the flow of the sand through the sand slot down into the chamber. The sand shot is followed by a squeezing step, where the sand is compacted to increase density and build up strength in the sand mould before the casting process.

The green sand consists of quartz sand as the primary component mixed with bentonite and water, which coats the sand grains to form a cohesive granular material. After filling the chamber, the green sand is squeezed (Fig. 1 right) and the material forms bonds to create a stable and relatively strong mould. The quality of the mould is affected by many factors, including the mixture of quartz sand, the complexity of

the mould chamber geometry and the compressed air pressure driving the flow of the green sand where the final mould must be homogeneous and stable.

The discrete element method (DEM) is a particle based method that is often used to model granular flow and it has received increased attention in the last decade. The general industrial application areas of the DEM method is typically flow in hoppers, mixers, drums and mills this is all discussed in the review [1]. A general review of the theoretical foundation has been published in [2] and a comparison of different frequently used DEM models is presented in [3]. DEM is gaining popularity as the computational power available to researchers increases and with the introduction of parallel computing in DEM [4] [5]. Newer codes based on the GPU framework are developed as e.g. [6] for realistic simulation of sand behaviour. The GPU framework of [7] was used for simulations of mill charge in [8] applying the GPU for faster simulating millions of a non-spherical particles.

DEM has been used to simulate the sand mould manufacture for the lost foam process [9], where it was suggested that the particle-particle static friction coefficient and rolling resistance are the most important parameters for the flow behaviour. The DEM model in [9] was calibrated with the repose angle of a sand pile. The calibration of the DEM simulation for blade-granular interaction in earth moving equipment was

* Corresponding author at: Produktionstorvet, Building 425, DK-2800 Kgs., Lyngby, Denmark.

E-mail address: emilh@mek.dtu.dk (E. Hovad).

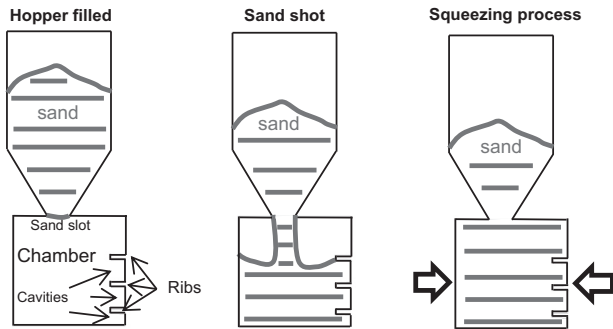


Fig. 1. The sand shot, (left) starts when the hopper is filled with green sand, compressed air from an air receiver (not shown) blows air into the top of the hopper which drives the sand from the hopper through the sand slot into the moulding chamber. In the chamber the cavities and ribs are positioned on the pattern plate positioned on the right hand side (the air exits the chamber through small air vents). (middle) The sand is filling the chamber and its three cavities. (right) Finally when the mould is filled, then the mould is squeezed until the pressure has reached a preset value and the mould is pressed out of the chamber ready for casting and to receive the molten metal. Then the sequence of (left) to (right) can be repeated to construct more moulds.

performed using a direct shear test for calibrating the internal friction angle and a compression test for the estimation of the particle stiffness [10].

DEM simulations of the green sand moulding process have earlier been conducted by [11] with the particle diameter of 6.0 mm and the squeezing process was simulated in [12]. Earlier two-dimensional DEM simulations of the sand shot in the DISAMATIC process [13] were conducted in the simplified chamber geometry illustrated in Fig. 1 focusing on the ribs that deflect the sand flow causing “shadow effects” around the cavities of the mould. The study considered a constant particle inlet velocity and particle diameters of 2 mm and 4 mm as representative sand particles for the granular flow. The sensitivity of the granular flow was studied with respect to the particle-particle rolling resistance and particle-particle static friction coefficient in [13]. The study found that the particle inlet velocity was of greater importance for the results than the particle parameters tested.

In the present study of the DISAMATIC process the sand slot particle inlet velocity and particle flow rate is estimated by using the filling times of the different parts of the mould chamber from video footage. In addition the DEM model is calibrated from experiment to obtain the rolling resistance, cohesion, static friction coefficients assuming a 2 mm particle diameter. Finally a comparison is performed between a two- and three-dimensional DEM model simulating the DISAMATIC process for three different compressed air pressures.

The 2-D simulation appears to give an overestimated energy transfer compared to the 3-D simulations due to the larger number of particle-particle interactions and the additional degrees of freedom in 3-D. The particles in 3-D display a stronger scatter at later filling times as compared to the 2-D simulations.

2. Method: Testing green sand

In the DISAMATIC process compactability testing of the sand is performed done to guarantee the quality of the mould for the subsequent casting step. However, this does not provide sufficient information about the flowability of the sand mixture and it is of great interest to develop new test methods and procedures to characterize the sand flow. This is of particular importance for geometrically complex castings where it can be a challenge to ensure a homogeneous filling, which in turn is needed for the subsequent compaction step.

2.1. Purpose of the experiments: Finding the DEM parameters

The DEM particle density for the 2-D simulations ($\rho_{DEM,2D}$) and 3-D simulations ($\rho_{DEM,3D}$), is found from a ramming test, see Fig. 2.



Fig. 2. Green sand (left), sieving the green sand into the cylinder (middle) and the ramming station used to determine the compactability of the sand mixture (right).

The static friction coefficient for the green sand-green sand interaction and the static friction coefficient for the green sand-steel plate interaction were found from the ring shear tester of the type RST-SX. The values found from the ring shear tester are used for the DEM model to obtain the particle-particle static friction coefficient ($\mu_{s, p-p}$) and the particle-wall friction coefficient ($\mu_{s, p-w}$).

With a sand pile experiment, the parameters investigated in the DEM calibration are the rolling resistance modelling the non-uniform sand particles resistance to rolling and the cohesion value modelling the binding of the green sand due to the bentonite. The cohesion value, W_{p-p} and the rolling resistance, $\mu_r, p-p$ are found from the sand pile experiment by matching the corresponding height of the sand pile, h_p . Calibration simulations are performed to study the effect of these parameters on the height of the final sand pile.

2.2. The green sand

The green sand consists of quartz sand as primary component mixed with bentonite which together with water coats the quartz sand and makes the sand mixture cohesive and sufficiently strong when the mould is finally squeezed.

2.3. Standard testing of green sand

The standard procedures for testing the green sand is from the American Foundry Society (AFS) and described in [14] where the following two standard tests were conducted in the present study: the water content and standard ramming test. For the standard ramming a standard specimen tube was used where the initial green sand sample was weighted before compaction and since the volume was known the density of the un-compacted and compacted green sand test sample could be calculated. The ramming test was conducted with the standard of 3 strokes and to find the maximum density 10 strokes were executed. The green sand values from the standard tests can be seen in Table 1.

2.4. Ring shear tester

The ring shear tester of the type RST-SX is described in [15].

Table 1
Material values for the green sand used for the sand pile experiment.

Material properties	Avr.	Std.	Measurements
Green sand water content	3.6%	0.2%	11
Average compactability level (AFS standard)	42%	0.7%	7
Average maximum compactability (10 ramming)	47%	0.9%	7
Average loose density	832 kg/m ³	11 kg/m ³	14
Average maximum density, ρ_{bulk} (10 ramming)	1557 kg/m ³	8.8 kg/m ³	7

2.4.1. Internal friction angles (φ)

The ring shear tester is used to find flow properties as the three internal friction angles:

- The linearized yield locus, φ_{lin}
- The effective angle of friction, φ_e
- The angle of internal friction at steady-state flow, φ_{sf}

These three internal friction angles and the cohesion of the material (τ_c) can be seen in Fig. 3.

The linearized yield locus, μ_{lin} is the tangent to both the Mohr stress circles defining σ_c and σ_1 .

From the ratio of the shear stress, τ_{pre} to normal stress, σ_{pre} a friction angle can be found from the angle of internal friction at steady-state flow, φ_{sf} from the pre-shear point, $\varphi_{\text{sf}} = \tan^{-1}(\tau_{\text{pre}}/\sigma_{\text{pre}})$ and the effective internal friction angle, φ_e is defined as the ratio of the minor principal stress, σ_2 to the major principal stress, σ_1 at steady-state flow, $\sin(\varphi_e) = (\sigma_1 - \sigma_2)/(\sigma_1 + \sigma_2)$.

For poorly flowing bulk solids e.g. moist clay the effective angle of internal friction, φ_e can become large compared to the angle of internal friction at steady-state flow, φ_{sf} for the bulk solids layers that are sliding against each other as they do in a shear test during steady-state flow [15]. Thereby the angle of internal friction at steady-state flow, φ_{sf} and the linearized yield locus, φ_{lin} are used as indicators for the DEM models particle-particle internal friction interval. The cohesion of the material, τ_c is defined at zero normal stress ($\sigma = 0$).

Note that the DEM model particle-particle cohesion value, $W_{\text{p-p}}$ together with the rolling resistance, $\mu_{\text{r, p-p}}$ is found from the sand pile experiment by the corresponding height of the sand pile, h_p .

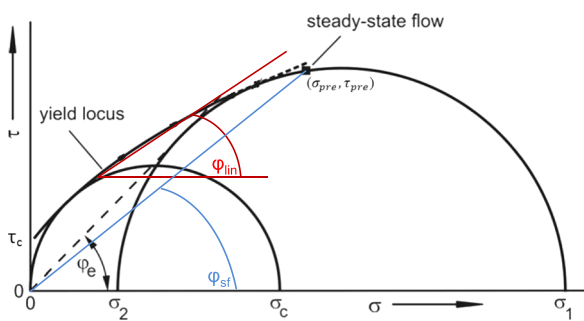


Fig. 3. Yield locus and the three internal friction angles: φ_e (black dotted line) is the linearized yield locus, φ_{lin} (green line) is the effective angle of friction and φ_{sf} (blue line) the angle of internal friction at steady-state flow from the pre-shear point ($\sigma_{\text{pre}}, \tau_{\text{pre}}$). The normal stress is in the x-axis (σ) and the shear stress is in the y-axis (τ). The major principal stress is σ_1 and the minor principal stress σ_2 for the confined sample (large circle) and the major principal stress is σ_c for the unconfined sample (small circle). The cohesion value found from the ring shear tester of the material is denoted τ_c . Note the edited figure is originally from [16] and the theory is from [15]. (For interpretation of the references to color in this figure legend, the reader is referred to the web version of this article.)

2.4.2. Wall friction angle (φ_x)

To find the wall friction angle, also called the wall yield locus, a bulk sample is subjected to a selected normal load ($\sigma_{w1}, \sigma_{w2}, \sigma_{w3}, \dots$). When a constant shear stress is reached the points (σ_w, τ_w) are recorded as shown in Fig. 4.

The sliding friction angle is found from the slope of the wall yield locus.

2.5. The sand pile experiment

The sand pile experiment is used for estimating the rolling resistance and cohesion in the DEM model and the experimental setup is shown in Fig. 5.

First the hopper is filled with green sand through the sieve having a hole size of 3.5 mm–4.0 mm shown in Fig. 5 (left). After that the orifice is opened rapidly emulating an instantaneous opening of the orifice in the hopper simulation. The height of the sand pile (h_p) from the experiment is illustrated in Fig. 5 (right), and it is defined by the maximum height of the sand pile. This height is measured with a laser projected onto a ruler. In order to allow a 2-D model approach either through a 2-D DEM model or a 3-D slice, the hopper was designed with a long side (1) compared to the width (w_2) of the box with the ratio of $1/w_2 = 0.4$.

3. Numerical method

3.1. Discrete element method (DEM)

The commercially available software STAR-CCM+ is used for the simulations to allow studies of flow in the complex geometry [17]. In DEM the forces are decomposed into a normal and tangential direction, as originally proposed by [18]. The Hertz-Mindlin contact model is chosen due to its ability to obtain the normal and tangential stiffness from real material parameters. Hertzian contact mechanics is used in the normal direction of impact [19] and a simplified Mindlin model is used in the tangential direction of impact [20], from which the non-linear damping can be derived. The non-linear damping model was tested in Refs. [21,22]. The selected model for rolling resistance is the constant torque method first developed by [23] and tested in [24]. The cohesion model selected is the Johnson-Kendall-Roberts (JKR) model described in [25].

3.2. Particle kinematics

The notation applied for describing the equations applied in DEM is from [26], where the two particles in contact is denoted $\{i, j\}$ positioned at $\{\mathbf{r}_i, \mathbf{r}_j\}$ with the velocities $\{\mathbf{v}_i, \mathbf{v}_j\}$ and angular velocities $\{\boldsymbol{\omega}_i, \boldsymbol{\omega}_j\}$. The distance between the two particles is denoted

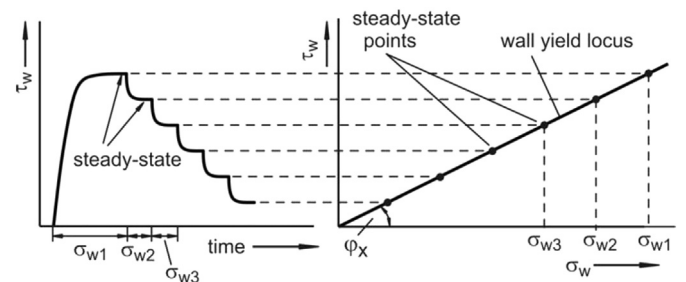


Fig. 4. The selected normal loads ($\sigma_{w1}, \sigma_{w2}, \sigma_{w3}, \dots$) and the shear stresses history, τ_w (left figure). Wall yield locus found from the steady-state points (right figure). Note the edited figures is from [16].

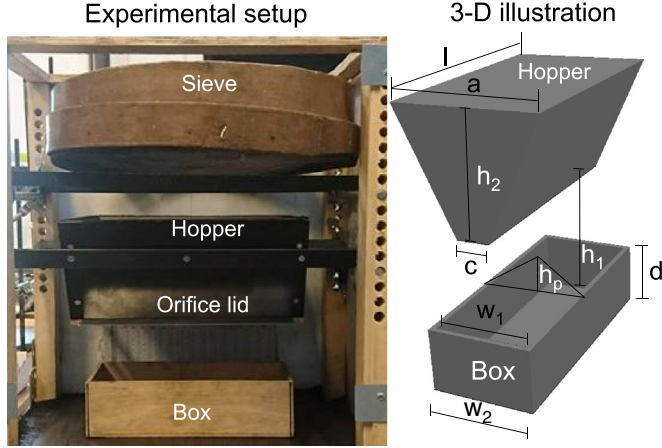


Fig. 5. (Left) The hopper experiment can be seen with the Sieve on the top, the hopper, orifice lid and finally the box in the bottom. (Right) In the 3-D illustration the hopper measurement can be seen with the length $l = 300$ mm, width of $a = 180$ mm, orifice width $c = 40$ mm and the box measurements with the internal width $w_1 = 120$ mm, external width $w_2 = 134$, the height of the box $d = 82$ mm, the measured height of the sand pile is denoted h_p , and the drop height of $h_1 = 169$ mm and hopper height of $h_2 = 150$ mm. Note the box side and bottom thickness is 7 mm.

$r_{ij} = \|\mathbf{r}_i - \mathbf{r}_j\|_2$, the position vector from particle j to i is $\mathbf{r}_{ij} = \mathbf{r}_i - \mathbf{r}_j$, and the normal overlap $\delta_{n_{ij}}$ is

$$\delta_{n_{ij}} = (R_i + R_j) - r_{ij} = 2R - r_{ij} \quad (1)$$

Since all the particles have the same radius and physical properties $(R_i + R_j) = 2R$ for the particle-particle interaction. The relative normal velocity is

$$\mathbf{v}_{n_{ij}} = (\mathbf{v}_{ij} \cdot \mathbf{n}_{ij}) \mathbf{n}_{ij} \quad (2)$$

Where the normal vector is defined, $\mathbf{n}_{ij} = \mathbf{r}_{ij}/r_{ij}$. The relative tangential velocity is

$$\mathbf{v}_{t_{ij}} = \mathbf{v}_{ij} - \mathbf{v}_{n_{ij}} - \frac{1}{2}(\boldsymbol{\omega}_i + \boldsymbol{\omega}_j) \times \mathbf{r}_{ij} \quad (3)$$

the tangential displacement vector is $\mathbf{t}_{ij} = \mathbf{v}_{t_{ij}} \Delta t$ and the tangential displacement is defined as $\delta_{t_{ij}} = \|\mathbf{t}_{ij}\|_2$.

3.3. Normal force

The normal interaction force on particle i from particle j is given by,

$$\mathbf{F}_{n_{ij}} = \mathbf{n}_{ij} K_n \delta_{n_{ij}}^{\frac{3}{2}} - N_{n_{ij}} \mathbf{v}_{n_{ij}} + \mathbf{F}_{coh_{ij}} \quad (4)$$

$N_{n_{ij}}$ is the normal non-linear damping coefficient and $\mathbf{F}_{coh_{ij}}$ is force due to cohesion.

The stiffness in the normal direction can be found as,

$$K_n = \frac{4}{3} E_{eq} \sqrt{R_{eq}} \quad (5)$$

where the equivalent Young's modulus is given by $E_{eq} = \frac{1}{\frac{1-\nu^2}{E_i} + \frac{1-\nu^2}{E_j}}$ and the equivalent radius is given by, $R_{eq} = \frac{1}{\frac{1}{R_i} + \frac{1}{R_j}} = \frac{R}{2}$.

The cohesion is described by the Johnson-Kendall-Roberts (JKR) model with the factor -1.5 , where the particle-particle constant cohesion force in the normal direction is defined as

$$\mathbf{F}_{coh_{ij}} = -1.5\pi R_{min} W \mathbf{n}_{ij} \quad (6)$$

$R_{min} = R$ is the minimum radius of contact, W is the cohesion parameter.

The damping coefficient in the normal direction is defined as,

$N_{n_{ij}} = \frac{4}{3} \sqrt{5K_n M_{eq} \delta_{n_{ij}}}^{1/4} N_{n,damp}$ where $N_{n,damp} = \frac{-\ln(e_n)}{\sqrt{\pi^2 + \ln(e_n)^2}}$ and the coefficient of restitution is formally defined as $e_n = -\frac{v_{out}}{v_{in}}$, where v_{in} is the velocity before impact and v_{out} is the velocity after impact and the equivalent mass is given by, $M_{eq} = \frac{1}{\frac{1}{m_i} + \frac{1}{m_j}} = \frac{m}{2}$.

Note for the particle-wall interaction the radius of the wall is $R = \infty$ and the cohesion ($\mathbf{F}_{coh_{ij}}$) is neglected in Eq. (4).

3.4. Tangential force

The tangential force on particle i from particle j can be found as,

$$\mathbf{F}_{t_{ij}} = K_t \frac{\mathbf{t}_{ij}}{\|\mathbf{t}_{ij}\|_2} \delta_{t_{ij}}^{3/2} - N_{t_{ij}} \mathbf{v}_{t_{ij}} + \mathbf{T}_{rol_{ij}} \quad (8)$$

The tangential stiffness is defined as $K_t = 8G_{eq} \sqrt{R_{eq} \delta_{n_{ij}}}$ and the equivalent shear modulus as $G_{eq} = \frac{1}{\frac{2(2-\nu_i)(1+\nu_j)}{E_i} + \frac{2(2-\nu_j)(1+\nu_i)}{E_j}} = \frac{E}{4(2-\nu)(1+\nu)}$. The

$N_{t_{ij}}$ is the non-linear damping coefficient in the tangential direction and is defined as,

$$N_{t_{ij}} = \frac{4}{3} \sqrt{5K_t M_{eq} N_{t,damp}} \quad (9)$$

$N_{t,damp} = \frac{-\ln(e_t)}{\sqrt{\pi^2 + \ln(e_t)^2}}$ and the coefficient of restitution is formally defined as $e_t = -\frac{\boldsymbol{\omega}_{in}}{\boldsymbol{\omega}_{out}}$, where $\boldsymbol{\omega}_{in}$ is the angular velocity before impact and $\boldsymbol{\omega}_{out}$ is the velocity after impact.

Note that there is a maximal tangential force due to Coulomb's law,

$$\|\mathbf{F}_{t_{ij}}\|_2 < \|\mu_s \mathbf{F}_{n_{ij}}\|_2 \quad (10)$$

where μ_s is the static friction coefficient and the particle-particle static friction coefficient is denoted $\mu_{s,p-p}$ and particle-wall static friction coefficient is denoted $\mu_{s,p-w}$.

The rolling resistance for the particle-particle interaction uses is the constant torque method, defined as,

$$\mathbf{T}_{rol_{ij}} = -\frac{\boldsymbol{\omega}_{ij}}{\|\boldsymbol{\omega}_{ij}\|} \mu_r R_{eq} \|\mathbf{F}_{n_{ij}}\| \quad (11)$$

The relative angular velocity between the two particles is defined as $\boldsymbol{\omega}_{ij} = \boldsymbol{\omega}_i - \boldsymbol{\omega}_j$ and the torque from the rolling resistance is $\mathbf{T}_{rol_{ij}}$. Note for the particle-wall interaction the rolling resistance ($\mathbf{T}_{rol_{ij}}$) is neglected in Eq. (8).

3.5. Summing the forces

Finally the total force on the i 'th particle is

$$\mathbf{F}_i^{tot} = m_i \mathbf{g} + \sum_j (\mathbf{F}_{n_{ij}} + \mathbf{F}_{t_{ij}}) \quad (12)$$

where \mathbf{g} is acceleration due to gravity. The torque on the i 'th particle is

$$\mathbf{T}_i = -R_i \sum_j (\mathbf{n}_{ij} \times \mathbf{F}_{t_{ij}}) \quad (13)$$

From this the acceleration, velocity and position are calculated numerically by Newton second law.

3.6. Maximum time step

The maximum time step is found from the smallest value of the following three constrains; The first time constraint, τ_1 is the Rayleigh wave velocity [25,28,17]. The second constraint, τ_2 on the time step is that it takes at least 10 time-steps for the particle to move the full length of the radius. The third constrain on the time steps is τ_3 , which is the duration of impact of two perfectly elastic spheres with the Hertz contact theory derived by Timoshenko [29]. Thus, the time step takes the value $\tau = \min(\tau_1, \tau_2, \tau_3)$, where in practice τ_1 is typically the limiting factor [17].

4. Result of testing the green sand and calibrating the DEM model

4.1. Standard testing of green sand (AFS)

The values from the three tests; the water content, the AFS standard 3 and 10 stroke rammer procedure can be seen in Table 1.

4.2. RST-SX: Internal friction angles (φ)

On the ring shear tester of the type RST-SX 95, five experiments were conducted and the results can be seen in Fig. 6.

The average values obtained were the internal friction angles $\mu_e = 46.5^\circ$ (std = 2.7°), $\mu_{lin} = 28.6^\circ$ (std = 1.6°) and $\mu_{sf} = 38.4^\circ$ (std = 1.4°) and earlier tri-axial experimental values of $\mu_s = \tan^{-1}(29^\circ) = 0.47$ were attained from [30]. The linearized internal friction coefficient obtained is $\mu_{lin} = \tan^{-1}(\varphi_{lin}) = 0.54$, the internal friction coefficient at steady-state flow gives a higher value, $\mu_{sf} = \tan^{-1}(\varphi_{sf}) = 0.79$, where the effective internal friction coefficient gives the highest value of $\mu_e = \tan^{-1}(\varphi_e) = 1.05$.

The cohesion value (τ_0) can be found by extrapolating the linearized yield locus (μ_{lin}) to the intersection of the yield locus with the shear stress axis. The effective angle of internal friction (φ_e) is larger compared to the angle of internal friction at steady-state flow (φ_{sf}) for the green sand and thereby the effective angle of internal friction (φ_e). The average cohesion value of the five tests was $\tau_0 = 586$ Pa with std = 51 Pa.

4.3. RST-SX: Sliding friction angles (μ)

The result from the sliding friction of the green sand on stainless steel on the ring shear tester can be seen in Fig. 7.

Using the overall average of the three tests each with six points of different normal pressure where an average angle of 19.2° with a standard deviation of 1.33° was obtained. The corresponding sliding friction coefficient of green sand on the stainless steel plate is measured $\mu_{s,p-w} = 0.35$.

4.4. Material values for simulating the experimental sand pile

Obtaining accurate DEM parameters to realistically simulate the DISAMATIC process is important but the small particle radius of 0.1 mm makes a direct numerical simulation impractical due to the large number of particles required. However the complexity of cohesion properties of their combination of water and bentonite coating coats the quartz sand and also binds the quartz sand particles together creating larger clusters of particles. This indicates that the used particle size in the calculation should be somewhat closer to the selected size of $R = 1$ mm in radius to represent a cluster of quartz sand particles.

The elastic properties for the steel in the chamber wall and for the sand they are selected to be of the same values as those for a similar material, brick (Fire Clay) in STAR-CCM+ cf. Table 2. It should be noticed that the choice of these values is found to be of less importance compared to the rolling resistance and cohesion value for the shape of the sand pile in [9]. This makes the sand pile experiment ideal for calibrating the values of particle-particle rolling resistance ($\mu_{r,p-p}$) and the particle-particle cohesion value (W_{p-p}) from the sand pile height (h_p).

The representative DEM particle density of green sand is found from the maximum density of the 10 strokes in the ramming station cf. Table 1, $\rho_{DEM,2D} = 2\sqrt{3}\rho_{Bulk}/\pi \approx 1720$ kg/m³ and $\rho_{DEM,3D} = 2\sqrt{3}\rho_{Bulk}/\pi \approx 2100$ kg/m³ assuming the maximum packing fraction (hexagonal close packing).

The coefficient of restitution (e) for both the particle-particle and particle-wall is chosen to be very small and very close to critical damping because of the high damping properties of the bentonite coated green sand.

The particle-wall static friction applied in all the simulations is $\mu_{s,p-w} = 0.35$ corresponding to the average value obtained from the ring shear tests (RST-SX) for the green sand samples interaction with a stainless steel plate. The particle-particle static friction coefficient of $\mu_{s,p-p} = 0.5$ is initially used for the calibration of the DEM simulation, and this is close to the obtained value from the ring shear test of $\mu_{lin} = 0.54$ and the value of $\mu_{lin} = 0.47$ found in [30].

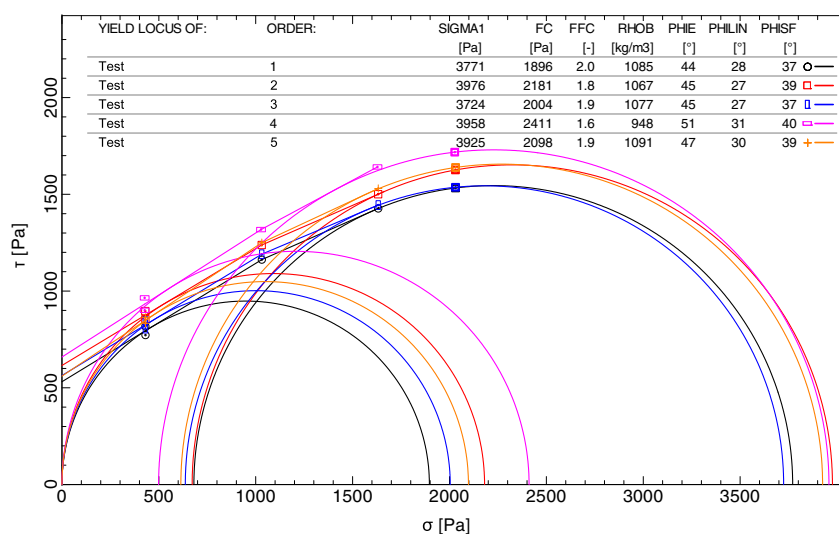


Fig. 6. Yield locus determination for green sand, five experiments was conducted on the same batch of green sand.

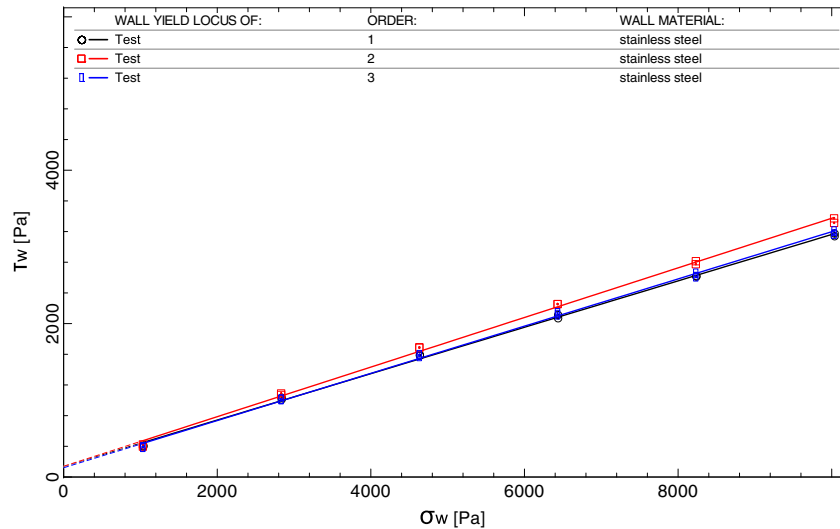


Fig. 7. The sliding friction test was conducted on the green sand interaction with a “smooth” stainless steel plate similar to the plates in the DISAMATIC chamber. Three tests were conducted on the same batch.

In the 2-D simulation the particles are injected from a line above the hopper with 100 points until the hopper is filled. To save computational time in the simulation of the 3-D hopper, the system is filled with an injector where the particles are placed randomly until the hopper is filled. For the 3-D hopper simulation a periodic boundary is applied in the z-direction (depth direction).

4.5. Result of the hopper experiment and the hopper simulation

Three sand pile experiments were conducted on the green sand batch and the average maximum height of the sand pile above the box

Table 2

Material values for the DEM simulation of the sand pile experiments. The calibration of the 2-D simulation parameters: the rolling friction coefficient for the particle-particle interaction is varied with 4 different values, and the cohesion value for particle-particle interaction has 3 different values, giving a total of 12 simulations. For the calibration of the 3-D simulation parameters: the rolling friction coefficient for the particle-particle interaction is varied with 3 different values for one cohesion value.

Material properties	Value
Green sand particle radius (R)	0.001 m
Solid density – chamber wall (ρ_{wall})	7500 kg/m ³
Young's modulus – green sand, (E_p)	17,000 MPa
Young's modulus – chamber wall, (E_w)	200,000 MPa
Poisson ratio – green sand, (ν_p)	0.3
Poisson ratio – chamber walls, (ν_w)	0.3
Coefficient of restitution particle-particle, (e_n)	0.01
Coefficient of restitution particle-wall, (e_t)	0.01
Gravity (g)	9.82 m/s ²
Particle-Wall static friction, ($\mu_{s,p-w}$)	0.35
Particle-Particle static friction, ($\mu_{s,p-p}$)	0.50
The simulation time step, (Δt)	10 ⁻⁵ s
2-D specification	
Representative particle density – green sand ($\rho_{DEM,2D}$)	1720 kg/m ³
Particle-Particle rolling friction coefficient (μ_r)	[0.1 0.2 0.3 0.4]
Cohesion work (W_{p-p})	[0 0.5 0.7] J/m ²
3-D specification	
Representative particle density – green sand ($\rho_{DEM,3D}$)	2100 kg/m ³
Particle-Particle rolling friction coefficient (μ_r)	[0.2 0.3 0.4]
Cohesion work (W_{p-p})	[0.3] J/m ²

was $h_p = 54$ mm with a standard deviation of $\sigma = 2$ mm and with an estimated tolerance precision of ± 2.0 mm. Due to the high bonding effect of bentonite, when the water content is increased, the height of the sand pile will also increase. The shape of the sand pile changes at the same time to being less conical [11].

In Fig. 8 the maximum height of the sand pile in the experiment (black line) and the DEM calibration simulations are found and compared. For the 2-D simulations a cohesion value of $W_{p-p} = 0.7$ J/m² results in higher sand piles than a cohesion value of $W_{p-p} = 0.5$ J/m² for the same rolling resistance. However, for this value the sand pile attains an unphysical shape. Based on these results the selected parameters for the 2-D simulation are: particle-particle cohesion $W_{p-p} = 0.5$ J/m², rolling resistance $\mu_{r,p-p} = 0.3$, static friction coefficient $\mu_{s,p-p} = 0.50$ (height of $h_p = 0.054$ m). The corresponding parameters for the 3-D simulation are: the particle-particle cohesion $W_{p-p} = 0.3$ J/m², the rolling resistance $\mu_{r,p-p} = 0.3$ and the static friction coefficient $\mu_{s,p-p} = 0.50$. Changing the particle static friction from $\mu_{s,p-p} = 0.50$ to $\mu_{s,p-p} = 0.75$ for the selected 2-D and 3-D hopper simulations changes the height of the pile less than 8%.

Fig. 9 compares the shape of the sand pile for the experiment 2-D simulation and 3-D simulation in general good agreement is observed.

4.6. Material values chosen for simulating the DISAMATIC process

The settings applied for simulating the DISAMATIC process are the rolling friction coefficient and cohesion value for particle-particle interaction which were found from calibration of the sand pile simulation. The particle-particle static friction coefficients of $\mu_{s,p-p} = 0.50$ and $\mu_{s,p-p} = 0.75$ are chosen so the simulated values are close to the interval of the obtained values from the ring shear tests of $\mu_{iin} = 0.54$ and $\mu_{sf} = 0.79$ and the lower value of $\mu_{iin} = 0.47$ found in [30]. The values from Table 2 are applied for the DISAMATIC simulations, where the final calibrated parameters for the particle-particle interactions are listed in Table 3.

5. Experimental video footage

The experimental video footage was captured with a Go-pro camera positioned in the right hand side top corner of the mould chamber and looking downwards on the flow around the ribs and cavities cf. Fig. 10.

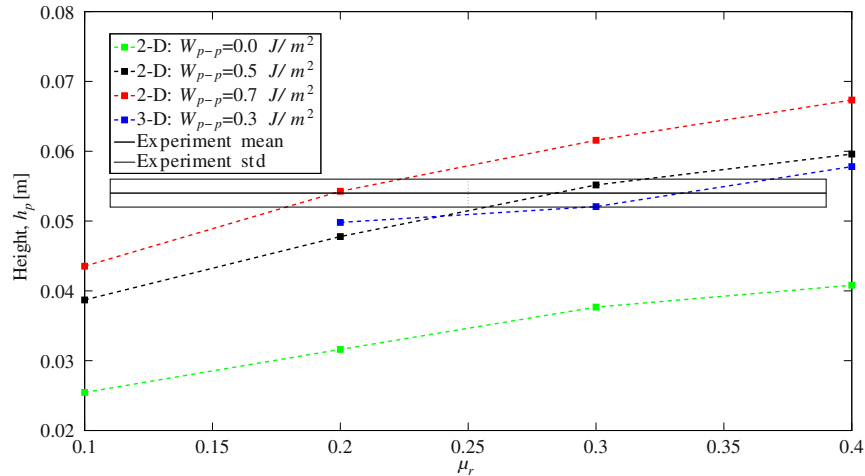


Fig. 8. The height of the simulated sand pile (h_p) as function of the particle-particle rolling resistance ($\mu_{r,p-p}$). The black line is the mean height of the green sand pile experiment of $h_p = 0.054 \pm 0.002$ m with standard deviation of $\sigma = 0.002$ m (the two grey lines). 2-D DEM simulations have the settings of the cohesion value $W_{p-p} = 0$ J/m² (green dotted line), $W_{p-p} = 0.5$ J/m² (black dotted line) and $W_{p-p} = 0.7$ J/m² (red dotted line) all values simulated for the four rolling resistances of $\mu_{r,p-p} = 0.1$, $\mu_{r,p-p} = 0.2$, $\mu_{r,p-p} = 0.3$, $\mu_{r,p-p} = 0.4$ and a particle-particle static friction coefficient of $\mu_{s,p-p} = 0.5$. DEM simulations for the 3-D simulations have the settings of the cohesion value $W_{p-p} = 0.3$ J/m² (blue dotted line) for the three rolling resistances of $\mu_{r,p-p} = 0.2$, $\mu_{r,p-p} = 0.3$, $\mu_{r,p-p} = 0.4$ and a particle-particle static friction coefficient of $\mu_{s,p-p} = 0.5$. (For interpretation of the references to color in this figure legend, the reader is referred to the web version of this article.)

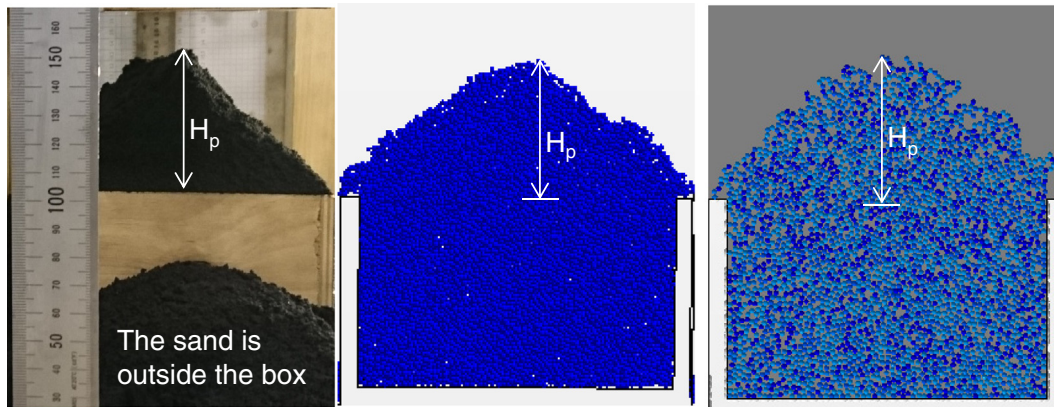


Fig. 9. (left) The sand pile experiment is compared to selected simulations, (middle) the 3-D simulation with particle-particle cohesion of $W_{p-p} = 0.3$ J/m², rolling resistance $\mu_{r,p-p} = 0.3$ and (right) the 2-D simulation particle-particle cohesion of $W_{p-p} = 0.7$ J/m², rolling resistance $\mu_{r,p-p} = 0.2$.

Table 3
The material properties of the 2-D and 3-D DEM simulations of the DISAMATIC process.

Material properties	Value
Particle-Wall static friction, ($\mu_{s,p-w}$)	0.35
Particle-Particle rolling friction coefficient ($\mu_{r,p-p}$)	0.3
Particle-Particle rolling friction coefficient ($\mu_{r,p-w}$)	Not applied
Particle-Wall cohesion work (W_{p-w})	Not applied
2-D specification	
Particle-Particle static friction, ($\mu_{s,p-p}$)	0.50, 0.75
Cohesion work (W_{p-p})	0.5 J/m ²
2-D Particle-Wall sensitivity analysis ^a	
Particle-Wall interaction parameters ($\mu_{r,p-w}, W_{p-w}$)	(0.3, 0.1 J/m ²), (0.5, 0.5 J/m ²)
3-D specification	
Particle-Particle static friction, ($\mu_{s,p-p}$)	0.50, 0.75 ^b
Cohesion work (W_{p-p})	0.3 J/m ²

^a A sensitivity study of the particle-wall interaction with respect to the rolling resistance ($\mu_{r,p-w}$) and the cohesion value (W_{p-w}) is conducted for one of the 2-D simulations of the DISAMATIC process. The 2-D particle-wall sensitivity analysis had the particle-particle values as the other 2-D simulations with $\mu_{s,p-p} = 0.50$ and is only investigated for the compressed air pressure of 2.0 bar experiment.

^b For the 3-D simulation with the particle-particle value static friction of $\mu_{s,p-p} = 0.75$ is only applied for simulating the 2.0 bar experiment.

The camera was run at 240 fps and the sand shot with the compressed air pressures for the successive trials were 2.0 bar, 2.5 bar and 3.0 bar.

5.1. The experimental video footage flow dynamics (t_1 - t_6)

In Fig. 10, the progression of the sand shot in the chamber can be followed and the shape of the sand pile can be seen for the compressed air pressure of 2.0 bar. Eight filling times are defined and denoted t_1 - t_8 , where the times t_1 , t_3 , t_5 and t_7 denote when the sand pile reaches cavity 1, 2, 3 and 4 respectively. The times t_2 , t_4 and t_6 denote when the sand pile reaches the bottom corners of ribs 1, 2 and 3 respectively and t_8 when the mould chamber is completely full. The video images at these eight times are shown for 2.0 bar in the following Fig. 10.

The times t_1 - t_8 for all three experiments can be seen in Fig. 11.

In Fig. 11 it is evident that varying the air pressure affects the flow pattern. The filling times for completion of the sand shots were $t_8 = 0.74$ s for 2 bar (black curve), $t_8 = 0.65$ s for 2.5 bar (red curve) and $t_8 = 0.64$ s for 3 bar (blue curve). The filling times (t_1 - t_8) and the area filled with green sand in the mould were used in the following sub-section to fit the three vertical inlet velocities and particle flow rates for the sand slot in the DEM simulations of the DISAMATIC process.

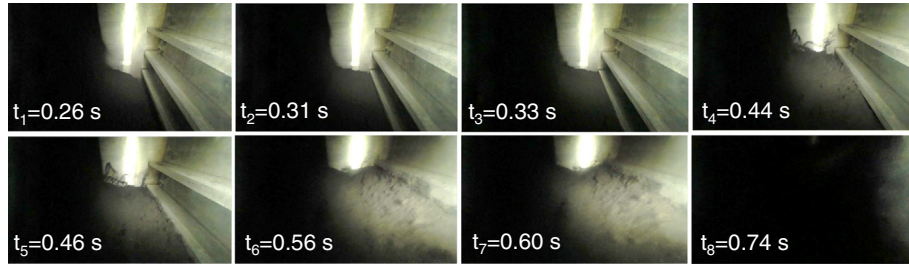


Fig. 10. The progression of the flow front starts from the upper left going to the lower right. From the experimental video footage shot with the air pressure of 2.0 bar.

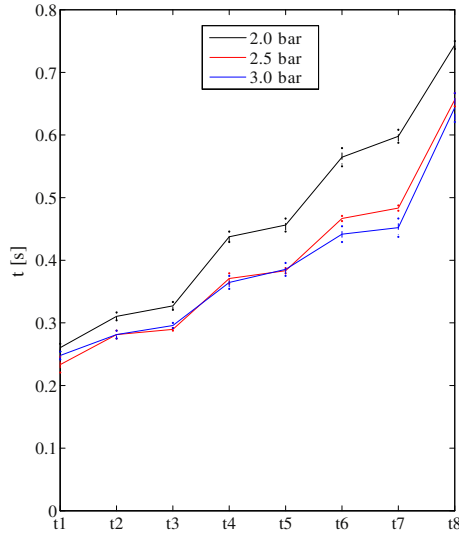
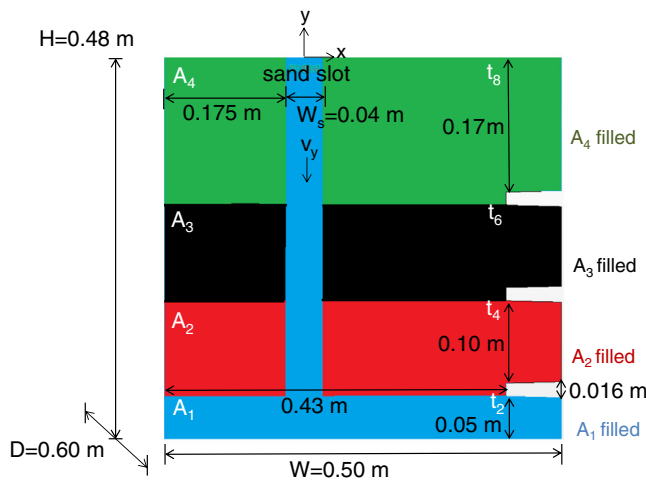


Fig. 11. The experimental progression of the sand pile flow front with respect to the eight filling times t_1 - t_8 for the compressed air pressures of 2.0 bar (black curve), 2.5 bar (red curve) and 3.0 bar (blue curve). (For interpretation of the references to color in this figure legend, the reader is referred to the web version of this article.)

5.2. The geometry of the DISAMATIC process simulation

The reference geometry of the chamber is shown in Fig. 1 and Fig. 12 (left). These figures show the mould chamber with three ribs mounted



on the fixed pattern plate forming four cavities positioned on the right hand side. The cross section in the middle of the chamber depth is first imported as a CAD file and subsequently selected for a 2-D section simulation and a 3-D slice simulation. The sand enters the chamber at the intersection between the hopper and chamber which is denoted the “sand slot”. The dimension of the chamber is $W \times H \times D = 0.48 \text{ m} \times 0.50 \text{ m} \times 0.60 \text{ m}$ and the sand slot has a width of $W_s = 0.04 \text{ m}$ and a depth of 0.54 m and is centred at the middle of the chamber depth. The flow is modelled as a section (2-D) placed in the middle of the chamber depth. The 3-D slice simulation has a depth of 0.04 m placed around the middle of the chamber depth and applying a periodic boundary in the z-direction (depth direction).

5.3. Calculating the sand slot velocity and the particle flow rate

The sand slot inlet velocity, $v_y(t)$ in the DEM simulations is fitted from the experimental video footage cf. e.g., Fig. 10 with respect to the filling times t_2, t_4, t_6, t_8 . The four inlet velocities (v_1, v_2, v_3, v_4) are calculated from the four filled areas (A_1, A_2, A_3, A_4) divided by the filling times of the four areas ($t_2, t_4-t_2, t_6-t_4, t_8-t_6$) and the sand slot width (W_s). The velocities (v_1, v_2, v_3, v_4) are assumed to vary linearly in time with a constant final velocity of v_4 , cf. Fig. 12 (right).

The particle flow rate (particle/s) is obtained from the sand slot velocity from the area of the sand slot, the ideal particle packing fraction (hexagonal packing fraction), and radius of the particle.

5.4. Particle velocity distribution

The initial particle velocity in the vertical direction is given by the sand slot inlet velocity ($v_y(t)$) adding a normally distributed random

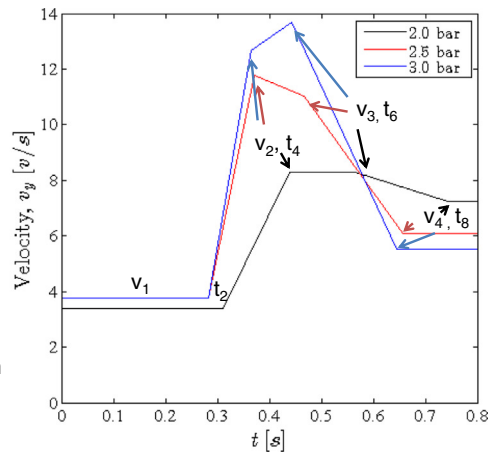


Fig. 12. (Left) From the green sand filling time of the four areas A_1 - A_4 (A_1 blue, A_2 red, A_3 black, A_4 green), four velocities (v_1 - v_4) can be calculated with the four selected time intervals $[0 \leq t \leq t_2, t_2 \leq t \leq t_4, t_4 \leq t \leq t_6, t_6 \leq t \leq t_8]$. (Right) The four velocity intervals are illustrated for the velocities (v_1, v_2, v_3, v_4) and are assumed to vary linearly in time with a constant final velocity of v_4 . (For interpretation of the references to color in this figure legend, the reader is referred to the web version of this article.)

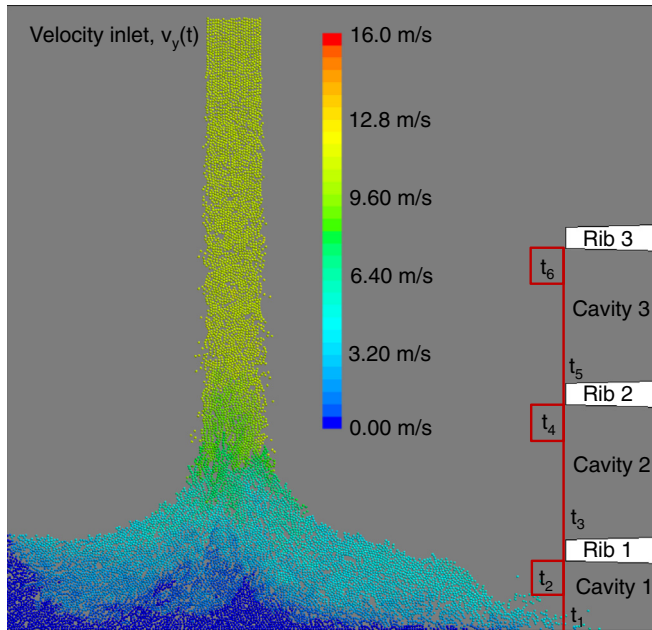


Fig. 13. Definition of the six filling times (t_1 – t_6): The times t_1 , t_3 and t_5 in the simulations are defined as when one particle enter cavity 1, cavity 2 and cavity 3 respectively. The times t_2 , t_4 and t_6 in the simulations are defined as when one particle enters the small boxes (red boxes with area of 100 mm²) at the rib edge of cavity 1, cavity 2 and cavity 3 respectively. The magnitude of the velocity has been plotted with a scaling of 0–16 m/s with the scale going from minimum dark blue, 0 m/s to the maximum velocity red 16 m/s. (For interpretation of the references to color in this figure legend, the reader is referred to the web version of this article.)

fluctuation with zero mean and standard deviation 0.1 m/s truncated at ± 0.2 m/s. A similar perturbation is added to the horizontal velocity ($v_x(t)$) with a mean of 0.0 m/s and with a maximum fluctuation of ± 1.0 m/s. The fluctuations emulate the random nature of the green sand flow in the chamber.

5.5. Definition of the filling times (t_1 – t_6) for the DEM simulation of the DISMATIC process

The filling times t_1 – t_8 are measured in the experiment, but only t_1 – t_6 are defined for the simulations as seen in Fig. 13.

In Fig. 13, the time intervals are defined as when a particle crosses the red lines and goes into the boxes (t_2 , t_4 , t_6) and cavities (t_1 , t_3 , t_5).

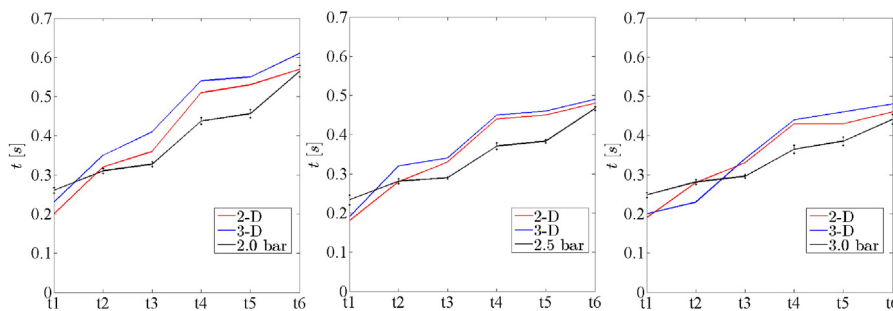


Fig. 14. Filling times obtained for 2.0 bar, 2.5 bar and 3.0 bar (from left to right). Experiments (black line), calibrated DEM simulations: 2-D (red line) and 3-D (blue line). (For interpretation of the references to color in this figure legend, the reader is referred to the web version of this article.)

6. Results of the simulation and the experiment for the DISMATIC process

6.1. Comparison of the selected times (t_1 – t_6) for the simulation versus the experiments

The simulations are compared to the video footage with respect to the six time intervals (t_1 – t_6) in Fig. 14. The simulated filling times of (t_1 – t_6) are in general in good agreement with the experimental values with small differences for the filling of t_1 and t_4 – t_5 as shown in Fig. 14. The 2-D simulation with increased particle–particle static friction coefficient of $\mu_{s, p-p} = 0.75$ (not shown) predicts filling times with deviation less than 10% of the reference simulation ($\mu_{s, p-p} = 0.50$). Similar small deviations are observed in 3-D when increasing the particle–particle static friction coefficient from $\mu_{s, p-p} = 0.50$ to $\mu_{s, p-p} = 0.75$.

In addition the particle–wall sensitivity analysis simulated in 2-D for the compressed air pressure of 2.0 bar predicts filling times with deviation less than 5.0% of the reference simulation.

6.2. The sand flow profile and dynamics of the flow

In Figs. 15–17 to Fig. 17, the experiments (left) and simulations (to the right) are presented for the three selected times t_2 , t_4 and t_6 and the contour of the flow profile of the sand can also be seen on the rear wall of the experiments.

In general for Figs. 15–17 the simulations show similar behaviour and filling times (t_2 , t_4) as the corresponding video footage rear wall profile for the three compressed air pressures. The filling time of t_4 is consistently longer for the simulations than the experiment. Generally the sand is observed to move more dynamically in the vertical direction for both the 2-D and 3-D simulations than in the experiments which results in stronger curvature of the flow front. The 3-D simulations predict longer filling times than the corresponding 2-D simulations.

In Fig. 18 the dynamics of the filling in the top of the chamber is investigated for the different air pressures. A slower deposition of the green sand in the larger top cavity can be seen in Fig. 18 for the 3-D simulations compared to the 2-D simulations. For 3.0 bar (Fig. 18 to the right) the 2-D has more energy than the corresponding 3-D, especially for later times where the green sand interferes with the particle jet coming from the sand slot. In general a larger scatter of particles is observed in the 3-D simulations than in the 2-D simulation, due to the extra degrees of freedom [8]. Compared to the 2.0 bar simulation a more chaotic flow front is observed for the simulated air pressures of 2.5 bar and 3 bar where the sloshing upwards at the two sides is more pronounced cf. Fig. 18.

For 2-D simulations the particle–particle static friction coefficient of $\mu_{s, p-p} = 0.75$ had virtually the same qualitative behaviour

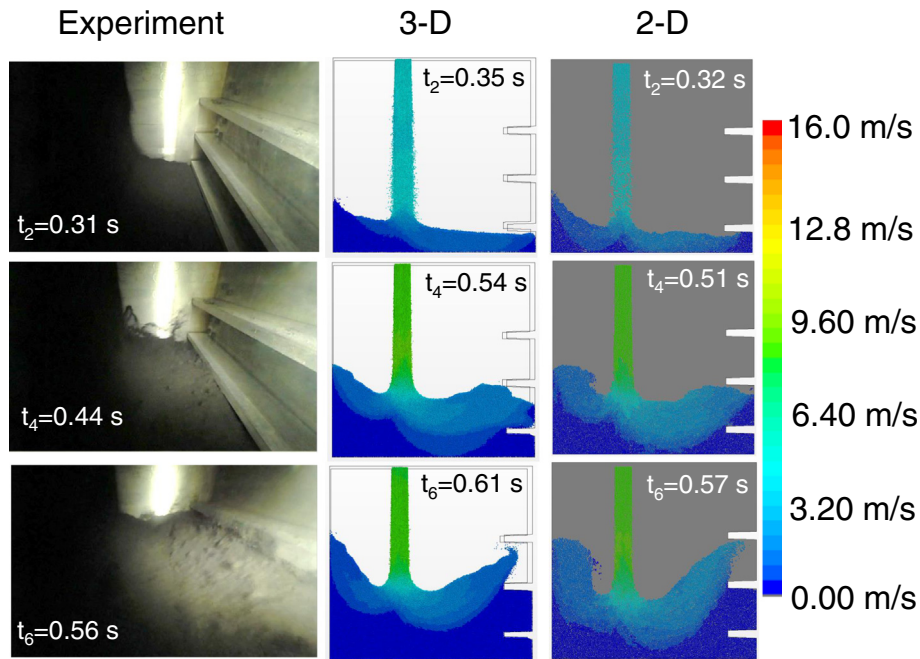


Fig. 15. Flow contours obtained for the compressed air pressure of 2.0 bar: (left) The experimental video footage, (middle) the 3-D simulation $\mu_s = 0.50$, (right) the 2-D simulation $\mu_s = 0.50$. The experiments and simulations are all presented for the three selected times t_2 , t_4 and t_6 (from the upper figure to the lower figure) and the contour of the flow profile of the sand can also be seen on the rear wall. The magnitude of the velocity is plotted with a scaling of 0–16 m/s.

as $\mu_{s-p} = 0.50$ shown in Figs. 15–18. For the particle-wall sensitivity study in the 2-D simulation of the compressed air pressure of 2.0 bar, incorporating the rolling resistance and cohesion had virtually the same qualitative behaviour as the reference simulation.

7. Conclusion

The main findings of the discrete element method for modelling green sand flow during production of DISA moulds are.

- The DEM models material properties was found from the experiment, where cohesion simulates the bonding effect of bentonite and water content in the creation of the sand pile showing an increase in height for the increased cohesion. The 2-D and 3-D simulation of the sand pile is in good agreement with the sand pile experiment.
- The behaviour of the filling time of the cavities in the mould is similar to the three experiments. The dynamic flow behaviour of the particles in the simulations is in general similar to that of the DISAMATIC process sand shot. More specifically, with

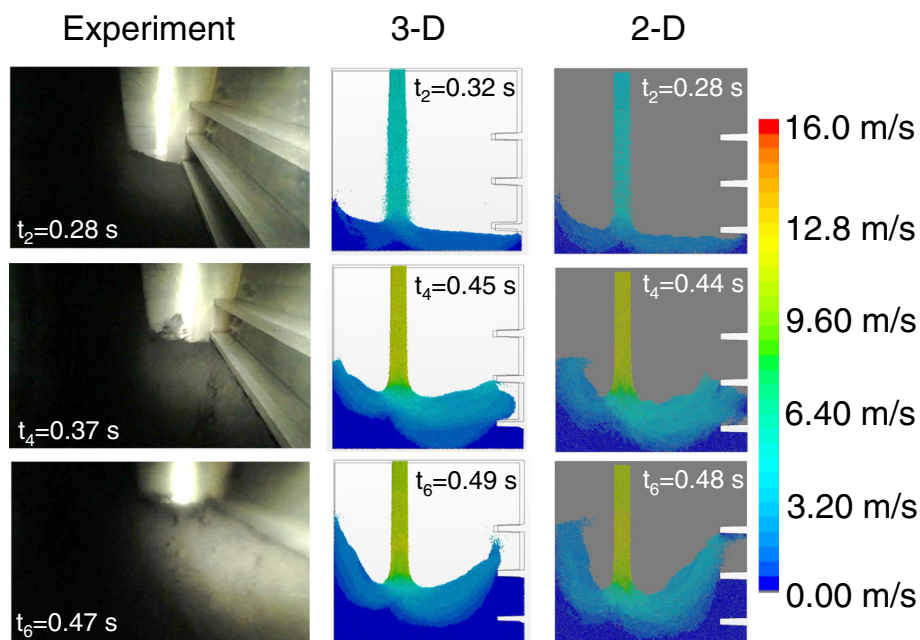


Fig. 16. Flow contours obtained for the compressed air pressure of 2.5 bar: (left) The experimental video footage, (middle) the 3-D simulation $\mu_s = 0.50$, (right) the 2-D simulation $\mu_s = 0.50$. The experiments and simulations are all presented for the three selected times t_2 , t_4 and t_6 (from the upper figure to the lower figure) and the contour of the flow profile of the sand can also be seen on the rear wall. The magnitude of the velocity is plotted with a scaling of 0–16 m/s.

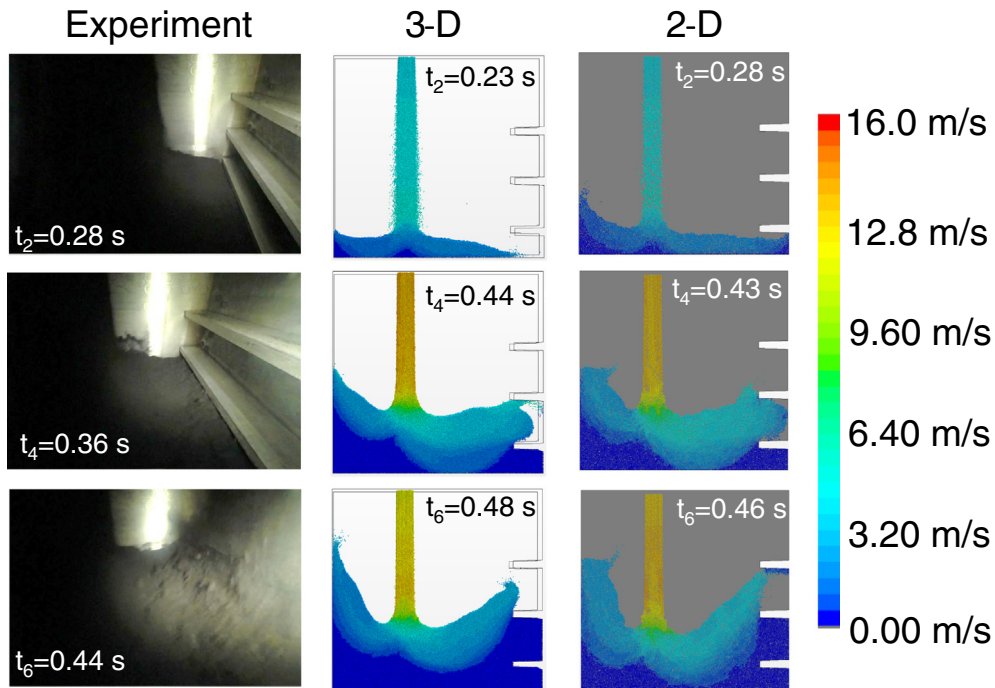


Fig. 17. Flow contours obtained for the compressed air pressure of 3.0 bar: (left) The experimental video footage, (middle) the 3-D simulation $\mu_s = 0.50$, (right) the 2-D simulation $\mu_s = 0.50$. The experiments and simulations are all presented for the three selected times t_2 , t_4 and t_6 (from the upper figure to the lower figure) and the contour of the flow profile of the sand can also be seen on the rear wall. The magnitude of the velocity is plotted with a scaling of 0–16 m/s.

well selected coefficient of restitution, flow rate, damping coefficient, rolling resistance and static friction coefficient it is possible to simulate the experimental video footage very well. When the

model is calibrated the flow rate and the velocity are obviously important factors for the flow dynamics during the filling of the chamber.

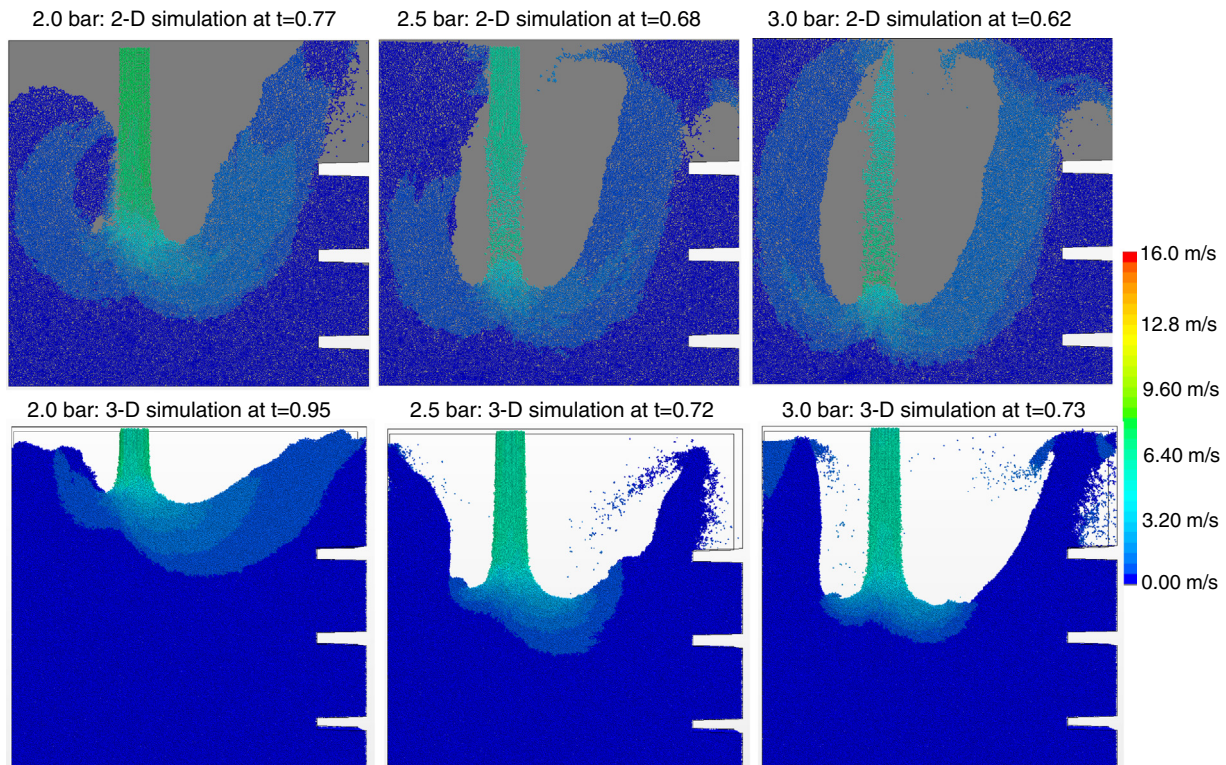


Fig. 18. The simulation for the three compressed air pressures 2.0 bar, 2.5 bar and 3.0 bar from the left to the right at (left), (middle), (right) the 2-D simulation is placed in the top and the 3-D simulation is placed in the bottom. In the top for the 2-D simulation when the sand reaches the top at $t = 0.77$ for (left), at $t = 0.68$ for (middle) and at $t = 0.62$ for (right). In the bottom for the 3-D simulation when the sand reaches the top at $t = 0.95$ for (left), at $t = 0.72$ for (middle) and at $t = 0.73$ for (right). The magnitude of the velocity is plotted with a scaling of 0–16 m/s the scale going from minimum dark blue, 0 m/s to the maximum velocity red 16 m/s.

- The increased scattering in the simulations also might be due to a smaller selected cohesion value of the 3-D simulations compared to the 2-D simulations. Although differences are seen from 2-D to the 3-D simulation the results remains in good agreement and the fast execution of 2-D simulations can still be used for parameter studies in simple geometries.
- A sensitivity study of the particle-wall interaction parameters: the rolling resistance and cohesion was performed and it was found that the quantitative and qualitative behaviour are virtually the same as the reference 2-D DISAMATIC simulation. Thereby these particle-wall parameters are of lesser importance for simulating the DISAMATIC process.
- It is found that the geometrical configuration as well as the applied compressed air pressure is highly affecting the filling pattern of the mould. More specifically, the lower compressed air pressure of 2.0 bar gives a slower deposition of green sand in general and in the top cavities in particular. The compressed air pressure and thereby the green sand velocity is of great importance especially for the filling of the top part of the mould.

Funding

The study was supported by Innovation Fund Denmark project [Grant number. 1355-00087B] in collaboration with the Danish company "DISA Industries A/S" in the period 15-08-2013 to 15-08-2016.

Acknowledgement

A thanks to Lars Georg Kiørboe for the use of the Ring shear tester at DTU CHEMICAL ENGINEERING, Department of Chemical and Biochemical Engineering.

A thanks to Niels Tiedje at DTU MECHANICAL ENGINEERING Department of Mechanical Engineering for the use of the foundry equipment.

References

- [1] H.P. Zhu, Z.Y. Zhou, R.Y. Yang, A.B. Yu, Discrete particle simulation of particulate systems: a review of major applications and findings, *Chem. Eng. Sci.* 63 (2008) 5728–5770, <http://dx.doi.org/10.1016/j.ces.2008.08.006>.
- [2] H.P. Zhu, Z.Y. Zhou, R.Y. Yang, A.B. Yu, Discrete particle simulation of particulate systems: theoretical developments, *Chem. Eng. Sci.* 62 (2007) 3378–3396, <http://dx.doi.org/10.1016/j.ces.2006.12.089>.
- [3] A. Di Renzo, F.P. Di Maio, Comparison of contact-force models for the simulation of collisions in DEM-based granular flow codes, *Chem. Eng. Sci.* 59 (2004) 525–541, <http://dx.doi.org/10.1016/j.ces.2003.09.037>.
- [4] P.W. Cleary, Industrial particle flow modelling using discrete element method, *Eng. Comput.* 26 (2009) 698–743, <http://dx.doi.org/10.1108/02644400910975487>.
- [5] J.H. Walther, I.F. Sbalzarini, Large-scale parallel discrete element simulations of granular flow, *Eng. Comput.* 26 (2009) 688–697, <http://dx.doi.org/10.1108/02644400910975478>.
- [6] J.P. Longmore, P. Marais, M.M. Kuttel, Towards realistic and interactive sand simulation: a GPU-based framework, *Powder Technol.* 235 (2013) 983–1000, <http://dx.doi.org/10.1016/j.powtec.2012.10.056>.
- [7] N. Govender, D.N. Wilke, S. Kok, Blaze-DEMGPU: Modular High Performance DEM Framework for the GPU Architecture, *SoftwareX*, 2016 <http://dx.doi.org/10.1016/j.softx.2016.04.004>.
- [8] N. Govender, R.K. Rajamani, S. Kok, D.N. Wilke, Discrete element simulation of mill charge in 3D using the BLAZE-DEM GPU framework, *Miner. Eng.* 79 (2015) 152–168, <http://dx.doi.org/10.1016/j.mineng.2015.05.010>.
- [9] J. Rojek, F. Zarate, C.A. de Saracibar, C. Gilbourne, P. Verdor, Discrete element modelling and simulation of sand mould manufacture for the lost foam process, *Int. J. Numer. Methods Eng.* 62 (2005) 1421–1441, <http://dx.doi.org/10.1002/nme.1221>.
- [10] C.J. Coetzee, D.N.J. Els, Calibration of discrete element parameters and the modelling of silo discharge and bucket filling, *Comput. Electron. Agric.* 65 (2009) 198–212, <http://dx.doi.org/10.1016/j.compag.2008.10.002>.
- [11] H. Makino, Y. Maeda, H. Nomura, Computer simulation of various methods for green sand filling, *Trans. Am. Foundry Soc.* 110 (2002) 1–9.
- [12] Y. Maeda, Y. Maruoka, H. Makino, H. Nomura, Squeeze molding simulation using the distinct element method considering green sand properties, *J. Mater. Process. Technol.* 135 (2003) 172–178, [http://dx.doi.org/10.1016/S0924-0136\(02\)00872-5](http://dx.doi.org/10.1016/S0924-0136(02)00872-5).
- [13] E. Hovad, Flow dynamics of green sand in the DISAMATIC moulding process using discrete element method (DEM), *IOP Conf. Ser. Mater. Sci. Eng.* 84 (2015).
- [14] A.F. Society, *Mold & Core Test Handbook*, 4th Edition American Foundry Society, 2015.
- [15] D. Schulze, J. Schwedes, J.W. Carson, *Powders and Bulk Solids: Behavior, Characterization, Storage and Flow*, 2008 <http://dx.doi.org/10.1007/978-3-540-73768-1>.
- [16] D. Schulze, *Flow Properties of Powders and Bulk Solids*, Braunschweig/Wolfenbu Ttel, Ger. Univ, 2006 1–21 <http://dietmar-schulze.de/grdle1.pdf>.
- [17] STAR-CCM+, *USER GUIDE STAR-CCM+, Version 8.02*, 2013.
- [18] P.A. Cundall, O.D.L. Strack, A discrete numerical model for granular assemblies, *Géotechnique*, 29 (1979) 47–65, <http://dx.doi.org/10.1680/geot.1979.29.1.47>.
- [19] H. Hertz, Über die Berührung fester elastischer Körper, *J. Für Die Reine Und Angew. Math.* 171 (1881) 156–171, <http://dx.doi.org/10.1515/crll.1882.92.156>.
- [20] Y. Tsuji, T. Tanaka, T. Ishida, Lagrangian numerical simulation of plug flow of cohesionless particle in a horizontal pipe, *Powder Technol.* 71 (1992) 239–250.
- [21] D. Zhang, W.J. Whiten, The calculation of contact forces between particles using spring and damping models, *Powder Technol.* 88 (1996) 59–64, [http://dx.doi.org/10.1016/0032-5910\(96\)03104-X](http://dx.doi.org/10.1016/0032-5910(96)03104-X).
- [22] G. Hu, Z. Hu, B. Jian, L. Liu, H. Wan, On the determination of the damping coefficient of non-linear spring-dashpot system to model Hertz contact for simulation by discrete element method, *2010 WASE Int. Conf. Inf. Eng.* 295–298 (2010) <http://dx.doi.org/10.1109/ICIE.2010.247>.
- [23] Y.C. Zhou, B.D. Wright, R.Y. Yang, B.H. Xu, A.B. Yu, Rolling friction in the dynamic simulation of sandpile formation, *Physica A* 269 (1999) 536–553, [http://dx.doi.org/10.1016/S0378-4371\(99\)00183-1](http://dx.doi.org/10.1016/S0378-4371(99)00183-1).
- [24] J. Ai, J.F. Chen, J.M. Rotter, J.Y. Ooi, Assessment of rolling resistance models in discrete element simulations, *Powder Technol.* 206 (2011) 269–282, <http://dx.doi.org/10.1016/j.powtec.2010.09.030>.
- [25] K.L. Johnson, *Contact Mechanics*, 1985 <http://dx.doi.org/10.1115/1.3261297>.
- [26] L.E. Silbert, D. Ertas, G.S. Grest, T.C. Halsey, D. Levine, S.J. Plimpton, Granular flow down an inclined plane: Bagnold scaling and rheology, *Phys. Rev. E Stat. Nonlinear Soft Matter Phys.* 64 (2001) 051302, <http://dx.doi.org/10.1103/PhysRevE.64.051302>.
- [27] L. Rayleigh, On Waves Propagated along the Plane Surface of an Elastic Solid, *Proc. Lond. Math. Soc.* s1–17 (1885) 4–11, <http://dx.doi.org/10.1112/plms/s1-17.1.4>.
- [28] S. Timoshenko, *Theory of Elasticity*, 1986 <http://dx.doi.org/10.1007/BF00046464>.
- [29] J. Frost, M.J. Hillier, I. Holubec, *The mechanics of green molding sand*, *AFS Trans.* 75 (1967) 126–132.



E. Hovad, born in Fredericia, Denmark 1982, obtained his M.Sc. in Mathematical Modelling and Computing (MMC) from the Technical University of Denmark (DTU) in 2011 with selected courses related to scientific computing and fluid dynamics. He is currently working as an industrial PhD student simulating flow dynamics of green sand in the DISAMATIC moulding process, for the Danish company DISA Industries A/S and the Department of Mechanical Engineering at DTU.



J. Spangenberg, born in Denmark 1982, obtained his M.Sc. in civil engineering in 2009 and his Ph.D. in mechanical engineering in 2012 both from the Technical University of Denmark (DTU). Subsequently, he was a postdoctoral research associate at the civil and environmental engineering department at Princeton University until 2014 where he was appointed assistant professor at the mechanical engineering department at DTU. His research interests are computational fluid dynamics, complex fluids, granular materials and process optimization.



P. Larsen, Born in Denmark, 1971, obtained his M.Sc. in process technology in 1996 and his industrial PhD in 2004 from Technical University of Denmark (DTU) in collaboration with DISA Industries A/S. He has been working for DISA Industries A/S for the last 19 years in various positions. His has also been a supervisor for several Ph.d. projects, e.g. "New Sol-Gel coatings to improve casting quality".

J.H. Walther is professor of fluid mechanics at the Department of Mechanical Engineering at the Technical University of Denmark, and research associate at the Computational Science and Engineering Laboratory at ETH Zurich, Switzerland. His research areas include the development of high order Lagrangian methods in computational fluid dynamics, efficient implementation of these methods on modern computer architectures, and the generation and analysis of data through simulations for problems in fluid mechanics. Walther holds a PhD degree in mechanical engineering from the Technical University of Denmark.



J. Thorborg, born in Denmark 1972, studied at the Technical University of Denmark, where he obtained his M.Sc. in 1997 and his Ph.D. in 2001 in mechanical engineering. During his Ph.D. project and subsequent postdoctoral fellowship he worked in the field of solid mechanics and constitutive modelling of high temperature processes. He joined the development group at MAGMA GmbH in 2004 and today he is working as a research and developer on the MAGMA stress module.



J.H. Hattel, born in Copenhagen, Denmark 1965, obtained his M.Sc. in structural engineering in 1989 and his Ph.D. in mechanical engineering in 1993 both from the Technical University of Denmark (DTU). He currently holds a full professorship in modelling of manufacturing processes at the Department of Mechanical Engineering, DTU. His research interests are modelling of processes like casting, joining, composites manufacturing and additive manufacturing. This involves the use of computational methods within the disciplines of heat transfer, fluid dynamics, solid mechanics as well as materials science. Applications range from microelectronics over automotive industry to large structures like wind turbines.

PAPER 3

Accepted Manuscript

Cavity prediction in sand mould production applying the DISAMATIC process

Emil Hovad, Per Larsen, Jon Spangenberg, Jens H. Walther, Jesper Thorborg,
Jesper H. Hattel

PII: S0032-5910(17)30680-0
DOI: doi:[10.1016/j.powtec.2017.08.037](https://doi.org/10.1016/j.powtec.2017.08.037)
Reference: PTEC 12776

To appear in: *Powder Technology*

Received date: 27 March 2017
Revised date: 14 July 2017
Accepted date: 9 August 2017



Please cite this article as: Emil Hovad, Per Larsen, Jon Spangenberg, Jens H. Walther, Jesper Thorborg, Jesper H. Hattel, Cavity prediction in sand mould production applying the DISAMATIC process, *Powder Technology* (2017), doi:[10.1016/j.powtec.2017.08.037](https://doi.org/10.1016/j.powtec.2017.08.037)

This is a PDF file of an unedited manuscript that has been accepted for publication. As a service to our customers we are providing this early version of the manuscript. The manuscript will undergo copyediting, typesetting, and review of the resulting proof before it is published in its final form. Please note that during the production process errors may be discovered which could affect the content, and all legal disclaimers that apply to the journal pertain.

Cavity prediction in sand mould production applying the DISAMATIC process [☆]

Emil Hovad^{a,c}, Per Larsen^c, Jon Spangenberg^a, Jens H. Walther^{a,d}, Jesper Thorborg^{a,b}, Jesper H. Hattel^a

^aDepartment of Mechanical Engineering, Technical University of Denmark (DTU), Denmark. Produktionstorvet, Building 425, DK-2800 Kgs., Lyngby, Denmark.

^bMAGMA Giessereitechnologie GmbH, Kackertstr. 11, 52072 Aachen, Germany

^cDISA Industries A/S, Højager 8, Høje Taastr., 2630 Taastrup, Denmark

^dComputational Science and Engineering Laboratory, ETH Zurich, CH 8092, Switzerland

Abstract

The sand shot in the DISAMATIC process is simulated by the discrete element method (DEM) taking into account the influence and coupling of the airflow with computational fluid dynamics (CFD). The DEM model is calibrated by a ring shear test, a sand pile experiment and a slump test. Subsequently, the DEM model is used to model the propagation of the green sand inside the mold chamber and the results are compared to experimental video footage. The chamber contains two cavities designed to quantify the deposited mass of green sand. The deposition of green sand in these two cavities is investigated with three cases of different air vent settings which control the ventilation of the chamber. These settings resulted in different air- and particle-velocities as well as different accumulated masses in the cavities, which were successfully simulated by the model.

Keywords: DISAMATIC process, Sand casting, Green sand, Granular flow, Discrete element method

2010 MSC: 00-01, 99-00

[☆]Fully documented templates are available in the elsarticle package on CTAN.

*Corresponding author: Emil Hovad

Email address: emilh@mek.dtu.dk (Emil Hovad)

1. Introduction

The DISAMATIC process [1] is a sand casting process applying green sand as the molding material [2, 3]. The DISAMATIC process is typically used in the automotive industry to produce molds for metal castings in order to manufacture e.g. brake disks, differential cases and steering knuckles.

The DISAMATIC moulding process has been used since the early 1960s. Compared to conventional green sand moulding processes, it has a vertical parting line. Furthermore, it is a flaskless process, meaning there are no boxes supporting the moulds. The DISAMATIC moulding process is very productive compared to other processes, as it can produce up to 555 moulds per hour. Additionally, it can produce parts with low tolerances. Due to its efficiency and accuracy it is widespread used within the automotive sector.

The ever-rising demands to casting quality, especially within the automotive sector, lead among other things to higher demands to the mould quality. To comply with the higher demands to the mould quality, simulation tools come in handy in the development work having to be done. Until now most of the development work has been based on experience and a trial and error approach as no commercial simulation tools have been available for simulating the combined flow of green sand and air. The lack of commercial available simulation tools is partly driven by lack of material data of the green sand needed to describe the flow. Hence determination of material data has been a major part of this study.

The green sand consists mostly of quartz sand mixed with coal dust, bentonite (active clay) and water, which coats the sand grains to form a cohesive granular material where the green sand flow-ability is affected by the amount of bentonite and water. In [4] a regression model was applied to determine the relationship between the input value of the sand mixture, i.e active clay, dead clay, water content to the related output values of compactability, compressive strength, spalling strength and permeability. These relationships were developed from a DISAMATIC foundry. The green sand flow-ability was investigated in [5], [6] and the fluidized viscosity of green sand was investigated in

[7]. In [6] it was suggested that the green sand can be investigated as an yield stress material and an analytical derivation based on the yield stress material with additional overpressure similar to the conditions when the sand enters the chamber was made in [8]. Tri-axial tests have also been performed on green sand in order to obtain the yield locus in [9]. Uni-axial compression tests were made for green sand and the stress-strain curves were analysed in [10]. Green sand was tested with a ring shear tester obtaining the yield locus and a sand pile experiment in [11].

DEM simulations of the ring shear tester have been performed in [12] where the particle shape, cohesion and static friction were investigated with respect to the resulting tangential pre-shear stress and the peak stress (yield stress). A sensitivity study was performed in [13] simulating a Schulze ring shear tester studying the effect of several material parameters on the resulting tangential pre-shear stress. The resulting tangential pre-shear stress relationship to the particle-particle static friction coefficient ($\mu_{s,p-p}$) was asymptotic up to the value of $\mu_{s,p-p} < 0.70$ and a linear dependence was found on the parameters rolling friction coefficient ($\mu_{r,p-p}$) and the Young's modulus. A DEM adhesive elasto-plastic contact model was used to simulate uni-axial consolidation followed by unconfined compression to failure in [14].

A simulation of the sand casting process with a two phase continuum model has earlier been presented in [15] and continuum models have been designed to model granular materials as e.g. in [16, 17]. In [18] a multiphase model was applied to simulate a core shooting process numerically in 2-D and 3-D dimensions. The DISAMATIC process was first studied with a 2-D DEM model in [19] where the granular flow was compared to video footage. This study focused on the deflection of the sand flow causing "shadow effects" around the ribs placed in the geometry of the mould. The model applied a constant particle inlet velocity and particle diameters of 2 mm and 4 mm as representative sand particle clusters for the granular flow. In [11] the same geometry was investigated with a 2-D and 3-D DEM slice model applying the representative particle cluster diameter of 2 mm. A 2-D sensitivity study was performed with respect

to the particle-wall interaction which showed the particle-wall values to be of less importance for the flow behaviour and filling times than e.g. particle inlet velocity. The DEM model was calibrated from experiments (ring shear test and sand pile experiment) and afterwards a velocity function for the granular flow was found from video footage.

In this study the framework of [11] is applied for calibrating the DEM model using a ring shear tester to obtain the static friction coefficients and a sand pile experiment for calibrating the rolling resistance and cohesion value for the particle-particle interaction. Additionally the mass of the DEM particle is recalculated and a slump experiment is used for calibrating the rolling resistance for the particle-wall interaction. Finally a DEM model and a CFD-DEM model are tested by simulating the flow and deposition of green sand in the two cavities and subsequently compared to the experimental observations for the three cases of the air vent settings.

2. Governing equations

2.1. Granular flow: Discrete element method

The framework of [11] is applied in this work where the commercially available software of STAR-CCM+ [20] is used for simulating the DISAMATIC process.

2.1.1. Contact notation

The notation for the particle contact is from [21], where particle i and particle j in contact are denoted by their respective positions at $\{\vec{r}_i, \vec{r}_j\}$, the velocities $\{\vec{v}_i, \vec{v}_j\}$, the angular velocities of $\{\vec{\omega}_i, \vec{\omega}_j\}$ and the distance between the two particles is denoted $r_{ij} = \|\vec{r}_i - \vec{r}_j\|_2$. The position vector from particle j to i is $\vec{r}_{ij} = \vec{r}_i - \vec{r}_j$ and the normal overlap $\delta_{ij} = (R_i + R_j) - r_{ij} = 2R$ with a uniform radius of R for all the particles.

2.1.2. Normal contact force

The normal force on particle i from particle j can be found as,

$$\vec{F}_{n_{ij}} = \vec{n}_{ij} k_n \delta_{ij}^{\frac{3}{2}} - N_{n_{ij}} \vec{v}_{n_{ij}} + \vec{F}_{coh_{ij}} \quad (1)$$

$\vec{n}_{ij} = \frac{\vec{r}_{ij}}{r_{ij}}$ is the unit normal vector, $\vec{v}_{n_{ij}}$ is the relative normal velocity and δ_{ij} is the normal overlap. $N_{n_{ij}}$ is the normal non-linear damping coefficient, $F_{coh_{ij}}$ is the cohesion, K_n is the stiffness in the normal direction, $N_{n_{ij}}$ is the damping in the normal direction, for further details see [11]. The particle-particle constant cohesion force in the normal direction is,

$$\vec{F}_{coh_{ij}} = -1.5\pi R_{min} W \vec{n}_{ij} \quad (2)$$

$R_{min} = R$ is the minimum radius of contact, W is the cohesion parameter. The cohesion $\vec{F}_{coh_{ij}}$ selected is the Johnson-Kendall-Roberts (JKR) model from [22] with the factor of -1.5.

2.1.3. Tangential contact force

The tangential force on particle i from particle j can be found as,

$$\vec{F}_{t_{ij}} = K_t \frac{\vec{t}_{ij}}{\|\vec{t}_{ij}\|_2} \delta_{t_{ij}}^{\frac{3}{2}} - N_{t_{ij}} \vec{v}_{t_{ij}} + \vec{T}_{rol_{ij}} \quad (3)$$

\vec{t}_{ij} is the tangential direction of the overlap, $\delta_{t_{ij}}$ is the tangential overlap, K_t is the tangential stiffness, G_{eq} is the equivalent shear modulus, $N_{t_{ij}}$ is the tangential non-linear damping coefficient. The rolling resistance for the particle-particle interaction used is the constant torque method defined as,

$$\vec{T}_{rol_{ij}} = -\frac{\omega_{rel}}{|\omega_{rel}|} \mu_r R_{eq} |\vec{F}_{n_{ij}}| \quad (4)$$

The relative angular velocity between the two particles is defined as $\vec{\omega}_{rel} = \vec{\omega}_i - \vec{\omega}_j$ and the torque from the rolling resistance is $\vec{T}_{rol_{ij}}$.

Note that there is a maximal tangential force due to Coulomb's law,

$$\|\mu_s \vec{F}_{n_{ij}}\|_2 < \|\vec{F}_{t_{ij}}\|_2 \quad (5)$$

the particle-particle static friction coefficient is denoted $\mu_{s,p-p}$ and particle-wall static friction coefficient is denoted $\mu_{s,p-w}$.

2.1.4. Summing the forces

The total resultant force on particle i is then computed by summing the contributions of all particles j with which it currently interacts, thus:

$$\vec{F}_i^{tot} = m_i \vec{g} + \sum_j \left(\vec{F}_{n_{ij}} + \vec{F}_{t_{ij}} \right) \quad (6)$$

where \vec{g} is the acceleration due to gravity. The total torque acting on particle i is given by

$$\vec{T}_i^{tot} = -R_i \sum_j \vec{n}_{ij} \times \vec{F}_{t_{ij}} \quad (7)$$

From these two expressions the acceleration, velocity, position and rotation, are calculated by Newton's second law, numerically for each time step.

2.2. Air flow: Navier Stokes equations

The low air pressures (P) measured in the chamber during the sand shot and the corresponding low air velocities (\mathbf{v}_g) make the assumption of the air phase being an incompressible fluid valid for small values of the Mach number ≤ 0.3 . Then the continuity equation becomes,

$$\rho_g \frac{\partial}{\partial t} (\epsilon_g) + \rho_g \nabla \cdot (\epsilon_g \mathbf{v}_g) = 0 \quad (8)$$

where ϵ_g is the air volume fraction found from $\epsilon_g = \frac{V_g}{V_g + V_s}$ where V_g is the volume of the air phase and V_s is the volume of solid phase. Navier-Stokes equations for the incompressible air phase are,

$$\rho_g \frac{\partial}{\partial t} (\epsilon_g \mathbf{v}_g) + \rho_g \nabla \cdot (\epsilon_g \mathbf{v}_g \mathbf{v}_g) = -\epsilon_g \nabla P + \epsilon_g \rho_g \mathbf{g} - \nabla \cdot (\epsilon_g \boldsymbol{\tau}_g) - \mathbf{I}_f \quad (9)$$

where $\rho_g = 1.18415 \frac{\text{kg}}{\text{m}^3}$ is the density of the air phase, $\mathbf{g} = [0, -9.82, 0] \frac{\text{m}}{\text{s}^2}$ is gravity and the shear stress on the air is $\boldsymbol{\tau}_g$ where the air is assumed to be a Newtonian fluid with the dynamic viscosity of $\mu = 1.85508 \times 10^{-5} \text{ Pa} \cdot \text{s}$. The two-way coupling between the air phase and the solid phase is enforced via the inter-phase momentum transfer of \mathbf{I}_f due to the drag on the solid phase.

2.3. The inter-phase momentum transfer

A source smoothing method is applied for the inter-phase momentum transfer of \mathbf{I}_f which averages the momentum transfer from larger parts of the mesh to the solid phase stabilizing the simulations to ensure converging simulations. The drag force on the solid phase is,

$$\mathbf{F}_D = -\frac{1}{8}\pi d^2 \rho_g C_d (\mathbf{v}_g - \mathbf{u}) |\mathbf{v}_g - \mathbf{u}| \quad (10)$$

where \mathbf{u} is the velocity of the solid phase and d is the diameter of the particle. The interaction of the solid phase with the air phase is described by the Schiller-Naumann drag model,

$$C_d(Re_p) = \begin{cases} \frac{24}{Re_p} (1 + 0.15 Re_p^{0.687}), & Re_p \leq 10^3 \\ 0.44, & Re_p > 10^3 \end{cases} \quad (11)$$

where Re_p is the particle Reynolds number and it is defined as,

$$Re_p = \frac{\rho_g |\mathbf{v}_g - \mathbf{u}| d}{\mu} \quad (12)$$

where $|\mathbf{v}_g - \mathbf{u}|$ is the slip velocity.

2.4. Turbulence model

Modelling the air phase as a continuum is done by solving Navier Stokes equations with the finite volume method (FVM) applying a polyhedral mesh. The k- ϵ turbulence model is used and all the methods are described in [20].

3. The green sand tests and calibrating of the DEM model

The following green sand tests and calibrations of the DEM model are performed.

3.1. The water content test

The percentage of water content is found by heating a sample of green sand and measuring the mass of water which is lost. The details of the water content test also denoted the moisture determination is described in [3]. This is a standard test typically performed in a foundry.

3.2. The Schulze ring shear tester

The Schulze ring shear tester is applied for characterizing the flow of granular materials in order to obtain the yield locus and the wall yield locus. The test procedures can be found in [23, 24]. The particle-wall static friction coefficient ($\mu_{s,p-w}$) is acquired directly from the wall friction angle as demonstrated in [11]. The particle-particle static friction coefficient in the simulation is found directly from the linearized yield locus angle. The linearized yield locus angle is described in [11, 23, 24, 25].

3.3. The sand pile experiment and the DEM calibration.

The sand pile experiment is applied for characterizing and calibrating the DEM model with respect to the height of the sand pile (h_p) above the box cf. Fig. 1(left) and described in [11]. The parameters that are calibrated from the sand pile height are the particle-particle rolling resistance interaction ($\mu_{r,p-p}$) and the particle-particle cohesion value (W_{p-p}).

[Figure 1 about here.]

3.4. The compactability test

The compactability test described in [3, 11] is applied to characterize the green sand condition and this is the standard test performed in the foundries. The green sand is poured into the cylinder with a tube filler accessory, subsequently the mass is measured before the ramming and from this the loose density of the green sand ρ_{exp} is calculated cf. Fig. 1(middle). The compactability of the sand mixture is finally found by the rammer method described in [3]. The cylinder has a height of $H_{cyl} = 0.12$ m and a diameter of $D_{cyl} = 0.05$ m.

3.5. Scaling the DEM particle density

The preliminary density of the DEM particles (ρ_{DEM}^\dagger) used in the sand pile simulations (Fig. 1(left)) is corrected to ρ_{DEM}^* to obtain a correct simulated

bulk density (ρ_{sim}^*) equal to the loose density measured before the ramming (ρ_{exp}) cf. Fig. 1(middle)

$$\rho_{DEM}^* \approx \rho_{DEM}^\dagger \left(\frac{\rho_{exp}}{\rho_{sim}} \right). \quad (13)$$

Here ρ_{sim} denotes the preliminary bulk density obtained from the sand pile simulation. Thus the subsequent slump calibration has the correct simulated bulk density (ρ_{sim}^*) shown in Fig. 1(right).

3.6. The slump cylinder experiment and the DEM calibration

The slump cylinder experiment is performed by lifting the cylinder rapidly upwards emulating the instantaneous wall opening in the simulation to finally find the slump length. The cylinder applied for the slump test is the same as the cylinder applied in the compactability test. The slump cylinder experiment is shown in Fig. 2(top) and the slump simulation is shown in Fig. 2(bottom).

[Figure 2 about here.]

When the green sand slump has settled the two diameters orthogonal to each other (l_x, l_y) are measured and the average is calculated for the final slump length l_p where the simulated slump length is found in a similar way from the algorithm first applied in [26] and described in [25]. The rolling resistance of the particle-wall interaction $\mu_{r,p-w}$ is calibrated with respect to the slump length. The slump simulation is applying the values found from the earlier calibrations together with the re-calculated DEM particle density (ρ_{DEM}^*).

For a correct density in the slump simulation the number of initial injected particles are found from the re-calculated DEM particle density (ρ_{DEM}^*) together with the experimental loose density in the cylinder (ρ) in the following way,

$$N \approx \frac{\rho_{sim} H_{cyl} \frac{\pi}{4} D_{cyl}^2}{\rho_{DEM}^* \frac{\pi}{6} d^3} \quad (14)$$

The particle are initially placed on an initial lattice with an initial random velocity to ensure a random packing.

4. The experimental tests of the DISAMATIC process

4.1. The DISAMATIC process

The DISAMATIC process is illustrated with a special setup in the chamber shown in Fig. 3 with two cavities on the left hand side each having a narrow opening for testing the ability of green sand to enter the two cavities. During the sand shot the compressed air in the air tank drives the sand flow vertically down from the hopper through the sand slot into the chamber filling the mold chamber and the two cavities.

[Figure 3 about here.]

In the casting process the sand mold is squeezed also, but in this experiment the swing plate on the left hand side is opened instead and the green sand is then brushed out of the cavities so that the mass of the green sand in the cavities can be measured at the end of each experiment. The flow inside the chamber is captured with the video camera (v_1) placed on the right hand side on the chamber (Pressure plate: PP) and photos are shown in Fig. 4 for eight stages of the sand shot.

[Figure 4 about here.]

The red light shown in Fig. 4(a) indicates when the valve between the air tank and the hopper is activated, this moment is defined as $t_{start} = 0$. A very short time after the valve activation the air pressure over the sand in the hopper starts to increase. Later during the sand shot, the sand starts flowing into the chamber shown in Fig. 4(a) and this moment is denoted t_0 . Seven lines are marked to quantify the seven filling times $t_1 - t_7$, which is defined as when the green sand reaches the seven lines as shown in Fig. 4(b)-(h).

In Fig. 5 the flow in the cavities is captured with the mini video cameras v_2 and v_3 where the filling times of the cavities are monitored as t_1 when the sand enters the cavity and t_2 when the camera is blocked by the green sand. The times for the two cavities are denoted the following way: For the bottom cavity $t_{b,1}$ and $t_{b,2}$ and for the top cavity $t_{t,1}$ and $t_{t,2}$.

[Figure 5 about here.]

4.2. The two air vent types

Two types of air vents are applied for ventilating the chamber where one type is placed in the chamber (a_c) and another type is placed on the SP side inside the cavities (a_p). Experiments for the air vents flow rate versus pressure drop are shown for the air vent in the chamber in Fig. 6(blue line) and for the air vents on the pattern plate in Fig. 6(black line). The pattern plate air vents are placed in the cavities.

[Figure 6 about here.]

The physical behaviour shown in Fig. 6 resembles the Darcy flow,

$$Q = -a\Delta p \quad (15)$$

where Q is the air flow rate and ΔP is the pressure difference across the air vent and a is the permeability of the air vent. The chamber air vent type has the value of $a_c = 1.274 \times 10^{-6} \frac{\text{m}^3}{\text{sPa}}$ and the air vent type placed in the cavities on the pattern plate has the value of $a_p = 2.34 \times 10^{-6} \frac{\text{m}^3}{\text{sPa}}$.

4.3. The air vent settings and the three test cases

The air vents and their positions are illustrated in Fig. 7 where a total of 294 air vents are opened and this is denoted case 1. There are 238 air vents of the type a_c where 112 air vents are placed at the top of the PP chamber side, 52 air vents are placed at the top of the SP side shown in Fig. 7(Chamber top view) and 2×37 air vents are placed on the chamber sides in Fig. 7(Chamber side view). On the pattern plate shown in Fig. 7(Swing plate view) each cavity has 28 cavity air vents of the type (a_p) where the purpose of the air vents in the cavities is to ensure a better ventilation and thereby transporting a larger amount of green sand into the cavities.

[Figure 7 about here.]

The three cases of the air vents settings are investigated with 2.0 bar overpressure where the three air vent settings are presented in table 1. The three air vents settings are: case 1 with all the air vents opened, case 2 with all the air vents closed in the top of the SP side and 5 closed side air vents and finally case 3 with 14 air vents closed in each pattern plate.

[Table 1 about here.]

The chamber measurements without the pattern plate have the width $W = 0.50$ m, height $H = 0.48$ m and depth $D = 0.60$ m. The cavities in the pattern plate has the depth $D_c = 0.57$ m and is also centred at the middle of the chamber depth. The orifice opening height of the cavities are set to 0.015 m and the height of the cavities is $H_c = 0.085$ m. The sand slot has the width $W_i = 0.04$ m and a depth $D_s = 0.54$ m and is centred at the middle of the chamber depth. The encapsulation areas for the air vents A_p , A_{SP} , A_{PP} are applied for calculating the porous resistance for the simulations together with the two types of air vents in eq. 18.

5. Simulation settings for the DISAMATIC process

5.1. The simulated geometry

[Figure 8 about here.]

The flow is modelled as a 3-D slice placed in the middle of the chamber shown in Fig. 8 with a slice depth of $D_s = 0.01$ m in the z-direction where this direction has symmetry. Thereby the side air vents are not simulated due to the slice geometry of the simulation.

5.2. Boundary conditions for the granular flow

5.2.1. DEM particle flow rate

The chamber is divided into the eight different volumes ($V_1 - V_8$) where $V_n = A_n D_s$ and the sand jet is included in the first volume (V_1) and thereby excluded from the other volumes as shown in Fig. 8. The volumes are filled with

green sand at the subsequent filling times ($t_1 - t_7$). From this the flow rates are calculated ($f_1 - f_7$) where the flow rate for the last area A_8 is assumed to be equal to the flow rate of f_7 . The particle flow rate function $f_y(t)$ in the DEM simulations is calculated from the volumes of the chamber $V_1 - V_7$ (neglecting the cavities on the swing plate) multiplied with the maximum particle packing fraction of approximately $\eta_h = 0.74$ divided with the volume of the particle and the individual flow rate intervals $\Delta t_1 = t_1$, $\Delta t_2 = t_2 - t_1$, $\Delta t_3 = t_3 - t_2$ etc. in the following way,

$$f_n = \frac{V_n \eta_h}{\frac{\pi}{6} d^3 \Delta t_n} \quad (16)$$

Volume conservation for the number of injected particles is established in the transition zone from the flow rate of f_n to f_{n+1} with a linear interpolation in the time interval of $\Delta t_{n,s} = \min(\Delta t_n, \Delta t_{n+1})$. The slope of linear interpolation in the time interval is calculated as $s_n = \frac{f_{n+1} - f_n}{\Delta t_{n,s}}$ and the particle flow rate function $f_y(t)$ then becomes,

$$\begin{aligned} f_y(t) &= f_n && \text{if } t_{n-1} + \frac{\Delta t_{n-1,s}}{2} \leq t \leq t_n - \frac{\Delta t_{n,s}}{2} \\ f_y(t) &= f_n + \left(t - \left(t_n - \frac{\Delta t_{n,s}}{2} \right) \right) s_n && \text{if } t_n - \frac{\Delta t_{n,s}}{2} \leq t \leq t_n + \frac{\Delta t_{n,s}}{2} \end{aligned} \quad (17)$$

The calculated flow rate of $f_y(t)$ is applied for all the following DEM particle inlet velocities. The filling times applied for obtaining the flow rate are shown in Fig. 9 where the full lines represent the selected experiment used for simulating each of the three cases.

5.2.2. DEM particle inlet velocity

The time dependent inlet particle velocity ($v_y(t)$) in the vertical y -direction is obtained from the estimated velocities $v_n = \frac{A_n}{t_n W_i}$, where the seven areas ($A_1 - A_7$) are shown in Fig. 8. The transition from velocity v_n to v_{n+1} is found using eq. 17.

[Figure 9 about here.]

The filling times ($t_1 - t_7$) used for calculating the inlet velocity are shown in Fig. 9 for the selected experiments. The resulting time dependent velocities

$v_y(t)$ for three simulations are shown in Fig. 10(a) where the spikes are due to the video frame rate 60 frames/s making it difficult to exactly determine the filling times shown in Fig. 9. To smooth out the spikes a two stage time dependent inlet velocity $v_{2y}(t)$ is constructed, where v_1 and v_2 are connected by eq. 17. The first constant velocity is obtained as previously whereas the second constant velocity v_2 is chosen among the velocities $v_y(t > t_1)$ with the longest duration cf. Fig. 10(a). An exception is made in case 3, where the second longest time duration is chosen to avoid an otherwise unrealistic velocity. The two stage time dependent inlet velocities are shown in Fig. 10(b). Lastly, two constant particle velocities of $v_y(t) = -5 \frac{\text{m}}{\text{s}}$ and of $v_y(t) = -7 \frac{\text{m}}{\text{s}}$ are considered. For each of the three cases all the four different vertical velocities are simulated for both pure DEM simulations (vacuum) and CFD-DEM (including air phase) and this gives a total of 24 simulations.

[Figure 10 about here.]

A normal distribution is applied for the horizontal velocity to emulate the random nature of the green sand flow in the chamber and was originally applied in [11]. Thus, the horizontal velocity $v_x(t)$ has a mean of $0.0 \frac{\text{m}}{\text{s}}$ and a standard deviation $0.1 \frac{\text{m}}{\text{s}}$ and a maximum fluctuation of $\pm 1.0 \frac{\text{m}}{\text{s}}$ as in [11].

5.3. Boundary conditions for the air flow

5.3.1. Air inlet pressure

In this study the focus is on simulating the flow of air and green sand in the chamber, the air inlet pressure boundary for the chamber is placed at the sand slot where the green sand also enters, as shown in Fig. 11. The air pressure at the boundary is obtained from the top pressure sensor shown in Fig. 7 (red circle).

5.3.2. Air outlets

A symmetry boundary is applied in the z -direction (depth direction) which resembles the conditions in the center of the mold during the sand shot and the

boundary is shown in Fig. 11. The mesh has a polyhedral structure with the cell size of $\Delta x = 0.025$ m giving the number of cells of around ≈ 9000 . There are 4 porous baffle interfaces in the chamber each having an elongated air channel with a pressure outlet set to 0 bar relative to the pressure of the inlet.

[Figure 11 about here.]

5.3.3. Air outlet: Darcy flow in the porous baffle

The DISAMATIC air vents from eq. 15 are set in parallel because the n air vents are positioned side by side in the areas (A),

$$\beta = \frac{A}{\rho_g a n} \quad (18)$$

β is the constant porous viscous resistance [20] and is determined by the air vent type (a), the number of air vents (n) over the cross sectional area (A) and the density of the fluid ρ_g . The placements and areas of the air vents are illustrated in Fig. 7 and for the simulation shown in Fig. 11. The outlet boundary settings for all the three cases are shown in table 2 where in case 2 and in case 3 a number of air vents are blocked and thereby the porous areas are changed together with β .

[Table 2 about here.]

5.4. Monitoring the simulated flow

The seven filling times $t_1 - t_7$ are monitored for the simulations and found from the particle filling of the seven volumes ($V_1 - V_7$). A volume V_n is filled when the minimum volume of particles V_p is above the packing fraction of 0.4 and thereby the filling time is monitored t_n .

The mass of the DEM particles in the cavities of the slice geometry D_s are monitored with respect to time and scaled with $\frac{D_c}{D_s} = 57$ due to the ratio of the simulated geometry depth D_s versus the experimental depth of the cavities D_c .

6. Results of the green sand tests and the calibrations

6.1. Results of the green sand tests

The result of particle-particle static friction coefficient and the particle-wall static friction coefficient from the ring shear test, the sand pile height, the green sand density, the slump length, the compactability and water content are shown in table 3.

[Table 3 about here.]

6.2. Calibration of the DEM model

6.2.1. General settings for all the DEM simulations

The radius of the DEM particle, coefficient of restitution, Poisson's ratio and Young's modulus are obtained the framework of [11] and listed in table 4. The particle-wall static friction coefficient applied in the simulation takes the value of $\mu_{s,p-w} = 0.33$ corresponding to the average value obtained from the ring shear tests for the green sand samples interaction with a stainless steel plate with the procedure described in [11]. The particle-particle static friction coefficient of $\mu_{s,p-p} = 0.57$ is obtained from the ring shear test's linearized yield locus angle, where all the parameters are listed in table 3.

[Table 4 about here.]

In the sand pile simulations it is assumed that the particle-wall rolling resistance is $\mu_{r,p-w} = 0.4$, this is a reasonable assumption based on prior simulations of the slump cylinder test. Note, that the particle-wall rolling resistance $\mu_{r,p-w}$ will be calibrated later in the slump cylinder simulation. The initial DEM particle density of $\rho_{DEM}^\dagger = 1750 \frac{\text{kg}}{\text{m}^3}$ is a reasonable assumption based on prior simulations of the sand pile density.

6.2.2. Results of the sand pile calibration

The experimental sand pile height is plotted together with the simulated sand pile heights in Fig. 12. The simulations with $\mu_{r,p-p} = 0.4$ and $W_{p-p} =$

$0.3 \frac{\text{J}}{\text{m}^2}$ (blue dotted line) and $\mu_{r,p-p} = 0.2$ and $W_{p-p} = 0.5 \frac{\text{J}}{\text{m}^2}$ (red dot) both give values of the height which are within the standard deviation of the measured height shown in Fig. 12. The selected parameters are $\mu_{r,p-p} = 0.4$ and $W_{p-p} = 0.3 \frac{\text{J}}{\text{m}^2}$ because they give a more conically shaped sand pile which was also observed in the experiments and described in [11].

[Figure 12 about here.]

6.2.3. Re-calculating the DEM particle density

In Fig. 13 the simulated sand pile density (ρ_{sim}) is compared to the experimental loose poured bulk density (ρ_{exp}) measured in the cylinder before the compactability test.

[Figure 13 about here.]

The chosen particle density for the sand pile simulation is $\rho_{DEM}^\dagger = 1750 \frac{\text{kg}}{\text{m}^3}$ which is too small for the selected h_p with the particle-particle value of $\mu_{r,p-p} = 0.4$ and $W_{p-p} = 0.3 \frac{\text{J}}{\text{m}^2}$ when compared to the bulk density measured in the cylinder. Therefore the density is re-calculated from eq. 13 which gives $\rho_{DEM}^* = 1900 \frac{\text{kg}}{\text{m}^3}$.

6.2.4. Results of the slump length simulation

The slump simulation is applied for determining the particle-wall rolling resistance $\mu_{r,p-w}$ with less than a standard deviation away from the the slump experiment l_p . The obtained values from the sand pile experiment of $\mu_{r,p-p} = 0.4$ and $W_{p-p} = 0.3 \frac{\text{J}}{\text{m}^2}$, the scaled DEM particle density of $\rho_{DEM}^* = 1900 \frac{\text{kg}}{\text{m}^3}$ and the number of particles injected into the cylinder which is found from eq. 3.6 are applied for the slump calibration.

[Figure 14 about here.]

The slump length result from the experiment is shown in Fig. 14 where the mean slump length l_p is the black diamond and the standard deviation is indicated by the two black horizontal lines. The particle-wall interaction of $\mu_{r,p-w} = 0.5$ is

below a standard deviation away from the average experimental slump length shown in Fig. 14.

6.2.5. Settings for the final simulations of the DISAMATIC process

The results from the calibration of the DEM model are listed in table 5 where the general simulation settings were presented in table 4.

[Table 5 about here.]

7. Results of the DISAMATIC process and simulations

7.1. Experimental air pressures measured from the sensors

For the selected sand shot in case 1, the measured air pressures can be seen as a function of time in Fig. 15. The air pressure builds up in the hopper (black line) in the start of the sand shot as the pressure decreases in the air tank (black dotted line) shown in Fig. 15. The pressure in the hopper starts to decrease after t_1 when the green sand has reached the bottom line l_1 of the chamber shown earlier in Fig. 4(b). The pressure decrease in the hopper is due to an equilibrium pressure is reached with the air tank and the air pressure now drops and the air flow propagates towards the chamber. In Fig. 15 the duration of time from t_0 to t_1 is longer than the subsequent next time intervals t_1 to t_2 etc. which is due to the larger pressure difference in the hopper versus the chamber. Video footage of the times $t_0 - t_7$ are shown in Fig. 4(a)-(h) for the selected sand shot in case 1. The filling times of the two cavities with the top cavity times $t_{t,1} - t_{t,2}$ (red) and the bottom cavity times $t_{b,1} - t_{b,2}$ (blue) are shown in Fig. 15.

[Figure 15 about here.]

The green sand starts entering the chamber at the monitored time of t_0 at this time the air pressure in the top of the chamber starts slowly to increase which is shown in Fig. 16 for the three selected cases. The air pressure in the top of the chamber shown in Fig. 16 is plotted from the time of t_0 where the green sand starts to enter the chamber, which is chosen to be the initial starting time for

the simulations. The three plotted pressures are applied as the sand slot inlet pressure in the CFD-DEM simulations with the minimum pressure of zero.

[Figure 16 about here.]

7.2. The filling times $t_0 - t_7$ of the chamber

The selected experimental and simulation filling times for case 1 are shown in Fig. 17 for the initial starting time of $t_0 = 0$.

[Figure 17 about here.]

The constant velocity of $7 \frac{\text{m}}{\text{s}}$ and $5 \frac{\text{m}}{\text{s}}$ have the shortest filling times in the initial part of the simulated sand shot $t_1 - t_4$ whereas the later filling times are too long $t_4 - t_7$. The filling times of the time dependent velocity $v_y(t)$ has the best agreement with the experiments and the two stage time dependent velocity function $v_{2y}(t)$ has the second best agreement with the experiment. The starting velocity of v_1 for both of the time dependent velocities were set too slow because the simulated filling time of t_1 was too long when compared to the experimental time shown in Fig. 17.

The filling times of the simulations and the selected experiment in case 1 are in good agreement with the other selected cases case 2 and case 3.

7.3. The sand deposited in the two cavities

[Table 6 about here.]

The deposited masses in the two cavities from the three cases and the selected experiments are listed in table 6. Considering all the experimental cases, case 2 showed the largest mass of deposited sand in both the top cavity and bottom cavity, being 1220 g and 933 g, respectively. As earlier mentioned one experiment was selected for simulation for each of the three cases considered.

The simulated masses in the two cavities are monitored with respect to time and compared to the selected experiment for the three cases shown in Fig. 18 - Fig. 20. For all the three cases of the CFD-DEM simulations the deposited

mass in the two cavities were overestimated when compared to the selected experiments. For case 3 the CFD-DEM simulations had better agreement with the selected experiment shown in Fig. 20 as compared to the other simulated cases.

[Figure 18 about here.]

[Figure 19 about here.]

For case 1 and case 2 the deposited mass in DEM simulations' for the two cavities are underestimated when compared to the selected experiments shown in Fig. 18 - Fig. 19, except for $v_y(t)$ in the top cavity shown in Fig. 19(b) plotted with the blue dotted line. In case 3 the DEM simulations has a good agreement with the selected experiment shown in Fig. 20, except for $v_y(t)$ in especially the top cavity which is shown in Fig. 20(b) which is due to the high particle velocity in the end of the simulation shown earlier in Fig. 10(a).

The inlet velocity for the DEM particles in the simulated sand shot was initially larger for the two constant inlet particle velocities as compared to the simulations with the time dependent velocities and thereby the particles entered earlier in the bottom cavity in all the three simulated cases with DEM.

[Figure 20 about here.]

7.4. The qualitative flow behaviour

The CFD-DEM simulated results of case 1 - 3 are shown in Fig. 21. The three simulations overestimated the mass in the cavities as when compared to the experiments and the DEM simulations. For the cases 1 and 2 simulated air velocities in the cavities were around $15 - 30 \frac{m}{s}$ as compared to case 3 where the cavity air velocities were around $10 - 20 \frac{m}{s}$. When comparing case 2 to both case 1 and case 3 in Fig. 21(middle figures) the particles have greater velocities and a more pronounced particle jet when the particles entered the bottom cavity. When comparing the simulations to the experiments shown in Fig. 21 all the simulations were in good agreement with the experiments with respect to the sand pile shape at the time $t=0.50$ s.

[Figure 21 about here.]

8. Conclusion

In the present paper the sand shot in the DISAMATIC process was investigated with three different air vent settings with respect to the mass of green sand deposited in two cavities, this investigation was performed experimentally as well as simulated. For the three cases all the simulations were performed with only the discrete element method (DEM) and additionally with the discrete element method (DEM) combined with computational fluid dynamics (CFD) denoted CFD-DEM. The CFD part took into account the influence and coupling of the airflow.

From the experiments the following conclusions can be drawn: With the standard air vent settings (case 1) where all the air vents were open, the experiments showed the second largest average mass in the top cavity as expected and the smallest average mass in the bottom cavity, although the average mass in the bottom cavity was only 5.1 % smaller as compared to the case with half of the air vents closed in the cavities (case 3). When 52 out of 164 of the air vents were blocked in the chamber (case 2) it gave an enhanced local air flow through the cavities and as expected the mass in the two cavities were largest with at least 21.2 % difference from the other cases. With half of the air vents blocked in the cavities (case 3), the smallest average mass in the top cavity was observed and the second smallest average mass in the bottom cavity was observed. Thus, the local air flow can be controlled e.g. by blocking air vents in the chamber and therefore increasing the local air flow through the air vents placed in the cavities as done in case 2. Decreasing the number of air vents in the cavities as done in case 3 decreased the deposited mass of green sand in the cavities as compared to case 2.

From the simulations the following conclusions can be drawn: With the chosen particle flow rates and particle velocities it was possible to simulate the deposited mass of green sand in the cavities and the qualitative flow behaviour. Larger inlet velocities for the DEM particles increased the final mass in the cavities.

The CFD-DEM simulations show larger masses in the cavities than the experimental results due to the air flow in the simulations still drags the particles into the cavities at the end of the sand shot. The side air vents could not be simulated due to the running time of the number of DEM particles when simulating a larger part of the chamber and thereby the volume of air that exits the cavities is correspondingly overestimated. In case 3 the CFD-DEM simulations were in better agreement with the selected experiment due to the lower air inlet pressure in the simulations which gave subsequently lower air velocities through the cavities.

Predictions of the mass of the green sand in the cavities were obtained with good agreement by the DEM simulations however with a tendency to underestimate the mass.

The CFD-DEM simulations predict the cavity fillings times better as compared to the DEM simulations although the CFD-DEM simulations still show too long filling times for the cavities as compared to the experiments. The results indicate that it is important to include the influence of the air flow in pneumatic transport of granular material including the 2-way coupling between the phases.

References

- [1] DISA Industries A/S, DISA 231/DISA 231 Var. Sand Moulding System Instructions for Use (9157).
- [2] J. Campbell, Castings (Second Edition), Butterworth-Heinemann, 2003. doi:10.1016/B978-075064790-8/50022-X. URL <http://www.sciencedirect.com/science/article/pii/B978075064790850022X>
- [3] Mold & Core Test Handbook, 4rd Edition, American Foundry Society, 2015.
- [4] R. Banchhor, S. Ganguly, Modeling of moulding sand characteristics in disamatic moulding line green sand casting process, Proceedings of BITCON-2015 Innovations For National Development. National Conference on: Innovations In Mechanical Engineering For Sustainable Development.
- [5] Y. Chang, H. Hocheng, The flowability of bentonite bonded green molding sand, Journal of Materials Processing Technology 113 (1-3) (2001) 238–244. doi:10.1016/S0924-0136(01)00639-2.
- [6] J. Bast, A new method for the measurement of flowability of green moulding sand, Archives of Metallurgy and Materials 58 (3) (2013) 945–952. doi:10.2478/amm-2013-0107.
- [7] J. Masoud, J. Spangenberg, E. Hovad, R. C. J. H. Hattel, K. I. Hartmann, D. Schuutz, Rheological characterization of green sand flow, Proceedings of the ASME 2016 International Mechanical Engineering Congress and Exposition.
- [8] E. Hovad, J. Spangenberg, P. Larsen, J. Thorborg, J. H. Hattel, An analytical solution describing the shape of a yield stress material subjected to an overpressure, AIP Conference Proceedings 1738 (1). doi:http:

[//dx.doi.org/10.1063/1.4951805](http://dx.doi.org/10.1063/1.4951805).

URL <http://scitation.aip.org/content/aip/proceeding/aipcp/10.1063/1.4951805>

- [9] J. Frost, J. Hiller, The mechanics of green sand moulding, AFS Trans 74 (1966) 177–186.
- [10] F. W. S. Scott M. Strobl, Using stress-strain curves to evaluate control clay bonded moldings sands.
URL <http://www.simpsongroup.com/tech/StressStrainCurves.pdf>
- [11] E. Hovad, J. Spangenberg, P. Larsen, J. Walther, J. Thorborg, J. Hattel, Simulating the disamatic process using the discrete element method a dynamical study of granular flow, Powder Technology 303 (2016) 228 – 240. doi:<http://dx.doi.org/10.1016/j.powtec.2016.09.039>.
URL <http://www.sciencedirect.com/science/article/pii/S0032591016306234>
- [12] O. Baran, A. DeGennaro, E. Rame, A. Wilkinson, Dem simulation of a schulze ring shear tester, AIP Conference Proceedings 1145 (2009) 409–412.
- [13] T. A. H. Simons, R. Weiler, S. Strege, S. Bensmann, M. Schilling, A. Kwade, A ring shear tester as calibration experiment for dem simulations in agitated mixers: a sensitivity study, Procedia Engineering 102 (2015) 741–748.
- [14] S. C. Thakur, J. P. Morrissey, J. Sun, J. F. Chen, J. Y. Ooi, Micromechanical analysis of cohesive granular materials using the discrete element method with an adhesive elasto-plastic contact model, Granular Matter 16 (3) (2014) 383–400. doi:[10.1007/s10035-014-0506-4](https://doi.org/10.1007/s10035-014-0506-4).
- [15] J. Wu, H. Li, W. Li, H. Makino, M. Hirata, Two phase flow analysis of aeration sand filling for green sand molding machine, International Foundry Research/Giessereiforschung 60 (1) (2008) 20–28.

- [16] D. G. Schaeffer, Instability in the evolution equations describing incompressible granular flow, *Journal of Differential Equations* 66 (1) (1987) 19–50. doi:10.1016/0022-0396(87)90038-6.
URL [http://linkinghub.elsevier.com/retrieve/pii/0022039687900386](http://linkinghub.elsevier.com/retrieve/pii/S0022039687900386)
- [17] P. C. Johnson, R. Jackson, Frictional-collisional constitutive relations for granular materials, with application to plane shearing, *Journal of Fluid Mechanics* 176 (1987) 67–93. doi:10.1017/S0022112087000570.
- [18] B. Winartomo, U. Vroomen, A. Buhig-Polacek, M. Pelzer, Multiphase modelling of core shooting process, *International Journal of Cast Metals Research* 18 (1) (2005) 13–20. doi:10.1179/136404605225022811.
- [19] E. Hovad, P. Larsen, J. H. Walther, J. Thorborg, J. H. Hattel, Flow dynamics of green sand in the disamatic moulding process using discrete element method (dem), *IOP Conference Series: Materials Science and Engineering* 84 (1) (2015) 012023.
- [20] STAR-CCM+, USER GUIDE STAR-CCM+, Version 8.02, 2013.
- [21] L. Silbert, D. Ertas, G. Grest, T. Halsey, D. Levine, S. Plimpton, Granular flow down an inclined plane: Bagnold scaling and rheology, *Physical Review E* 64 (5) (2001) 051302, 051302/1–051302/14. doi:10.1103/PhysRevE.64.051302.
- [22] K. L. Johnson, *Contact Mechanics*, 1985. doi:10.1115/1.3261297.
URL <http://www.amazon.fr/Contact-Mechanics-K-L-Johnson/dp/0521347963>
- [23] D. Schulze, J. Schwedes, J. W. Carson, *Powders and bulk solids: Behavior, characterization, storage and flow*, Springer Berlin Heidelberg, 2008. doi:10.1007/978-3-540-73768-1.
- [24] D. Schulze, *Flow properties of powders and bulk solids* (2006) 1–21.
URL <http://dietmar-schulze.de/grdle1.pdf>

- [25] E. Hovad, Numerical simulation of flow and compression of green sand, PHD-Thesis from Danish Technical University of Denmark (DTU).
- [26] J. Spangenberg, R. Cepuritis, E. Hovad, G. W. Scherer, S. Jacobsen, Shape effect of crushed sand filler on rheology: A preliminary experimental and numerical study, Rilem State of the Art Reports (2016) 193–202.

List of Figures

1	The sand pile simulation (left), the slump experiment (middle) and the slump simulation (right) are used to calibrating the particle static friction coefficient ($\mu_{r,p-p}$), the particle-particle cohesion value (W_{p-p}) and the DEM particle density (ρ_{DEM}^*). The simulated bulk density inside the box is denoted ρ_{sim} , the loose experimental density inside the cylinder is ρ_{exp} and the DEM particle density in the slump simulation is ρ_{DEM}^* . The edited figure to the left are originally from [11].	30
2	The slump cylinder test: experiment (top) and simulation (bottom). The slump filling (left), wall removal (middle) and the measurements of the slump length $l_p = \frac{1}{2}(l_x + l_y)$	31
3	The sand shot: (a) The hopper is filled with green sand. (b) The sand shot fills the mold chamber and cavities with green sand. (c) The swing plate (SP) opens to access the green sand in the two cavities. The air pressures are monitored by sensors in the air tank (light black cross), the shot valve (green cross), the hopper (black cross), the top of the chamber (red cross) and the bottom of the chamber (blue cross).	32
4	(a) Video footage of the green sand starting to enter the chamber where this occurrence is defined by the time t_0 . In the chamber seven equally spaced lines are drawn and indicated by the names $l_1 - l_7$. (b)-(h) When the sand passes the seven lines, the seven filling times are recorded $t_1 - t_7$	33
5	Video footage of the green sand filling of the cavity where a camera is placed in each cavity. (a) The red light indicates when the activation of the sand shot valve occurs. (b) The green sand entering the cavity t_1 . (c) The filling of cavity by the green sand blocking the camera view t_2	34
6	The air flow rate (Q) through the air vent as a function of the pressure drop (ΔP). The chamber air vent permeability is denoted a_c (blue line) and the pattern plate air vents permeability is denoted a_p (black line)	35
7	(a) The chamber top view showing the two air outlets - one on the SP side and one on the PP side. (b) The chamber side view with the placements of pressure sensors (top and bottom), side air vents, sand slot, SP side, PP side. (c) The chamber SP view with the pattern plate area for the two air vent areas indicated by name air outlet.	36
8	The flow rate found from the chamber measurements and the video footage in the chamber. The chamber is divided into the different areas ($A_1 - A_7$) that are filled with green sand at the subsequent times ($t_1 - t_7$).	37

9	The average experimental filling times of $t_0 - t_7$ for the three cases 1 - 3(dotted lines) and the three selected experimental filling times from cases 1 - 3(full lines).	38
10	The vertical inlet velocities for the simulations. The time dependent velocities $v_y(t)$ for the three cases. The two stage time dependent velocities $v_{2y}(t)$ and the constant velocities for the three cases	39
11	Placements of the boundaries.	40
12	The black diamond is the mean height of the green sand pile experiment of $0.054 \text{ m} \pm 0.002 \text{ m}$ (black horizontal lines).	41
13	Plot of the density: The black diamond is the mean density of the green sand pile experiment of $902 \pm 30 \frac{\text{kg}}{\text{m}^3}$ (thin black line). The DEM simulations were made for the settings for the cohesion value $W_{p-p} = 0.3 \frac{\text{J}}{\text{m}^2}$ (blue dotted line).	42
14	The black diamond is the mean length (diameter) of the green sand slump experiment of $0.186 \pm 0.0548 \text{ m}$ with the standard deviation of $\sigma = 5.48 \text{ mm}$ (thin black line).	43
15	Example from Case 1: The pressure as a function of time is shown in the positions listed from the top to the bottom: The air tank (black dotted line), the shot valve (green), the hopper (black line), the top of the chamber (red line) and the bottom of the chamber (blue line). The atmospheric pressure is used as the reference pressure. The filling times $t_0 - t_7$ in the chamber from the chamber camera v_1 (black dotted lines).	44
16	The three cases of experimental pressures measured at the top of the chamber as a function of time with the initial starting time of $t_0 = 0.0 \text{ s}$. The atmospheric pressure is used as the reference pressure.	45
17	The experimental and simulation filling times of $t_0 - t_7$ for case 1.	46
18	Case 1: The mass as a function of time for the bottom cavity (a) and for the top cavity (b).	47
19	Case 2: The mass as a function of time for the bottom cavity (a) and for the top cavity (b).	48
20	Case 3: The mass as a function of time for the bottom cavity (a) and for the top cavity (b).	49
21	For the selected three cases: The time dependent velocity $v_y(t)$ simulation at time $t=0.50 \text{ s}$. (Top) The velocity of the air phase. (Middle) The velocity of the particles. (Bottom) The experimental video footage at time $t=0.50 \text{ s}$	50

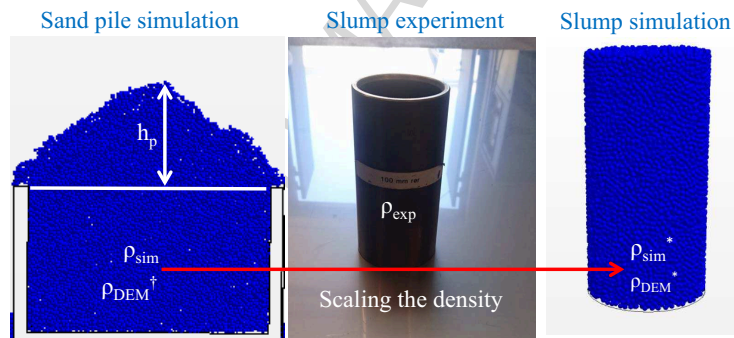


Figure 1: The sand pile simulation (left), the slump experiment (middle) and the slump simulation (right) are used to calibrating the particle static friction coefficient ($\mu_{r,p-p}$), the particle-particle cohesion value (W_{p-p}) and the DEM particle density (ρ_{DEM}^*). The simulated bulk density inside the box is denoted ρ_{sim} , the loose experimental density inside the cylinder is ρ_{exp} and the DEM particle density in the slump simulation is ρ_{DEM}^* . The edited figure to the left are originally from [11].

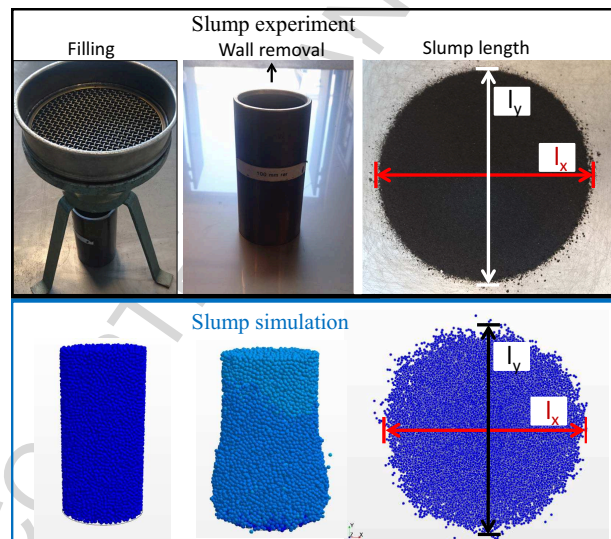


Figure 2: The slump cylinder test: experiment (top) and simulation (bottom). The slump filling (left), wall removal (middle) and the measurements of the slump length $l_p = \frac{1}{2}(l_x + l_y)$.

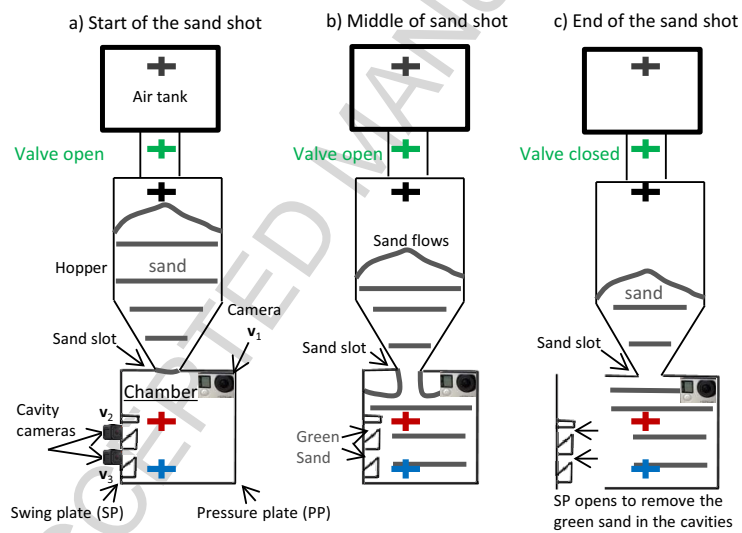


Figure 3: The sand shot: (a) The hopper is filled with green sand. (b) The sand shot fills the mold chamber and cavities with green sand. (c) The swing plate (SP) opens to access the green sand in the two cavities. The air pressures are monitored by sensors in the air tank (light black cross), the shot valve (green cross), the hopper (black cross), the top of the chamber (red cross) and the bottom of the chamber (blue cross).

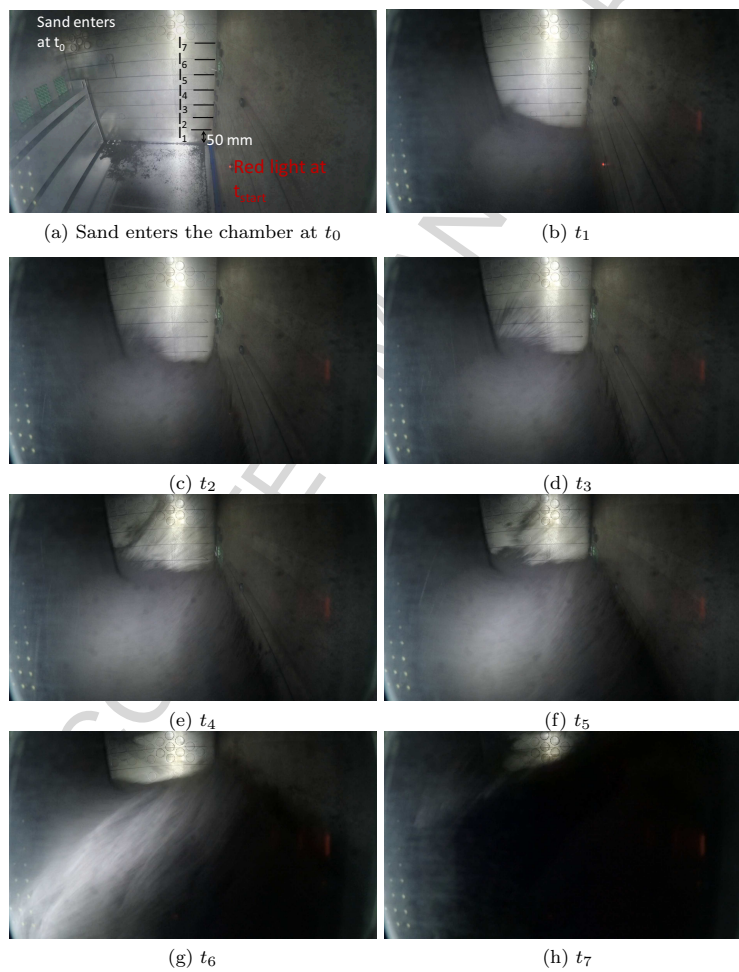


Figure 4: (a) Video footage of the green sand starting to enter the chamber where this occurrence is defined by the time t_0 . In the chamber seven equally spaced lines are drawn and indicated by the names $l_1 - l_7$. (b)-(h) When the sand passes the seven filling times are recorded $t_1 - t_7$.

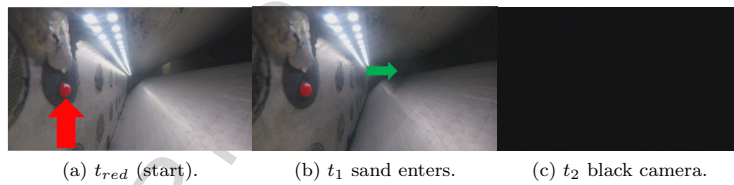


Figure 5: Video footage of the green sand filling of the cavity where a camera is placed in each cavity. (a) The red light indicates when the activation of the sand shot valve occurs. (b) The green sand entering the cavity t_1 . (c) The filling of cavity by the green sand blocking the camera view t_2 .

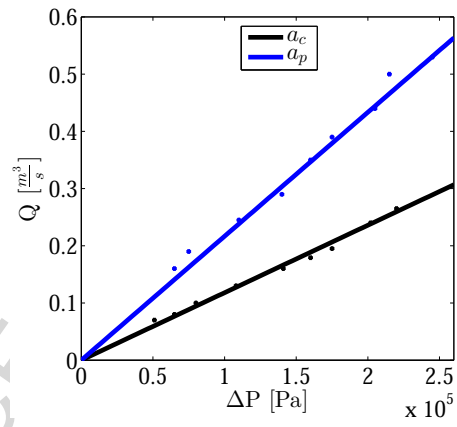


Figure 6: The air flow rate (Q) through the air vent as a function of the pressure drop (ΔP). The chamber air vent permeability is denoted a_c (blue line) and the pattern plate air vents permeability is denoted a_p (black line) .

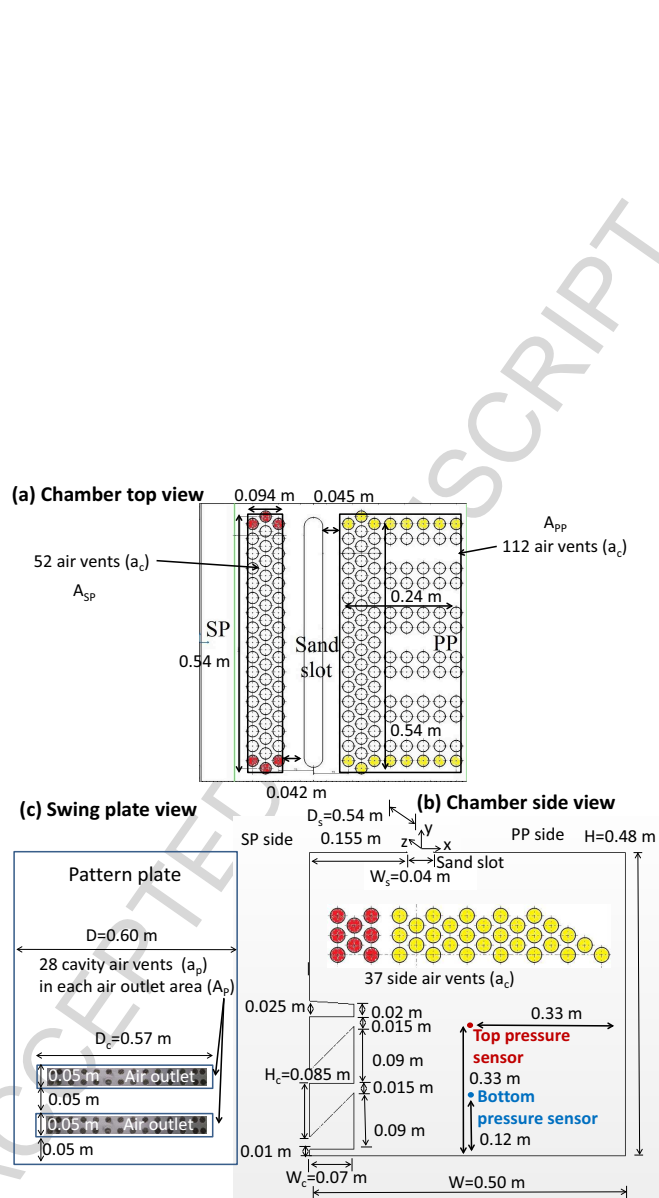


Figure 7: (a) The chamber top view showing the two air outlets - one on the SP side and one on the PP side. (b) The chamber side view with the placements of pressure sensors (top and bottom), side air vents, sand slot, SP side, PP side. (c) The chamber SP view with the pattern plate area for the two air vent areas indicated by name air outlet.

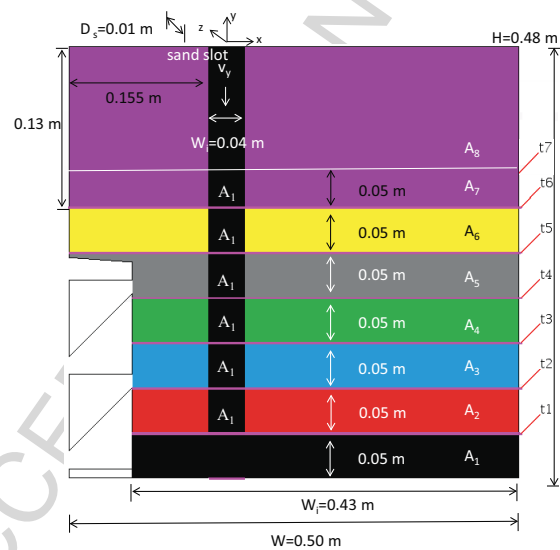


Figure 8: The flow rate found from the chamber measurements and the video footage in the chamber. The chamber is divided into the different areas ($A_1 - A_7$) that are filled with green sand at the subsequent times ($t_1 - t_7$).

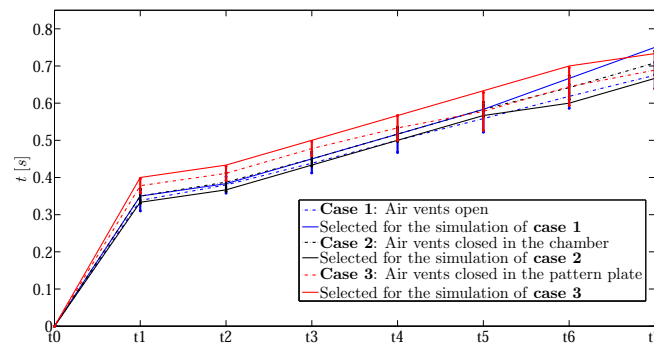


Figure 9: The average experimental filling times of $t_0 - t_7$ for the three cases 1 - 3 (dotted lines) and the three selected experimental filling times from cases 1 - 3 (full lines).

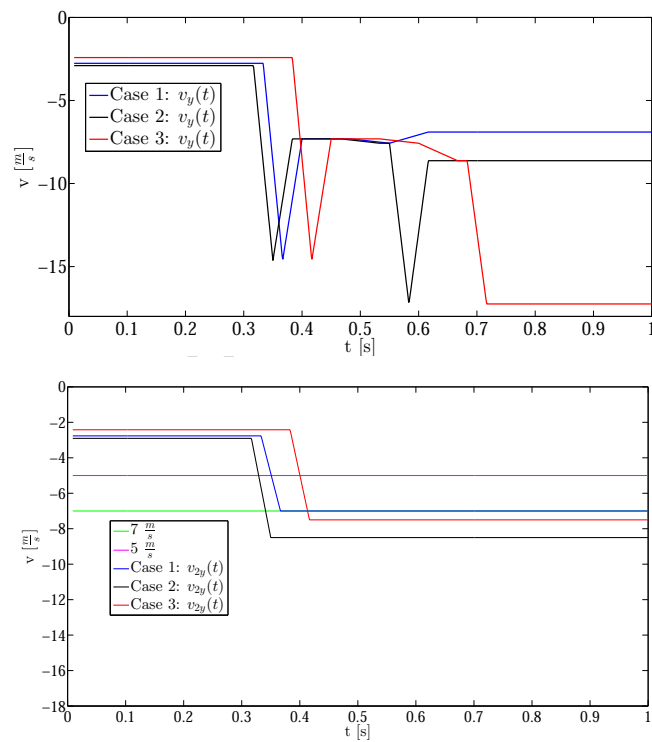


Figure 10: The vertical inlet velocities for the simulations. The time dependent velocities $v_y(t)$ for the three cases. The two stage time dependent velocities $v_{2y}(t)$ and the constant velocities for the three cases

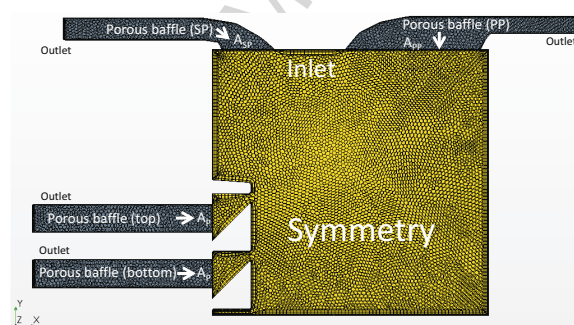


Figure 11: Placements of the boundaries.

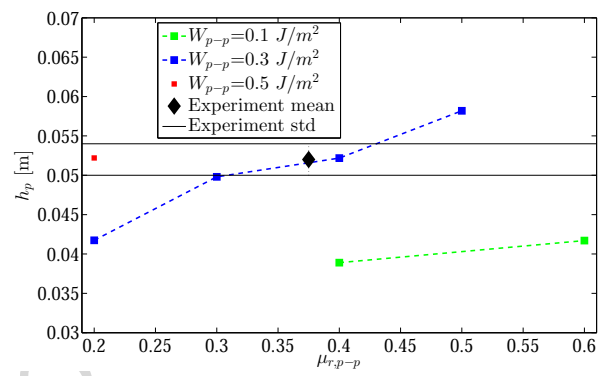


Figure 12: The black diamond is the mean height of the green sand pile experiment of $0.054 \text{ m} \pm 0.002 \text{ m}$ (black horizontal lines).

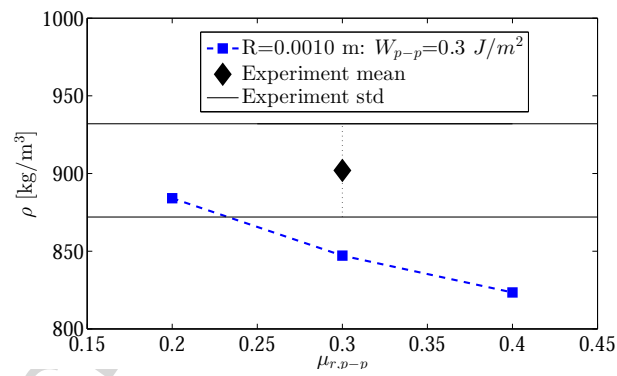


Figure 13: Plot of the density: The black diamond is the mean density of the green sand pile experiment of $902 \pm 30 \frac{\text{kg}}{\text{m}^3}$ (thin black line). The DEM simulations were made for the settings for the cohesion value $W_{p-p} = 0.3 \frac{\text{J}}{\text{m}^2}$ (blue dotted line).

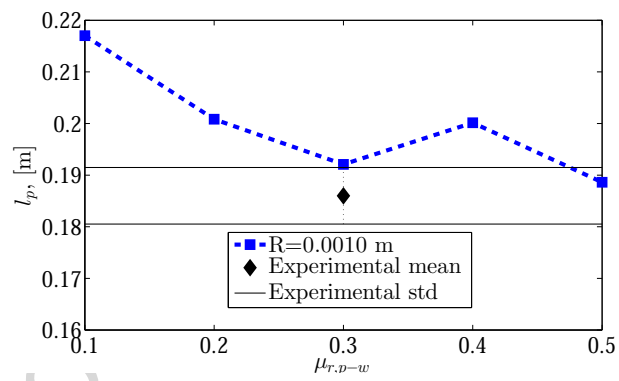


Figure 14: The black diamond is the mean length (diameter) of the green sand slump experiment of 0.186 ± 0.00548 m with the standard deviation of $\sigma = 5.48$ mm (thin black line).

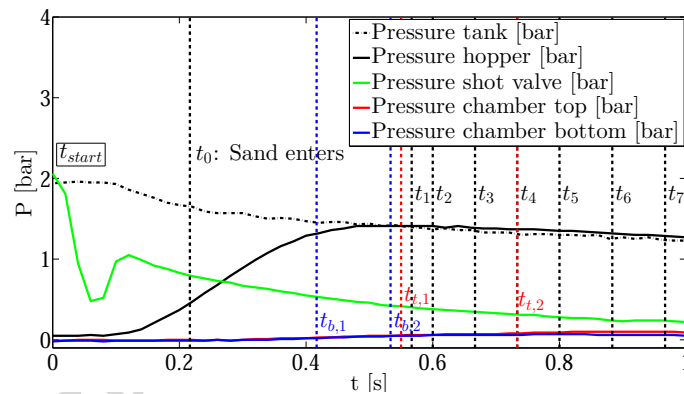


Figure 15: Example from Case 1: The pressure as a function of time is shown in the positions listed from the top to the bottom: The air tank (black dotted line), the shot valve (green), the hopper (black line), the top of the chamber (red line) and the bottom of the chamber (blue line). The atmospheric pressure is used as the reference pressure. The filling times $t_0 - t_7$ in the chamber from the chamber camera v_1 (black dotted lines).

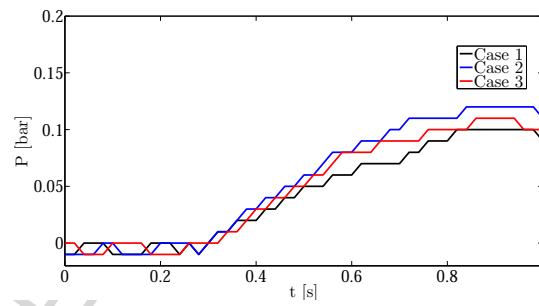


Figure 16: The three cases of experimental pressures measured at the top of the chamber as a function of time with the initial starting time of $t_0 = 0.0$ s. The atmospheric pressure is used as the reference pressure.

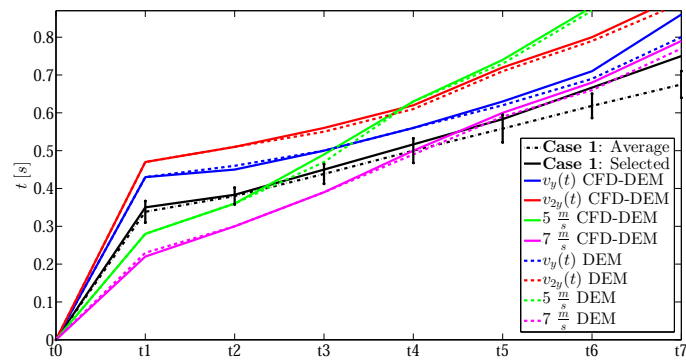


Figure 17: The experimental and simulation filling times of $t_0 - t_7$ for case 1.

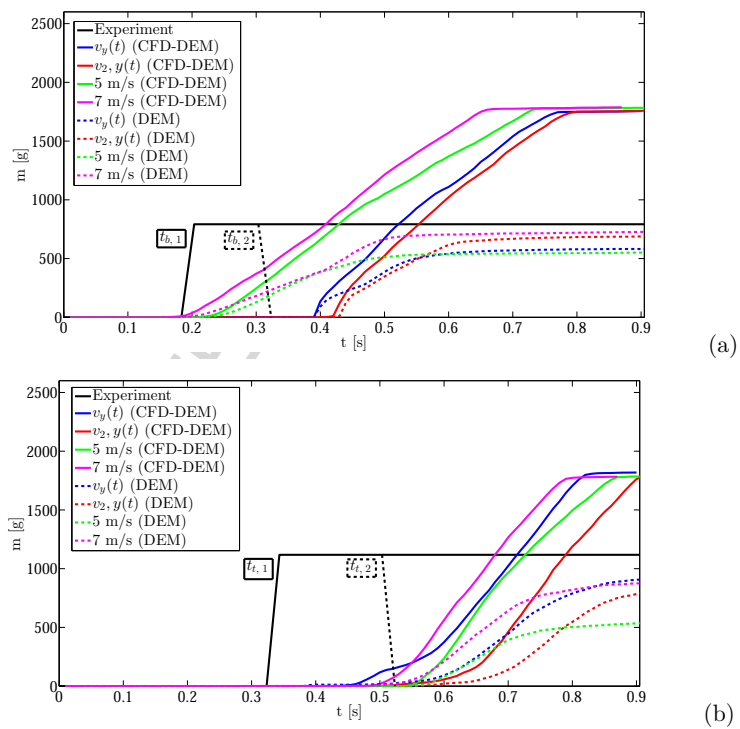


Figure 18: Case 1: The mass as a function of time for the bottom cavity (a) and for the top cavity (b).

SCRIPT

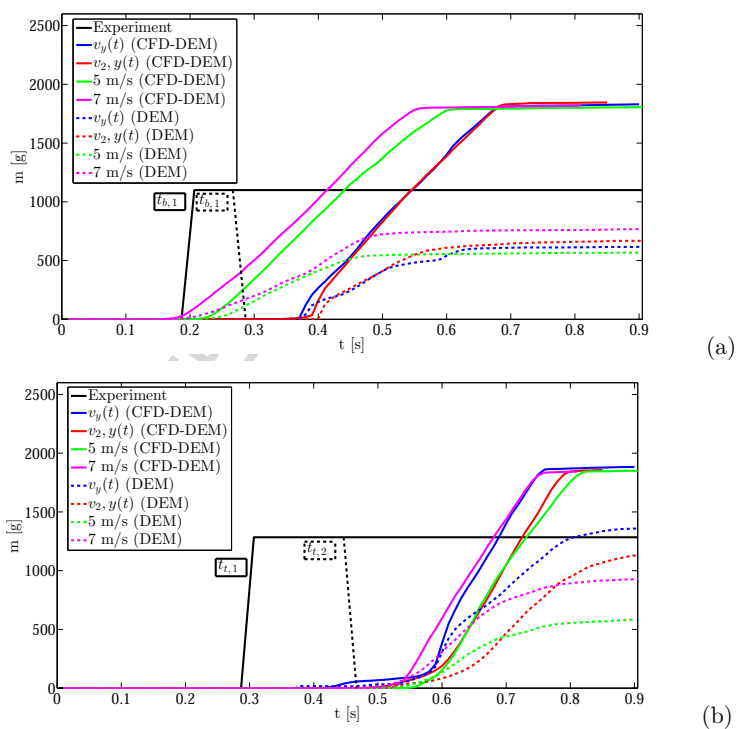


Figure 19: Case 2: The mass as a function of time for the bottom cavity (a) and for the top cavity (b).

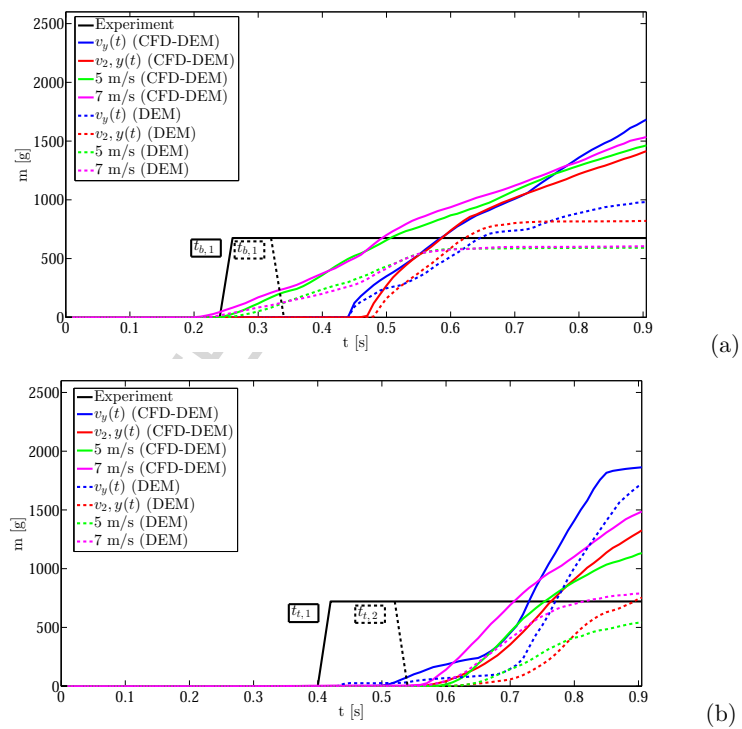


Figure 20: Case 3: The mass as a function of time for the bottom cavity (a) and for the top cavity (b).

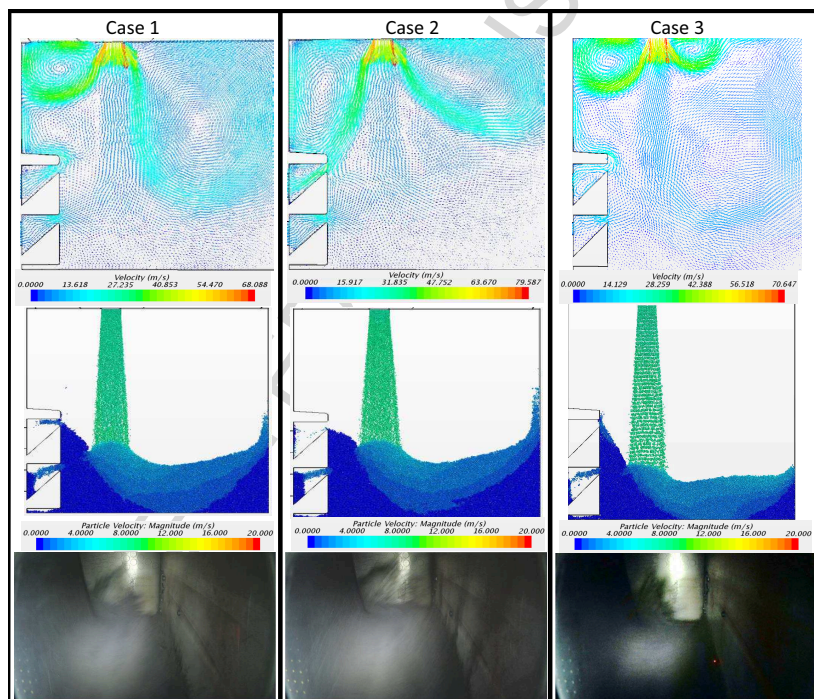


Figure 21: For the selected three cases: The time dependent velocity $v_y(t)$ simulation at time $t=0.50$ s. (Top) The velocity of the air phase. (Middle) The velocity of the particles. (Bottom) The experimental video footage at time $t=0.50$ s.

List of Tables

1	The experimental air vents settings in the chamber for the three cases. In case 2, 62 air vents of the type a_c are blocked in the chamber. Case 3, 14×2 air vents of the type a_p are blocked in each cavity on the pattern plate.	52
2	Simulating of the air vent's settings in the chamber for the three cases. (a) Two sets of air vents are placed on the pattern plate, one in each cavity.	53
3	Results from the test of the green sand calibrating the model. . .	54
4	General material values for all the simulations.	55
5	The calibrated DEM model for simulating the DISAMATIC process.	56
6	(left) Masses in the two cavities from the three cases together with the selected experiments. (right) The compactability test results from the three cases.	57

Table 1: The experimental air vents settings in the chamber for the three cases. In case 2, 62 air vents of the type a_c are blocked in the chamber. Case 3, 14×2 air vents of the type a_p are blocked in each cavity on the pattern plate.

Case	1	2	3
SP top air vents opened (a_c)	52	0	52
PP air vents, opened (a_c)	112	112	112
Pattern plate air vents opened (a_p)	2×28	2×28	2×14
Side air vents opened, (n)	2×37	2×32	2×37
Total opened air vents ($a_c + a_p$)	294	232	266
Experimental repetitions	7	3	3

Table 2: Simulating of the air vent's settings in the chamber for the three cases. (a) Two sets of air vents are placed on the pattern plate, one in each cavity.

Case	1	2	3
SP air vents, (n)	52	0	52
A_{SP} , [m^2]	507.6×10^{-4}	No	507.6×10^{-4}
β_{SP} , [$\frac{m}{s}$]	766.2	No	766.2
PP air vents, (n)	112	112	112
A_{PP} , [m^2]	1296×10^{-4}	1296×10^{-4}	1296×10^{-4}
β_{PP} , [$\frac{m}{s}$]	908.3	908.3	908.3
Pattern plate ^a , (n)	28	28	14
A_p , [m^2]	285.0×10^{-4}	285.0×10^{-4}	142.5×10^{-4}
β_p , [$\frac{m}{s}$]	435.0	435.0	435.0

Table 3: Results from the test of the green sand calibrating the model.

Material property	average	std	Rep.
Static friction coefficient $\mu_{s,p-p}$	0.57	± 0.04	90
Static friction coefficient $\mu_{s,p-p}$	0.33	± 0.02	26
Sand pile height h_p	52×10^{-3} m	2×10^{-3} m	15
Density ρ_{Bulk}	$902 \frac{\text{kg}}{\text{m}^3}$	$\pm 30.0 \frac{\text{kg}}{\text{m}^3}$	27
Slump length l_p	186×10^{-3} m	5.48×10^{-3} m	25
Compactability	36 %	± 2.1 %	27
Water content %	3.5 %	± 0.2 %	42

Table 4: General material values for all the simulations.

Material property	Value
DEM particle radius, (R)	0.001 m
Solid density of the chamber wall (ρ_{wall})	7500 kg/m ³
Youngs modulus of the green sand, (E_p)	17000 MPa
Youngs modulus of the chamber wall, (E_w)	200000 MPa
Poisson ratio of the green sand, (ν)	0.3
Poisson ratio of the chamber wall, (ν)	0.3
Coefficient of restitution particle-particle, (e_n)	0.01
Coefficient of restitution particle-wall, (e_t)	0.01
Gravity (g)	9.82 $\frac{m}{s^2}$
Particle-wall static friction, ($\mu_{s,p-w}$)	0.33
Particle-particle static friction, ($\mu_{s,p-p}$)	0.57
The simulation time step, (Δt)	10 ⁻⁵ s

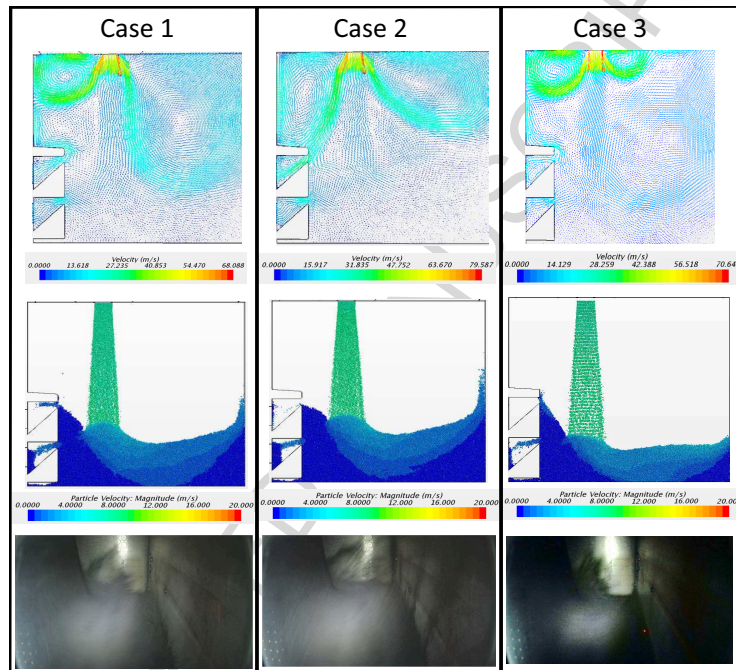
Table 5: The calibrated DEM model for simulating the DISAMATIC process.

Material property	Value
Particle-particle rolling friction coefficient ($\mu_{r,p-p}$)	0.4
Particle-particle cohesion work (W_{p-p})	$0.3 \frac{\text{J}}{\text{m}^2}$
Particle density ρ_{DEM}^*	$1900 \frac{\text{kg}}{\text{m}^3}$
Particle-wall rolling friction coefficient ($\mu_{r,p-w}$)	0.5
The simulation time step, (Δt)	10^{-4} s

Table 6: (left) Masses in the two cavities from the three cases together with the selected experiments. (right) The compactability test results from the three cases.

Case	Rep.	Bottom cavity [g]	Top cavity [g]	Rep.	ρ_{sand} [kg/m ³]
1	7	593±189	961±237	18	920±50.1
1	Selected for simulation	792	1118		
2	3	933±215	1220 ±72.5	9	970±19.7
2	Selected for simulation	1100	1284		
3	3	623±47.7	687±30.2	9	937±28.6
3	Selected for simulation	674.8	721		

Graphical abstract



- The DISAMATIC process and the geometry with the two specially designed cavities for the simulation and the experiment.
- Case 1, case 2 and case 3 for the simulated air flow (top row), the simulated granular flow (middle row) and the experimental flow profile (bottom row).

Highlights

- The calibration of the DEM model was performed with several experiments.
- A special cavity geometry was designed for investigating the locally deposition of green sand during the DISAMATIC process.
- Comparing the dynamics of the granular flow process to DEM and CFD-DEM simulations.

PAPER 4

An analytical solution describing the shape of a yield stress material subjected to an overpressure

E. Hovad, J. Spangenberg, P. Larsen, J. Thorborg, and J. H. Hattel

Citation: *AIP Conference Proceedings* **1738**, 030049 (2016); doi: 10.1063/1.4951805

View online: <http://dx.doi.org/10.1063/1.4951805>

View Table of Contents: <http://aip.scitation.org/toc/apc/1738/1>

Published by the *American Institute of Physics*

An Analytical Solution Describing the Shape of a Yield Stress Material Subjected to an Overpressure

E. Hovad^{*,†}, J. Spangenberg^{*}, P. Larsen[†], J. Thorborg^{**} and J.H. Hattel^{*}

^{*}Process Modelling Group, Department of Mechanical Engineering, Technical University of Denmark, Nils Koppels Allé, 2800 Kgs. Lyngby, Denmark.

[†]DISA Industries A/S, Højager 8, Høje Taastrup, 2630 Taastrup, Denmark

^{**}MAGMA, Kackertstr. 11, 52072 Aachen, Germany.

Abstract. Many fluids and granular materials are able to withstand a limited shear stress without flowing. These materials are known as yields stress materials. Previously, an analytical solution was presented to quantify the yield stress for such materials. The yields stress is obtained based on the density as well as the spread length and height of the material when deformed in a box due to gravity. In the present work, the analytical solution is extended with the addition of an overpressure that acts over the entire body of the material. This extension enables finding the shape of a yield stress material with known density and yield stress when for instance deformed under water or subjected to a forced air pressure.

Keywords: Rheology, Yield stress, Analytical solutions

PACS: 81.05.Je, 02.60.Lj, 47.56.+r, 83.10.-y

INTRODUCTION

Yield stress materials come in many varieties such as green sand [1], concrete [2], and ceramic slurries [3]. Recently, an analytical solution was derived to determine the yield stress of a given material (i.e. a very fluid concrete also known as a self-compacting concrete) [4]. The solution utilizes the density along with the height h_0 and spread length L measured in the LCPC-box test in order to back out the yield stress. The LCPC-box test is performed by pouring 6 liters of material into a box with a height of 0.12 m, a width of 0.2 m, and a length of 1 m, see fig. 1(a-b). This methodology is a cheap low-tech procedure to obtain the yield stress which often is a key parameter when evaluating the flowability of yield stress materials.

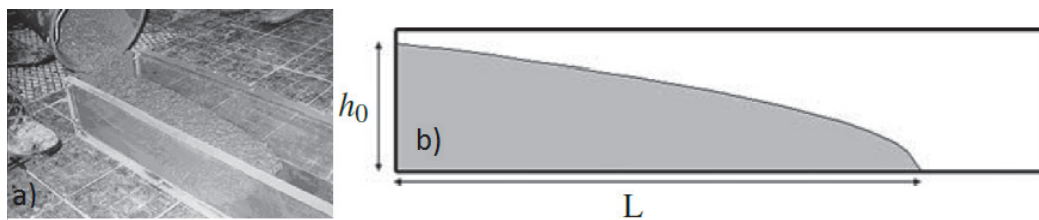


FIGURE 1. (a) LCPC BOX test and (b) height h_0 and length L in the LCPC BOX test are correlated to the yield stress, figures from [5].

In this paper, the analytical solution is presented with an overpressure. This new solution mimics a situation where the yield stress material deforms for instance subsurface or when exposed to an additional air pressure. The deformation is expressed as the length as a function of the height while the input parameters needed are the density and yield stress. In the following, the new solution is first derived in three- and two dimensions and afterwards plotted for different pressures.

3D ANALYTICAL SOLUTION WITH AN OVERPRESSURE

The forces acting on an infinitesimal slice of the yield stress material in the LCPC-box comes from the friction at the bottom and side walls, the hydrostatic pressure, and the overpressure, see fig. 2.

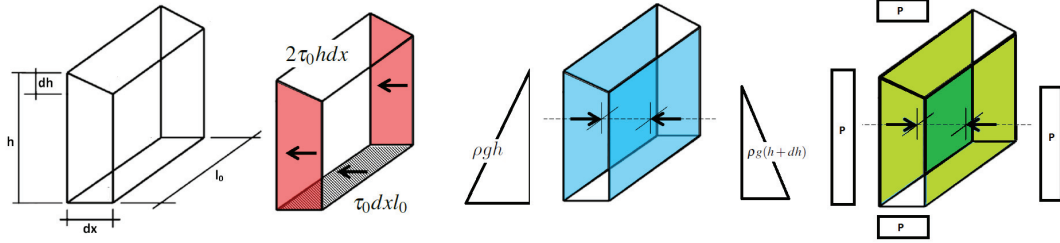


FIGURE 2. An illustration of the friction from the bottom and side walls, the hydrostatic pressure, and the overpressure that act on an infinitesimal slice of the yield stress material in the LCPC-box. The figure is edited from [4] and originates from [5].

The force equilibrium is given by,

$$\left(P + \frac{1}{2}\rho g h\right)h l_0 - \left(P + \frac{1}{2}\rho g(h + dh)\right)(h + dh)l_0 - \tau_0 dx l_0 - 2\tau_0 h dx = 0 \quad (1)$$

where P is the overpressure, ρ is the density, g is the gravitational acceleration, h is height, l_0 is the width of the box and τ_0 is the yield stress. Note that the increment dh is negative due to the decreasing height of the material in the box and that the vertical overpressure is eliminated by the reaction force from the bottom and thereby transferred into a horizontal overpressure.

Assuming that dh^2 is negligible one obtains,

$$\left(\frac{P}{\rho g} + h\right) \frac{dh}{dx} = - \left(\tau_0 + 2\tau_0 \frac{h}{l_0}\right) \frac{1}{\rho g} \quad (2)$$

Solving the differential equation yields the length as a function of the height,

$$x(h) = \frac{(h_0 - h)\rho g l_0}{2\tau_0} + \left(\frac{l_0^2 \rho g}{4\tau_0} - \frac{P l_0}{2\tau_0}\right) \ln\left(\frac{2h + l_0}{2h_0 + l_0}\right) \quad (3)$$

Note that if $P = 0$, then the original solution from [5] is obtained $x(h) = \frac{(h_0 - h + \frac{l_0}{2} \ln(\frac{2h + l_0}{2h_0 + l_0}))\rho g l_0}{2\tau_0}$. The integral of the material is given by the following when assuming that h does not vary with l_0 ,

$$V = l_0 \int_0^{h_0} x(h) dh = l_0 \int_0^{h_0} \frac{(h_0 - h)\rho g l_0}{2\tau_0} + \left(\frac{l_0^2 \rho g}{4\tau_0} - \frac{P l_0}{2\tau_0}\right) \ln\left(\frac{2h + l_0}{2h_0 + l_0}\right) dh \quad (4)$$

Based on the initial volume and width and the assumption that $A = \frac{V}{l_0}$, one obtains,

$$A = \int_0^{h_0} x(h) dh = \frac{\rho g l_0}{2\tau_0} \int_0^{h_0} h_0 - h + \left(\frac{l_0}{2} - \frac{P}{\rho g}\right) \ln\left(\frac{2h + l_0}{2h_0 + l_0}\right) dh \quad (5)$$

which yields,

$$A = \frac{l_0}{8\tau_0} \left(2\rho g h_0^2 - 2l_0 h_0 \rho g + 4P h_0 + (2P l_0 - g l_0^2 \rho) \ln\left(\frac{l_0}{l_0 + 2h_0}\right)\right) \quad (6)$$

Now h_0 can be found iteratively e.g. with the Newton Raphson method. Utilizing h_0 in eqn. (3) together with a known viscosity and density facilitates the solution for the deformed yield stress material.

2D ANALYTICAL SOLUTION WITH AN OVERPRESSURE

In the ideal 2D case, as opposed to the 3D case, there is no influence from the front and back lateral walls ($l_0 \rightarrow \infty$), see fig. 3.

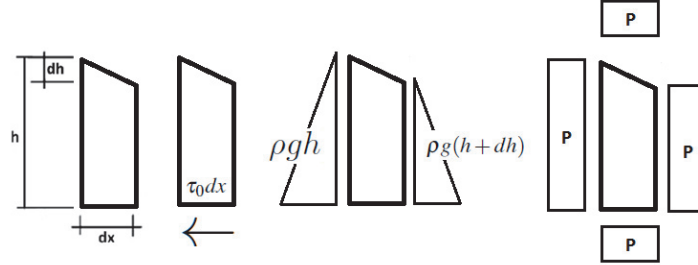


FIGURE 3. An illustration of the friction from the bottom, the hydrostatic pressure, and overpressure that act on an infinitesimal slice of the yield stress material in the ideal 2D case. The figure is edited from [4] and originates from [5].

The force equilibrium is now given by,

$$(P + \frac{1}{2}\rho gh)h - (P + \frac{1}{2}\rho g(h + dh))(h + dh) - \tau_0 dx = 0 \quad (7)$$

Assuming that dh^2 is negligible one obtains,

$$(P + \rho gh)\frac{dh}{dx} = -\tau_0 \quad (8)$$

Solving the differential equation yields the height as function of the length,

$$h(x) = \frac{-P + \sqrt{P^2 + 2\rho g(\tau_0 L - \tau_0 x)}}{\rho g} \quad (9)$$

or the length as function of the height,

$$x(h) = \frac{h_0^2 \rho g}{2\tau_0} - \frac{h^2 \rho g}{2\tau_0} + \frac{Ph_0}{\tau_0} - \frac{Ph}{\tau_0} \quad (10)$$

Note that if $P = 0$, then the original solution from [5] is obtained $x(h) = \frac{h_0^2 \rho g}{2\tau_0} - \frac{h^2 \rho g}{2\tau_0}$. The integral, giving the area, can be expressed as,

$$A = \int_0^{h_0} x(h)dh = \int_0^{h_0} \left(\frac{h_0^2 \rho g}{2\tau_0} - \frac{h^2 \rho g}{2\tau_0} + \frac{Ph_0}{\tau_0} - \frac{Ph}{\tau_0} \right) dh \quad (11)$$

Solving the integral yields,

$$A = \frac{\rho gh_0^3}{3\tau_0} + \frac{h_0^2 P}{2\tau_0} \quad (12)$$

h_0 is then given by,

$$h_0 = \frac{C^{\frac{1}{3}}}{2\rho g} + \frac{P^2}{2\rho g C^{\frac{1}{3}}} - \frac{P}{2\rho g} \quad (13)$$

Where $C = 12A\tau_0\rho^2g^2 + 2\sqrt{6}\sqrt{A\tau_0(6A\rho^2g^2\tau_0 - P^3)}\rho g - P^3$. Utilizing h_0 in eqn. (10) together with a known viscosity and density facilitates the solution for the deformed yield stress material.

Results and Discussion

The final deformed shapes of a yield stress material obtained with the 3D and 2D analytical solutions are illustrated in Fig. 4. The material properties chosen are a density of 1000 kg/m^3 and a yield stress of 100 Pa. The applied over pressures are 0 Pa, 10 Pa, 100 Pa, 1000 Pa and 10000 Pa.

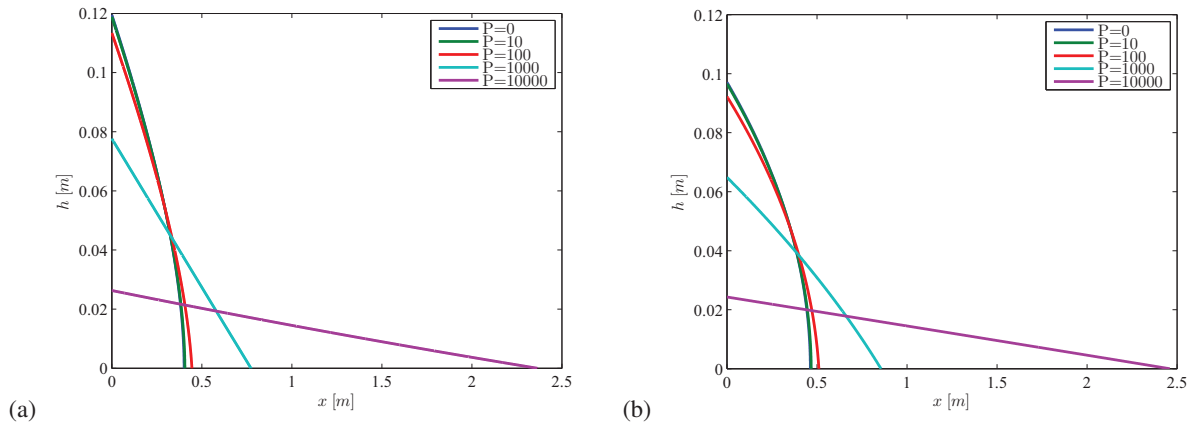


FIGURE 4. Final deformed shapes of a yield stress material obtained with the (a) the 3D analytical solution and an initial volume of 6 liters and a width of $l_0=0.2$ m, (b) the 2D analytical solution and an initial area of 0.03 m^2 and an infinite width $l_0 \rightarrow \infty$. The physical settings are the same for the two simulations: a density of 1000 kg/m^3 , a yield stress of 100 Pa, and an overpressure that varies between 0 Pa and 10000 Pa. Note the different length scales on the axes.

Generally the horizontal pressure squeezes out the material, thereby increasing the spread length L and decreasing h_0 as seen in fig. 4. For small overpressures, the profile becomes more parabolic, while it becomes more and more linear when the overpressure starts to dominate. The figure also illustrates that the spread length for the 3D solution is somewhat less than for the 2D solution especially for low over pressures, since the 3D solution takes into account the friction at the front and back wall.

CONCLUSION

In the present work an extension of the original solution in [5] for the shape of a yield stress material under the influence of gravity has been derived with an over pressure. The basic force in both 2D and 3D equilibrium for an infinitesimal fluid element is established and the resulting differential equations are solved analytically. The final deformation shapes are plotted as a function of distance for increasing values of the overpressure and it is noticed that the shape transfers from parabolic to a more linear shape for increased values of the overpressure.

REFERENCES

1. J. Bast, *Archives of Metallurgy and Materials* **58** (2013).
2. J. Spangenberg, N. Roussel, J. H. Hattel, E. Sarmiento, and M. R. G. G. Zirgulis, *Cement and Concrete Research*. **42**, 1571–1578 (2012).
3. M. Jabbari, and J. Hattel, *Mater. Sci. Tech.* **30**, 283–288 (2014).
4. J. Spangenberg, *PHD-Thesis from Danish Technical University of Denmark (DTU)* (2012).
5. N. Roussel, *Materials and Structures* **40**, 1789–1796 (2007).

PAPER 5

Shape effect of crushed sand filler on rheology: a preliminary experimental and numerical study

J. Spangenberg¹, R. Cepuritis^{2,3}, E. Hovad^{1,4}, G. W. Scherer⁵, S. Jacobsen²

¹Department of Mechanical Engineering, Technical University of Denmark, 2800 Lyngby, Denmark

²Department of Structural Engineering, Norwegian University of Science and Technology, 7491 Trondheim, Norway

³Norcem AS, R&D Department (HeidelbergCementGroup), 3950 Brevik, Norway

⁴DISA Industries A/S, 2630 Taastrup, Denmark

⁵Department of Civil and Environmental Engineering, Princeton University, Princeton, NJ 08544, USA

Abstract Two types of filler from crushed sand were mixed with cement paste with constant superplasticizer dosage per mass of cement to investigate how their shape affects the rheology. The fillers were mylonitic quartz diorite and limestone produced using Vertical Shaft Impact (VSI) crusher and air classification, and had length/thickness (L/T) aspect ratios of 2.00 and 1.82, respectively. The particles were characterized with X-ray micro-computed tomography, coupled with spherical harmonic analysis to mathematically describe the full 3-D shape of the particles, while the rheological performance was quantified with the slump flow test (i.e. mini cone). The shape effect was isolated in the experiments by the use of non-overlapping bimodal particle distributions of cement particles with a number average diameter of ≈ 0.01 mm and filler particles with a number average diameter of ≈ 0.1 mm. The two filler types were tested with a range of χ -values (volume of cement divided by total volume of solids). The flowability of the matrix increased with decreasing aspect ratios of the filler. However, the χ -value at which the maximum volume fraction threshold was obtained varied for the two filler types. Subsequently, a discrete element model was utilized to simulate the experimental data, thereby providing an initial step toward a numerical tool that can assist when proportioning self-compacting concrete with high volumes of crushed sand fines.

Keywords: *Crushed sand filler, shape effect, rheology, numerical modelling, aggregate proportioning*

Introduction

The use of crushed sand filler in concrete production is increasing due to shortage of natural aggregate deposits around the world. This development has implications for the rheological behaviour of the concrete as the crushed sand particles are less equi-dimensional than natural sand grains. The effect of particle shape has been studied by a number of researchers and found to affect rheology to various degrees depending on parameters such as length/width (L/W) ratio [1], packing ability [2], and the cubicity of the particle [3]. However, still more knowledge is needed to account for the filler shape in the design phase of concrete proportioning. Consequently, here the effects of particle shape of industrially produced crushed sand filler on flow are investigated by experiments and modelling to improve the understanding of the effect of the shape of the fines on rheology. This would allow progress in the development and optimization of crushed sand for concrete. The first part of the paper describes the methodology used to characterize the shape of the two filler types (i.e. mylonitic quartz diorite and limestone) and the procedure used to quantify the rheological behaviour of the matrix (comprising water, superplasticizer, cement, and filler). This is followed by a description of the governing equations and calibration of the discrete element method (DEM) computational fluid dynamics model that is used to mimic the experimental findings. Finally, the experimental and numerical results are analysed and the model's potential utility for proportioning self-compacting concrete (SCC) is discussed.

Experiments

The characterization of the shape of the mylonitic quartz diorite and limestone was carried out with X-ray micro-computed (μ CT) tomography, coupled with spherical harmonic (SH) analysis to mathematically describe the full 3-D shape of the particles. The methodology is described in depth by Cepuritis et al. [4, 5]. In general, the procedure involved casting 5 vol% of crushed powders in epoxy and allowing hardening without segregation. After hardening, the samples were scanned using μ CT equipment and complete three-dimensional renderings of the digitized particle size and shape were obtained within the limitation of the voxel size used. The SH coefficients [6] were generated using the μ CT data for each of the particles. The SH approach gives an analytical, differentiable mathematical form for the particle surface and volume, so one can compute any geometric quantity of the particle that can be defined by integrals over the volume or the surface, or over points on the surface or within the volume. The average equivalent particle size was ≈ 0.01 mm for the cement (determined by wet-method laser diffraction) and ≈ 0.1 mm for the two filler types (volume equivalent particle diameter = VESD, obtained from the μ CT SH analysis), see Fig. 1. The mean aspect ratios (length/thickness = L/T and length/width = LW) describing mutually

orthogonal dimensions which form a box that just encloses a particle were the following for the two filler fractions:

- Mylonitic quartz diorite: $L/T = 2.00$ and $L/W = 1.38$ as number-weighted mean values and $L/T = 2.09$ and $L/W = 1.39$ as volume-weighted mean values;
- Limestone: $L/T = 1.82$ and $L/W = 1.32$ as number-weighted mean values and $L/T = 1.90$ and $L/W = 1.30$ as volume-weighted mean values.

The L/T aspect ratios of separate bins of particles from the mylonitic quartz diorite and limestone samples are provided in Fig. 2. Examples of 3-D images (created with Virtual Reality Modelling Language, VRML) based on the SH method of approximating the shape [6] of the two filler types, having the same aspect ratios as introduced above, are shown in Fig. 3.

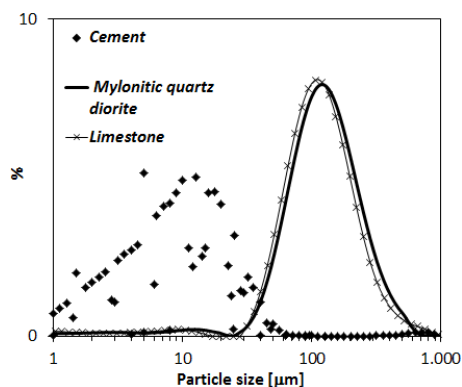


Figure 1. The mass- (or volume-) weighted particle size distributions of the cement, mylonitic quartz diorite and limestone.

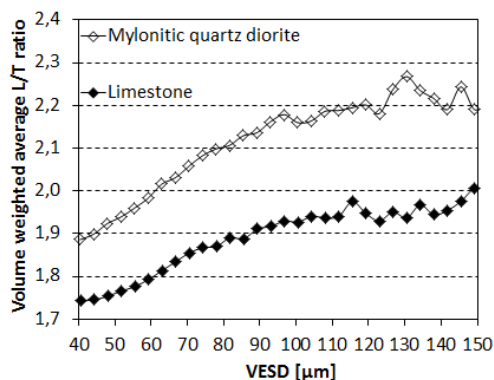


Figure 2. The volume weighted average L/T aspect ratio as a function of the size of the two fillers. Size given as volume equivalent sphere diameter (VESD). The average L/T for each size is based on a high enough number of particles to give converging L/T [5].

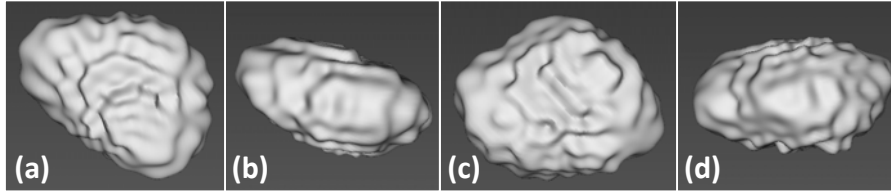


Figure 3. VRML images of particles based on the results from μ CT scanning and SH analysis; (a), (b) two views of a mylonitic quartz diorite particle of $VESD = 52 \mu\text{m}$, $L/T = 2.00$ and $L/W = 1.38$; (c), (d) two views of a limestone particle of $VESD = 52 \mu\text{m}$, $L/T = 1.82$ and $L/W = 1.32$. The number-weighted particle aspect ratios represents the mean values of the whole powder samples, as introduced above.

The density measurements of the three particles were performed with He-pycnometry. The density was 3130 kg/m^3 for the cement and 2770 kg/m^3 for both fillers. Measurements of compacted dry packing gave slightly lower values (0.526) for T1 Quartz than for T6 Limestone (0.536) as expected from differences in average L/T and similar PSD. The procedure used to mix the matrix was developed by Ng et al. [7] and consists of five steps: 1. dry mixing the cement and the filler in question; 2. adding the water and superplasticizer (10 g per kg cement); 3. mixing the matrix for 2 minutes; 4. pausing the mixing for 1 minute; 5. mixing the matrix for additional 2 minutes. The mixing was conducted with a drill machine with a whisk-shaped drill in a plastic cylinder with a diameter of 11 cm and a height of 29.7 cm. The rheological characterization of the matrix was carried out with the slump flow test. The mini cone used for the test had a height of 73 mm, a lower diameter of 89 mm, and an upper diameter of 39 mm, making the cone of similar size as the one used by Roussel et al. [8] when relating the mini-cone test to Abrams cone test.

Numerical model

In this work, the discrete element method (DEM) was used to simulate the flow of the matrix. The DEM method has previously been utilized to emulate the non-Newtonian flow behaviour of fresh cementitious materials in the J-ring test [9], slump flow test [10], and LCPC-box test [11]. The DEM method is an approach where particles are included for discretization purposes (e.g. to describe the flow of a fluid in which the particle could be seen as a virtual particle) and/or for representation of aggregates. In our numerical model, particles were used to discretize the flow of the water as well the movement of cement and filler particles. The model was developed in the commercial software STAR-CCM+. The governing equations that were solved to obtain the flow behaviour of all three phases of the matrix are described in the following.

Normal direction. Hertzian contact mechanics was used [12]. The normal interaction force between the particles i and j is given by

$$\mathbf{F}_{n_{ij}} = \mathbf{n}_{ij} K_n \delta_{n_{ij}}^{3/2} - N_n \mathbf{v}_{n_{ij}}, \quad (1)$$

where \mathbf{n}_{ij} is the normal vector of the plane of the two particles, K_n is the stiffness in the normal direction, $\delta_{n_{ij}}$ is the normal overlap, N_n is the normal damping coefficient, and $\mathbf{v}_{n_{ij}}$ is the normal relative velocity.

Tangential direction. A simplified Mindlin model was used [13]. The tangential force between the particles i and j is defined as

$$\mathbf{F}_{t_{ij}} = K_t \frac{\mathbf{t}_{ij}}{|\mathbf{t}_{ij}|} \delta_{t_{ij}}^{3/2} - N_t \mathbf{v}_{t_{ij}}, \quad (2)$$

where subscript t denotes the tangential direction and \mathbf{t}_{ij} is the tangential displacement given by the product of the tangential relative velocity and the time increment.

Rolling resistance. The torque from the rolling resistance that counteracts the tangential force is defined as

$$\mathbf{T}_{rol} = -\frac{\boldsymbol{\omega}_{rel}}{|\boldsymbol{\omega}_{rel}|} \mu_r R_{eq} |\mathbf{F}_{n_{ij}}|, \quad (3)$$

where $\boldsymbol{\omega}_{rel}$ is the relative rotation between the particle i and j, μ_r is coefficient of rolling friction, and R_{eq} is equivalent radius.

Cohesion force. The cohesion force is obtained with the Johnson-Kendall-Roberts model with the factor of -1.5,

$$\mathbf{F}_{coh} = -1.5 \mathbf{n}_{ij} \pi R_{mn} W, \quad (4)$$

where R_{mn} is the radius of the smallest particle in contact and W is the constant work of cohesion.

Summing forces and torques. The total force on the particle is given by

$$\mathbf{F}_i^{tot} = m_i \mathbf{g} + \sum_j (\mathbf{F}_{n_j} + \mathbf{F}_{t_j} + \mathbf{F}_{coh}), \quad (5)$$

where m_i is the mass of particle i and \mathbf{g} is gravity. The total torque is given by

$$\mathbf{T}_i^{tot} = -R_i \sum_j (\mathbf{n}_{ij} \times \mathbf{F}_{t_j}) + \sum_j (\mathbf{T}_{rot}), \quad (6)$$

where R_i is the radius of particle i . From Eqns. (5) and (6), the acceleration, velocity and position are calculated incrementally for each time step by Newtons 2nd law.

The water and cement particles were both simulated as spheres with a diameter of 0.0025 m, while the fillers were modelled by combining three spheres with a diameter of 0.005 m in order to obtain their individual aspect ratio. These choices had the following implications: 1. the hydrodynamic effect of the water decreased, as the water was modelled as hard spheres; 2. the cement particles would not as easily flow between the larger particles as the size ratio (size of cement particle divided by size of the filler) was less than 1:10; 3. the number of cement and filler particle interactions decreased as the cement and filler were modelled larger than their real size. However, in spite of these simplifications, we believe the model mimics the matrix in a sensible way. In Fig. 5, the particle that represents the mylonitic quartz diorite filler is shown (aspect ratio 2.00). The total number of particles used in each simulation was ~20,000 and the calculation time was a couple of days.

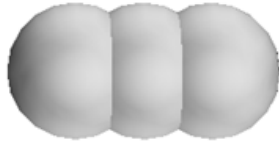


Figure 5: The particle that represents the mylonitic quartz diorite filler.

The simulation of the slump flow test was carried out by randomly filling the cone geometry with particles that represented the three phases, see Fig. 6. Subsequently, the cone geometry constraint was removed and the matrix was able to deform. Finally, the slump was computed when the matrix stopped flowing.

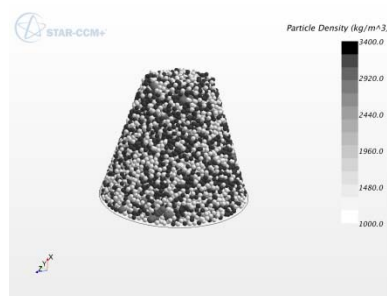


Figure 6. The initial condition for the numerical model. The three phases are water, cement, and mylonitic quartz diorite.

Model Calibration

The DEM approach requires a large set of material parameters such as a rolling resistance and cohesion value describing the interaction between two particles of the same phase, as well as the interaction between two different phases. In this study, these material parameters were obtained with an inverse analysis. Firstly, the rolling resistance and cohesion value were obtained for water and cement by fitting the numerically predicted slump to an experimental result where only those two phases were used. In this experiment, the volume fraction of the cement was 0.416. Secondly, the material parameters were acquired for each type of filler by a similar procedure, now keeping constant the properties of the water and cement and only calibrating the filler parameters. In this experiment, the total volume fraction of solids was 0.5 and the volume of cement divided with the total volume of solids, χ_c was 0.1. After the calibration was performed, the rest of the experiments was simulated only by changing the volume fraction of the phases. The rolling resistance for all three phases was modelled with a coefficient of 0.2. In Table I, the cohesion parameter for the cement and fillers is shown.

Table I. The DEM cohesion parameter for cement, mylonitic quartz diorite, and limestone.

Material	Interaction	Cohesion [J/m ²]
Cement	Water	0.51
	Cement	
Mylonitic quartz diorite	Water	4.10
	Cement	
	Mylonitic quartz diorite	
Limestone	Water	0.45
	Cement	
	Limestone	

Results

In Fig. 7, an example of the experimental and numerical slump flow test is illustrated. In this test, the matrix consisted of water, cement, and mylonitic quartz diorite. The volume fraction of solids in the matrix was 0.533 and χ was 0.35. The slump was found to be 205 mm and 195 mm in the experiment and simulation, respectively. Note that some of the simulated particles are detached from the bulk of the simulated material. This artefact is a consequence of the relative coarse discretization and is disregarded when calculating the numerical slump.



Figure 7. (left) Experimental and (right) numerical slump flow test.

In Fig. 8(left), the experimental slump results for the mylonitic quartz diorite and limestone based matrices are shown for different volume fraction of solids when using $\chi=0.35$. The results illustrate that for a given volume fraction with this χ -value, the limestone based matrix is more flowable than the mylonitic quartz diorite based matrix, which is expected, since the mylonitic quartz diorite has a greater L/T aspect ratio than the limestone. In addition, it is seen that the results can be approximated with a linear relationship and that this relationship can be used to approximate the volume fraction at which the matrix for the given χ -value does not flow (i.e. the slump is equal to the bottom diameter of the mini-cone). This volume fraction is here referred to as the volume fraction threshold. Comparing the experimental and numerical results for the limestone based matrix with $\chi=0.35$, see Fig. 8(right), the predictions of the numerical model are within 10% of the experiment values, but the slope (based on only 3 points) appears to be quite different resulting in a larger volume fraction threshold for the numerical results. A similar analysis to find experimental and numerical volume fraction thresholds for the two types of filler with $\chi=0.1$, 0.4 and 1 is shown in Fig. 9. The experimental results indicate that the maximum volume fraction threshold is found at increasing χ -values when the aspect ratio of the filler increases. It is interesting to see that this trend is observed for aspect ratios that vary by less than 10 %, which emphasises the importance of taking the shape effect of the filler into account when proportioning SCC. The numerical predictions differ by 4-10 % (relative) from the experimental values, which is not bad, considering that the

cement and filler phases in the numerical model were calibrated for a single volume fraction at $\chi=1$ and 0.1, respectively. In general, the numerical solution overestimates the volume fraction threshold and its gradient from $\chi = 0.35$ to 0.4 (in one case it predicts a wrong gradient), but it correctly accounts for the relative positions of the curves for the two aspect ratios. The discrepancies might be decreased by refining the discretization and/or exploiting other interactions models.

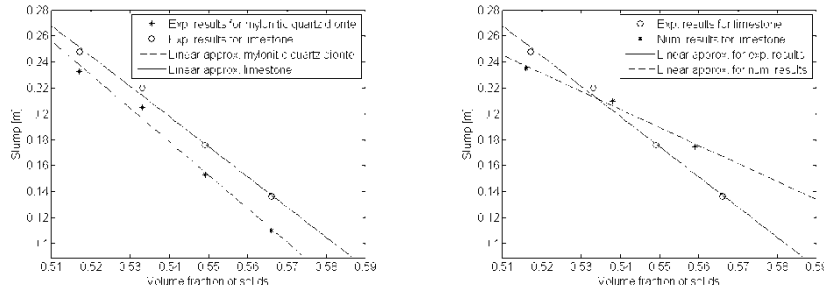


Figure 8. (left) Experimental slump results and linear approximation for the mylonitic quartz diorite and limestone based matrices at different volume fraction of solids when using $\chi=0.35$. (right) Experimental and numerical slump results and linear approximation for the limestone based matrices at different volume fraction of solids when using $\chi=0.35$.

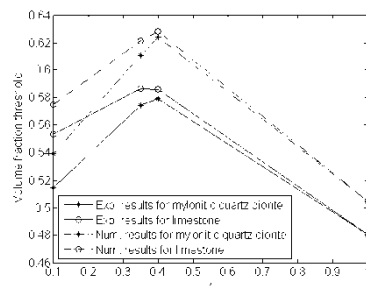


Figure 9. Experimental and numerical volume fraction thresholds as a function of χ for the two types of filler.

Conclusion

In this paper, we isolated the shape effect of crushed sand fillers on rheology by the use of non-overlapping bimodal particle distributions of cement and filler. The experimental findings showed that the flowability of the matrix decreased with increasing aspect ratio of the filler, and that the maximum volume fraction threshold varied for the two types of filler. We used a DEM model to simulate the slump flow tests and obtained numerical predictions that were within 10 % of the

experimental results. The discrepancy resulted in a slight overestimation of the volume fraction threshold by the model. Nevertheless, the numerical results seem promising and we intend to further develop the DEM model by refining the discretization and exploring other interaction models.

Acknowledgements

The authors would like to thank Dr. Edward J. Garboczi of NIST for help with the μ CT SH analysis and Dr. Ya Peng for helping with the rheology measurements. We also acknowledge the support of the Scientific Research Council on Technology and Production Sciences a part of the Danish Council for Independent Research (Contract No. 4005-00381), and the Norwegian Research Council (Contract No. 247619/O30).

References

- [1] Douglas, J. F., Garboczi, E. (1995), *Adv. Chem. Phys.*, vol. XCI, pp. 85-153.
- [2] Larrard, F. de, (1999), E & FN Spon, London.
- [3] Andus, D. J., Hassan, A. M., Garboczi, E. J., Douglas, J. F. (2015), *Soft Matter*, vol. 11, n. 17, pp. 3360-3366.
- [4] Cepuritis, R., Garboczi, E. J., Jacobsen, S., and Snyder, K., *Powder Technol.*, (submitted).
- [5] Cepuritis, R., Garboczi, E. J., and Jacobsen, S., *Cem. Concr. Comp.*, (submitted).
- [6] Garboczi, E. (2002), *Cem. Concr. Res.*, vol. 32, pp. 1621-1638.
- [7] Ng., S., Mujica, H., and Smeplass, S. (2014), *Nord. Concr. Res.*, vol. 51, no. 3, pp. 15-28.
- [8] Roussel, N., Stefani, C., and Leroy, R. (2005), *Cem. Concr. Res.* vol. 35, pp. 817-822.
- [9] Gram, A. (2009), Licentiate thesis, Royal Institute of Technology (KTH)
- [10] Mechtcherine, V., Gram, A., Krenzer, K., Schwabe, J-H., Shyshko, S., Roussel, N. (2014), *Mater. Struct.*, vol. 47, pp. 615-630.
- [11] Roussel, N., Gram, A., Cremonesi, M., Ferrara, L., Krenzer, K., Mechtcherine, V., Shyshko, S., Skocek, J., Spangenberg, J., Svec, O., Thrane, L. N., Vasilic, K., *Cem. Concr. Res.*, (in press).
- [12] Hertz, H. (1881), *J. Angew. Math.*, vol. 171, pp. 156-171.
- [13] Tsuji, Y., Tanaka, T., Ishida, T. (1992), *Powder Technol.* vol. 71, pp. 239-250.

PAPER 6

Proceedings of the ASME 2016 International Mechanical Engineering Congress and
Exposition
IMECE 2016
November 11–17, 2016, Phoenix, AZ, USA

IMECE2016-66469

RHEOLOGICAL CHARACTERIZATION OF GREEN SAND FLOW

Masoud Jabbari*

Jon Spangenberg

Emil Hovad

Raphaël Comminal

Jesper H. Hattel

Process Modelling Group

Department of Mechanical Engineering

Technical University of Denmark

2800 Kgs. Lyngby, Denmark

Katja I. Hartmann

Anton Paar Germany GmbH

73760 Ostfildern

Germany

Denis Schütz

Anton Paar GmbH

8054 Graz

Austria

ABSTRACT

The main aim of this paper is to characterize experimentally the flow behaviour of the green sand that is used for casting of sand moulds. After the sand casting process is performed, the sand moulds are used for metal castings. The rheological properties of the green sand is important to quantify as they can be used to evaluate whether the casting process will be successful. In addition, the properties can potentially be implemented in a computational fluid dynamics model which can be used as a tool to optimize the process. The rheological experiments are carried out on a MCR 502 rheometer with a new module for characterizing granular materials. The new module enables viscosity measurements of the green sand as function of the shear rate at different flow rates, i.e. 0, 2, 4, 6, 8, 10, 12 and 15 L/min. The results show generally that the viscosity decreases with both the shear- and flow rate. In addition, the measurements show that the green sand flow follows a shear-thinning behaviour even after the full fluidization point.

INTRODUCTION

Flow of granular materials is an important and complex phenomenon that is relevant when trying to understand many technical and natural processes, such as sand moulding, slurry

pipelines, fluidized beds, mining and milling operations, abrasive water jet machining, food processing, debris flows, and avalanches. One main difficulty when studying granular materials is that it behaves differently depending on the way it is handled. For strongly agitated particles, the granular material behaves like a dissipative gas [1]. Whereas, for quasi-static deformations, it is often described by a plasticity theory [2]. In between these two regimes, granular materials flows like a liquid, and this is incompatible with the assumptions of the kinetic theory [3, 4]. For this reason, a continuum treatment is often used, in which the variables are averaged properties whose governing equations are derivable, in principle, from the known microscopic laws [5, 6].

Over the last decades there have been many theoretical [7–11] and experimental [12–15] attempts conducted to characterize dense granular flows in different configurations. Bakhtiyarov and Overfelt reviewed related literature of the hydrodynamics of aggregative fluidization (gas-solid beds) with special emphasis on rheological quantification of silica sand [16]. They also showed how to measure the apparent viscosity of fluidized silica sand utilizing both Poiseuille flows (capillary viscometer) and Couette flows (rotational viscometer) [17]. In this paper, we focus on characterizing the flow properties of green sand that is used to produce sand moulds for metal castings. The characterization is carried out with a state-of-the-art device that allows

*Address all correspondence to this author. Email: mjab@mek.dtu.dk

for viscosity measurements while an air stream is forced through the granular material. Being able to quantify the rheological behaviour under a given air stream is particularly important for this process, as the sand casting is performed by forcing green sand from a hopper via an air overpressure into a cavity, see Fig. 1. The paper is divided into three sections: 1) 'Experiments' where the material and experimental set-up is described; 2) 'Results' where the viscosity measurements are presented and discussed; 3) 'Conclusion' where the main findings are summarized.

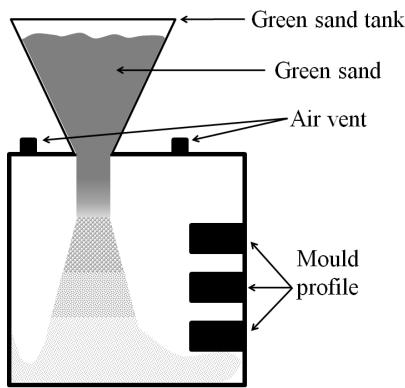


FIGURE 1. Schematic illustration of green sand moulding.

EXPERIMENTS

The green sand used in the experiments consisted of sand, bentonite clay (5 to 11%), pulverized coal and water (2 to 4%), see Fig. 2. The water reacts with the bentonite clay and produces a bind between the sand particles, which is one of the key parameters in controlling the fluidity of the green sand and thereby differentiates its flow behavior from "normal" silica sand. All measurements were carried out on a MCR 502 (Anton Paar, Ostfildern, Germany) rheometer with the powder cell seen in Fig. 3, in a profiled cylinder according to standard liquid rheological tests (DIN 53019, and ISO 3219) [18]. A pressure drop test and a rheology test (viscosity as a function of the shear- and flow rate) were performed. In the pressure drop test, the device increases the rate of the air flow that is introduced from vents below the sample and detects the volumetric flow rates that causes a pressure drop in the cell. The drop indicates the minimum volumetric flow that is needed to fully fluidize the sample, i.e. every particle is surrounded by air and a homogeneous powder bed is created. This test was carried out with a sample volume of 80 mL (104.4 gr). In the rheology test, the air flow was kept fixed at different rates while the rotating velocity of the stirring blade was increased. At the same time, the torque was continuously measured in order to back-out the apparent viscosity. This test was

carried out with a sample volume of 90 mL (114 gr) and before every measurement the sample was fully fluidized in a sample preparation step.



FIGURE 2. Green sand sample used for shear dependent behaviour measurements.

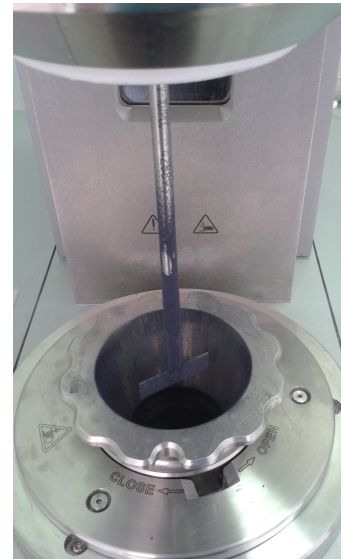


FIGURE 3. The powder cell.

RESULTS

Fig. 4 shows the results of the pressure drop tests for the green sand. It can be seen that the initial fluidization occurs at the flow rate of approximately 5 L/min, while the full fluidization of the green sand is taking place at a flow rate of approximately 10 L/min. The two tests are identical and they have been conducted to verify the reproducibility of the experiments.

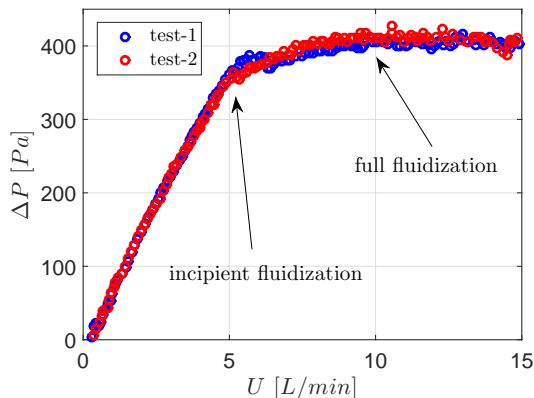


FIGURE 4. Pressure drop measurement on green sand.

In Fig. 5, the viscosity as a function of the shear rate is plotted for different flow rates. The results show that by increasing the flow rate, the viscosity of the green sand decreases. The decrease in viscosity is more pronounced at lower flow rates (i.e. from 0 to 2 L/min). Interestingly, the figure also depicts that the viscosity decreases after the full fluidization point (10 L/min). In addition, the measurements illustrate a shear-thinning behaviour for all flow rates, and that this phenomenon is less dominant at higher flow rates. A similar trend was observed for silica sand in [16, 17].

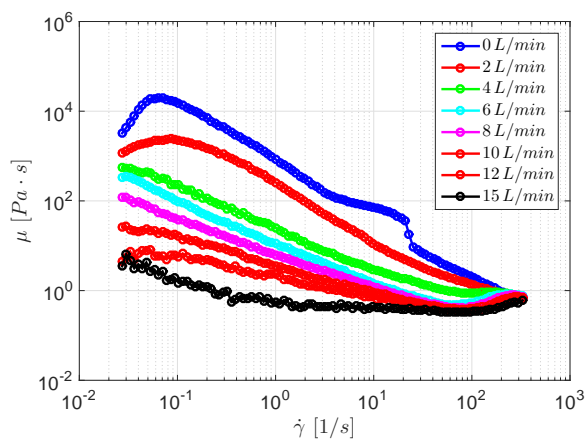


FIGURE 5. Shear dependent behavior of green sand at different flow rates (viscosity vs. shear rate).

Influence of an increase in the flow rate on the viscosity of the green sand is depicted in Fig. 6. It can be seen clearly from the results (for 50 and 100 rpm), that the same trend was found compared to the results presented by Bakhtiyarov and Overfelt [16].

The differences in the magnitude are due to different samples—silica sand and green sand—and different dimensions used for sampling.

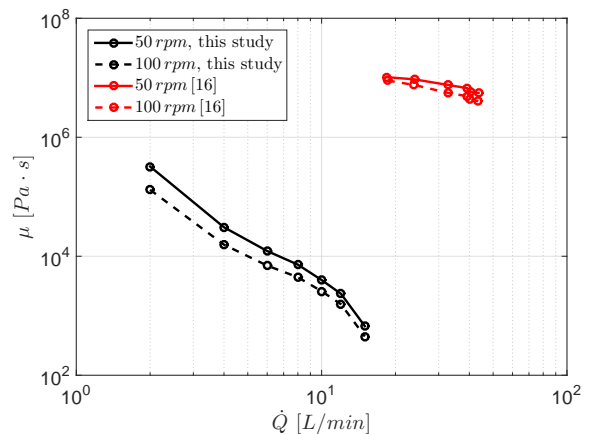


FIGURE 6. Influence of flow rate on the viscosity, compared to the results from [16].

In Fig. 7, the shear stress as a function of the shear rate is plotted for different flow rates. It can be seen that when extrapolating the data towards zero shear rate, the green sand has a yield point for any given flow rate. This yield point decreases with increasing flow rate.

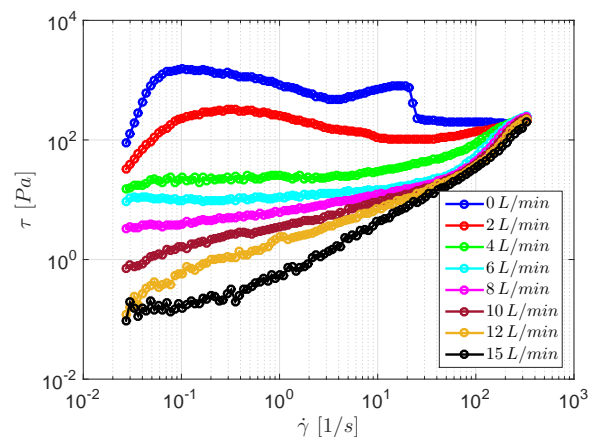


FIGURE 7. Shear stress vs. shear rate relationship for green sand at different flow rates.

CONCLUSION

In this paper, we have characterized experimentally the flow behaviour of the green sand. The rheological tests were conducted on a MCR 502 (Anton Paar, Ostfildern, Germany) to quantify the viscosity of the green sand as a function of the shear and flow rate.

We have shown that the green sand flow behaves like a shear-thinning fluid, in which the viscosity is reduced by increasing the shear rate. On the other hand, the viscosity of the green sand is decreased by increasing the flow rate, and hence, the shear-thinning behaviour becomes less pronounced.

We have moreover shown that there is a yield point in the shear stress-shear rate curve for the green sand, and this yield point decreases with increasing flow rate.

Finally, these information can be used as a tabular data in conducting continuum based CFD simulations.

REFERENCES

- [1] Campbell, C., 1990. "Rapid granular flows". *Annual Review of Fluid Mechanics*, **22**(1), pp. 57–90.
- [2] Goldhirsch, I., 2003. "Rapid granular flows". *Annual review of fluid mechanics*, **35**(1), pp. 267–293.
- [3] Tan, M., and Goldhirsch, I., 1998. "Rapid granular flows as mesoscopic systems". *Physical Review Letters*, **81**(14), p. 3022.
- [4] Mort, P., Michaels, J., Behringer, R., Campbell, C., Kondic, L., Langroudi, M. K., Shattuck, M., Tang, J., Tardos, G., and Wassgren, C., 2015. "Dense granular flow—A collaborative study". *Powder Technology*, **284**, pp. 571–584.
- [5] Silbert, L., Ertas, D., Grest, G., Halsey, T., Levine, D., and Plimpton, S., 2001. "Granular flow down an inclined plane: Bagnold scaling and rheology". *Physical Review E*, **64**(5), p. 051302.
- [6] Jop, P., Forterre, Y., and Pouliquen, O., 2006. "A constitutive law for dense granular flows". *Nature*, **441**(7094), pp. 727–730.
- [7] Louge, M. Y., 2003. "Model for dense granular flows down bumpy inclines". *Physical Review E*, **67**(6), p. 061303.
- [8] Josserand, C., Lagrée, P.-Y., and Lhuillier, D., 2004. "Stationary shear flows of dense granular materials: a tentative continuum modelling". *The European Physical Journal E*, **14**(2), pp. 127–135.
- [9] da Cruz, F., Emam, S., Prochnow, M., Roux, J., and Chevoir, F., 2005. "Rheophysics of dense granular materials: Discrete simulation of plane shear flows". *Physical Review E*, **72**(2), p. 021309.
- [10] Halsey, T., 2011. "Theoretical considerations for granular flow". In *Glasses and Grains*. Springer, pp. 111–135.
- [11] Barker, T., Schaeffer, D., Bohorquez, P., and Gray, J., 2015. "Well-posed and ill-posed behaviour of the $\mu(I)$ -rheology for granular flow". *Journal of Fluid Mechanics*, **779**, pp. 794–818.
- [12] Pouliquen, O., and Forterre, Y., 2002. "Friction law for dense granular flows: application to the motion of a mass down a rough inclined plane". *Journal of Fluid Mechanics*, **453**, pp. 133–151.
- [13] Forterre, Y., and Pouliquen, O., 2003. "Long-surface-wave instability in dense granular flows". *Journal of Fluid Mechanics*, **486**, pp. 21–50.
- [14] MiDi, G., 2004. "On dense granular flows". *The European Physical Journal E*, **14**(4), pp. 341–365.
- [15] Jop, P., Forterre, Y., and Pouliquen, O., 2005. "Crucial role of sidewalls in granular surface flows: consequences for the rheology". *Journal of Fluid Mechanics*, **541**, pp. 167–192.
- [16] Bakhtiyarov, S., and Overfelt, R., 1999. "Recent advances in the rheology of fluidized materials". *Rheology Series*, **8**, pp. 1399–1433.
- [17] Bakhtiyarov, S., and Overfelt, R., 1998. "Fluidized bed viscosity measurements in reduced gravity". *Powder technology*, **99**(1), pp. 53–59.
- [18] Mezger, T., 2006. *The rheology handbook: for users of rotational and oscillatory rheometers*. Vincentz Network GmbH & Co KG.

PAPER 7

An non-dimensionized analytical solution describing the shape of a yield stress material subjected to an overpressure

E. Hovad^{*,†}, J. Spangenberg^{*}, P. Larsen[†], J. Thorborg^{**} and J.H. Hattel^{*}

^{*}Process Modelling Group, Department of Mechanical Engineering, Technical University of Denmark, Nils Koppels Allé, 2800 Kgs. Lyngby, Denmark.

[†]DISA Industries A/S, Højager 8, Høje Taastrup, 2630 Taastrup, Denmark

^{**}MAGMA, Kackertstr. 11, 52072 Aachen, Germany.

Abstract. Many fluids and granular materials are able to withstand a limited shear stress without flowing. These materials are known as yield stress materials. Previously, an analytical solution was presented to quantify the yield stress for such materials. The yield stress is obtained based on the density as well as the spread length and height of the material when deformed in a box due to gravity. In the present work, the analytical solution is non-dimensionalized and extended with the addition of an overpressure that acts over the entire body of the material. This extension enables finding the shape of a yield stress material with the known density and yield stress when for instance deformed under water or subjected to a forced air pressure.

Keywords: Rheology, Yield stress, Analytical solutions

PACS: 81.05.Je, 02.60.Lj, 47.56.+r, 83.10.-y

INTRODUCTION

Yield stress materials come in many varieties such as green sand [1], concrete [2], and ceramic slurries [3]. Recently, an analytical solution was derived to determine the yield stress of a given material (i.e. a very fluid concrete also known as a self-compacting concrete) [4]. The solution utilizes the density along with the height h_0 and spread length L measured in the LCPC-box test in order to back out the yield stress. The LCPC-box test is performed by pouring 6 liters of material into a box with a height of 0.12 m, a width of 0.2 m, and a length of 1 m, see fig. 1(a-b). This methodology is a cheap low-tech procedure to obtain the yield stress which often is a key parameter when evaluating the flowability of yield stress materials.

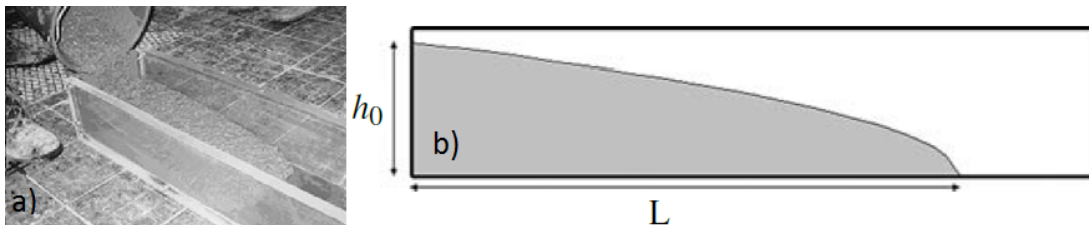


FIGURE 1. (a) LCPC BOX test and (b) height h_0 and length L in the LCPC BOX test are correlated to the yield stress, figures from [5].

In this paper, the analytical solution is presented non-dimensionized and with an additional overpressure. This new solution mimics a situation where the yield stress material deforms for instance subsurface or when exposed to an additional air pressure. The original two- and three dimensional analytical solutions are non-dimensionized with respect to a characteristic length scale derived from initial volume poured in the box. Three new non-dimensionized numbers are introduced via the characteristic length scale and they are density and characteristic length scale versus yield stress, pressure versus yield stress and at last for the three dimensional case the width of the box versus characteristic length scale. The deformation is expressed as the length as a function of the height non-dimensionized characteristic length scale while the original input parameters needed was the density and yield stress. Then the new solution is first derived in two- and three in non-dimensionized form and afterwards plotted for the three different non-dimensionized numbers. A parameter study of these three non-dimensionized numbers effect on the solutions is investigated and perfect connection is found between the two dimensional and three dimensional solutions with or without additional

overpressure.

NON-DIMENSIONLIZING THE ORIGINAL ANALYTICAL 2-D SOLUTION

The original ideal 2-D case from [5] as illustrated in fig. 2 without pressure (P), gives the force equilibrium,

$$mg \quad (1)$$

$$\frac{1}{2}\rho gh^2 - \frac{1}{2}\rho g(h+dh)(h+dh) - \tau_0 dx = 0 \quad (2)$$

Assuming that dh^2 is negligible one obtains,

$$\rho gh \frac{dh}{dx} = -\tau_0 \quad (3)$$

the characteristic length scale (S) is chosen from the initial yield stress material poured in the 2-D LCPC-box. The length scale is the initial area (A) poured into the LCPC-box squared,

$$S = \sqrt{A} \quad (4)$$

Using eqn. (4) to non-dimensionlize the variables $\tilde{x} = \frac{x}{S}$ and $\tilde{h} = \frac{h}{S}$ in eqn. (3),

$$\rho g S \tilde{h} \frac{d\tilde{h}}{d\tilde{x}} = -\tau_0 \quad (5)$$

Separating the variables non-dimensionlized variables,

$$\frac{\rho g S}{\tau_0} \tilde{h} d\tilde{h} = -d\tilde{x} \quad (6)$$

the non-dimensionlized spread length number is introduced,

$$D_s = \frac{\rho g S}{\tau_0} \quad (7)$$

Note, D_s can be interpreted as the hydrostatic pressure that drives the flow versus the yield stress that resist the flow of the yield stress material.

Inserting eqn. (7) in eqn. (6) and integrating to find the relation of the non-dimensionlized height \tilde{h} as a function of the non-dimensionlized length \tilde{x} ,

$$\tilde{h}(\tilde{x}) = \sqrt{\frac{2(-\tilde{x} + \tilde{L})}{D_s}} \quad (8)$$

Note the length \tilde{L} is found from the function $\tilde{h}(\tilde{L}) = 0$, the height is zero at the length \tilde{L} .

The length variable \tilde{x} can be found as a function of the height \tilde{h} ,

$$\tilde{x} = \tilde{L} - \frac{D_s}{2} \tilde{h}^2 \quad (9)$$

the non-dimensional spread length can be found at $\tilde{x} = 0$,

$$\tilde{L} = \frac{D_s}{2} \tilde{h}_0^2 \quad (10)$$

Inserting eqn. (10) into eqn. (9) which gives the shape of the yield stress material as a function of the the non-dimensionlized length of the box \tilde{x} and non-dimensionlized height \tilde{h} ,

$$\tilde{x}(\tilde{h}) = \frac{D_s}{2} (\tilde{h}_0^2 - \tilde{h}^2) \quad (11)$$

Using the initial poured yield stress materials area (A) and thereby finding the final height h_0 by integrating over the height function $x(h)$,

$$A = \int_0^{h_0} x(h) dh \quad (12)$$

inserting the original ideal 2-D dimensionalized solution $x(h) = \frac{\rho g}{2\tau_0} (h_0^2 - h^2)$ from [5] into (12) and dividing with the characteristic length scale squared ($S^2 = A$) from eqn. (4),

$$\frac{A}{S^2} = \frac{\rho g}{2\tau_0 S^2} \int_0^{h_0} h_0^2 - h^2 dh \quad (13)$$

and inserting the non-dimensional spread length (D_s) eqn. (7) into (13),

$$1 = \frac{D_s}{2S^3} \int_0^{h_0} h_0^2 - h^2 dh \quad (14)$$

solving the integral yields and finding the non-dimensional height $\tilde{h}_0 = \frac{h_0}{S}$,

$$\tilde{h}_0 = \left(\frac{3}{D_s} \right)^{\frac{1}{3}} \quad (15)$$

since the final height \tilde{h}_0 is a function of only the parameter D_s in eqn. (15) the only parameter changing the final shape of the yield stress material eqn. (11) is the non-dimensionalized spread length D_s ,

$$\tilde{x}(\tilde{h}) = \frac{1}{2} \left(3^{\frac{2}{3}} D_s^{\frac{1}{3}} - D_s \tilde{h}^2 \right) \quad (16)$$

Note that the interval for the height \tilde{h} is $0 \leq \tilde{h} \leq \tilde{h}_0 = \left(\frac{3}{D_s} \right)^{\frac{1}{3}}$, where the length is zero at the top height \tilde{h}_0 of the deformed yield stress material $\tilde{x}(\tilde{h}_0) = 0$.

The spread length \tilde{L} can also be expressed only by D_s from inserting $\tilde{x}(\tilde{h} = 0) = \tilde{L}$,

$$\tilde{L} = \frac{3^{\frac{2}{3}} D_s^{\frac{1}{3}}}{2} \quad (17)$$

2D ANALYTICAL SOLUTION WITH AN OVERPRESSURE

The original 2-D case from [5] with an additional overpressure, see fig. 2.

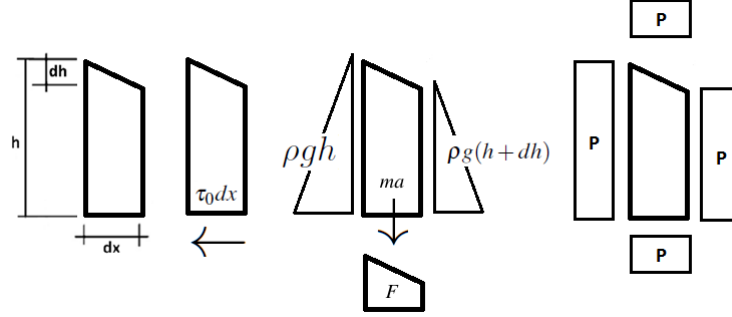


FIGURE 2. An illustration of the friction from the bottom, the hydrostatic pressure, and overpressure that act on an infinitesimal slice of the yield stress material in the ideal 2D case. The figure is edited from [4] and originates from [5].

The force equilibrium is now given by,

$$\left(P + \frac{1}{2}\rho g h\right)h - \left(P + \frac{1}{2}\rho g (h + dh)\right)(h + dh) - \tau_0 dx = 0 \quad (18)$$

Assuming that dh^2 is negligible one obtains,

$$(P + \rho g h) \frac{dh}{dx} = -\tau_0 \quad (19)$$

using the characteristic length scale (S) from eqn. (4), gives the non-dimensionalized variables $\tilde{x} = \frac{x}{S}$ and $\tilde{h} = \frac{h}{S}$,

$$\left(\frac{P}{\tau_0} + \frac{\rho g S}{\tau_0} \tilde{h}\right) d\tilde{h} = -d\tilde{x} \quad (20)$$

Introducing the non-dimensional pressure number,

$$D_p = \frac{P}{\tau_0} \quad (21)$$

and using the non-dimensional spread length D_s eqn. (7) in eqn. (20),

$$(D_p + D_s \tilde{h}) d\tilde{h} = -d\tilde{x} \quad (22)$$

Integrating yields the height as function of the length,

$$\tilde{h}(\tilde{x}) = \frac{-D_p + \sqrt{D_p^2 - 2D_s(\tilde{x} - \tilde{L})}}{D_s} \quad (23)$$

Note the length \tilde{L} is found from $\tilde{h}(\tilde{L}) = 0$, where the height is zero.

The \tilde{x} length can be found as a function of the height \tilde{h} ,

$$\tilde{x}(\tilde{h}) = -D_s \frac{\tilde{h}^2}{2} - D_p \tilde{h} + \tilde{L} \quad (24)$$

The non-dimensional spread length \tilde{L} is found at $\tilde{x}(\tilde{h}_0) = 0$,

$$\tilde{L} = D_p \tilde{h}_0 + D_s \frac{\tilde{h}_0^2}{2} \quad (25)$$

inserting the length \tilde{L} from eqn. (25) into eqn. (24) gives the length as a function of the height non-dimensionalized. The final shape of the yield stress material from the non-dimensionalized length \tilde{x} as a function of the non-dimensionalized height \tilde{h} ,

$$\tilde{x}(\tilde{h}) = D_s \left(\frac{\tilde{h}_0^2}{2} - \frac{\tilde{h}^2}{2} \right) + D_p (\tilde{h}_0 - \tilde{h}) \quad (26)$$

From the area A of the initial yield stress material and integrating over the dimensional solution $x(h)$, the dimensional solution can be found by multiplying eqn. (26) with eqn. (4). Then the height can be found,

$$A = \int_0^{h_0} x(h) dh = \int_0^{h_0} \frac{h_0^2 \rho g}{2\tau_0} - \frac{h^2 \rho g}{2\tau_0} + \frac{Ph_0}{\tau_0} - \frac{Ph}{\tau_0} dh \quad (27)$$

Dividing with the characteristic length scale squared $S^2 = A$ from eqn. (4) and inserting $D_s = \frac{\rho g S}{\tau_0}$ and $D_p = \frac{P}{\tau_0}$ in eqn. (27), gives the non-dimensional integral,

$$1 = \int_0^{h_0} \frac{D_s}{S^3} \left(\frac{h_0^2}{2} - \frac{h^2}{2} \right) + \frac{D_p}{S^2} (h_0 - h) dh \quad (28)$$

integrating gives,

$$1 = \frac{D_s}{3} h_0^3 + \frac{D_p}{2} h_0^2 \quad (29)$$

finding \tilde{h}_0 by solving the cubic equation,

$$\tilde{h}_0 = \frac{C_1^{\frac{1}{3}}}{2D_s} + \frac{D_p^2}{2D_s C_1^{\frac{1}{3}}} - \frac{D_p}{2D_s} \quad (30)$$

Where $C = 2\sqrt{6}D_s\sqrt{-D_p^3 + 6D_s^2 - D_p^3 + 12D_s^2}$ and note if $D_p = 0$, then eqn. (30) gives eqn. (15) for the height with no additional pressure.

Since the final height \tilde{h}_0 is a function of only the parameters D_s and D_p thereby inserting eqn. (30) into eqn. (26) gives the final shape of the yield stress material and the function is only dependent on D_s and D_p .

Now the length is a function of only the parameters D_s and D_p also and can be found by $\tilde{x}(\tilde{h} = 0) = \tilde{L}$, the length was found earlier in eqn. (25).

THE NON-DIMENSIONLIZING ORIGINAL ANALYTICAL 3-D SOLUTION

The original 3-D case from [5] is as in fig. 3 without the pressure term.

The original force equilibrium is now given by,

$$\rho g \frac{h^2}{2} l_0 - \rho g \frac{(h+dh)^2}{2} l_0 - 2\tau_0 dxh - \tau_0 dxl_0 = 0 \quad (31)$$

removing second order terms dh^2 ,

$$\rho gh \frac{dh}{dx} = - \left(1 + \frac{2h}{l_0} \right) \tau_0 \quad (32)$$

Introducing the new non-dimensional length number by the characteristic length scale (S) from eqn. (4) as,

$$\tilde{l}_0 = \frac{l_0}{S} \quad (33)$$

this gives the non-dimensional variables $\tilde{x} = \frac{x}{S}$, $\tilde{h} = \frac{h}{S}$ and $D_s = \frac{\rho g S}{\tau_0}$ and thereby the non-dimensional differential equation,

$$D_s \frac{\tilde{h}}{\left(1 + \frac{2\tilde{h}}{\tilde{l}_0} \right)} \frac{d\tilde{h}}{d\tilde{x}} = -1 \quad (34)$$

Solving the differential equation yields the non-dimensionalized solution for the length as a function of height,

$$\tilde{x} = \frac{\tilde{l}_0 D_s}{2} \left(\tilde{h}_0 - \tilde{h} + \frac{\tilde{l}_0}{2} \ln \left(\frac{2\tilde{h} + \tilde{l}_0}{2\tilde{h}_0 + \tilde{l}_0} \right) \right) \quad (35)$$

Note that the constant from the integration in eqn. (34) is found by setting $\tilde{x}(\tilde{h}_0) = 0$.

Finding \tilde{h}_0 from the known initial volume poured in the box which is equal to the area under the deformed material $x(h)$ multiplied by the width l_0 ,

$$V = l_0 \int_0^{h_0} x(h) dh = l_0 \int_0^{h_0} \frac{\rho g l_0 \left(h_0 - h + \frac{l_0}{2} \ln \left(\frac{2h + l_0}{2h_0 + l_0} \right) \right)}{2\tau_0} dh \quad (36)$$

the original solution $x(h)$ from [5] can be found by multiplying eqn. (35) with S . The assumption of l_0 is independent of h is used. Integrating and based on the initial volume and the width, then the area is $\frac{V}{l_0} = A$,

$$A = \frac{l_0 \rho g}{8\tau_0} \left(2h_0^2 - 2l_0 h_0 - l_0^2 \ln \left(\frac{l_0}{l_0 + 2h_0} \right) \right) \quad (37)$$

Non-dimensionalizing by dividing with $S^2 = A$ and using $D_s = \frac{\rho g S}{\tau_0}$ gives the non-dimensional equation,

$$1 = \frac{D_s \tilde{l}_0}{8} \left(2\tilde{h}_0^2 - 2\tilde{l}_0 \tilde{h}_0 - \tilde{l}_0^2 \ln \left(\frac{\tilde{l}_0}{\tilde{l}_0 + 2\tilde{h}_0} \right) \right) \quad (38)$$

the height \tilde{h}_0 needs to be solved by a numerical method as e.g. Newton-Raphson method.

Since the final height \tilde{h}_0 is a function of only the two parameters D_s and \tilde{l}_0 by inserting the numerical solution of eqn. (38) into eqn. (35) gives the final shape of the yield stress material by these two parameters.

Now the length ($\tilde{L} = \frac{L}{s}$) can also be found from inserting $\tilde{x}(\tilde{h} = 0) = \tilde{L}$ into eqn. (35)

$$\tilde{L} = \frac{\tilde{l}_0 D_s}{2} \left(\tilde{h}_0 + \frac{\tilde{l}_0}{2} \ln \left(\frac{\tilde{l}_0}{2\tilde{h}_0 + \tilde{l}_0} \right) \right) \quad (39)$$

The length is a function of only the two parameters D_s and \tilde{l}_0 also.

3D ANALYTICAL SOLUTION WITH AN OVERPRESSURE

The forces acting on an infinitesimal slice of the yield stress material in the LCPC-box comes from the friction at the bottom and side walls, the hydrostatic pressure, and the overpressure, see fig. 3.

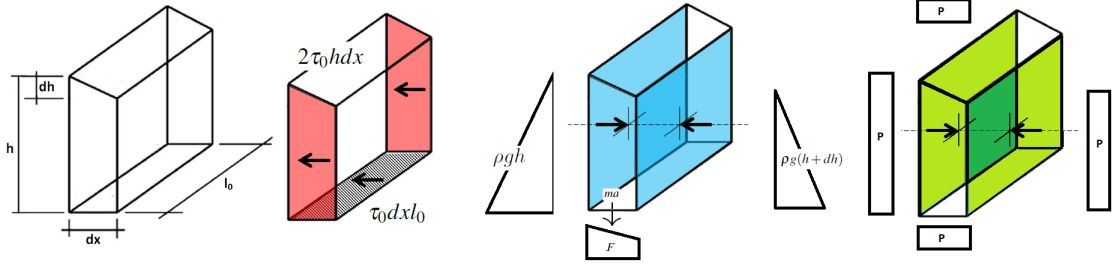


FIGURE 3. An illustration of the friction from the bottom and side walls, the hydrostatic pressure, and the overpressure that act on an infinitesimal slice of the yield stress material in the LCPC-box. The figure is edited from [4] and originates from [5].

The force equilibrium is given by,

$$\left(P + \frac{1}{2}\rho g h\right)h l_0 - \left(P + \frac{1}{2}\rho g (h + dh)\right)(h + dh)l_0 - \tau_0 dx l_0 - 2\tau_0 h dx = 0 \quad (40)$$

where P is the overpressure, ρ is the density, g is the gravitational acceleration, h is height, l_0 is the width of the box and τ_0 is the yield stress. Note that the increment dh is negative due to the decreasing height of the material in the box and that the vertical overpressure is eliminated by the reaction force from the bottom and thereby transferred into a horizontal overpressure.

Assuming that dh^2 is negligible one obtains,

$$\left(\frac{P}{\rho g} + h\right) \frac{dh}{dx} = - \left(\tau_0 + 2\tau_0 \frac{h}{l_0}\right) \frac{1}{\rho g} \quad (41)$$

using the non-dimensional numbers; the characteristic length scale of $S = \sqrt{A}$, $D_s = \frac{\rho g S}{\tau_0}$, $D_p = \frac{P}{\tau_0}$ and $\tilde{l}_0 = \frac{l_0}{S}$ gives the non-dimensional equation,

$$\left(\frac{D_p}{D_s} + \tilde{h}\right) \frac{d\tilde{h}}{d\tilde{x}} = - \left(1 + 2\frac{\tilde{h}}{\tilde{l}_0}\right) \frac{1}{D_s} \quad (42)$$

Solving the non-dimensionalized differential equation yields the length as a function of the height getting the non-dimensional solution of the height as a function length

$$\tilde{x} = \frac{D_s \tilde{l}_0}{2} (\tilde{h}_0 - \tilde{h}) + \left(\frac{D_s \tilde{l}_0^2}{4} - \frac{\tilde{l}_0 D_p}{2}\right) \ln \left(\frac{2\tilde{h} + \tilde{l}_0}{2\tilde{h}_0 + \tilde{l}_0}\right) \quad (43)$$

converting to the dimensional solution by multiplying with S from eqn. (4) and inserting $D_s = \frac{\rho g S}{\tau_0}$ and $D_p = \frac{P}{\tau_0}$,

$$x = \frac{(h_0 - h)\rho g l_0}{2\tau_0} + \left(\frac{l_0^2 \rho g}{4\tau_0} - \frac{P l_0}{2\tau_0}\right) \ln \left(\frac{2h + l_0}{2h_0 + l_0}\right) \quad (44)$$

Volume integral can be made from the initial volume with the assumption of l_0 is independent of h is used,

$$V = l_0 \int_0^{h_0} x dh = l_0 \int_0^{h_0} \frac{(h_0 - h)\rho g l_0}{2\tau_0} + \left(\frac{l_0^2 \rho g}{4\tau_0} - \frac{P l_0}{2\tau_0}\right) \ln \left(\frac{2h + l_0}{2h_0 + l_0}\right) dh \quad (45)$$

Dividing with l_0 getting the area A ,

$$A = \int_0^{h_0} x(h) dh = \int_0^{h_0} \frac{(h_0 - h)\rho g l_0}{2\tau_0} + \left(\frac{l_0^2 \rho g}{4\tau_0} - \frac{P l_0}{2\tau_0}\right) \ln \left(\frac{2h + l_0}{2h_0 + l_0}\right) dh \quad (46)$$

getting the relation of h_0 and the area A ,

$$A = \frac{l_0}{8\tau_0} \left(2\rho g h_0^2 - 2l_0 h_0 \rho g + 4Ph_0 + (2Pl_0 - gl_0^2 \rho) \ln \left(\frac{l_0}{l_0 + 2h_0} \right) \right) \quad (47)$$

the non-dimensional equation of (47) is found by dividing with $S^2 = A$ and inserting D_s and D_p ,

$$1 = \frac{\tilde{l}_0}{8} \left(2D_s \tilde{h}_0^2 - 2\tilde{l}_0 \tilde{h}_0 D_s + 4D_p \tilde{h}_0 + (2D_p \tilde{l}_0 - \tilde{l}_0^2 D_s) \ln \left(\frac{\tilde{l}_0}{\tilde{l}_0 + 2\tilde{h}_0} \right) \right) \quad (48)$$

To find the height \tilde{h}_0 of the final deformed yield stress material from eqn. (48) a numerical as e.g. Newton-Raphson method is needed.

Since the final height \tilde{h}_0 is only dependent of the three parameters D_s , D_p and \tilde{l}_0 by inserting the numerical solution of eqn. (48) into eqn. (43) gives the final shape of the yield stress material.

By inserting $\tilde{x}(\tilde{h} = 0) = L$ in eqn. (43) the spread length can be found from,

$$L = \frac{D_s \tilde{l}_0}{2} \left(\tilde{h}_0 + \frac{\tilde{l}_0}{2} \ln \left(\frac{\tilde{l}_0}{\tilde{l}_0 + 2\tilde{h}_0} \right) \right) + \frac{D_p \tilde{l}_0}{2} \ln \left(\frac{\tilde{l}_0 + 2\tilde{h}_0}{\tilde{l}_0} \right) \quad (49)$$

The length is only dependent of the three parameters D_s , D_p and \tilde{l}_0 also.

Results and discussion

The three parameters D_s , D_p and l_0 are changed to investigate the behaviour of the physical system. The final deformed shapes of a yield stress material obtained with the 2D and 3D analytical solutions with and without additional horizontal pressure are illustrated and presented in Fig. 4 to Fig.7 and the next sections.

2-D non-dimensionalized

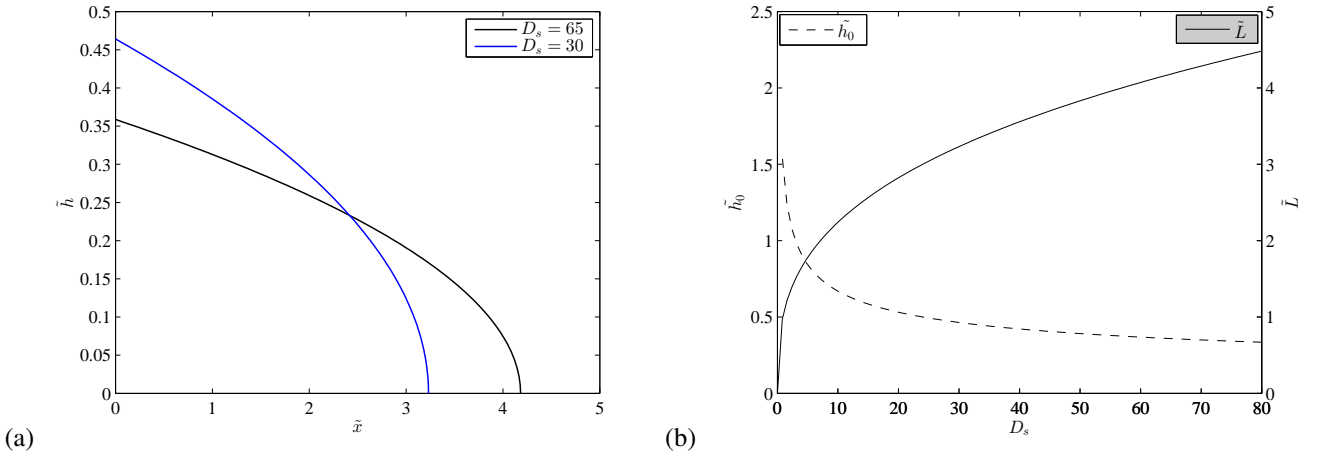


FIGURE 4. Final deformed shapes of a yield stress material obtained with the (a) the 2D analytical solution with the non-dimensionalized spread length number of $D_s = 65$ (black line) and $D_s = 30$ (blue line), (b) The final height \tilde{h}_0 at the y-axis on the left and the final length \tilde{L} at the y-axis on the right as a function of the non-dimensionalized spread length number of D_s . Note the different length scales on the axes.

The material properties chosen are the non-dimensional spread lengths of $D_s = 30$, $D_s = 65$ for the non-dimensionalized 2-D case. Increasing the non-dimensional spread length from $D_s = 30$ to $D_s = 65$ increases flow ability by increasing the gravity effect compared to the yield stress effect and thereby gives a lower and wider

profile seen in Fig. 4(a). The relationship of the height \tilde{h}_0 versus the length \tilde{L} for the non-dimensional spread length D_s can be seen in Fig. 4(b). When D_s is increased then the length increases \tilde{L} and the height \tilde{h}_0 decreases due to the effect of the non-dimensionalized spread length number, again due to the gravity effect making the slumb wider compared to the yield stress effect making the yield stress material "slumb" higher.

2-D non-dimensionalized with additional overpressure

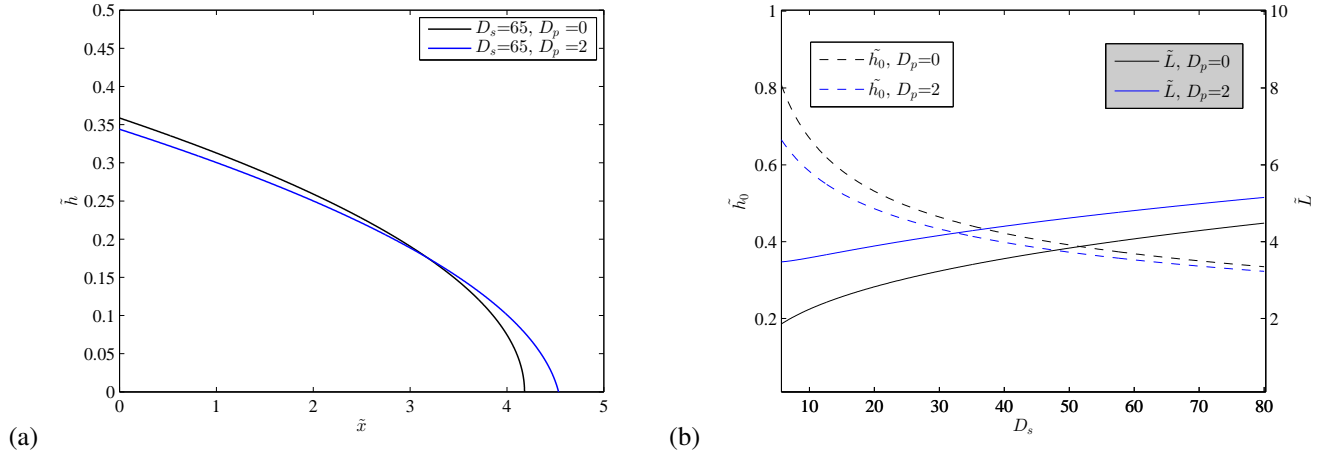


FIGURE 5. Final deformed shapes of a yield stress material obtained with the (a) the 2D analytical solution with the non-dimensionalized spread length number of $D_s = 65$ with the values of $D_p = 0$ (black line) and $D_p = 2$ (blue dotted line). (b) The final height \tilde{h}_0 at the y-axis on the left and the final length \tilde{L} at the y-axis on the right as a function of the non-dimensionalized spread length number of D_s for $D_p = 0$ and $D_p = 2$. Note the different length scales on the axes.

The non-dimensional overpressure of $D_p = 2$ (blue line) gives a wider profile of the yield stress material, since it "squeezes" the material out to the sides compared $D_p = 0$ (black line) Fig.5(a). When D_s is increased in Fig. 5(b), then the length increases \tilde{L} and the height \tilde{h}_0 decreases due to the effect of the non-dimensionalized spread length number, again due to the gravity effect making the slumb wider compared to the yield stress effect making the yield stress material "slumb" higher. The overpressure of $D_p = 2$ makes the profile yield stress material wider and lower.

3-D non-dimensionalized

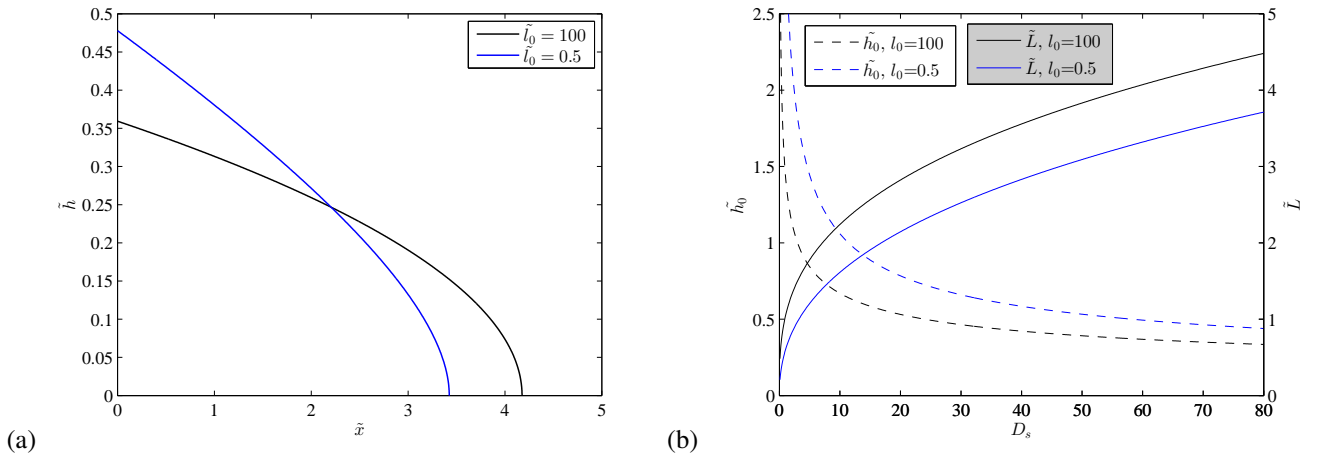


FIGURE 6. Final deformed shapes of a yield stress material obtained with the (a) the 3D analytical solution with the non-dimensionlized spread length number of $D_s = 65$ with the values of $l_0 = 100$ (black line) and $l_0 = 0.5$ (blue line) (b) The final height \tilde{h}_0 at the y-axis on the left and the final length \tilde{L} at the y-axis on the right as a function of the non-dimensionlized spread length number of D_s . Note the different length scales on the axes.

Decreasing the non-dimensional width of the box from $l_0 = 100$ to $l_0 = 0.5$ increases the height due to the increased yield stress due to the side wall and can be seen in Fig. 6(a). The relationship of the height \tilde{h}_0 versus the length \tilde{L} for the non-dimensional spread length D_s can be seen in Fig. 6(b) and when D_s is increased then the length increases \tilde{L} and the height \tilde{h}_0 decreased. When the non-dimensional width is decreased from $l_0 = 100$ to $l_0 = 0.5$ the height is increased and the curve is shifted upward, the opposite effect is seen on the length.

3-D non-dimensionalized with additional overpressure

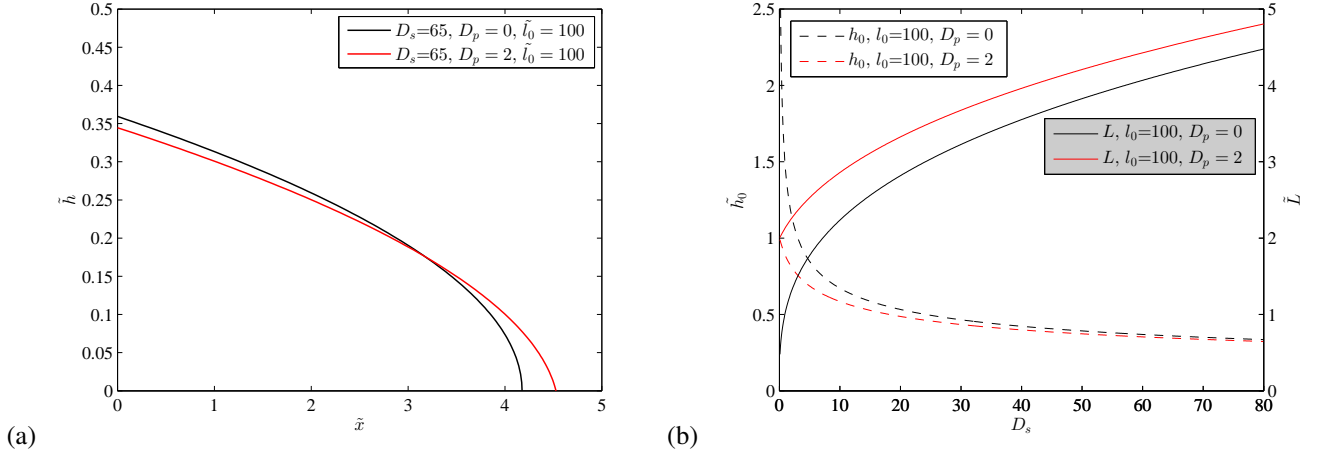


FIGURE 7. Final deformed shapes of a yield stress material obtained with the (a) the 3D analytical solution with the non-dimensionalized spread length number of $D_s = 65$, the width of $l_0 = 100$ and the additional overpressures of $D_p = 0$ (black line and $D_p = 2$ (blue line) (b) The final height \tilde{h}_0 at the y-axis on the left and the final length \tilde{L} at the y-axis on the right as a function of the non-dimensionalized spread length number of D_s . Note the different length scales on the axes.

Generally the non-dimensionalized horizontal pressure squeezes out the material, thereby increasing the spread length L and decreasing h_0 as seen in fig. 7(a) for $D_p = 2$. The relationship of the height \tilde{h}_0 versus the length \tilde{L} for the non-dimensional spread length D_s can be seen in Fig. 7(b) and when D_s is increased then the length increases \tilde{L} and the height \tilde{h}_0 decreased. When the non-dimensional pressure is increased from $D_p = 0$ to $D_p = 2$ the height is decreased and the curve is shifted downward, the opposite effect is seen on the length.

CONCLUSION

In the present work the original solution in [5] for the shape of a yield stress material under the influence of gravity was non-dimensionalized and additional over pressure was added to the derivations. The basic force in both 2D and 3D equilibrium for an infinitesimal fluid element is established and the resulting differential equations are solved analytically. Three non-dimensional numbers D_s , D_p and \tilde{l}_0 was introduced and investigated. The final deformation shapes are plotted as a function of the three non-dimensional numbers. The non-dimensional spread length numbers D_s makes the profile wider and lower, the non-dimensional pressure makes the profile wider, lower and more linear. The non-dimensional width \tilde{l}_0 makes the profile higher and more narrow. The parameter study of three non-dimensionalized numbers effect on the solutions was investigated and perfect connection was found between the two dimensional and three dimensional solutions.

REFERENCES

1. J. Bast, *Arch Metall Mater.* **58** (2013).
2. J. Spangenberg, N. Roussel, J. H. Hattel, E. Sarmiento, and M. R. G. G. Zirculis, *Cem. Concr. Res.* **42**, 1571–1578 (2012).
3. M. Jabbari, and J. Hattel, *Mater. Sci. Tech.* **30**, 283–288 (2014).
4. J. Spangenberg, *PHD-Thesis from Danish Technical University of Denmark (DTU)* (2012).
5. N. Roussel, *Mat. Struct.* **40**, 1789–1796 (2007).

DTU Mechanical Engineering
Section of Manufacturing Engineering
Technical University of Denmark

Produktionstorvet, Bld. 427A
DK-2800 Kgs. Lyngby
Denmark
Phone (+45) 4525 4763
Fax (+45) 4593 0190
www.mek.dtu.dk
ISBN: 978-87-7475-496-1